

# Punching of Flat Slabs with Large Amounts of Shear Reinforcement

THÈSE N° 5409 (2012)

PRÉSENTÉE LE 13 JUILLET 2012

À LA FACULTÉ DE L'ENVIRONNEMENT NATUREL, ARCHITECTURAL ET CONSTRUIT  
LABORATOIRE DE CONSTRUCTION EN BÉTON  
PROGRAMME DOCTORAL EN STRUCTURES

ÉCOLE POLYTECHNIQUE FÉDÉRALE DE LAUSANNE

POUR L'OBTENTION DU GRADE DE DOCTEUR ÈS SCIENCES

PAR

**Stefan LIPS**

acceptée sur proposition du jury:

Prof. L. Laloui, président du jury  
Prof. A. Muttoni, directeur de thèse  
Prof. K. Beyer, rapporteur  
Prof. J. Hegger, rapporteur  
Prof. A. M. Pinho Ramos, rapporteur



ÉCOLE POLYTECHNIQUE  
FÉDÉRALE DE LAUSANNE

Suisse  
2012



*In loving memory of my Dad  
Albert Lips*





## Préface

Les planchers-dalles sont une méthode de construction très répandue en plusieurs pays. Cependant, dans certains cas leur comportement à l'état limite ultime est encore insatisfaisant à cause de la fragilité trop importante en cas de rupture par poinçonnement et plusieurs aspects liés à leur dimensionnement sont encore peu clairs. Pour ces raisons, depuis une douzaine d'années, le poinçonnement des dalles en béton armé représente un domaine important de recherche au Laboratoire de Construction en Béton de l'EPFL. Comme l'ont montré les travaux précédents, une armature transversale n'est pas seulement utile pour augmenter la résistance au poinçonnement, mais permet aussi d'améliorer sensiblement la capacité de déformation. Pour ces raisons, dans la construction des planchers-dalles, l'utilisation d'armature contre le poinçonnement est de plus en plus répandue et un modèle physique permettant de dimensionner l'armature transversale a été développée par M. Fernández Ruiz et le soussigné. Dans le cadre de sa recherche, M. Lips a pu valider ce modèle par une campagne d'essais systématique sur des échantillons de dimensions réelles et avec armatures proches de la réalité ainsi qu'améliorer le modèle dans sa prédiction de la capacité de déformation. Pour le mode de rupture caractérisé par l'écrasement de la première bielle comprimée qui définit la limite supérieure de la résistance au poinçonnement, M. Lips a développé un nouveau modèle basé partiellement sur la théorie de la fissure critique. Ce modèle permet de déterminer de façon très précise la capacité de déformation des dalles en cas de poinçonnement et représente donc une amélioration importante des connaissances dans ce domaine.

Flat slabs are a widespread construction method in several countries, in spite of the fact that, in some cases, their ultimate limit state behavior is unsatisfactory because of their brittleness in the case of failure by punching shear. Some points related to their design and dimensioning of flat slabs remain unclear, which is why, over the past twelve years, the phenomenon of punching shear failure of reinforced concrete slabs has been an important research field for the Structural Concrete Laboratory of EPFL. As previous research works have shown, transverse shear reinforcement does not only help increasing the punching shear strength, but also significantly increasing the deformation capacity of flat slabs, for which the use of punching shear reinforcement is becoming very common. The undersigned and Dr. Fernández Ruiz have developed a physical model for the design and dimensioning of transverse reinforcement to prevent punching failure of flat slabs. In the framework of his research, Mr. Lips has validated this model through a systematic test campaign on life-size specimens with realistic reinforcement configurations. For the failure mode characterized by the crushing of the first compression strut, which defines the upper limit of the punching shear strength, Mr. Lips developed a new model partly based on the critical shear crack theory. This model allows precisely determining the deformation capacity of flat slabs in case of punching and thus constitutes a significant improvement of the knowledge in this field.

Lausanne, June 2012

Prof. Dr. Aurelio Muttoni



## Acknowledgements

This research work was carried out at the Structural Concrete Laboratory (IBETON) at the Ecole Polytechnique Fédérale de Lausanne (EPFL) under the supervision of Prof. A. Muttoni. Thus, first of all, I would like to thank Prof. Muttoni for giving me the opportunity to do what I like most and the liberty to do it as I like.

I would like to thank the jury members Prof. K. Beyer, head of the Earthquake Engineering and Structural Dynamics Laboratory at the EPFL, Prof. J. Hegger, head of the Institute of Concrete Structures at the Rheinisch-Westfälische Technische Hochschule Aachen, Prof. A.M. Pinho Ramos, head of the Structural Engineering Laboratory at the Universidade Nova de Lisboa, for their engagement and for their valuable comments and suggestions. Additionally, I would like to thank Prof. L. Laloui, head of the Laboratory of Soil Mechanics at the EPFL for his service as president of the jury.

I wish to express my gratitude and sincere appreciation to the Swiss National Science Foundation (Project # 121566) for financing this research work. Additionally, I would like to thank the punching shear reinforcement manufacturer Fischer-Rista AG for allowing me to use and to publish certain experimental data.

I would like to thank Dr. O. Burdet and Dr. M. Fernández-Ruiz, Yvonne Bühl and all the current and former PhD students of IBéton with whom I shared a pleasant time with. Special thanks go to my officemates Yaser Mirzaei and Jürgen Einpaul for the interesting, not always work related, discussions and to Galina Argirova for the proof reading of my thesis as well as for the moments of comfortable silence. Additionally, I would like to thank Fabio Brantschen for the help with the French translation of the abstract.

I would like to address thanks to the lab technicians with special thanks to Gérald Rouge and Gilles Guignet without whom it would not have been possible to test 16 slabs in less than 4 months.

I would like to thank the members of the laboratories EESD and MCS for the enjoyable memories. Special thanks to Talayeh Noshiravani and Hadi Kamyab for the great time inside as well as outside of the EPFL.

I would like to thank all the people who in one way or another contributed and supported me throughout my education although it is impossible to name here all by name. However, special thanks go to Prof. A. Kenel who largely contributed to the fact that I started my PhD.

Finally, I would like to thank my family whose support allowed me to follow my dreams whenever and especially wherever I wanted to.



## Abstract

Punching shear reinforcement is an efficient method to increase not only the strength but also the deformation capacity of flat slabs supported by columns. Especially, the increase in deformation capacity is desired so that the load can be distributed to other supports preventing a total collapse of the structure in the case of the occurrence of a local failure. Thus, the research presented herein addresses the punching strength as well as the deformation capacity of flat slabs. Thereby, the focus is set on the analysis of the maximum increase in strength and rotation capacity due to punching shear reinforcement. Therefore, the principal aim is the analysis of flat slabs with large amounts of punching shear reinforcement. In addition to an experimental and numerical investigation of flat slabs, another principal objective of the research project was the development of an analytical model that enables accurate predictions of the punching strength and the rotation capacity of flat slabs with large amounts of shear reinforcement. Thus, the research presented herein can basically be divided into three main parts.

An experimental investigation of sixteen flat slab specimens with and without shear reinforcement leads to new findings with respect to the punching strength and the load-deformation response of flat slabs. The results of the tests serve for the validation of current design codes and the Critical Shear Crack Theory. In addition to the specimens tested within this research project, tests found in literature are used to investigate the influence of certain parameters on the prediction of the punching strength.

A non-linear numerical model on the basis of the Finite Element Method enables the modeling of the test specimens. This approach uses plane stress fields to calculate the moment-curvature response of a discrete slab element. The thereby obtained flexural and torsional stiffness serve as input parameters for a linear-elastic finite element analysis. This analysis enables the modeling of the load-deformation response of the tested slab specimens leading to valuable information regarding the state of deformation at different load levels.

The findings of the experimental and the numerical investigation support the development of an analytical model. The theoretical background of this model is the Critical Shear Crack Theory, which describes the punching strength as a function of the slab rotation. Thus, the developed analytical model enables the calculation of the load-rotation response of flat slab specimens. Moreover, the developed failure criteria enable the prediction of the punching strength as well as the maximum rotation capacity. Finally, it is shown that the results obtained from the developed model are in good agreement with results of tests performed within this research project and of tests found in literature.

**Keywords:** punching shear, shear reinforcement, flat slabs, flexural response



## Kurzfassung

Die Anordnung einer Durchstanzbewehrung ist eine wirksame Methode, um nicht nur den Durchstanzwiderstand sondern auch das Verformungsvermögen von Flachdecken zu erhöhen. Vor allem das verbesserte Verformungsverhalten ist erstrebenswert, so dass die Lasten bei einem lokalen Versagen umgelagert und ein sprödes Versagen des Bauwerks verhindert werden kann. Deshalb befasst sich die hier präsentierte Forschungsarbeit mit dem Durchstanzwiderstand sowie dem Verformungsvermögen von Flachdecken. Dabei stand die Untersuchung der maximalen Erhöhung von Widerstand und Verformungsvermögen bei der Nutzung von Durchstanzbewehrung im Vordergrund. Folglich ist das grundsätzliche Thema der Arbeit die Untersuchung von Flachdecken mit hohem Durchstanzbewehrungsgehalt. Neben einer experimentellen und numerischen Untersuchung von Flachdecken soll ein Modell entwickelt werden, welches den Durchstanzwiderstand sowie das Verformungsvermögen ermitteln kann. Daher kann die Arbeit grundsätzlich in drei Teile gegliedert werden.

Eine experimentelle Untersuchung von sechzehn Plattenausschnitten mit und ohne Durchstanzbewehrung führt zu neuen Erkenntnissen betreffend des Durchstanzwiderstandes und des Verformungsvermögens. Die Versuchsergebnisse dienen zur Validierung von aktuellen Bemessungsnormen und der Theorie des kritischen Schubrisses. Zusätzlich zu den Versuchsergebnissen dieser Forschungsarbeit werden Versuchsergebnisse aus der Literatur verwendet, um den Einfluss verschiedener Parameter auf den ermittelten Durchstanzwiderstand zu untersuchen.

Ein numerisches Modell, basierend auf der Methode der Finiten Elemente, dient zur Nachmodellierung der Versuchsplatten. Die Methode nutzt ebene Spannungsfelder um das Verformungsverhalten des Querschnitts zu ermitteln. Die daraus gewonnenen Biege- und Drillsteifigkeiten des Plattenquerschnitts dienen als Eingabeparameter für eine linear-elastische finite Elemente Berechnung. Diese Berechnung ermöglicht das Nachbilden des Verformungsverhaltens der Versuchsplatten, was zu wichtigen Erkenntnissen bezüglich des Verformungszustandes auf verschiedenen Laststufen führt.

Die Erkenntnisse der experimentellen und numerischen Untersuchung bilden die Grundlagen für die Entwicklung eines analytischen Modells. Als theoretische Basis dient das Modell des kritischen Schubrisses, welches den Durchstanzwiderstand als Funktion der Plattenrotation ermittelt. Dementsprechend erlaubt das analytische Modell die Berechnung des Rotationsverhaltens der Versuchsplatten. Des Weiteren ermöglichen die entwickelten Bruchkriterien die Bestimmung des Durchstanzwiderstandes und des maximalen Rotationsvermögens. Schliesslich kann gezeigt werden, dass die Resultate des entwickelten Modells gut mit Versuchsergebnissen dieses Forschungsprojekts und Versuchsergebnissen aus der Literatur übereinstimmen.

**Stichworte** : Durchstanzen, Durchstanzbewehrung, Flachdecken, Verformungsverhalten





## Résumé

L'armature de poinçonnement est une méthode efficace pour augmenter non seulement la résistance mais aussi la capacité de déformation des planchers-dalles. En particulier, l'amélioration de la capacité de déformation est souhaitable afin qu'il soit possible de redistribuer la charge en cas de rupture locale évitant ainsi un effondrement de toute la structure. De ce fait, la présente recherche traite de la résistance au poinçonnement et de la capacité de déformation des planchers-dalles, avec pour point central l'effet de l'armature de poinçonnement sur l'augmentation maximale de la résistance au poinçonnement et la capacité de rotation. L'objectif principal est donc l'analyse des planchers-dalles avec une quantité importante d'armatures de poinçonnement. Parallèlement à l'analyse expérimentale et numérique, un modèle pouvant prédire la résistance au poinçonnement ainsi que la capacité de la déformation d'un plancher-dalle a été développé. Le travail peut dès lors être divisé en trois parties principales.

L'investigation expérimentale des seize spécimens des planchers-dalles sans et avec armature de poinçonnement donne de nouvelles informations concernant la résistance au poinçonnement et le comportement charge-déformation. Les résultats de ces essais servent de validation des normes de dimensionnement et de la théorie de la fissure critique. En plus des essais contenus dans le cadre de ce projet de recherche, des essais de la littérature sont utilisés pour la recherche de l'influence de certains paramètres quant à la prédiction de la résistance au poinçonnement.

Un modèle numérique basé sur la méthode des éléments finis permet la modélisation des spécimens essayés. Cette méthode utilise des champs de contrainte en plan pour déterminer le comportement en section. La rigidité obtenue par ce calcul est utilisée comme valeur d'entrée au calcul d'éléments finis linéaires-élastiques et permet la modélisation pertinente du comportement charge-déformation des spécimens testés.

Les résultats des essais et du calcul numérique servent au développement d'un modèle analytique. Le modèle est basé sur la théorie de la fissure critique, qui définit la résistance au poinçonnement en fonction de la rotation de la dalle. Le modèle analytique permet ainsi le calcul du comportement charge-rotation d'un plancher-dalle. De plus, les critères de rupture développés dans cette recherche permettent la prédiction de la résistance au poinçonnement et de la capacité de la rotation. Les résultats du modèle proposé donnent de bonnes corrélations avec les résultats des essais dans le cadre de cette recherche ainsi qu'avec les essais trouvés dans la littérature.

**Mots-clés:** poinçonnement, armature de poinçonnement, planchers-dalles, comportement à la flexion



# Table of contents

<b>Préface</b> .....	<b>i</b>
<b>Acknowledgements</b> .....	<b>iii</b>
<b>Abstract</b> .....	<b>v</b>
<b>Kurzfassung</b> .....	<b>vii</b>
<b>Résumé</b> .....	<b>ix</b>
<b>Table of contents</b> .....	<b>xi</b>
<b>Abbreviations</b> .....	<b>xvii</b>
<b>Notations</b> .....	<b>xix</b>
<b>1. Introduction</b> .....	<b>1</b>
1.1. Research significance .....	3
1.2. Objectives .....	3
1.3. Scope .....	4
1.4. Organization .....	5
1.5. Personal contributions .....	6
<b>2. Literature Review</b> .....	<b>7</b>
2.1. Overview of previous research .....	8
2.2. ACI 318-11 (ACI 318 2011).....	11
2.2.1. Slabs without shear reinforcement.....	11
2.2.2. Slabs with shear reinforcement.....	11
2.3. Eurocode 2 (EC2 2004) .....	13
2.3.1. Slabs without shear reinforcement.....	13
2.3.2. Slabs with shear reinforcement.....	14
2.4. German National Annex (NAD 2011).....	16
2.4.1. Slabs without shear reinforcement.....	16
2.4.2. Slabs with shear reinforcement.....	16
2.5. SIA 262 (SIA 262 2003).....	18
2.5.1. Slabs without shear reinforcement.....	18
2.5.2. Slabs with shear reinforcement.....	19
2.6. Model Code (MC 2011).....	21

2.6.1.	Slabs without shear reinforcement .....	21
2.6.2.	Slabs with shear reinforcement .....	22
2.7.	Critical shear crack theory (CSCT) .....	25
2.7.1.	Slabs without shear reinforcement .....	25
2.7.2.	Slabs with shear reinforcement .....	26
2.8.	Load-rotation response .....	34
2.8.1.	Analytical models .....	34
2.8.2.	Numerical models .....	35
2.8.3.	The Quadrilinear model (Muttoni 2008).....	38
<b>3.</b>	<b>Experimental Campaign.....</b>	<b>43</b>
3.1.	Geometry and reinforcement .....	44
3.2.	Materials .....	46
3.3.	Test set-up.....	47
3.4.	Measurements .....	48
3.5.	Results.....	48
3.6.	Discussion of the results .....	52
3.6.1.	Performance of the shear reinforcement .....	52
3.6.2.	Column size .....	52
3.6.3.	Slab thickness.....	53
3.6.4.	Amount of shear reinforcement .....	54
3.6.5.	Shear deformations at column face .....	54
3.6.6.	Opening of the shear cracks .....	56
3.6.7.	Strains in the studs .....	57
3.6.8.	Deformations at the shear-critical region.....	62
<b>4.</b>	<b>Validation of Code Provisions and the CSCT .....</b>	<b>63</b>
4.1.	ACI 318-11 (ACI 318 2011).....	64
4.1.1.	Punching strength.....	64
4.1.2.	Slab thickness.....	64
4.1.3.	Column size .....	65
4.1.4.	Shear reinforcement ratio.....	65
4.2.	Eurocode 2 (EC2 2004) .....	66
4.2.1.	Strength prediction.....	66
4.2.2.	Slab thickness.....	66

4.2.3.	Column size .....	66
4.2.4.	Shear reinforcement ratio.....	67
4.3.	German National Annex to Eurocode 2 (NAD 2011) .....	68
4.3.1.	Strength prediction.....	68
4.3.2.	Slab thickness .....	68
4.3.3.	Column size .....	69
4.3.4.	Shear reinforcement ratio.....	69
4.4.	SIA 262 (SIA 262 2003).....	70
4.4.1.	Strength prediction.....	70
4.4.2.	Slab thickness .....	70
4.4.3.	Column size .....	71
4.4.4.	Shear reinforcement ratio.....	71
4.5.	fib Model code (MC 2011).....	72
4.5.1.	Strength prediction.....	72
4.5.2.	Slab thickness .....	72
4.5.3.	Column size .....	73
4.5.4.	Shear reinforcement ratio.....	73
4.6.	Critical shear crack theory (CSCT) .....	74
4.6.1.	Strength prediction.....	74
4.6.2.	Slab thickness .....	75
4.6.3.	Column size .....	75
4.6.4.	Shear reinforcement ratio.....	75
4.6.5.	Prediction of the slab response and failure criteria.....	76
4.7.	Overview of the performance of the codes.....	79
4.7.1.	Shear reinforcement ratio.....	83
4.7.2.	Effective depth.....	84
4.7.3.	Column size .....	85
4.7.4.	Flexural reinforcement ratio .....	87
4.7.5.	Concrete compressive Strength.....	88
<b>5.</b>	<b>Development of a Nonlinear Finite Element Approach.....</b>	<b>89</b>
5.1.	Flexural stiffness.....	91
5.1.1.	Compatibility conditions.....	91
5.1.2.	Material behavior .....	92

5.1.3.	Equilibrium conditions.....	96
5.2.	Shear stiffness.....	99
5.3.	Analysis.....	100
5.4.	Comparison.....	101
5.4.1.	Pure bending.....	102
5.4.2.	Pure torsion.....	104
5.4.3.	Punching of slabs without shear reinforcement.....	106
5.4.4.	Punching of slabs with shear reinforcement.....	109
<b>6.</b>	<b>Analysis of the Slab Response.....</b>	<b>113</b>
6.1.	Analysis procedure.....	114
6.2.	Global slab behavior.....	117
6.3.	Local slab behavior.....	126
<b>7.</b>	<b>Development of an Analytical Model.....</b>	<b>131</b>
7.1.	General slab behavior.....	132
7.2.	Load-rotation response.....	137
7.2.1.	Global slab behavior.....	137
7.2.2.	Local slab behavior.....	141
7.2.3.	Equilibrium conditions.....	144
7.3.	Failure criteria.....	148
7.4.	Definition of model parameters.....	158
7.4.1.	Limitation of the radial curvature $\chi_{r,lim}$ at radius $r_2$ .....	158
7.4.2.	Radius $r_0$ .....	160
7.4.3.	Shear crack distance $r_2$ .....	161
7.4.4.	Load distribution factor $\lambda$ .....	163
<b>8.</b>	<b>Validation of the Analytical Model.....</b>	<b>169</b>
8.1.	Transformation of the specimen.....	170
8.1.1.	Influence of the orthogonal reinforcement.....	171
8.1.2.	Transformation of the column shape.....	176
8.1.3.	Transformation of slab shape and loading conditions.....	178
8.1.4.	Load application.....	181
8.2.	Other failure modes considered.....	186
8.2.1.	Punching of slabs without shear reinforcement.....	186
8.2.2.	Punching outside the shear-reinforced area.....	187

8.3.	Validation with tests within this research.....	187
8.3.1.	Strength and rotation predictions.....	188
8.3.2.	Slab thickness.....	188
8.3.3.	Column size.....	189
8.3.4.	Shear reinforcement ratio.....	190
8.3.5.	Prediction of the slab response and the failure criteria.....	191
8.4.	Comparison to tests from literature.....	195
8.4.1.	General.....	195
8.4.2.	Shear reinforcement ratio.....	196
8.4.3.	Effective depth.....	197
8.4.4.	Column size.....	198
8.4.5.	Flexural reinforcement ratio.....	199
8.4.6.	Concrete compressive strength.....	200
8.4.7.	Maximum aggregate size.....	200
8.4.8.	Predicted rotation at failure.....	201
<b>9.</b>	<b>Conclusions and Future Research.....</b>	<b>205</b>
9.1.	Conclusions.....	206
9.2.	Recommendations for future research.....	210
	<b>Bibliography.....</b>	<b>211</b>

**Appendix A Test Database**

**Appendix B Example PL7**

**Appendix C Shear Reinforcement Ratio**





## Abbreviations

ACI 318-11	American Concrete Institute Building Code (refer to reference ACI 318 2011)
Avg.	Average value
CSCT	Critical shear crack theory (refer to references Muttoni 2008 and Fernández Ruiz and Muttoni 2009)
COV	Coefficient of variation
EC 2004	Eurocode 2 (refer to reference EC2 2004)
MC 2010	fib Model Code 2010 (refer to reference MC 2011)
NAD 2011	German National Annex to Eurocode (refer to reference NAD 2011)
NLFEA	Nonlinear finite element analysis
SIA 2003	Swiss code 262 (refer to reference SIA 262 2003)



## Notations

$A_{sw}$	cross-sectional area of shear reinforcement
$A_{sw1}$	cross-sectional area of shear reinforcement crossed by the outer shear crack
$C_a$	horizontal component of force in compression strut within the wedge element
$C_b$	horizontal component of force in compression strut in the outer slab segment
$C_c$	compression force due to bending
$C_{r2}$	total compression force action at radius $r_2$
$E_c$	Young's modulus of concrete
$E_{c0}$	Young's modulus of uncracked concrete
$E_s$	Young's modulus of flexural reinforcing steel
$E_{sw}$	Young's modulus of shear reinforcing steel
$EI_0$	flexural stiffness before cracking
$EI_1$	tangential flexural stiffness after cracking (CSCT)
$EI^{\text{II}}$	tangential flexural stiffness after cracking
$F_{c,a}$	inclined compression force in the strut within the wedge element
$F_{c,b}$	inclined compression force in the strut in the outer slab segment
$F_{c,c}$	compression force due to bending
$G_c$	shear modulus of concrete
$G_{c0}$	shear modulus of uncracked concrete
$K$	stiffness
$T_{rc}$	tensile force acting at the column face
$T_{r2}$	tensile force acting at radius $r_2$
$V$	punching shear load
$V_R$	punching shear strength
$V_{flex}$	shear force associated with the flexural capacity of the slab specimen
$V_{R,pred}$	predicted punching shear strength
$V_{R,test}$	measured punching shear strength
$V_{Rc}$	concrete contribution to the punching strength
$V_{Rs}$	shear reinforcement contribution to the punching strength
$V_{R,I}$	predicted punching strength for failure within the shear-reinforced area
$V_{R,II}$	predicted failure load for failure of the compression strut
$V_s$	shear reinforcement contribution to the punching strength (CSCT)

$T$	strain transformation matrix
$a$	parameter for quadratic function defining the distribution of the rotation
$a_{sx}, a_{sy}$	sectional area of longitudinal reinforcement per unit width
$b$	distance between load application points
$b_0$	control perimeter (unless noted otherwise set at $d/2$ of the border of the support region with circular corners)
$b_1$	distance between load application point and the slab edge
$b_{ext}$	control perimeter outside the shear-reinforced area
$b_w$	width of the compression strut
$c$	side length of the column parameter for quadratic function defining the distribution of the rotation
$d$	effective depth (i.e. distance from extreme compression fiber to the centroid of the longitudinal tensile reinforcement)
$d_{eff}$	measured effective depth (distance from extreme compression fiber to the centroid of the longitudinal tensile reinforcement)
$d_g$	maximum diameter of concrete aggregate
$d_{g0}$	reference aggregate size (16 mm)
$d_n$	nominal effective depth (distance from extreme compression fiber to the centroid of the longitudinal tensile reinforcement)
$d_w$	diameter of shear reinforcement
$d_v$	shear resisting effective depth of the slab (MC)
$d_{v,ext}$	distance between the flexural reinforcement and the bottom end of the vertical branch of the shear reinforcement
$f_c$	average compressive strength of concrete (measured on cylinders)
$f_{ct}$	average tensile strength of concrete
$f_y$	yielding strength of flexural reinforcement
$f_{yw}$	yielding strength of shear reinforcement
$f_{yw,ef}$	effective stress in the shear reinforcement accounting for limited anchorage of the shear reinforcement in thin slabs (EC, NAD)
$h$	slab thickness
$h_t$	stud length, length of the vertical branch of the stirrup
$\Delta h$	change in slab thickness
$k$	factor accounting for size effect (EC)
$k_1$	factor accounting for the reduction in strength due to transverse strains
$k_2$	factor accounting for the stress distribution within the compression strut

$k_r$	factor accounting for slab rotation (SIA)
$k_{sh}$	ratio of ultimate strength to the yielding strength of reinforcing steel
$k_{sys}$	coefficient accounting for the performance of the shear reinforcement system (MC)
$k_y$	factor accounting for slab rotation (MC)
$l$	side length of the slab specimen span between columns (SIA)
$l_{ai}$	smaller distance between one end of the shear reinforcement and the shear crack
$l_{as}$	larger distance between one end of the shear reinforcement and the shear crack
$l_{bi}$	distance between the bottom end of the shear reinforcement and the shear crack
$l_{bs}$	distance between the top end of the shear reinforcement and the shear crack
$l_{cut}$	length of the cut for the numerical modeling of the column vicinity
$l_w$	length of the vertical branch of the shear reinforcement
$m$	moment per unit width
$m_0$	reference moment per unit width
$m_1$	first principal moment per unit width
$m_c$	sectional moment per unit width due to the stresses in the concrete
$m_{cr}$	cracking moment per unit width
$m_r$	radial moment per unit width
$m_R$	nominal moment capacity per unit width
$m_s$	sectional moment per unit width due to the stresses in the longitudinal reinforcement (MC)
$m_t$	tangential moment per unit width
$m_{t,int}$	tangential moment per unit width within the shear-critical region
$m_{t,ext}$	tangential moment per unit width outside the shear-critical region
$m_x, m_y$	moment per unit length in direction of the reinforcing bars
$m_{xy}$	torsional moment per unit length
$n_{cut}$	number of vertical branches of shear reinforcement crossing the outer shear crack
$n_s$	number of vertical branches of shear reinforcement per radius
$n_r$	number of vertical branches of shear reinforcement in the first perimeter
$r_0$	radius from which the rotations are assumed to be constant radius of the critical shear crack (CSCT, Quadrilinear model)
$r_1$	radius of the resultant shear force crossing the crack radius of the zone in which cracking is stabilized (CSCT, Quadrilinear model)
$r_2$	radius of the critical shear crack
$r_c$	radius of a circular column

$r_{cr}$	radius of cracked zone
$r_q$	radius of the load introduction at the perimeter
$r_p$	radius of the zone in which cracking is stabilized
$r_s$	radius of circular isolated slab element
$r_y$	radius of yielded zone
$s_0$	distance measured with respect to slab plane between the border of the support region and the first vertical branch of shear reinforcement
$s_1$	distance measured with respect to slab plane between two adjacent vertical branches of shear reinforcement of same radius
$s_c$	horizontal width of the compression strut
$s_{cr}$	average crack spacing
$s_t$	distance measured with respect to slab plane between two adjacent vertical branches of the stirrups
$w$	vertical displacement
$w_i$	crack opening at the $i^{\text{th}}$ vertical branch of shear reinforcement
$w_{lim}$	limit crack width defining the anchorage condition of the shear reinforcement
$x_1$	height of the compression zone at the column face
$x_2$	height of the compression zone at the outer slab segment
$x_a$	height of the compression zone due to the force in compression strut between the 1 <sup>st</sup> row of shear reinforcement and the column
$x_b$	height of the compression zone due to the force in compression strut between the 2 <sup>nd</sup> row of shear reinforcement and the column
$x_c$	height of the compression zone due to bending
$x_{el}$	height of the compression zone calculated with linear-elastic material behavior
$x, y$	coordinates (unless noted otherwise corresponding to the horizontal slab plane)
$z$	coordinate perpendicular to the horizontal slab plane
$\Delta h$	change in slab thickness
$\Delta w$	vertical displacement due to shear deformations at the column face
$\Delta x$	length increment
$\Delta \sigma_w$	change in stress in the shear reinforcement
$\Delta \varphi$	angle of a slab segment

$\alpha_1$	inclination of the compression strut between the 1 <sup>st</sup> row of shear reinforcement and the column
$\alpha_b$	inclination of the compression strut between the 2 <sup>nd</sup> row of shear reinforcement and the column
$\alpha_{cr}$	inclination of the outer shear crack
$\beta$	efficiency factor of the bending reinforcement for stiffness calculation
$\gamma$	shear strains
$\gamma_c$	partial safety factor for concrete (NAD)
$\gamma_s$	partial safety factor for steel (NAD)
$\delta$	deformations
$\varepsilon$	strains
$\varepsilon_1, \varepsilon_2$	principal strains
$\varepsilon_p$	strain at the peak stress of concrete
$\varepsilon_t$	strain in the shear reinforcement
$\varepsilon_y$	yielding strain of the shear reinforcement
$\theta$	direction of the principal stresses and/or strains
$\kappa$	factor accounting for localization of rotation in the shear crack
$\lambda$	load distribution factor coefficient accounting for the performance of the shear reinforcement system (CSCT)
$\lambda_c$	partial load distribution factor (between concrete and shear reinforcement)
$\lambda_s$	partial load distribution factor (between perimeters of shear reinforcement)
$\xi_1, \xi_2$	fitting parameter
$\rho$	flexural reinforcement ratio
$\rho_w$	shear reinforcement ratio (calculated according to Appendix C)
$\sigma_s$	stresses in the flexural reinforcement
$\sigma_{smax}$	maximum stress in the flexural reinforcement
$\sigma_w$	stresses in the shear reinforcement
$\tau_b$	bond strength
$\chi_1$	curvature at stabilized crack phase (CSCT)
$\chi_{cr}$	curvature at cracking
$\chi_p$	curvature at stabilized crack phase
$\chi_r$	curvature in radial direction
$\chi_{r,lim}$	limit of curvature in radial direction
$\chi_t$	curvature in tangential direction
$\chi_y$	yielding curvature

$\chi_{TS}$	decrease in curvature due to tension stiffening
$\psi$	slab rotation
$\psi_0$	constant slab rotation at the outer part of the slab specimen
$\psi_{R,pred}$	predicted rotation at failure
$\psi_{R,test}$	measured rotation at failure



# 1. Introduction

The development of modern reinforced concrete enabled for the first time the use of slabs as a structural element in civil engineering. In contrast to steel and timber structures, reinforced concrete structures were no longer limited to columns and beams, thus allowing new constructions methods. At first, reinforced concrete slabs were still supported on girders. However, at the beginning of the 20<sup>th</sup> century the use of flat slabs prevailed. The advantages of flat slabs compared to slabs on girders were early recognized and are still valid today. In 1914, Eddy and Turner (Eddy and Turner 1914) wrote:

*“The superiority of flat slab floor supported directly on columns, over other forms of construction when looked at from the standpoint of lower cost, better lighting, greater neatness of appearance, and increased safety and rapidity of construction, is so generally, or rather universally conceded as to render any reliable information relative to the scientific computation of stresses in this type of construction of great interest.”*

Nearly hundred years ago, Eddy and Turner highlighted the principal challenge of the design of flat slabs at that time, which concerned the calculation of the stresses. Since no design guidelines existed at first, the design of flat slabs was generally based on experimental data. This led to the development of rather different approaches for the design of flat slabs, which can be best displayed in the varying layouts used for the flexural reinforcement. For example in the United States, Turner used a four-way flat slab system (Figure 1.1a; Figure 1.2a) whereas Condron introduced a two way system (Figure 1.1b; Figure 1.2b) (Eddy and Turner 1914; Condron 1913). At nearly the same time, Maillart independently developed a similar system in Europe (Maillart 1926). In this time period, other flat slab systems were proposed that one would today consider as rather special. For example, Smulski (Smulski 1918) developed a circumferential flat slab system, which consisted of radially and tangentially arranged reinforcement (Figure 1.1c).

Despite the different flexural reinforcement layouts, all previously mentioned approaches used an enlarged column head. Although in each approach the shape slightly differed, the main purpose of the enlargement was to enable the transfer of the load from the slab to the column and thus prevent a punching failure. Additionally, the enlargement contributed to the flexural capacity of the slab since it reduced the span between the columns. With time, the enlargement of the column was replaced by a steel head within the slab.

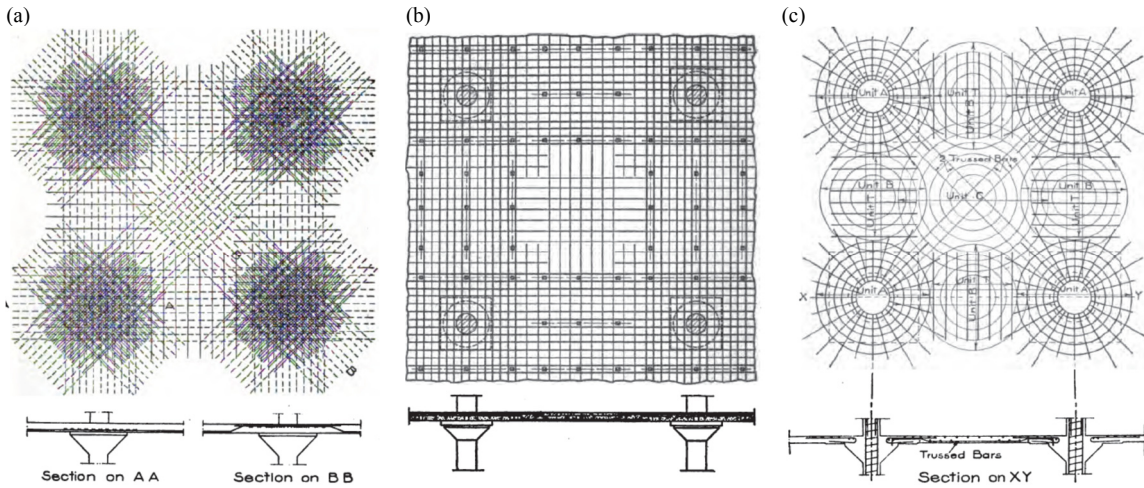


Figure 1.1: Reinforcement layouts for early developed flat slab systems: (a) four-way flat slab system, (b) two-way flat slab system, and (c) circumferential flat slab system (Taylor and Thompson 1916)

The increasing number of research on punching led to a better understanding and a better prediction of the punching strength. The consequence was that flat slabs could be designed without any special reinforcement against punching. However, the problematic of such an approach is that punching failure is a rather brittle failure mode and it can occur without any warning signs. Throughout history, this led to several severe collapses with numerous casualties. In order to prevent such accidents, integrity reinforcement was introduced to increase the residual strength of a slab-column connection after the occurrence of a punching failure.

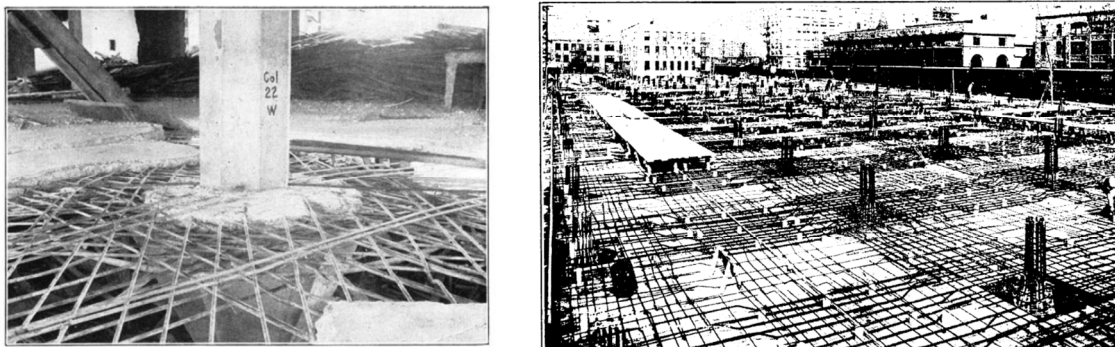


Figure 1.2: Longitudinal reinforcement layout in the case of (a) a four-way slab system (concrete removed after testing) (Talbot and Gonneman 1918) and (b) a two-way slab system (before casting) (Condron 1913)

However, in this context, the question rises if it is desired to prevent a collapse passively with integrity reinforcement or should active failure prevention be desired instead. Analogous to the first use of flat slabs, reinforcement can be placed in different ways but the objective should always be to place it where it performs best. In order to determine the performance of flat slabs,

the design should not only consider the force capacity but also of the deformation capacity. The consideration of the deformation capacity easily leads to the conclusion that generally slabs without shear reinforcement cannot provide sufficient deformation capacity. This is confirmed by several building collapses, Thus, the question should not be whether punching shear reinforcement should be used or not, but what amount of punching shear reinforcement is necessary and where should it be placed so that it provides a satisfactory deformation capacity.

These questions can only be answered by the investigation of the load-deformation response of flat slabs. However, the prediction of the displacements of flat slabs is not an easy task to achieve. Generally, the non-linear response of reinforced concrete is challenging. Moreover, the load concentration in the column vicinity requires a rather sophisticated model. Therefore, this thesis intends to not focus solely on the punching strength but also on the response of flat slabs.

## **1.1. Research significance**

Punching shear reinforcement is an efficient way to increase not only the strength but also the deformation capacity of slab-column connections. However, the analysis of such a connection is rather complex and includes several challenges. One challenge is the difference in performance of different types of punching shear reinforcement. Each type leads to a rather different performance, largely depending on the anchorage condition of the shear reinforcement system and the distribution of the shear reinforcement. Moreover, the amount and the arrangement of the shear reinforcement do not only influence the performance but also define the failure mode. Consequently, the punching strength depends on various parameters that have to be investigated individually. Currently, only scarce systematic research on this subject exists in literature for full-scale specimens. Therefore, this research project focuses on the detailed investigation of punching of full-scale slab specimens with large amounts of shear reinforcement.

## **1.2. Objectives**

The objective of this research is to gain a better understanding of punching of flat slabs with shear reinforcement. Thereby, the focus should be set on the analysis of the maximum increase in strength and rotation capacity due to punching shear reinforcement. Therefore, the principal aim is the analysis of flat slabs with large amounts of punching shear reinforcement. Within this framework, several aspects should be investigated such as the load-deformation response of the slab, the failure mechanism, and the load contribution of the shear reinforcement. Based on this investigation, a simplified model should be developed that enables the prediction of the punching strength and the rotation at failure for the investigated cases.

### 1.3. Scope

The research presented herein basically focuses on the investigation of punching of flat slabs with large amounts of shear reinforcement. This includes the investigation of slabs without and with low amounts of shear reinforcement in order to analyze the influence of the shear reinforcement. All the investigated cases refer to interior columns supported by square or circular columns without any constraints at the boundary. Thus, the research concerns solely symmetrically loaded slabs that were not subjected to membrane forces. The shear reinforcement considered was limited to vertical, pre-installed shear reinforcement systems (Figure 1.3).

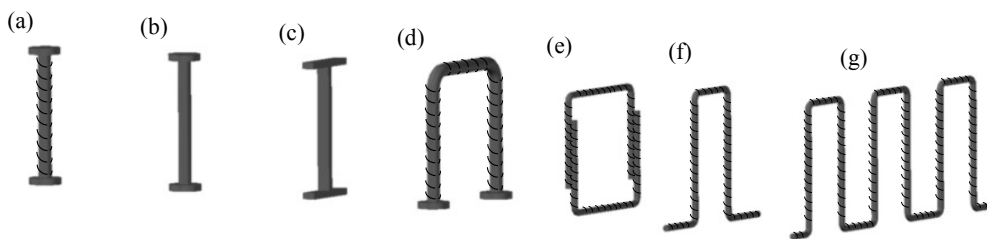


Figure 1.3: Examples of shear reinforcement systems: (a) corrugated double headed shear studs, (b) smooth double headed shear studs, (c) steel offcuts, (d) headed stirrups, (e) stirrups with lap at the vertical branch, (f) stirrups or shear links, (g) continuous stirrups or cages of shear links

The choice of the type, the amount, and the distribution of the shear reinforcement defined also the failure modes that were considered within this research. Therefore, the framework of the research was generally limited to the investigation of the failure within the shear reinforced area (Figure 1.4a) and the failure due to crushing of the concrete strut near the column (Figure 1.4c). However, failure outside the shear-reinforced area (Figure 1.4b) was not investigated in detail but was considered in the validation of the code provisions, the critical shear crack theory, and the model presented herein. On the other hand, failure modes such as delamination of the concrete core (Figure 1.4d) or failure between the transverse reinforcement (Figure 1.4e), which result directly from detailing that contradicts common design practice (e.g. large spacing, insufficient anchorage), were neither analyzed nor used for the validation.

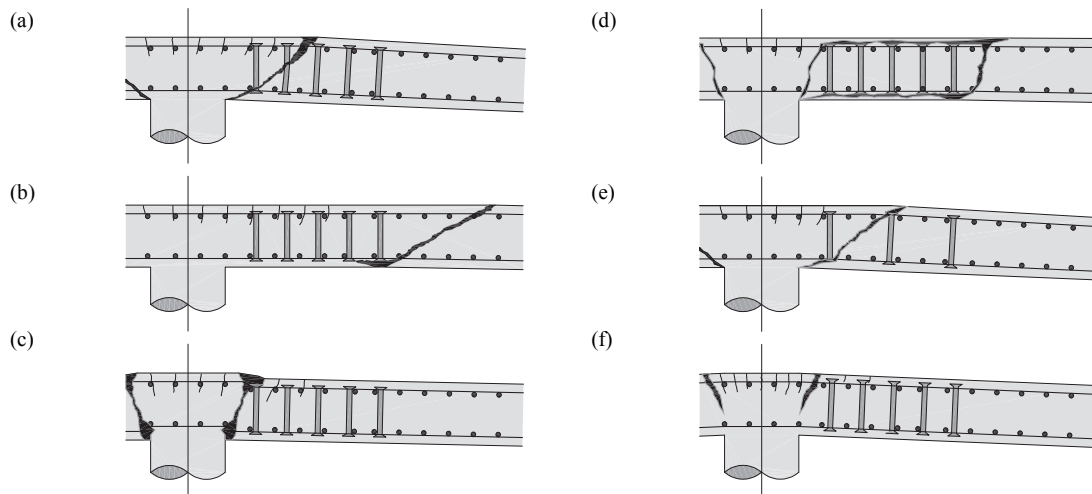


Figure 1.4: Possible failure modes of slabs with shear reinforcement: (a) failure within shear-reinforced area, (b) failure outside shear-reinforced area, (c) failure close to the column due to crushing of concrete, (d) delamination of the concrete core, (e) failure between the transverse reinforcement, and (f) flexural failure

## 1.4. Organization

The thesis covers three main parts, namely the experimental investigation including the validation of code provisions and the critical shear crack theory, the numerical analysis of the slab response, and the development and validation of an analytical model. After the introduction, Chapter 2 presents an overview of the previously performed research on punching of flat slabs with shear reinforcement. Additionally, it shows the code provisions and the formulations of the critical shear crack theory used for the calculation within this research.

Afterwards, Chapter 3 presents an overview of the test campaign that was carried out within this research project and presents selected results that are used and further discussed in the subsequent chapters. In addition, the experimental part consists of a code validation presented in Chapter 4 by which the test results from this research and test results found in literature are compared to the predictions of current design codes and the critical shear crack theory.

Chapter 5 presents the development of a nonlinear finite element approach that is based on plane stress fields. This approach is used for a detailed analysis of the global and local slab behavior presented in Chapter 6.

Based on the experimental investigation and the numerical analysis, an analytical model was developed. The mechanical basis and the derivation of the equations of this model are presented in Chapter 7. In Chapter 8, this model is validated based on test results from this research and test results found in literature.

Finally, the thesis closes with the conclusions of the three parts, followed by an outlook for future research.

## **1.5. Personal contributions**

Within the research presented herein, following personal contributions were made:

- Development and performance of an extensive experimental test campaign
- In-depth analysis of measurement data obtained from the test campaign
- Validation of current code provisions and the critical shear crack theory
- Development and application of a constitutive model in order to model the slab behavior subjected to a combination of flexural and torsional moments
- Investigation of the slab response with respect to a global and a local part
- Development and validation of an analytical model based on the critical shear crack theory for the prediction of the punching strength and the rotation capacity of flat slabs

## 2. Literature Review

The start of the use of flat slabs supported by columns in the beginning of the 20<sup>th</sup> century led to various research on the punching strength of flat slabs. At first, research covered mainly slabs without punching shear reinforcement, followed by investigations on flat slabs with punching shear reinforcement. Coming from the beam design, the first shear reinforcement used were bent-up bars. Later on, new systems have been developed such as different stirrup systems and shear studs. The change of the punching shear reinforcement system was always accompanied by research on this subject resulting in new findings for different shear reinforcement systems. Additionally, it can be noted that not only the shear reinforcement systems changed by time but also the demand on the behavior. At first the increase of the punching strength occupied researchers' interest. However, later they diverted their focus on the deformation capacity and safety of slab column connections. This influenced the research of flat slabs as well as the further development of punching shear reinforcement systems.

This chapter gives a brief overview of the developments regarding punching of flat slabs with shear reinforcement. Afterwards, it presents current code provisions and the critical shear crack theory (CSCT) with respect to the formulations that were used for the calculations within this research. Therefore, only formulations for symmetric slabs without shear reinforcement or with vertical shear reinforcement for failure within the shear-reinforced area, failure outside the shear-reinforced area, and failure of the concrete strut near the column are presented. Moment transfer, asymmetric geometrical or loading conditions, prestressing, or inclined shear reinforcement are not considered in the calculations. Thus, no formulations regarding these subjects will be presented.

Since certain punching shear models such as the critical shear crack theory depend on the slab deformation, this chapter additionally presents a short overview of different methods to predict the response of a flat slab. For this discussion, the approaches will be separated into analytical and numerical methods. Finally, a more detailed explanation of an analytical approach proposed by Muttoni (Muttoni 2008) will be presented.

## 2.1. Overview of previous research

This brief summary presents the main developments of research on the punching of flats slabs with punching shear reinforcement. Considering the extensive amount of research on flat slab-column performed over the last decades, a complete review of all experimental investigations and developed models would go beyond the scope of this work. Additionally, it can be noted that overviews of models already exist such as the fib Bulletin 12 (FIB 2001). Therefore, this brief summary concentrates on research that is seen as most crucial with respect to the work within the herein presented research project.

A good starting point for such a summary is certainly the research from Kinnunen and Nylander. Their contribution in 1960 (Kinnunen and Nylander 1960) was one of the first and probably most important contribution with respect to the modeling of punching. The proposed model led to the further development of other punching shear models. Although this approach was developed for slabs without punching shear reinforcement, it served as basis for other researchers who implemented punching shear reinforcement. In 1963, based on the model of Kinnunen and Nylander (Kinnunen and Nylander 1960), Andersson (Andersson 1963) developed an approach that considers shear reinforcement (Figure 2.1a). In the tests that he performed for the model validation, he used bent-up bars and continuous stirrups as punching shear reinforcement.

In 1974, the American Concrete Institute published the Special Publication 42 about shear in reinforced concrete in which Part 4 was devoted to shear in slabs. Amongst other contributions, Hawkins (Hawkins 1974) published a paper presenting an overview of tests performed with different punching shear reinforcement systems such as steel heads, bent-up bars, and stirrups. He concluded that shear reinforcement increases the punching strength even for small slabs and that the detailing is crucial to increase the strength and to avoid undesired failure modes.

During the seventies, Ghali and Dilger from the University of Calgary, Canada, focus on improving existing shear reinforcement systems, which were at this time generally bent-up bars or different types of stirrups. They found that the anchorage conditions of the shear reinforcement are crucial. At first, they used cut-off of standard I-shaped steel beams (Langohr et al. 1976). Afterwards, they collaborated with Andrä (Andrä 1979; Andrä et al. 1979; Andrä 1981) who introduced stud rails as new punching shear reinforcement in Germany. This new system led to an extensive research throughout the eighties and nineties (Seible et al. 1980; Dilger and Ghali 1981; Van der Voet et al. 1982; Mokhtar et al. 1985; Ghali 1989; Elgabry and Ghali 1990; Ghali and Hammill 1992; Megally and Ghali 1994; Hammill and Ghali 1994; Birkle and Dilger 2008). This research was accompanied by the development of the shear friction model that was first developed for shear in beams (Loov 1998; Tozser 1998) and later applied for slab-column connections (Dechka 2001; Birkle 2004).



During the eighties and nineties, Regan started his research on punching with and without shear reinforcement at the Polytechnic of Central London (Regan 1983; Regan 1985; Regan 1986). In the research team of Regan, Shehata developed a model for slabs without shear reinforcement that was based on the approach of Kinnunen and Nylander (Shehata 1985; Shehata and Regan 1989; Shehata 1990). Later, Gomes extended Shehata's model by implementing the contribution of the shear reinforcement (Gomes and Regan 1999a; Gomes and Regan 1999b) (Figure 2.1b). Further research has been conducted by Regan and Samadian (Regan and Samadian 2001) and Oliveira et al. (Oliveira et al. 2000) who continued their work in Brazil leading to several recent publications about punching tests with shear reinforcement (Trautwein et al. 2011; Carvalho et al. 2011).

In the United Kingdom in the beginning of the nineties, Chana and Desai performed an extensive experimental campaign of punching shear tests with shear reinforcement (Chana and Desai 1992; Chana 1993). Thereby, they tested slabs with conventional shear links and slabs with a special shear reinforcement system consisting of links welded together to a cage (known as "shearhoop" system). The main objective of this investigation was to show the improved performance of the prefabricated system compared to the conventional shear links and its code applicability.

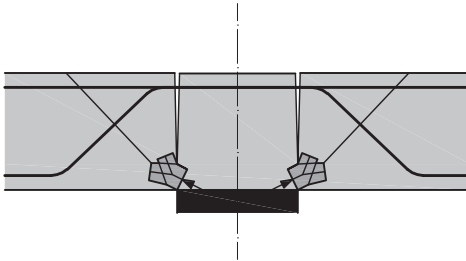
Starting in the nineties, Broms presented a further development of the model of Kinnunen and Nylander (Broms 1990a) and introduced a combination of stirrups and bent-up bars as punching shear reinforcement (Broms 1990b) (Figure 2.1c). He showed that this system allows an increase in the deformation capacity compared to slabs with only stirrups. The increase in deformation capacity of slab-column connections and the further development of this model have been his main research interest over the years leading to various publications (Broms 2000a; Broms 2000b; Broms 2006; Broms 2007a; Broms 2007b). In 2005, he summarized a main part of his earlier work in his dissertation treating design methods for punching of flat slabs and footings with and without shear reinforcement (Broms 2005).

Also in the last two decades, the research group of Hegger at the Rheinisch-Westfälischen Technischen Hochschule Aachen in Germany performed extensive experimental research on punching of flat slabs and foundations and thoroughly investigated the structural behavior of slabs with and without punching shear reinforcement (Hegger et al. 2006; Hegger et al. 2007; Hegger et al. 2009; Hegger et al. 2010; Siburg and Hegger 2011). With respect to punching of slabs with punching shear reinforcement, the dissertations written by Beutel (Beutel 2003) and Häusler (Häusler 2009) contributed largely to the understanding of the flat slab behavior.

As already mentioned, more recent work has been performed in Brazil regarding punching shear reinforcement in combination with prestressing (Carvalho et al. 2011) and the performance of punching shear reinforcement that does not embrace the flexural reinforcement (Trautwein et al. 2011). Other recent experimental research has been performed at Imperial College London in the United Kingdom by Vollum et al. (Vollum et al. 2010) in which the arrangement of the punching shear reinforcement was investigated.

In this summary, the research of Muttoni performed at the Ecole Polytechnique Fédérale de Lausanne is excluded since the latest contribution regarding the Critical Shear Crack Theory (CSCT) with respect to punching with punching shear reinforcement will be presented in detail subsequently in Subchapter 2.7. However, before the CSCT is described, the current code provisions used within this research will be presented.

(a)

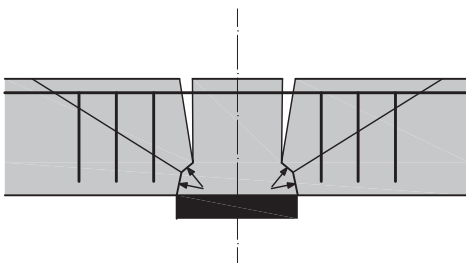


Andersson (Andersson 1963):

The slab part between the column face and the edge of the slab is assumed to rotate rigidly. This outer slab part is assumed to be carried by a compression zone that is supported by the column.

Failure occurs if a defined tangential compressive strain at a defined distance away of the column is reached.

(b)

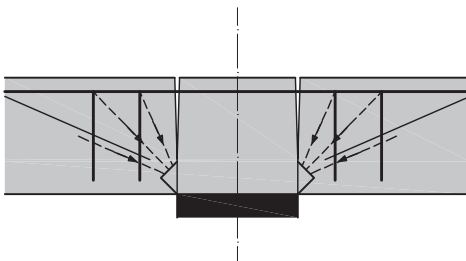


Gomes and Regan (Gomes and Regan 1999a):

It is assumed that the slab can be divided into three parts: an outer, a wedge, and a column part. However, despite the separation, it is assumed that the entire slab except the column part rotates as a rigid body.

Failure is assumed to occur either if the shear stress on any surface below the shear crack reaches the sliding resistance or if the maximum principal stress reaches the indirect tensile strength at a section with a defined radius.

(c)



Broms (Broms 2005):

Failure is assumed to occur either if the tangential compressive strain reaches a defined value or if the compression stress in the fictitious internal column capital reaches a critical value. In both cases, the failure criterion depends on the state of stress in the flexural reinforcement.

Figure 2.1: Selected models that are based on the model of Kinnunen and Nylander (Kinnunen and Nylander 1960): (a) model proposed by Andersson (Andersson 1963), (b) model proposed by Gomes and Regan (Gomes and Regan 1999a), and (c) model proposed by Broms (Broms 2005)

## 2.2. ACI 318-11 (ACI 318 2011)

### 2.2.1. Slabs without shear reinforcement

The code provision of ACI 318-11 regarding punching of slabs without shear reinforcement is rather simple and straightforward. The area at the control perimeter is multiplied by an admissible shear stress. Thus, the punching strength is defined as:

$$V_R = \frac{1}{3} b_{0,ACI} \cdot d \cdot \sqrt{f_c} \quad (2.1)$$

where  $b_0$  is a control perimeter,  $d$  is the effective depth of the slab,  $f_c$  is the compressive strength of concrete in MPa.

The control perimeter is defined in clause 11.11.1.2, which would suggest that the perimeter is, alike other codes, circular at the corners. However, clause 11.11.1.3 allows using straight sides at the corner in the case of square or rectangular columns. Since, in practice, it seems more reasonable to use the largest control perimeter allowed, the critical perimeter is used with straight lines for the comparison of the tests with the ACI 318-11 code. Therefore, the critical perimeter used within this research corresponds to the drawing shown in Figure 2.2b.

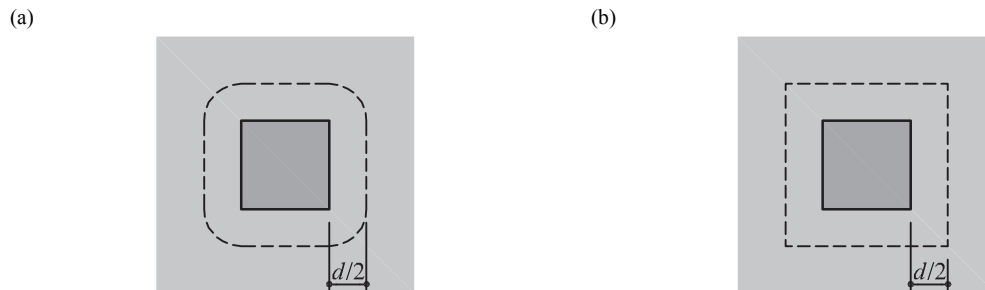


Figure 2.2: Control perimeter according to ACI 318-11 clause (a) 11.11.1.2 and (b) 11.11.1.3

### 2.2.2. Slabs with shear reinforcement

According to ACI 318-11 the punching strength for failure within the shear-reinforced area can be calculated by adding the concrete and the shear reinforcement contributions, whereby the concrete contribution generally corresponds to half of the punching strength of slabs without shear reinforcement. However, in the case of double headed studs, ACI 318-11 (11.11.5.1) proposes the concrete contribution as 3/4 of the punching strength of slabs without shear reinforcement. Thus, the punching strength in slabs with stirrups is defined as:

$$V_R = \frac{1}{6} b_{0,ACI} \cdot d \cdot \sqrt{f_c} + A_{sw} \cdot f_{yw} \cdot \frac{d}{s_w} \quad (2.2)$$

and in slabs with studs defined as:

$$V_R = \frac{1}{4} b_{0,ACI} \cdot d \cdot \sqrt{f_c} + A_{sw} \cdot f_{yw} \cdot \frac{d}{s_w} \quad (2.3)$$

where  $b_0$  is a control perimeter set at  $d/2$  of the border of the support region,  $d$  is the effective depth of the slab,  $f_c$  is the compressive strength of concrete in MPa,  $A_{sw}$  is the cross-sectional area of one perimeter of shear reinforcement around the column,  $s_w$  is the distance between perimeters of shear reinforcement, and  $f_{yw}$  is the yield strength of the shear reinforcement.

The provision for punching outside the shear-reinforced area is similar to the provision for the punching strength of slabs without shear reinforcement. However, for this failure mode, the control perimeter is set at a distance of  $d/2$  from the last line of shear reinforcement and the admissible shear stress at this perimeter is half of the one allowed in the case of punching without shear reinforcement. Thus, the punching strength for punching outside the shear-reinforced area is defined as:

$$V_R = \frac{1}{6} b_{out} \cdot d \cdot \sqrt{f_c} \quad (2.4)$$

where  $b_{out}$  is a control perimeter set at a distance of  $d/2$  from the last line of shear reinforcement,  $d$  is the effective depth of the slab, and  $f_c$  is the compressive strength of concrete in MPa.

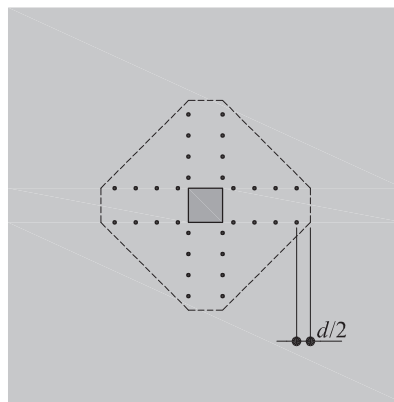


Figure 2.3: Control perimeter for punching shear verification outside the shear-reinforced area according to ACI 318-11

The maximum punching strength is defined as the multiple of the punching strength of slabs without shear reinforcement. Generally, ACI 318-11 proposes this factor to be 1.5. However, a factor of 2 may be used in the case of headed shear studs (ACI 318-11 11.11.5.1). It has to be noted that in the case of an increase of the maximum punching strength the detailing rules change. In fact, if a factor of 2 is used, the spacing between the studs is limited to  $0.5d$ . However, certain investigated test specimens within this research have a distance of  $0.75d$

between the studs and thus do not fulfill this detailing rule. Nevertheless, for the calculations performed within this research, this restriction of the spacing is not considered. Thus, for all the investigated specimens within this research, the maximum punching strength of specimens with stirrups is defined as:

$$V_R = \frac{1}{2} \cdot b_{0,ACI} \cdot d \cdot \sqrt{f_c} \quad (2.5)$$

and of specimens with studs as:

$$V_R = \frac{2}{3} \cdot b_{0,ACI} \cdot d \cdot \sqrt{f_c} \quad (2.6)$$

where  $b_0$  is a control perimeter set at  $d/2$  of the border of the support region,  $d$  is the effective depth of the slab, and  $f_c$  is the compressive strength of concrete in MPa.

## 2.3. Eurocode 2 (EC2 2004)

### 2.3.1. Slabs without shear reinforcement

The Eurocode provision for punching without shear reinforcement is based on an empirical formulation for the prediction of the shear strength of beams. The adjustment is mainly made by fitting the control perimeter so that the formulation agrees well with test results. Unlike ACI 318-11, the provision of EC2 2004 accounts for the flexural reinforcement ratio and size effects. Thus, the punching strength is defined as:

$$V_{Rc} = 0.18 \cdot b_{0,EC} \cdot d \cdot k \cdot (100 \cdot \rho \cdot f_c)^{\frac{1}{3}} \geq v_{min} \cdot b_{0,EC} \cdot d \quad (2.7)$$

where  $b_{0,EC}$  is a control perimeter set at  $2d$  of the border of the support region with circular corners,  $d$  is the effective depth of the slab,  $f_c$  is the compressive strength of concrete in MPa,  $\rho$  is the flexural reinforcement ratio limited to the maximum of 2%,  $k$  is a factor accounting for the size effect that is defined as:

$$k = 1 + \sqrt{\left(\frac{200}{d}\right)} \leq 2.0 \quad (2.8)$$

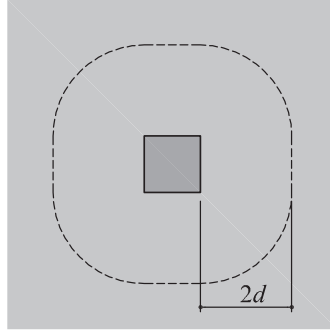


Figure 2.4: Control perimeter according to EC2 2004

Equation 2.7 leads to a resistance of zero if the reinforcement ratio goes to zero. Thus, it implies a low shear strength for small reinforcement ratios. Therefore, a minimum punching shear strength was introduced accounting only for the tensile strength of the concrete and a size effect factor  $k$ . The minimum punching shear stress is defined as:

$$v_{min} = 0.035 \cdot k^{3/2} \cdot f_c^{1/2} \quad (2.9)$$

### 2.3.2. Slabs with shear reinforcement

Similar to ACI 318-11, EC2 2004 proposes the summation of the concrete and the shear reinforcement contributions, whereby the concrete contribution corresponds to 75% of the punching strength of slabs without shear reinforcement. This reduction is made to account for the activation of the shear reinforcement and that the concrete strength reduces due to the vertical movement of the punching cone when the shear reinforcement is yielding (EC2 Commentary 2008). Thus, the punching strength can be calculated as:

$$V_R = 0.75 \cdot V_{Rc} + A_{sw} \cdot f_{yw,ef} \cdot 1.5 \cdot \left(\frac{d}{s_w}\right) \quad (2.10)$$

where  $A_{sw}$  is the area of one perimeter of shear reinforcement around the column,  $s_w$  is the radial spacing of perimeters of shear reinforcement,  $d$  is the effective depth, and  $f_{yw,ef}$  is the effective stress in the shear reinforcement accounting for limited anchorage of the shear reinforcement in thin slabs and  $f_{yw,ef}$  is defined as:

$$f_{yw,ef} = 1.15 \cdot (250 + 0.25d) \leq f_{yw} \quad (2.11)$$

where  $d$  is the effective depth in mm and  $f_{yw}$  is the yielding strength of the shear reinforcement in MPa.

The punching strength for failure outside the shear-reinforced area is similarly defined as for punching strength of slabs without shear reinforcement. The only difference to the formulation for punching of slabs without shear reinforcement is the length of the control perimeter, which is in this case is taken at the outer perimeter leading to the expression:

$$V_R = 0.18 \cdot b_{out} \cdot d \cdot k \cdot (100 \cdot \rho \cdot f_c)^{\frac{1}{3}} \quad (2.12)$$

where  $b_{out}$  is a control perimeter set at a distance of  $1.5d$  from the outermost perimeter of shear reinforcement. All other parameters correspond to the formulation of punching of slabs without shear reinforcement.

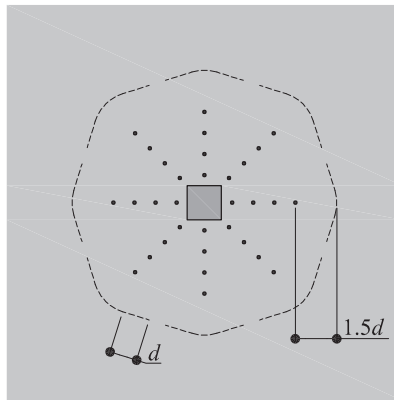


Figure 2.5: Control perimeter for punching shear verification outside the shear- reinforced area according to EC2 2004

For the maximum punching strength, EC2 2004 uses a similar approach as for the calculation of the strength of the compression strut in a reinforced concrete beam. Therefore, the strength is directly related to the concrete compressive strength, the column perimeter, and the effective depth. Thus, the maximum punching strength is defined as:

$$V_R = 0.3 \cdot \left(1 - \frac{f_c}{250}\right) \cdot f_c \cdot b_{0,in} \cdot d \quad (2.13)$$

where  $b_{0,in}$  is a control perimeter set at the border of the support region,  $d$  is the effective depth of the slab, and  $f_c$  is the compressive strength of concrete.

## 2.4. German National Annex (NAD 2011)

### 2.4.1. Slabs without shear reinforcement

NAD 2011 is an amendment of EC2 2004 for Germany. Therefore, only the differences between the two code provisions will be discussed. For the provision for slabs without shear reinforcement the only difference is the assumption for factor  $C_{R,c}$ , which depends on the ratio of the control perimeter to the effective depth in order to improve the performance of the provision of EC2 2004 for smaller column sizes. Thus, the punching strength is defined as:

$$V_{Rc} = C_{R,c} \cdot b_{0,EC} \cdot d \cdot k \cdot (100 \cdot \rho \cdot f_c)^{\frac{1}{3}} \geq v_{min} \cdot b_{0,EC} \cdot d \quad (2.14)$$

where  $b_{0,EC}$  is a control perimeter set at  $2d$  of the border of the support region with circular corners,  $d$  is the effective depth of the slab,  $f_c$  is the compressive strength of concrete,  $\rho$  is the flexural reinforcement ratio (see Equation 2.16 for additional conditions),  $k$ , which is defined according to Equation 2.8, is a factor accounting for the size effect, and factor  $C_{R,c}$ , which is defined as:

$$\begin{aligned} \frac{b_{0,in}}{d} \geq 4: C_{R,c} &= 0.18 \\ \frac{b_{0,in}}{d} < 4: C_{R,c} &= 0.18 \cdot \left(0.1 \cdot \frac{b_{0,in}}{d} + 0.6\right) \end{aligned} \quad (2.15)$$

where  $b_{0,in}$  is a control perimeter set at the border of the support region and  $d$  the effective depth.

As in EC2 2004, the flexural reinforcement ratio is limited to 2%. Additionally, NAD 2011 limits the flexural reinforcement ratio by:

$$\rho \leq 0.5 \cdot \alpha \cdot \frac{\gamma_s \cdot f_c}{\gamma_c \cdot f_y} = 0.5 \cdot 0.85 \cdot \frac{1.15 \cdot f_c}{1.5 \cdot f_y} \leq 2.0\% \quad (2.16)$$

where  $\gamma_c$  and  $\gamma_s$  are partial safety factors,  $f_c$  is the compressive strength of concrete, and  $f_y$  the yielding strength of the reinforcement.

### 2.4.2. Slabs with shear reinforcement

With respect to the failure mode within the shear-reinforced area no additional changes have been made. However, the reduction of  $V_{Rc}$  due to the adjusted definition of factor  $C_{R,c}$  (Equation 2.15) has to be considered. Thus, the punching strength is defined as:

$$V_R = 0.75 \cdot V_{Rc} + A_{sw} \cdot f_{yw,ef} \cdot 1.5 \cdot \left(\frac{d}{s_w}\right) \quad (2.17)$$

where  $A_{sw}$  is the area of one perimeter of shear reinforcement around the column,  $s_w$  is the radial spacing of perimeters of shear reinforcement,  $d$  is the effective depth, and  $f_{yw,ef}$  is the effective stress in the shear reinforcement defined by Equation 2.11.



The provision for failure outside the shear-reinforced area corresponds to the EC2 2004 provision except for the fact that an orthogonal layout of the shear reinforcement is not allowed. However, in this thesis, this limitation is neglected for the comparisons of the code predictions to the experimental data presented in Chapter 4. Additionally, for the calculations within this research, a reduced value of the effective depth  $d_{out}$  is used as it is proposed by Hegger et al. (Hegger et al. 2010). This reduction is due to the fact that at the outer perimeter the shear force is not transferred to the bottom surface of the slab such as in the case of a column but to the bottom end of the outermost shear reinforcement. Consequently, the punching strength predicted by NAD 2011 using the proposed (Hegger et al. 2010) reduced value of the effective depth  $d_{out}$  is somewhat smaller than the one predicted by EC2 2004. Thus, the punching strength is defined as:

$$V_R = C_{R,c} \cdot b_{out} \cdot d_{out} \cdot k \cdot (100 \cdot \rho \cdot f_c)^{\frac{1}{3}} \quad (2.18)$$

where  $b_{out}$  is a control perimeter set at a distance of  $1.5d$  from the outermost perimeter of shear reinforcement and  $d_{out}$  is the distance between the flexural reinforcement and the bottom end of the vertical branch of the shear reinforcement as proposed by Hegger et al. (Hegger et al. 2010). All other parameters correspond to the formulation of punching without shear reinforcement.

It has to be noted that NAD 2011 does not allow spacing larger of  $2d$  between vertical branches of shear reinforcement in the outermost perimeter. However, this rule was not considered in the comparison of the code provision to the test results in Chapter 4. In the cases in which the spacing was larger than  $2d$ , the external perimeter  $b_{out}$  was reduced according to the provision of EC2 2004 (Figure 2.5).

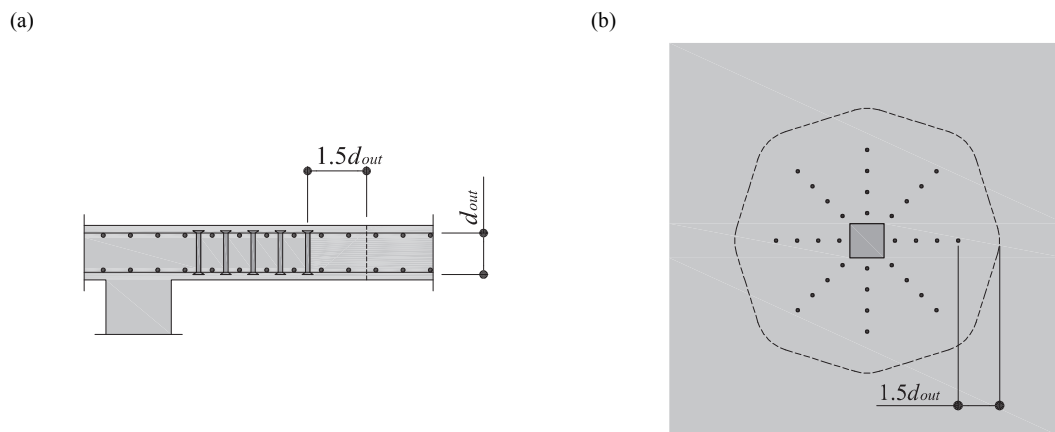


Figure 2.6: Control perimeter for punching shear verification outside the shear- reinforced area according to NAD 2011 and to the proposal of Hegger et al. (Hegger et al. 2010)

A clear difference exists for the code provisions for failure of the concrete strut (maximum punching strength) between NAD 2011 and EC2 2004. While EC2 2004 uses a beam analogy to estimate the punching strength for failure of the concrete strut, NAD 2011 uses a multiplication

of the punching strength of slabs without shear reinforcement. Thus, the maximum punching strength is given by:

$$V_R = 1.4 \cdot V_{Rc} \quad (2.19)$$

The multiplication factor of 1.4 can be changed for different shear reinforcement systems if an accreditation for the system is obtained. Thus, Chapter 4 shows additionally the results of the calculations that were performed with a factor of 1.9 for double headed studs.

## 2.5. SIA 262 (SIA 262 2003)

### 2.5.1. Slabs without shear reinforcement

The punching provision of SIA262 2003 for slabs without shear reinforcement is based on the CSCT. Therefore, the punching strength depends on the slab rotation. This rotation is estimated by the design shear load and the flexural strength of the slab. In design practice, it is sufficient to verify that the punching shear strength  $V_{Rd}$ , calculated with the design load  $V_d$ , is larger than the design load  $V_d$ . However, it has to be noted that the thereby calculated  $V_{Rd}$  does not correspond to the actual punching strength of the slab. The actual punching strength is obtained at the point where the punching strength  $V_R$  corresponds to the applied load  $V$ . Thus, in order to obtain the actual punching strength, the formulation has to be solved for  $V$  so that it equals  $V_R$ . Generally, the punching strength is defined as:

$$V_{Rc} = k_r \cdot 0.3 \cdot \sqrt{f_c} \cdot d \cdot b_0 \quad (2.20)$$

where  $b_0$  is a control perimeter set at  $d/2$  of the border of the support region with circular corners,  $d$  is the effective depth of the slab,  $f_c$  is the compressive strength of concrete, and  $k_r$  is defined as:

$$k_r = \frac{1}{0.45 + 0.9r_y} \geq \frac{1}{1 + 2.2d} \quad (2.21)$$

with

$$r_y = 0.15l \cdot \left(\frac{m_0}{m_R}\right)^{3/2} \quad (2.22)$$

where  $l$  is the span between the columns,  $m_R$  is the flexural strength, and  $m_0$  is the moment due to the applied load.

For inner columns,  $m_0$  can be assumed as:

$$m_0 = \frac{V}{8} \quad (2.23)$$

where  $V$  is the applied shear force.

If the slab is designed with either a concrete with maximum aggregate sizes  $d_g$  smaller than 32 mm or reinforcing steel with a yielding strength larger than 500 MPa,  $r_y$  and  $d$  in Equation 2.21 must be respectively adjusted using the following two equations:

$$r_{y,adj} = r_y \cdot \min\left(\frac{48}{16 + d_g}; 1\right) \cdot \min\left(\frac{f_y}{500}; 1\right) \quad (2.24)$$

and

$$d_{adj} = d \cdot \min\left(\frac{48}{16 + d_g}; 1\right) \quad (2.25)$$

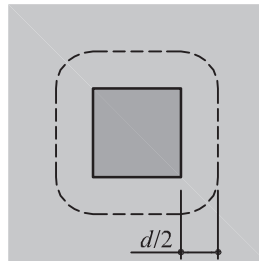


Figure 2.7: Control perimeter according to SIA262 2003

### 2.5.2. Slabs with shear reinforcement

With respect to the failure within the shear reinforced area, SIA262 2003 is mainly based on a strut and tie model used in design of beams by which the inclination angle is fixed at  $45^\circ$ . This means that it neglects any contribution of the concrete. Thus, the punching strength is defined as:

$$V_R = A_{sw} \cdot f_{yw} \quad (2.26)$$

where  $A_{sw}$  is the area of shear reinforcement intersected by the potential failure surface (conical surface with angle  $45^\circ$ ) and  $f_{yw}$  is the yield strength of the shear reinforcement.

Similar to the approach of EC2 2004 and NAD 2011, for the failure at the outer perimeter, SIA262 2003 uses the same approach as for slabs without shear reinforcement. The only difference to the provision for slabs without shear reinforcement is that the control perimeter is taken at a distance of  $0.5d_v$  from the outermost shear reinforcement perimeter. For the punching strength outside the shear-reinforced area, SIA262 2003 does not use the effective depth  $d$  to calculate the external perimeter but the distance from the flexural reinforcement to the bottom end of the shear reinforcement to account for the difference in shear transfer. This approach is also proposed by Hegger et al. (Hegger et al. 2010) for EC2 2004 and NAD 2011. Thus, the punching strength is defined as:

$$V_R = k_r \cdot 0.3 \cdot \sqrt{f_c} \cdot d_{out} \cdot b_{out} \quad (2.27)$$

where  $b_{out}$  is a control perimeter set at a distance of  $0.5d$  from the outermost perimeter of shear reinforcement and  $d_{out}$  is the distance between the flexural reinforcement and the bottom end of the vertical branch of the shear reinforcement. All other parameters correspond to the formulation of punching of slabs without shear reinforcement.

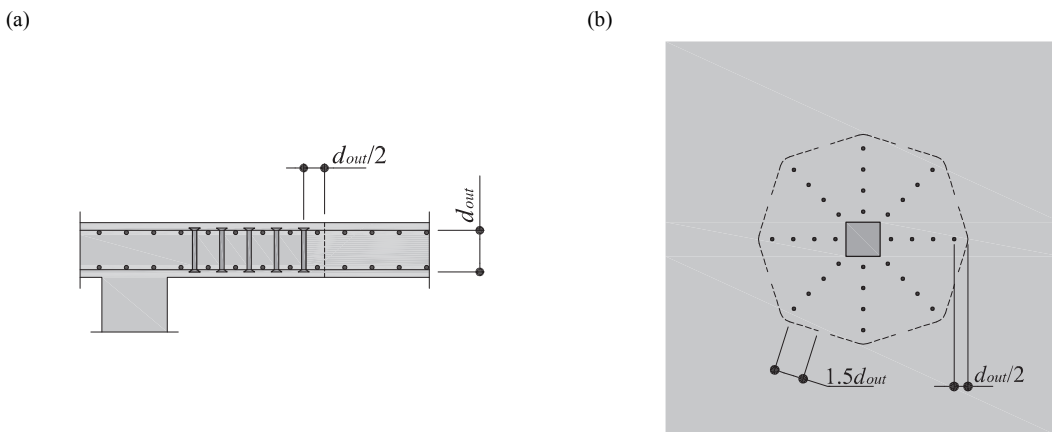


Figure 2.8: Control perimeter for punching shear verification outside the shear-reinforced area according to SIA262 2003

The provision of the failure of the concrete strut uses the assumption that the maximum punching strength is related to the punching strength of slabs without shear reinforcement. This is similar to the provision of NAD 2011. However, as already discussed for SIA262 2003 provisions for slabs without shear reinforcement, the predicted punching strength  $V_R$  is a function of the applied shear force  $V$  that is included in the factor  $k_r$ . Therefore, the maximum punching strength is not the proportionally increased punching strength estimated by the formulation for slabs without shear reinforcement. Thus, the maximum punching strength is defined as:

$$V_R = 2 \cdot V_{Rc}(k_r) \quad (2.28)$$

## 2.6. Model Code (MC 2011)

### 2.6.1. Slabs without shear reinforcement

The Model Code (MC 2010) is like SIA262 2003 based on the CSCT. The punching strength depends on the slab rotation, which results from the applied load and the stiffness of the slab defined by the flexural strength. Since the punching strength depends on the applied load, the equation has to be solved so that  $V_{Rc} = V$ , as it was described previously for SIA262 2003 in Section 2.5. Another specialty of the MC 2010 is that different levels of approximation exist. Level I approximation enables a fast pre-dimensioning, Level II approximation is recommended for the typical design of new structure, Level III approximation is recommended either for special design cases or for the analysis of existing structures, and Level IV approximation is recommended for special design cases or for a more detailed assessment of existing structures (Tassinari 2011). In this research, Level II and Level III approximation is used for the prediction of the tested specimen presented herein and Level II approximation is used for the comparison to tests from literature. For slabs without shear reinforcement, the punching strength is defined as:

$$V_{R,c} = k_{\psi} \cdot \sqrt{f_c} \cdot b_0 \cdot d_v \quad (2.29)$$

where  $b_0$  is a control perimeter set at  $d/2$  of the border of the support region with circular corners,  $d_v$  is the shear-resisting effective depth of the slab,  $f_c$  is the compressive strength of concrete in MPa, and  $k_{\psi}$  is defined as:

$$k_{\psi} = \frac{1}{1.5 + 0.9 \cdot \psi \cdot d \cdot k_{dg}} \leq 0.6 \quad (2.30)$$

where  $d$  is the effective depth in mm,  $\psi$  is the rotation of the slab, and  $k_{dg}$  is a factor accounting for the influence of aggregate size defined as:

$$k_{dg} = \frac{32}{16 + d_g} \geq 0.75 \quad (2.31)$$

where  $d_g$  is the maximum aggregate size in mm.

For a Level II calculation, the rotation of the slab can be estimated by:

$$\psi = 1.5 \cdot \frac{r_s}{d} \cdot \frac{f_y}{E_s} \cdot \left( \frac{m_s}{m_R} \right)^{1.5} \quad (2.32)$$

where  $r_s$  distance to the point where the radial bending moment is zero,  $d$  is the effective depth,  $E_s$  is the Young's modulus of the flexural reinforcement,  $m_R$  is the flexural strength, and  $m_s$  the average moment per unit length in the support strip due to the applied load.

For inner columns,  $m_s$  can be assumed as:

$$m_s = \frac{V}{8} \quad (2.33)$$

where  $V$  is the applied shear force.

In the case of a level III, the factor 1.5 can be decreased to 1.2 due to the more accurate prediction of the average bending moment  $m_s$ . Thus, the rotation for a Level III calculation can be estimated by:

$$\psi = 1.2 \cdot \frac{r_s}{d} \cdot \frac{f_y}{E_s} \cdot \left( \frac{m_s}{m_R} \right)^{1.5} \quad (2.34)$$

where  $r_s$  distance to the point where the radial bending moment is zero,  $d$  is the effective depth,  $E_s$  is the Young's modulus of the flexural reinforcement,  $m_R$  is the flexural strength, and  $m_s$  is the average moment per unit length in the support strip determined by a linear-elastic finite element analysis.

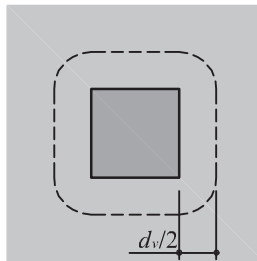


Figure 2.9: Control perimeter according to MC 2010

### 2.6.2. Slabs with shear reinforcement

While most punching provisions of MC 2010 are similar to SIA262 2003, the provision regarding failure within the shear-reinforced area is different. While SIA262 2003 completely neglects the contribution of concrete, MC 2010 takes the summation of the shear forces transferred by the concrete and the shear reinforcement. Both values, the shear contribution of the concrete and that of the shear reinforcement depend on the rotation of the slab accounting for the activation of the shear reinforcement and the reduction in the concrete contribution with increasing rotation. More information about the mechanical model behind this approach can be found in the next subchapter explaining the CSCT in detail.

The contribution of the shear reinforcement can be calculated as the sum of the multiplication of the cross-sectional area of the shear reinforcement within an area between a distance of  $0.35d_v$  and  $d_v$  from the column face (Figure 2.10) and the stresses in the shear reinforcement. Therefore, the contribution of the shear reinforcement is defined as:

$$V_{Rs} = \sum A_{sw} \cdot \sigma_{sw} \quad (2.35)$$

where  $\sum A_{sw}$  is the cross-sectional area of all the shear reinforcement intersected by the potential failure surface (conical surface with angle  $45^\circ$ ) within a distance of  $0.35d_v$  to  $d_v$  from the column face and  $\sigma_{sw}$  are the stresses in the shear reinforcement defined by the rotation of the slab and the bond conditions of the shear reinforcement. The stresses in the shear reinforcement are given by:

$$\sigma_{sw} = \frac{E_{sw}\psi}{6} \cdot \left( 1 + \frac{2f_{ct}}{f_{yw}} \cdot \frac{d}{\phi_w} \right) \leq f_{yw} \quad (2.36)$$

where  $E_{sw}$  is the Young's modulus of the shear reinforcement,  $\psi$  is the rotation of the slab,  $f_{ct}$  is the tensile strength of the concrete defining the maximum bond stress,  $f_{yw}$  is the yield strength of the shear reinforcement,  $d$  is the effective depth, and  $\phi_w$  is the diameter of the vertical branch of the shear reinforcement.

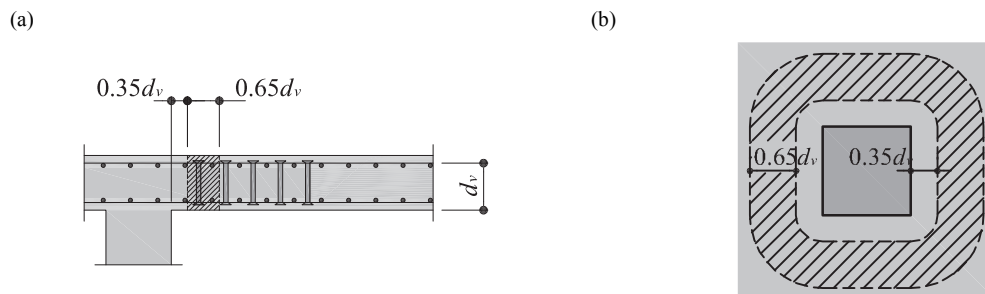


Figure 2.10: Shear reinforcement considered by MC 2010

The concrete contribution can be calculated according to the provisions for punching of slabs without shear reinforcement (Equation 2.29). Finally, the punching strength for failure within the shear-reinforced area can be obtained by the summation of the contributions of the concrete and the shear reinforcement.

$$V_R = V_{Rc} + V_{Rs} \quad (2.37)$$

Similar to other codes, MC 2010 uses the same formulation as for punching without shear reinforcement for the calculation of the punching strength for failure outside the shear-reinforced area. However, for failure outside the shear reinforced area, the control perimeter is

set at the distance of  $0.5d_{v,out}$  from the outermost shear reinforcement perimeter. Thus, the punching strength is defined as:

$$V_{RC} = k_{\psi} \cdot \sqrt{f_c} \cdot b_{out} \cdot d_{v,out} \quad (2.38)$$

where  $k_{\psi}$  is defined according to Equation 2.30,  $f_c$  is the concrete compressive strength,  $b_{out}$  is a control perimeter set at a distance of  $0.5d_{v,out}$  from the outermost perimeter of shear reinforcement, and  $d_{v,out}$  is the distance between the flexural reinforcement and the bottom end of the vertical branch of the shear reinforcement.

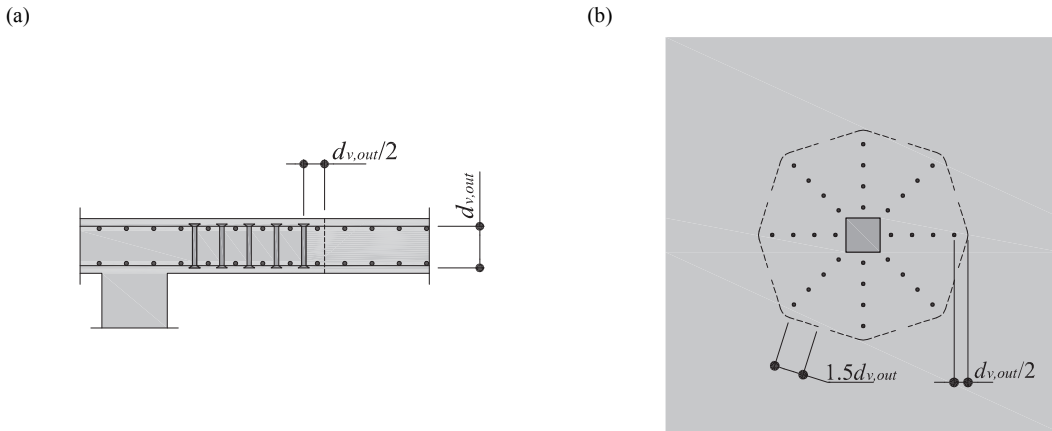


Figure 2.11: Control perimeter for punching shear verification outside the shear- reinforced area according to MC 2010

With respect to the failure of the concrete strut, MC 2010 uses a similar approach as other codes by increasing the punching strength of slabs without punching shear reinforcement by a factor. It has to be noted that the predicted punching strength  $V_R$  is a function of the applied shear force  $V$ , which is included in the calculation of the rotation. Therefore, the maximum punching strength is not the proportionally increased punching strength estimated by the formulation for slabs without shear reinforcement. The maximum punching strength is defined as:

$$V_R = k_{sys} \cdot k_{\psi} \cdot \sqrt{f_c} \cdot b_0 \cdot d_v \leq \sqrt{f_c} \cdot b_0 \cdot d_v \quad (2.39)$$

where factor  $k_{sys}$  is proposed as 2.4 for slabs with stirrups and 2.8 for slabs with double headed studs. All other parameters correspond to the formulation of punching of slabs without shear reinforcement.



## 2.7. Critical shear crack theory (CSCT)

### 2.7.1. Slabs without shear reinforcement

The principal hypothesis of the critical shear crack theory is that the punching strength depends on the opening and the roughness of a critical shear crack (Muttoni 2008; Fernández Ruiz and Muttoni 2009; Muttoni and Fernández Ruiz 2010). Therefore, the main parameters of the CSCT are the rotation of the slab, the effective depth, and the aggregate size. Since the latter two parameters are slab properties and are constant for each slab, the punching strength can be defined as a function of the slab rotation. This function can be illustrated as a failure criterion curve. The intersection point of the failure criterion and the flexural response of the slab (load-rotation relationship) define the punching strength of the slab (Figure 2.12).

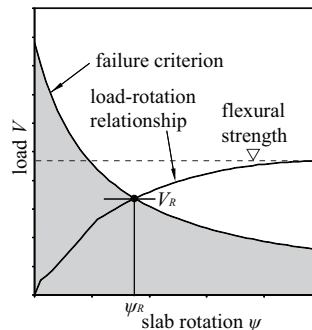


Figure 2.12: Calculation of the punching strength for slabs without shear reinforcement according to the CSCT

As mentioned previously, the failure criterion accounts for the opening of a critical shear crack and the roughness of the crack defining maximal admissible shear stresses at a control perimeter. By considering these parameters, a semi-empirical failure criterion was developed. The punching strength as a function of the slab rotation is defined as:

$$\frac{V_R}{b_0 \cdot d \cdot \sqrt{f_c}} = \frac{3/4}{1 + \frac{15 \cdot \psi \cdot d}{d_{g0} + d_g}} \quad (2.40)$$

where  $\psi$  is the slab rotation,  $d$  is the effective depth,  $d_{g0}$  is a reference aggregate size equal to 16 mm,  $d_g$  is the maximum aggregate size,  $f_c$  is the compressive strength of concrete in MPa, and  $b_0$  is the control perimeter set at a distance of  $0.5d$  from the support region with circular corners.

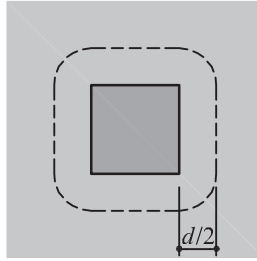


Figure 2.13: Control perimeter used for the CSCT

The load-rotation relationship can be assumed to be independent from the failure criterion and it can be determined by any suitable method such as an analytical model or a non-linear finite element analysis. Different methods will be discussed in Subchapter 2.8.

### 2.7.2. Slabs with shear reinforcement

Similar to the case without shear reinforcement, the CSCT defines different failure criteria as a function of the rotation of the slab for each failure mode if shear reinforcement is present (Fernández Ruiz and Muttoni 2009). Figure 2.14 shows an overview of the principal failure modes namely (a) failure within the shear-reinforced area, (b) crushing of the concrete strut, (c) failure outside the shear-reinforced area, and (d) flexural failure.

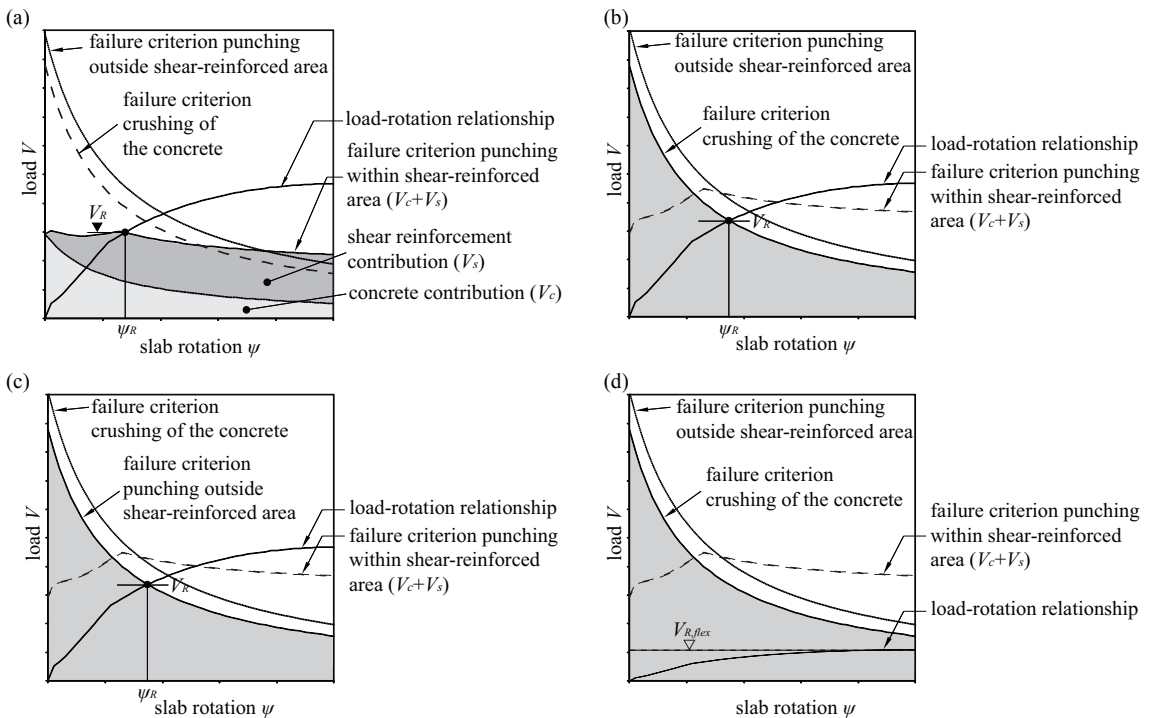


Figure 2.14: Calculation of the punching strength according to the CSCT for (a) failure within the shear-reinforced area, (b) crushing of concrete, (c) failure outside the shear-reinforced area, and (d) flexural failure

The failure within the shear reinforced area is assumed to occur when a critical shear crack opens and strains localize. It is assumed that the concrete carries a portion of the shear force depending on the crack opening and the roughness of the critical crack. The other portion is carried by the shear reinforcement, which also depends on the opening of the critical crack. Therefore, the strength can be defined as the sum of the two components:

$$V_R(\psi) = V_c(\psi) + V_s(\psi) \quad (2.41)$$

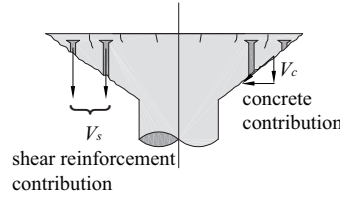


Figure 2.15: Contribution of the concrete and the shear reinforcement

The concrete contribution to the punching strength can be estimated using the same hypotheses as for slabs without shear reinforcement, according to Equation 2.40. Using the same hypotheses, one can calculate the contribution of the shear reinforcement as the sum of the stresses in the shear reinforcement  $\sigma_w$  times the cross sectional area of the shear reinforcement  $A_{sw}$ :

$$V_s = \sum_{i=1}^n \sigma_{wi}(\psi) \cdot A_{swi} \quad (2.42)$$

It is assumed that the strains and thus the stresses depend on the opening of a critical shear crack  $w$ , which is assumed to open proportionally to the product of the rotation  $\psi$  and the effective depth  $d$ . Thus, the crack width can be expressed as:

$$w \propto \psi \cdot d \quad (2.43)$$

or as:

$$w = \kappa \cdot \psi \cdot d \quad (2.44)$$

where  $\kappa$  is a constant value that is proposed to be 0.5 (Fernández Ruiz and Muttoni 2009).

Based on the distribution of the shear reinforcement and the location and the inclination of the critical shear crack, one can calculate the crack opening at the position of the shear reinforcement (Figure 2.16). Within this research, the tip of the critical shear crack is assumed to be at the column face with an inclination angle of  $45^\circ$  ( $\pi/4$ ) as it is proposed by Fernández Ruiz and Muttoni (Fernández Ruiz and Muttoni 2009).

Therefore, the crack width at the position of the shear reinforcement can be expressed as:

$$w_i = 0.5 \cdot \psi \cdot h_i \cdot \cos\left(\frac{\pi}{4}\right) \quad (2.45)$$

where  $\psi$  is the rotation of the slab and  $h_i$  is the vertical distance of the crack tip to the point where the crack crosses the shear reinforcement.

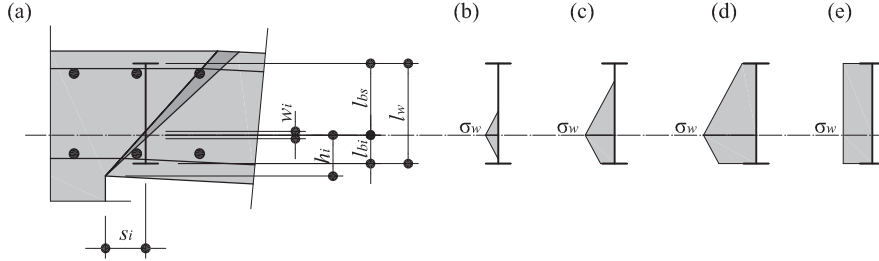


Figure 2.16: (a) Opening of the crack at an angle of  $45^\circ$ , (b-d) stress distribution in the stud depending on the crack opening and the bond conditions, and (e) stress distribution if no bond is considered

In the case of smooth shear reinforcement by which no bond between reinforcement and concrete occurs, the stresses and the strains are constant over the whole length of the shear reinforcement (Figure 2.16e). Therefore, the strains can be integrated along the whole length of the stud in order to obtain the crack width  $w_i$ . By using this relationship and assuming a linear-elastic material model, one can obtain the stresses in the shear reinforcement by:

$$\sigma_{wi} = E_s \cdot \frac{w_i}{l_w} \quad (2.46)$$

where  $E_s$  is the Young's modulus of and  $l_w$  is the length of the shear reinforcement.

In the case of ribbed shear reinforcement by which bond along the vertical branch occurs, the stresses in the shear reinforcement depend on the stress at the crack and on the bond conditions. The assumption of a perfectly-plastic bond law leads to a linear distribution of the stresses along the length of the shear reinforcement. The difference in stress in the shear reinforcement per unit length can be calculated by the bond force per unit length divided by the cross sectional area of the shear reinforcement. Thus, the difference in stress can be expressed as:

$$\Delta\sigma_w = \frac{f_b \cdot \Delta x}{A_{sw}} = \frac{\tau_b \cdot d_w \cdot \pi \cdot \Delta x}{d_w^2 \cdot \frac{\pi}{4}} = \frac{4 \cdot \tau_b \cdot \Delta x}{d_w} \quad (2.47)$$

where  $\tau_b$  is the bond strength,  $d_w$  is the diameter of the shear reinforcement, and  $\Delta x$  is a unit length.

Assuming a linear-elastic material model for the reinforcing steel the difference in strain can be obtained by:

$$\varepsilon_w = \frac{\Delta\sigma_w}{E_s} = \frac{4 \cdot \tau_b \cdot \Delta x}{d_w \cdot E_s} \quad (2.48)$$

where  $E_s$  is the Young's modulus,  $\tau_b$  is the bond strength,  $d_w$  is the diameter of the shear reinforcement, and  $\Delta x$  is a unit length.

The crack width can be stated as the total deformation within the shear reinforcement:

$$w = \int_a^b \varepsilon_w \cdot dx \quad (2.49)$$

where  $a$  and  $b$  are the anchorage points of the shear reinforcement and  $\varepsilon_w$  is the strain in the shear reinforcement.

Since the length of the shear reinforcement is rather short, full anchorage is not necessarily achieved by bond along the vertical branch but at each end of the shear reinforcement. Therefore, the stress distribution also depends on the distance between the crack and the anchorage provided at each end of the shear reinforcement leading to three different cases of stress distributions that can occur as shown in Figure 2.16(b-d).

In the first case, the anchorage is on both sides performed by bond (Figure 2.16b). This case occurs if the crack width  $w_i$  is smaller than the limit:

$$w_i \leq \frac{4 \cdot \tau_b}{E_s \cdot d_w} \cdot l_{ai}^2 \quad (2.50)$$

where  $E_s$  is the Young's modulus,  $\tau_b$  is the bond strength,  $d_w$  is the diameter of the shear reinforcement, and  $l_{ai}$  is the shorter distance between the crack and one end of the shear reinforcement ( $l_{ai} = \min(l_{bi}, l_{bs})$ ).

In this case, the stresses can be obtained from:

$$\sigma_{wi} = \sqrt{\frac{4 \cdot \tau_b \cdot E_s \cdot w_i}{d_w}} \leq f_{yw} \quad (2.51)$$

where  $E_s$  is the Young's modulus,  $\tau_b$  is the bond strength,  $d_w$  is the diameter of the shear reinforcement,  $w_i$  is the crack opening, and  $f_{yw}$  is the yielding strength of the shear reinforcement.

The second case occurs if the distance between the crack and one end of the shear reinforcement is too small to provide sufficient anchorage solely by bond. The distance at the other end however provides sufficient anchorage length (Figure 2.16c). This case occurs if the crack width  $w_i$  is between the limits:

$$\frac{4 \cdot \tau_b}{E_s \cdot d_w} \cdot l_{ai}^2 < w_i < \frac{2 \cdot \tau_b}{E_s \cdot d_w} \cdot [(l_{as} + l_{ai})^2 - 2 \cdot l_{ai}^2] \quad (2.52)$$

where  $E_s$  is the Young's modulus,  $\tau_b$  is the bond strength,  $d_w$  is the diameter of the shear reinforcement,  $l_{ai}$  is the shorter distance between the crack and one end of the shear reinforcement ( $l_{ai} = \min(l_{bi}; l_{bs})$ ), and  $l_{as}$  is the longer distance between the crack and one end of the shear reinforcement ( $l_{as} = \max(l_{bi}; l_{bs})$ ).

In this case, the stresses can be obtained from:

$$\sigma_{wi} = \frac{-l_{ai} + \sqrt{2 \cdot l_{ai}^2 + \frac{d_w \cdot E_s \cdot w_i}{2 \cdot \tau_b}}}{\frac{d_w}{4 \cdot \tau_b}} \leq f_{yw} \quad (2.53)$$

where  $E_s$  is the Young's modulus,  $\tau_b$  is the bond strength,  $d_w$  is the diameter of the shear reinforcement,  $w_i$  is the crack opening,  $l_{ai}$  is the shorter distance between the crack and one end of the shear reinforcement, and  $l_{as}$  is the longer distance between the crack and one end of the shear reinforcement, and  $f_{yw}$  is the yielding strength of the shear reinforcement.

The third case occurs if neither one of the distances between the crack and the ends of the shear reinforcement is large enough in order to provide sufficient anchorage solely by bond. This case occurs if the crack width  $w_i$  is larger than the limit:

$$w_i \geq \frac{2 \cdot \tau_b}{E_s \cdot d_w} \cdot [(l_{as} + l_{ai})^2 - 2 \cdot l_{ai}^2] \quad (2.54)$$

where  $E_s$  is the Young's modulus,  $\tau_b$  is the bond strength,  $d_w$  is the diameter of the shear reinforcement,  $l_{ai}$  is the shorter distance between the crack and one end of the shear reinforcement ( $l_{ai} = \min(l_{bi}; l_{bs})$ ), and  $l_{as}$  is the longer distance between the crack and one end of the shear reinforcement ( $l_{as} = \max(l_{bi}; l_{bs})$ ).

In this case, the stresses can be obtained from:

$$\sigma_{wi} = \frac{E_s \cdot w_i}{l_{as} + l_{ai}} + \frac{2 \cdot \tau_b}{d_w} \cdot \frac{l_{as}^2 + l_{ai}^2}{l_{as} + l_{ai}} \leq f_{yw} \quad (2.55)$$

where  $E_s$  is the Young's modulus,  $\tau_b$  is the bond strength,  $d_w$  is the diameter of the shear reinforcement,  $w_i$  is the crack opening,  $l_{ai}$  is the shorter distance between the crack and one end

of the shear reinforcement, and  $l_{as}$  is the longer distance between the crack and one end of the shear reinforcement, and  $f_{yw}$  is the yielding strength of the shear reinforcement.

Using these formulations, one can calculate the stresses at each vertical branch of the shear reinforcement. However, since this approach is very sensitive to the actual position of the shear reinforcement and even more to the distinction if a vertical branch is inside or just outside the critical crack, the calculation method is more applicable with a smeared shear reinforcement approach (refer to Chapter 7.4.3). Therefore, the calculations performed within this research use a shear reinforcement ratio calculated at a control perimeter set at a distance of  $0.5d$  from the border of the support:

$$\rho_w = \frac{n_r \cdot \frac{d_w^2}{4} \cdot \pi}{(4c + d\pi) \cdot d} \cdot \frac{d}{s_0 + \frac{s_1}{2}} \quad (2.56)$$

where  $n_r$  is the number of radii of shear reinforcement,  $d_w$  is the shear reinforcement diameter,  $s_0$  is the distance between the first row of shear reinforcement and the column face,  $s_1$  is the distance between two adjacent reinforcements at the same radius,  $c$  is the side length of the column, and  $d$  is the effective depth of the slab.

For the strains of the smeared shear reinforcement, an average value calculated at the half distance of the critical crack can be assumed. Using this assumption, the crack opening at mid-distance can be estimated by:

$$w = 0.5 \cdot \psi \cdot \frac{d}{2} \cdot \cos\left(\frac{\pi}{4}\right) \quad (2.57)$$

where  $\psi$  is the rotation of the slab and  $d$  is the effective depth.

In the case of this smeared shear reinforcement approach only two cases of stress distribution in the shear reinforcement have to be distinguished depending on the crack opening and the bond conditions. The first case covers small crack openings which allow the shear reinforcement to be activated solely by bond. Therefore, the bond length is smaller than the distance of the crack to the end of the shear reinforcement (assumed to be  $l_w/2$ ). This limit can be calculated by:

$$w_{lim} = 4 \cdot \frac{\tau_b}{E_s \cdot d_w} \cdot \left(\frac{l_w}{2}\right)^2 \quad (2.58)$$

where  $\tau_b$  is the bond strength,  $d_w$  is the diameter of the shear reinforcement,  $E_s$  is the Young's modulus, and  $l_w$  is length of the shear reinforcement.

For crack opening smaller than the limit ( $w < w_{lim}$ ), the stresses in the shear reinforcement can be calculated by:

$$\sigma_w = \sqrt{\frac{4 \cdot \tau_b \cdot E_s \cdot w}{d_w}} \leq f_{yw} \quad (2.59)$$

where  $\tau_b$  is the bond strength,  $d_w$  is the diameter of the shear reinforcement,  $E_s$  is the Young's modulus, and  $f_{yw}$  is the yielding strength of the shear reinforcement.

For crack opening equal or larger as the limit ( $w \geq w_{lim}$ ), the stresses in the shear reinforcement can be calculated by:

$$\sigma_w = \frac{E_s \cdot w}{l_w} + \frac{2\tau_b}{d_w} \cdot \frac{l_w}{2} \leq f_{yw} \quad (2.60)$$

where  $\tau_b$  is the bond strength,  $d_w$  is the diameter of the shear reinforcement,  $E_s$  is the Young's modulus,  $l_w$  is length of the shear reinforcement, and  $f_{yw}$  is the yielding strength of the shear reinforcement.

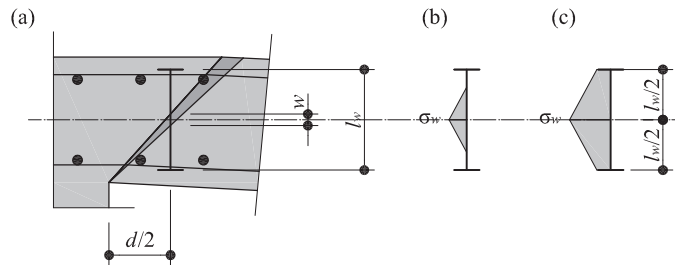


Figure 2.17: (a) Opening of the crack assuming smeared shear reinforcement concentrated at mid-distance, (b) stress distribution in the stud if  $w < w_{lim}$ , and (c) stress distribution in the stud if  $w \geq w_{lim}$

For failure at the outer perimeter, the CSCT uses a formulation that is similar to the formulation for slabs without shear reinforcement. In fact, the only difference to the formulation for slabs without shear reinforcement is that the control perimeter changes. Instead of being set a distance of  $d/2$  from the column face, the control perimeter is set at a distance of  $d/2$  from the outermost perimeter of shear reinforcement.

$$\frac{V_R}{b_{out} \cdot d_{out} \cdot \sqrt{f_c}} = \frac{3/4}{1 + \frac{15 \cdot \psi \cdot d}{d_{g0} + d_g}} \quad (2.61)$$

where  $\psi$  is the slab rotation,  $d$  is the effective depth,  $d_{g0}$  is a reference aggregate size equal to 16 mm,  $d_g$  is the aggregate size,  $f_c$  is the compressive strength of concrete,  $d_{out}$  is the distance between the flexural reinforcement and the bottom end of the vertical branch of the shear



reinforcement, and  $b_{out}$  is the control perimeter set at a distance of  $0.5d$  from the outermost perimeter of shear reinforcement.

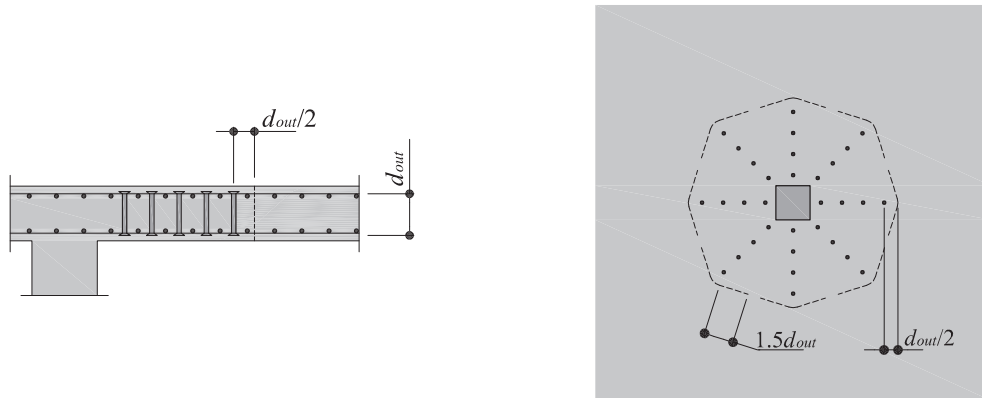


Figure 2.18: Control perimeter for punching shear verification outside the shear- reinforced area used in the CSCT

For the failure of crushing of the concrete strut, the CSCT uses a simplified formulation. It is assumed that the compressive strength in the strut depends on the transverse strains. Since the transverse strain depends on the rotation of the slab, a failure criterion as a function of the rotation is proposed that multiplies the punching strength of slabs without shear reinforcement by a factor  $\lambda$ , which accounts for different shear reinforcement systems. Factor  $\lambda$  of 3.0 is proposed by Fernández-Ruiz and Muttoni (Fernández Ruiz and Muttoni 2009) for studs or systems with perfect anchorage conditions (steel offcuts, headed reinforcement). For other systems, such as stirrups or where the reinforcement is developed by bond, a value of  $\lambda = 2.5$  is adopted. Additionally, the CSCT considers the aggregate size  $d_g$ , which accounts for the width of the crushing zone where strains localize (Muttoni and Fernández Ruiz 2010). Thus, the punching strength is given by:

$$\frac{V_R}{b_0 \cdot d \cdot \sqrt{f_c}} = \lambda \frac{3/4}{1 + \frac{15 \cdot \psi \cdot d}{d_{g0} + d_g}} \quad (2.62)$$

where  $\psi$  is the slab rotation,  $d$  is the effective depth,  $d_{g0}$  is a reference aggregate size equal to 16 mm,  $f_c$  is the compressive strength of concrete, and  $b_0$  is the control perimeter set at a distance of  $0.5d$  from the support region with circular corners.

If the load-rotation curve does not intersect with any of the previously mentioned failure criterion, it is assumed that no punching failure occurs and a flexural failure can be expected. This can be the case for slabs with low amount of flexural reinforcement.

## 2.8. Load-rotation response

As discussed previously, several models limit the punching strength depending on the state of deformation and thus depending on the slab response. Therefore, models such as the CSCT require the prediction of the load-rotation curve in order to obtain the punching strength. This prediction of the load-rotation curve of the slab is in the case of the CSCT independent of the failure criterion and can be obtained by any suitable model. Generally, the models can be separated into two groups: analytical and numerical models. The analytical models are typically limited to axisymmetric slab element whereby the numerical models provide the use of arbitrary shapes. The following subsections present a brief overview of the analytical and numerical models used for the prediction of the load-rotation behavior of slabs related to punching. Subsequently, a more detailed explanation of the Quadrilinear model proposed by Muttoni (Muttoni 2008) is given.

### 2.8.1. Analytical models

In the case of a linear-elastic slab analysis, an exact solution of the slab response can be found analytically for simple cases such as that of an axisymmetric slab. In fact, an axisymmetric slab with an axisymmetric loading leads to a rather simple differential equation (Equation 2.63) that can be solved by stepwise integration. However, an analytical solution can only be easily found for linear-elastic slab behavior for which the flexural rigidity  $D$  is constant.

$$\frac{1}{r} \cdot \frac{d}{dr} \cdot \left\{ r \cdot \frac{d}{dr} \cdot \left[ \frac{1}{r} \cdot \frac{d}{dr} \cdot \left( r \cdot \frac{dw(r)}{dr} \right) \right] \right\} = \frac{q(r)}{D} \quad (2.63)$$

where the flexural rigidity  $D$  is

$$D = \frac{E \cdot h^3}{12(1 - \nu^2)} \quad (2.64)$$

For nonlinear behavior such as it is the case of reinforced concrete, the flexural rigidity is a function of the state of stress defined by the internal forces acting at a distance  $r$  away from the support. However, the differential equation can still be solved by using a numerical method as it will be explained in the next subchapter or by using simplified method in which a certain kinematic of the slab is assumed. For this, Kinnunen and Nylander (Kinnunen and Nylander 1960) assumed a kinematic by which a slab portion outside a shear crack is regarded as rigid in radial direction. Therefore, it is assumed that this slab portion has a constant rotation. Using a bilinear slab behavior and the equilibrium condition at the outer slab segment, the load-rotation curve of the slab can be calculated. Muttoni (Muttoni 2008) proposed a more refined approach that assumes a quadrilinear slab behavior. This model (subsequently referred to it as

Quadrilinear) is considered to be the most suitable analytical model in combination with the CSCT and it will thus be explained in more detail in Subchapter 2.8.3.

## 2.8.2. Numerical models

Another method to calculate the load-rotation curve is the numerical approach. Either a numerical method can be applied to simply solve numerically the differential equation of an axisymmetric slab considering the nonlinear slab behavior or a more sophisticated numerical method can be used such as the finite element method to model the slab as a whole. Guandalini (Guandalini 2005) uses a numerical approach in order to numerically solve the axisymmetric case. For this, he calculates the forces acting on a small slab element as a function of the state of strain in the slab. By using the equilibrium conditions within a discrete element (Figure 2.19) and by applying the boundary conditions, he obtains the response of the axisymmetric slab.

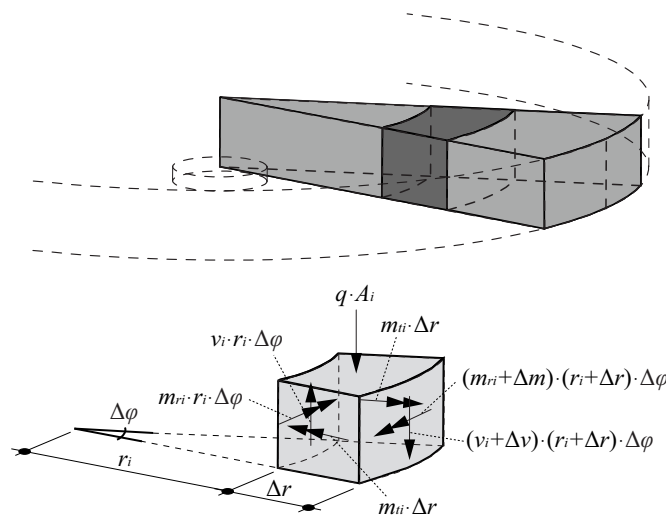


Figure 2.19: Solving of axisymmetric cases by numerical integration

However, for more general geometries and loadings, an axisymmetric solution might not be suitable. In these cases an approach based on the finite element method is more promising. Starting in the last century, various research has been performed regarding the application of the finite element method for reinforced concrete. Due to the enormous amount of different developments in this area, it is neither possible nor the objective of this research to present the development of elements used for the modeling of reinforced concrete in its entirety. Therefore, the following sections present a selection of finite elements analyses and developments.

Generally, the elements chosen for the analysis of flat slabs are either plate (or shell) elements or 3D solid elements. Whereby the latter is only used for the modeling of a limited portion of the slab (e.g. punching test specimens) since the modeling of a flat slab requires a large amount of elements leading to an extensive need of computational resources and calculation time. The advantage of the use of 3D solid elements is that the concrete and the reinforcement can be modeled separately so that the model accounts of the orthogonal reinforcement. Additionally, the punching shear reinforcement can be implemented in the same model allowing the analysis of the load transfer path in the column vicinity. With respect to punching of flat slabs, Beutel (Beutel 2003) and Häusler (Häusler 2009) investigated several punching tests with and without shear reinforcement by using models with 3D solid elements. The analysis led to acceptable results regarding the response of the investigated test specimens with and without shear reinforcement. Nevertheless, it has to be mentioned that a calculation using 3D elements is sophisticated so that the input and model parameters have to be chosen carefully and the details such as the anchorage of the shear reinforcement (Beutel 2003) have to be appropriately modeled.

A simpler approach is the use of 2D elements such as plate or shell elements. However, the main challenge by using plate or shell elements is the implementation of the nonlinear response of a reinforced concrete section. Several methods exist that can account for the nonlinearity in the 2D finite element analysis. One possibility is the use of elements that consist of different layers which are separately integrated (Figure 2.20) and later assembled for the whole element. Thus, every layer has its own stiffness matrix which depends on the state of deformation. Formulations for this method with respect to plate and shell elements have been developed, amongst others, by Hand et al. (Hand et al. 1973) and by Vecchio and Polak (Vecchio 1989; Polak 1992; Polak and Vecchio 1993). The main difficulty lies in the definition of the torsional stiffness. For this, Hand et al. (Hand et al. 1973) introduced a shear retention factor that accounts for dowel action and aggregate interlock so that the element can provide shear stiffness. Polak (Polak 1992) defined the torsional stiffness as a function of the concrete stiffness in the principal directions.

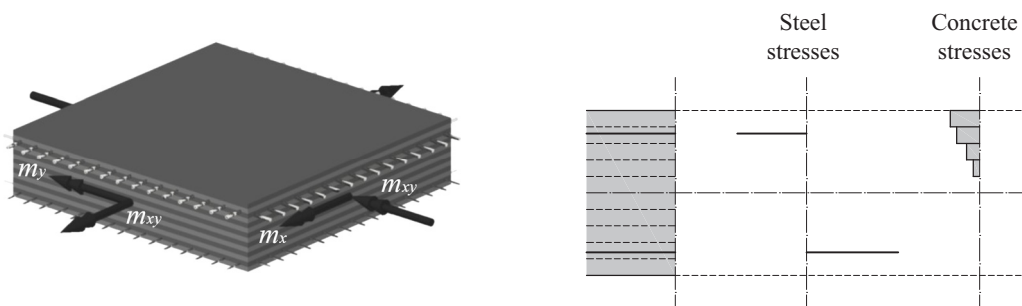
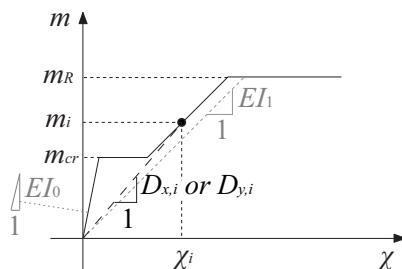


Figure 2.20: Layered element

Another possibility to introduce the material nonlinearity into the finite element method is by using a modified stiffness approach. This method was introduced by Jofriet and McNeice (Jofriet and McNeice 1971) and by Bell and Elms (Bell and Elms 1972). In this method, the constitutive relationship of a reinforced concrete element is calculated in advance leading to the secant stiffness of the element depending on the state of deformations. Afterwards, the secant stiffness is used for a linear finite element calculation leading to a new state of deformation for each element. This routine will be repeated until a certain tolerance is met. The main advantages of this method are firstly the calculation speed since the element response has to be calculated only once and secondly the robustness of the calculation. Due to the fact that the constitutive relationship is calculated in advance, the response of the element is well defined so that for each state of deformation, a defined stiffness exists.

Vaz-Rodrigues (Vaz Rodrigues 2007) and Tassinari (Tassinari 2011) used this method with respect to shear test and punching test calculations, respectively. The main problem however was the introduction of the torsional stiffness after cracking. Similar to the shear retention factor introduced by Hand et al. (Hand et al. 1973), Vaz-Rodrigues (Vaz Rodrigues 2007) introduced the torsion retention factor to account for the torsional stiffness of the slab (Figure 2.21). For regular punching tests Vaz Rodrigues (Vaz Rodrigues 2007) and Tassinari (Tassinari 2011) empirically determined the torsion retention factor to be  $\beta_t = 1/8$ . Since this value is completely empirical and thus it is only valid for the geometries and loadings according to the tests on which it is based on, a more sophisticated formulation is desired. Chapter 5 presents a constitutive model that allows modeling the bending and the torsional response of a reinforced slab element.



$$\{m\} = \begin{bmatrix} D_x & 0 & 0 \\ 0 & D_y & 0 \\ 0 & 0 & \beta_t \cdot (1 - \nu) \cdot \sqrt{D_x \cdot D_y} \end{bmatrix} \cdot \{\chi\}$$

Figure 2.21: Definition of the stiffness matrix using the torsion retention factor  $\beta_t$  (Tassinari 2011)

### 2.8.3. The Quadrilinear model (Muttoni 2008)

The Quadrilinear model assumes a similar slab behavior as Kinnunen and Nylander (Kinnunen and Nylander 1960). It is proposed to divide the slab into two parts: an inner and an outer part. The inner core over the column has a constant curvature and moment. The outer slab segment is assumed to undergo rigid body deformation in radial direction. Thus, the slab deforms accordingly to a conical shape which leads to a constant slab rotation  $\psi$ . Figure 2.22 illustrates the kinematic of the axisymmetric slab and the forces acting on the outer slab element.

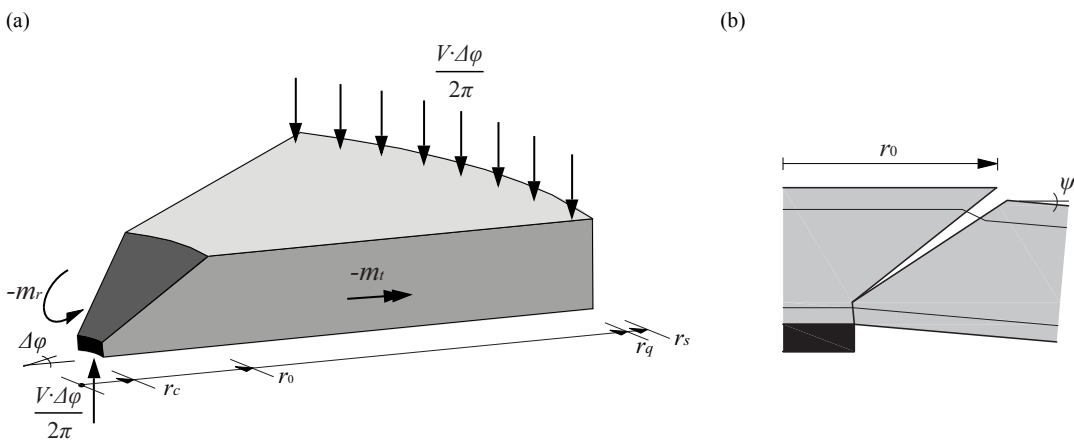


Figure 2.22: Assumed slab kinematic: (a) outer slab segment with acting forces and (b) deformed shape of the slab at the column vicinity

By looking at the outer slab segment, one can define the equilibrium of moments at the section at a radius of  $r_0$ :

$$V \cdot \frac{\Delta\varphi}{2\pi} \cdot (r_q - r_c) = -m_r \cdot \Delta\varphi \cdot r_0 - \Delta\varphi \int_{r_0}^{r_s} m_t \cdot dr \quad (2.65)$$

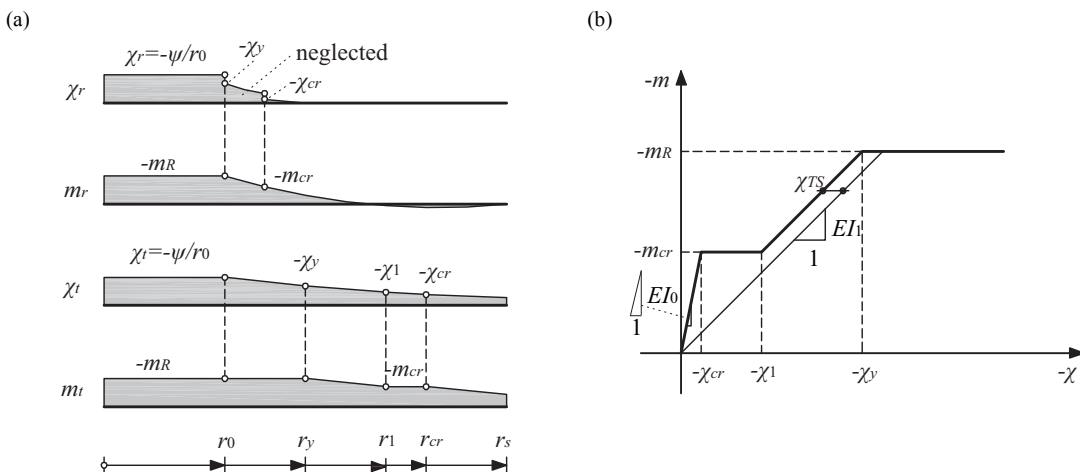


Figure 2.23: (a) Distribution of the radial and tangential moments and curvatures and (b) assumed quadrilinear moment-curvature relationship (Muttoni 2008)

At the inner slab element the radial and tangential curvatures are assumed to be constant. Thus, for  $r \leq r_0$ , the curvatures become:

$$\chi_r = \chi_t = -\frac{\psi}{r_0} \quad (2.66)$$

At the outer slab segment ( $r > r_0$ ) the tangential curvature becomes:

$$\chi_t = -\frac{\psi}{r} \quad (2.67)$$

In the axisymmetric slab element, this curvature distribution leads to the radial and tangential moments. Assuming a quadrilinear moment-curvature relationship as shown in Figure 2.23b, the moments are defined by the curvatures. The parameters for this relationship are defined as follows:

Assuming that the influence of the reinforcement can be neglected for the phase before cracking, the cracking moment can be estimated as:

$$m_{cr} = \frac{f_{ct} \cdot h^2}{6} \quad (2.68)$$

The stiffness before cracking can be expressed as:

$$EI_0 = \frac{E_c \cdot h^3}{12} \quad (2.69)$$

leading to the cracking curvature of:

$$-\chi_{cr} = \frac{m_{cr}}{EI_0} = \frac{2 \cdot f_{ct}}{h \cdot E_c} \quad (2.70)$$

After cracking, the stiffness of the reinforced slab specimen decreases. If a linear-elastic behavior of the concrete and the reinforcing steel is assumed, the stiffness after cracking can be estimated as:

$$EI_1 = \rho \cdot \beta \cdot E_s \cdot d^3 \cdot \left(1 - \frac{c}{d}\right) \cdot \left(1 - \frac{c}{3d}\right) \quad (2.71)$$

where  $c$  is the height of the compression zone defined as:

$$c = \rho \cdot \beta \cdot \frac{E_s}{E_c} \cdot d \cdot \left( \sqrt{1 + \frac{2 \cdot E_c}{\rho \cdot \beta \cdot E_s}} - 1 \right) \quad (2.72)$$

where  $E_s$  is the Young's modulus of the reinforcing steel,  $E_c$  is the Young's modulus of the concrete,  $\rho$  is the flexural reinforcement ratio,  $d$  is the effective depth, and  $\beta$  is an efficiency

factor that accounts for the orthogonal reinforcement layout. Within this research, a value of  $\beta = 0.75$  is used for the calculations of the punching strength. This value  $\beta$  will be discussed in detail in Chapter 8 regarding the validation of the analytical model developed within this thesis.

If one assumes a rigid-plastic concrete behavior, the flexural strength can be determined as:

$$m_R = \rho \cdot f_y \cdot d^2 \cdot \left(1 - \frac{\rho \cdot f_y}{2 \cdot f_c}\right) \quad (2.73)$$

where  $\rho$  is the flexural reinforcement ratio,  $d$  is the effective depth,  $f_y$  is the yielding strength of the reinforcement, and  $f_c$  is the compressive strength of the concrete.

The consideration of a constant contribution of the tension stiffening that can be estimated as:

$$\chi_{TS} = \frac{f_{ct}}{\rho \cdot \beta \cdot E_s} \cdot \frac{1}{6 \cdot h} \quad (2.74)$$

This equation leads to the curvature at the beginning of the stabilized cracked phase of:

$$-\chi_1 = \frac{m_{cr}}{EI_1} - \chi_{TS} \quad (2.75)$$

and to the curvature at yielding of:

$$-\chi_y = \frac{m_R}{EI_1} - \chi_{TS} \quad (2.76)$$

The different phases of the moment-curvature relationship divide the slab into four regions that have to be integrated (Figure 2.23): The region at which the reinforcement is yielding, which can be calculated by:

$$r_y = -\frac{\psi}{\chi_y} = \frac{\psi}{\frac{m_R}{EI_1} - \chi_{TS}} \leq r_s, \quad (2.77)$$

the region where the cracking is stabilized, which can be calculated by:

$$r_1 = -\frac{\psi}{\chi_1} = \frac{\psi}{\frac{m_{cr}}{EI_1} - \chi_{TS}} \leq r_s, \quad (2.78)$$

and the region where the concrete is cracked, which can be calculated by:

$$r_{cr} = -\frac{\psi}{\chi_{cr}} = \frac{\psi \cdot EI_0}{m_{cr}} \leq r_s. \quad (2.79)$$



Using these formulations, one can obtain the shear force as a function of the slab rotation at the outer slab segment by solving Equation 2.65:

$$V = \frac{2\pi}{r_q - r_c} \cdot \left( \begin{array}{l} m_r \cdot r_0 + m_R \langle r_y - r_0 \rangle + EI_1 \psi \langle \ln(r_1) - \ln(r_y) \rangle \\ + EI_1 \chi_{TS} \langle r_1 - r_y \rangle + m_{cr} \langle r_{cr} - r_1 \rangle + EI_0 \psi \langle \ln(r_s) - \ln(r_{cr}) \rangle \end{array} \right) \quad (2.80)$$

where  $r_q$  is the radius of the load application point,  $r_c$  is the radius of the column,  $m_r$  is the moment in radial direction acting at radius  $r_0$ ,  $r_0$  is the radius of the critical shear crack,  $m_R$  is the flexural strength,  $r_y$  is the radius of the yielded zone,  $r_1$  is the radius of the zone in which cracking is stabilized,  $r_{cr}$  is the radius of the cracked zone,  $r_s$  is the radius of the slab,  $EI_0$  is the flexural stiffness before cracking,  $EI_1$  is the flexural stiffness after cracking,  $\chi_{TS}$  is the decrease in curvature due to tension stiffening,  $\psi$  is the slab rotation at the outer slab segment, and operator  $\langle x \rangle$  is  $x$  for  $x \geq 0$  and 0 for  $x < 0$ .



### 3. Experimental Campaign

The experimental campaign within this research project consisted of sixteen full-scale slab specimens. All slabs had the same plan dimensions (3.00 m x 3.00 m) and the same flexural reinforcement ratio (1.5%). The investigated parameters were the column size (defined as column size to effective depth ratio  $c/d_n$ ), the slab thickness ( $h$ ), the amount of shear reinforcement ( $\rho_w$ ), and the type of shear reinforcement system. An overview of the test parameters is illustrated in Figure 3.1. Various continuous measurements have been taken such as the applied load, the slab rotation, the vertical displacements, the surface deformations, the change in slab thickness, and the strains in the shear reinforcement. This chapter that is based on the paper (Lips et al. 2012b) presents a summary of the tests performed within the research project. A more detailed description of the test set-up and the measurement devices as well as all the measured data can be found in the test reports (Lips et al. 2010; Lips et al. 2012a).

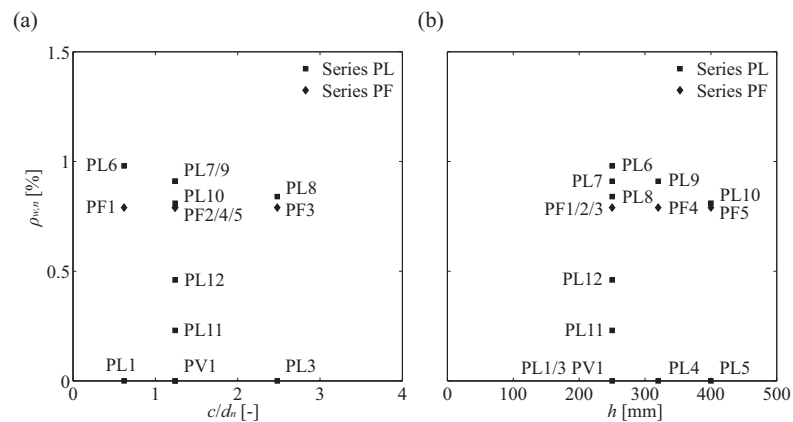


Figure 3.1: Overview of the test program: variation of the  $c/d_n$  ratio and (b) variation of the slab thickness (nominal values)

### 3.1. Geometry and reinforcement

All specimens had plan dimensions of 3.0 x 3.0 m and a constant flexural reinforcement ratio of 1.5%. The reinforcement layout was orthogonal and parallel to the slab edges. In a first series, the column size  $c$  was varied (130 mm; 260 mm; 520 mm), whereas the slab thickness  $h$  was kept constant (250 mm) leading to a constant effective depth  $d$  and thus to a variation of the column size to effective depth ratio  $c/d_n$ . In a second series, the slab thickness  $h$  was varied (250 mm; 320 mm; 400 mm) whereas the column size to effective depth ratio  $c/d_n$  was kept constant. In a third series, the amount of shear reinforcement was varied (0.93%; 0.47%; 0.23%). In this series the thickness ( $h = 250$  mm) and the column size ( $c = 260$  mm) were kept constant. The main parameters of the slab specimens are summarized in Table 3.1.

Table 3.1: Main parameters of the test specimens

	Specimen <sup>1</sup>	$h$ [mm]	$c$ [mm]	$d_{eff}$ [mm]	$c/d_{eff}$ [-]	$f_{c,test}$ [MPa]	$\rho_{eff}$ [%]	$f_y$ [MPa]	$\rho_{w,eff}$ [%]	$f_{yw}$ [MPa]	System
Series 1	PL1	250	130 x 130	193	0.67	36.2	1.63	583	-	-	-
	PL6	250	130 x 130	198	0.66	36.6	1.59	583	1.01	519	Studs
	PF1	250	130 x 130	209	0.62	31.1	1.50	583	0.79	536	Stirrups
	PV1	250	260 x 260	210	1.24	34.0	1.50	709	-	-	-
	PL7	250	260 x 260	197	1.32	35.9	1.59	583	0.93	519	Studs
	PF2	250	260 x 260	208	1.25	30.4	1.51	583	0.79	536	Stirrups
	PL3	250	520 x 520	197	2.64	36.5	1.59	583	-	-	-
	PL8	250	520 x 520	200	2.60	36.0	1.57	583	0.85	519	Studs
	PF3	250	520 x 520	209	2.49	37.1	1.50	583	0.79	536	Stirrups
Series 2	PL4	320	340 x 340	267	1.27	30.5	1.58	531 $\phi$ 20 580 $\phi$ 26	-	-	-
	PL9	320	340 x 340	266	1.28	32.1	1.59	531 $\phi$ 20 580 $\phi$ 26	0.93	516	Studs
	PF4	320	340 x 340	274	1.24	32.5	1.54	531 $\phi$ 20 580 $\phi$ 26	0.79	550	Stirrups
	PL5	400	440 x 440	353	1.25	31.9	1.50	580	-	-	-
	PL10	400	440 x 440	343	1.28	33.0	1.55	580	0.82	563	Studs
	PF5	400	440 x 440	354	1.24	33.4	1.50	580	0.79	550	Stirrups
S. 3	PL11	250	260 x 260	201	1.29	34.2	1.56	554	0.23	592	Studs
	PL12	250	260 x 260	201	1.29	34.6	1.56	554	0.47	592	Studs

<sup>1</sup> PL: (Lips et al. 2012a); PF: (Lips et al. 2010); PV: (Fernández Ruiz et al. 2010)

In addition to the geometric variation, series one and two were performed with two different shear reinforcement systems: corrugated double-headed shear studs and cages of continuous stirrups. Figure 3.2 illustrates the two shear reinforcement systems. The shear studs were radially arranged whereby the number of studs in a row was determined so that no punching at the outer perimeter could occur. The diameter and the number of radii were chosen so that the

shear reinforcement ratio was approximately equal ( $\rho_{w,eff}$  between 0.79 and 1.01%) except for specimen PL11 and PL12, for which a quarter and a half of the previous shear reinforcement ratios were used ( $\rho_w$  equal to 0.23% and 0.46%, respectively). Table 3.2 shows the diameter and number of studs used for each specimen. The cages of continuous stirrups consisted of bent bars ( $\varnothing 10$  mm) that were welded together with straight bars ( $\varnothing 6$  mm) to form a cage. The spacing between each vertical branch of the stirrups was constant 100 mm, leading to a constant shear reinforcement ratio of  $\rho_w = 0.79\%$ . One cage with dimensions 1200 x 1200 mm was placed at the center of the slab surrounded by eight smaller cages with dimensions 600 x 600 mm to prevent a failure at the outer perimeter of the shear-reinforced area. Table 3.3 shows the parameters of the continuous stirrups for each specimen.

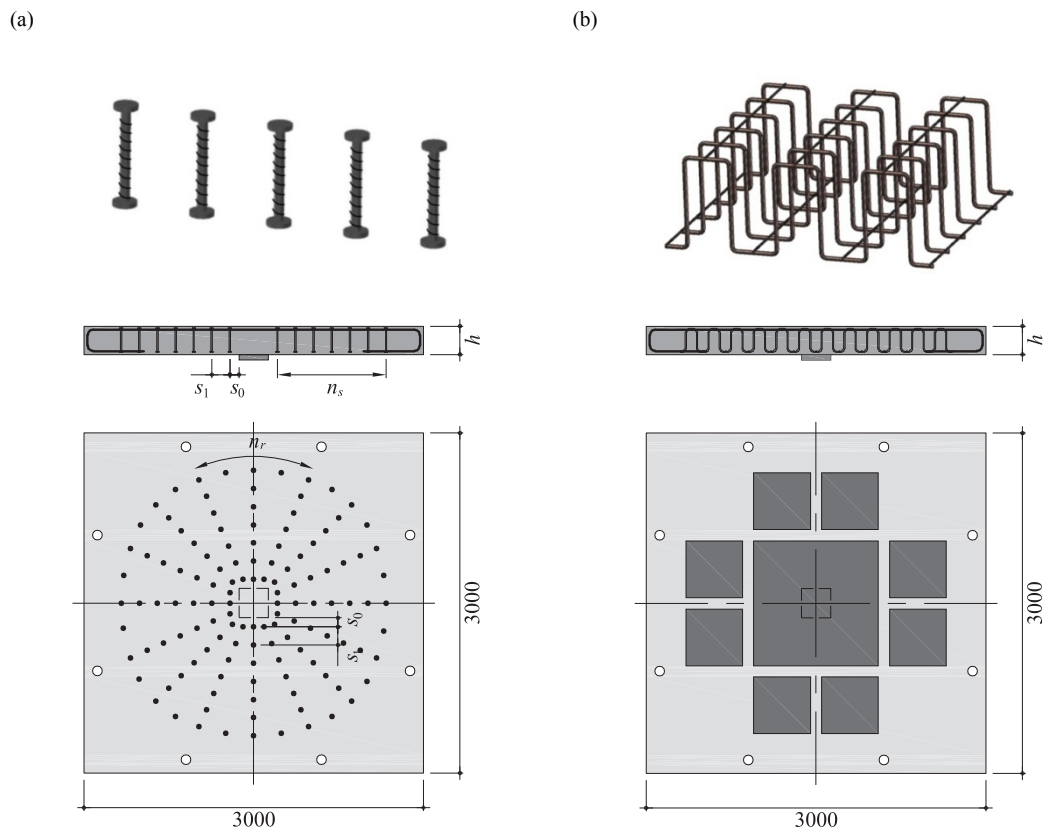


Figure 3.2: Shear reinforcement used and their distribution: (a) corrugated studs and (b) cages of continuous stirrups (dimensions in mm)

Table 3.2: Parameters of the corrugated studs

Specimen	$\phi_w$ [mm]	$s_0$ [mm]	$s_1$ [mm]	$n_r$ [-]	$n_s$ [-]	$\rho_w$ [%]	$h_w$ [mm]
PL6	14	80	160	12	6	1.01	215
PL7	14	80	160	16	7	0.93	215
PL8	14	80	160	24	7	0.85	215
PL9	18	100	200	16	6	0.93	285
PL10	22	130	260	16	5	0.82	365
PL11	10	80	160	8	7	0.23	215
PL12	10	80	160	16	7	0.47	215

Table 3.3: Parameters of the continuous stirrups

Specimen	$d_t$ [mm]	$s_t$ [mm]	$\rho_t$ [%]	$h_t$ [mm]
PF1-3	10	100	0.79	200
PF4	10	100	0.79	270
PF5	10	100	0.79	345

### 3.2. Materials

For all specimens, normal strength concrete with a maximum aggregate size of 16 mm was used. The compressive strength was determined on cylinders with a height of 320 mm and a diameter of 160 mm at 14 days, 28 days, and the day of testing. For the flexural reinforcement, hot-rolled steel with an average yielding strength ranging between 531 and 583 MPa was used. For the punching shear reinforcement, the studs consisted of hot-rolled steel with an average yielding strength ranging between 516 to 591 MPa, whereas the stirrups consisted of cold-formed steel with an average yielding strength ranging between 536 and 550 MPa. Details can be found in Table 3.1.

### 3.3. Test set-up

Figure 3.3a shows the test set-up for the specimen with a thickness of 250 mm. This test set-up was already used for previous punching tests. However, for the specimen with a thickness of 320 mm and 400 mm, it had to be strengthened (Figure 3.3b). In both cases the load was applied by four hydraulic jacks underneath the strong floor. Four tension bars running through the floor were connected to four spreader beams that distributed the load to eight tension bars. These bars applied the load at the top surface of the slab. The support consisted of two massive steel beams that distributed the load on the strong floor.

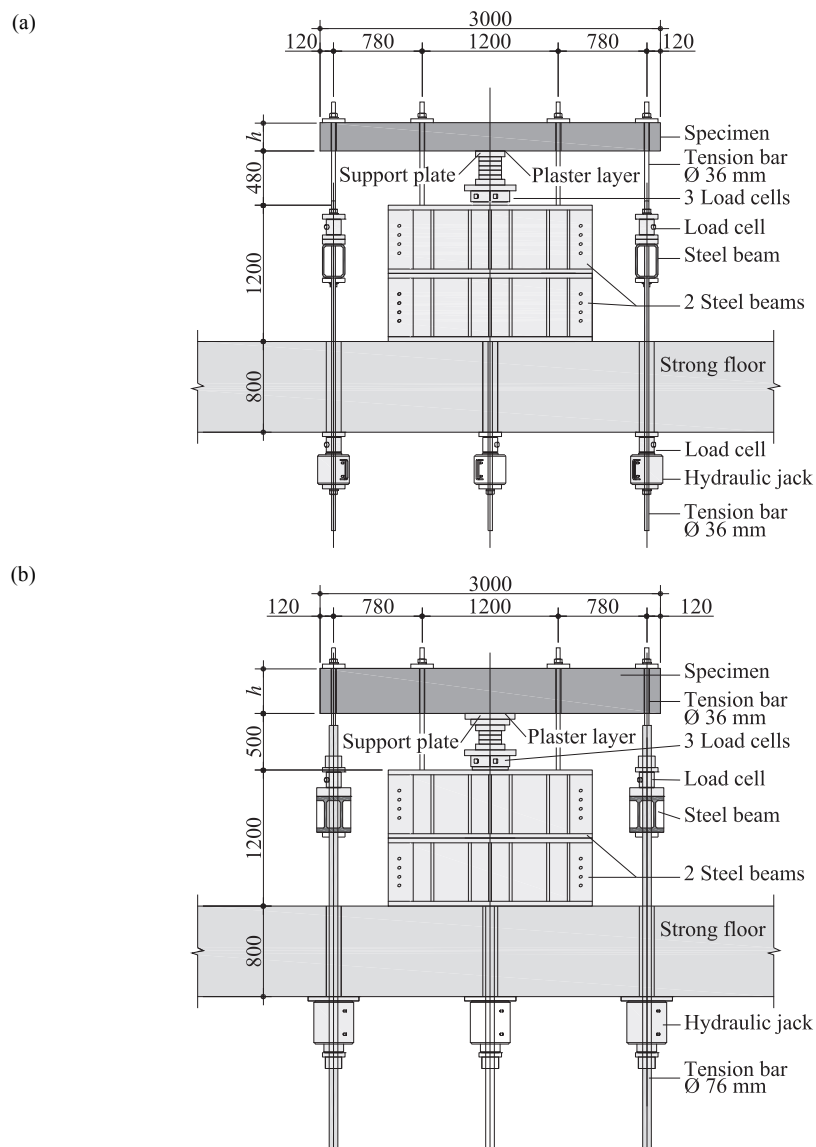


Figure 3.3: Test set-up for slabs with thickness of (a)  $h=250$  mm and (b)  $h=320$  mm and  $h=400$  mm (dimensions in mm)

### 3.4. Measurements

Various continuous measurements were recorded during the tests. Load cells measured the applied load at the hydraulic jacks as well as the reaction forces at the support. Five inclinometers circularly arranged on the top surface of the slab at a distance of 1.38 m from the center measured the rotation of the slab (Figure 3.4b). Several Linear Variable Differential Transducers (LVDTs) have been placed on the top and the bottom side of the slab to measure the vertical displacements. Additionally, two LVDTs were used to measure the change of thickness of the slab by using a small rod, which was fixed at the bottom surface, put through a hole in the slab ( $\phi 8$  mm) and connected to the LVDT fixed on the top surface of the slab (Figure 3.14). Omega-shaped extensometers with a measuring length of 50 and 100 mm measured the surface deformation of the slab. They were placed axially and diagonally at the top and bottom surface of the slab. In addition, 12 strain gauges measured the strains in the punching shear reinforcement. After the test, the slab specimens were cut in half along the weaker axis to analyze the punching cone in detail.

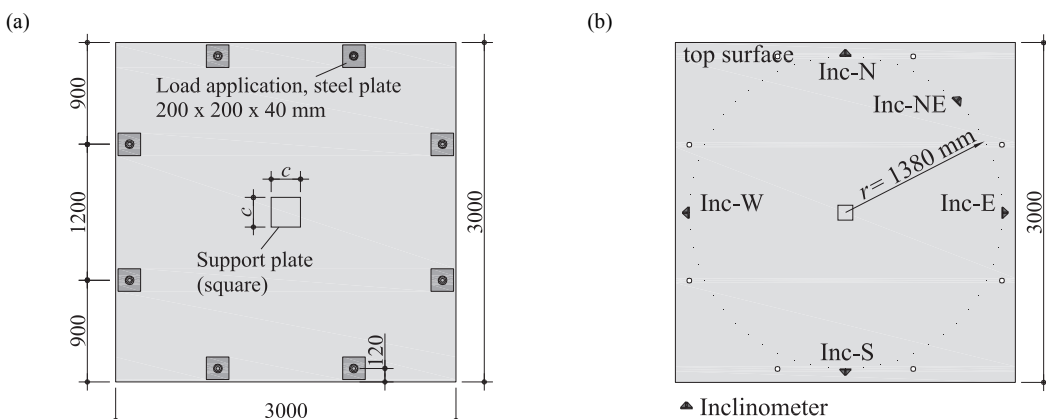


Figure 3.4: Plan view of the location of (a) the load application and (b) the rotation measurements (dimensions in mm)

### 3.5. Results

All specimens failed in punching, except specimen PL8, which underwent large deformation without failure. This test was stopped before flexural failure occurred. Table 3.4 presents the experimentally obtained punching strength and the measured rotation along the weaker axis at failure of all specimens. Additionally, Table 3.4 lists the normalized punching strength and the normalized rotation at failure for each slab. The normalization of the strength accounts for column size, depth of the member, and concrete compressive strength and the normalization of the strength accounts for the critical shear crack width and the roughness of the crack. The normalized results are graphically shown in Figure 3.5.



Table 3.4: Overview of the test results

Specimen	$V_{R,test}$	$\psi_{R,test}$	$\frac{V_{R,test}}{b_0 \cdot d \cdot \sqrt{f_c}}$	$\frac{\psi_{R,test} \cdot d}{d_{g0} + d_g}$
	[kN]	[‰]	[ $\sqrt{\text{MPa}}$ ]	[-]
PL1	682	6.0	0.52	0.04
PL6	1363	18.6	1.00	0.12
PF1	1043	9.5	0.76	0.06
PV1 <sup>1</sup>	974	7.6	0.47	0.05
PL7	1773	32.0	0.91	0.20
PF2	1567	16.7	0.81	0.11
PL3	1324	13.2	0.41	0.08
PL8	2256	-	0.69	-
PF3	2242	46.8	0.64	0.31
PL4	1625	6.5	0.50	0.05
PL9	3132	26.2	0.95	0.22
PF4	2667	14.0	0.77	0.12
PL5	2491	4.7	0.44	0.05
PL10	5193	18.0	0.93	0.19
PF5	4717	13.4	0.80	0.15
PL11	1176	11.9	0.60	0.07
PL12	1633	22.0	0.83	0.14

<sup>1</sup> (Fernández Ruiz et al. 2010)

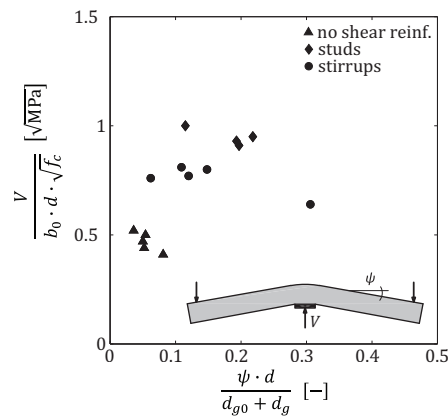


Figure 3.5: Normalized strength as a function of the normalized rotation for the test specimens

Figure 3.6 illustrates the crack pattern at the section along the axis after punching failure, obtained by a saw cut after testing. In addition, pictures of the cut sections are shown in Figure 3.7. The inclination of the failure surface was rather steep for members with large amounts of shear reinforcement and particularly for specimens with studs. For lower amounts of shear reinforcement and for specimens with stirrup cages, the angle of the failure surface was somewhat flatter and the critical shear crack crossed two or three rows of shear reinforcement. Specimens with studs as shear reinforcement had basically two failure areas: spalling of the concrete cover at the bottom side of the column and crushing of concrete at the top surface near the anchorage of the first row of studs. In the case of stirrups, these two failure areas could still be recognized but were less dominant than for specimens with studs.

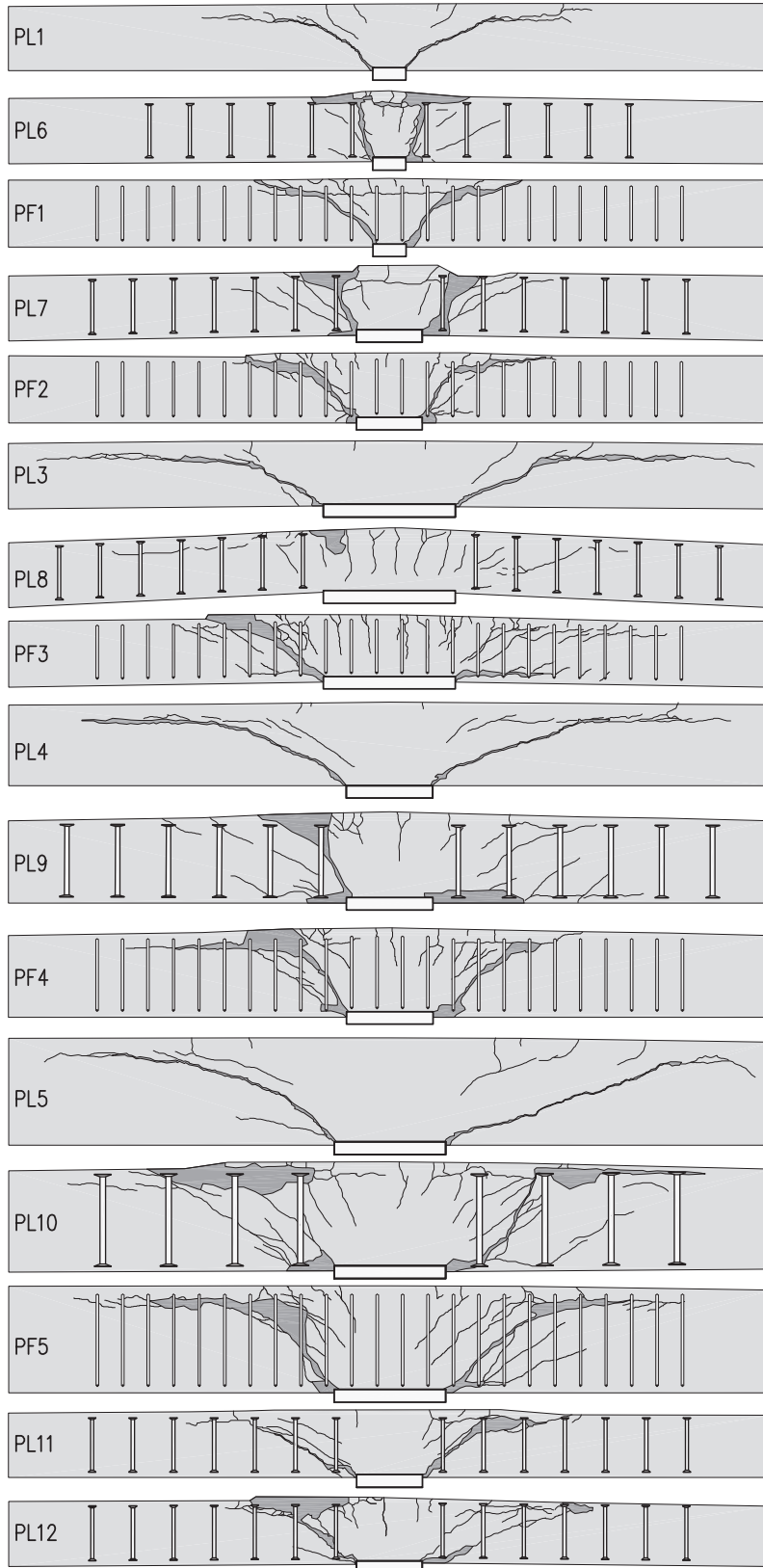


Figure 3.6: Cracking pattern along the weak axis after punching failure

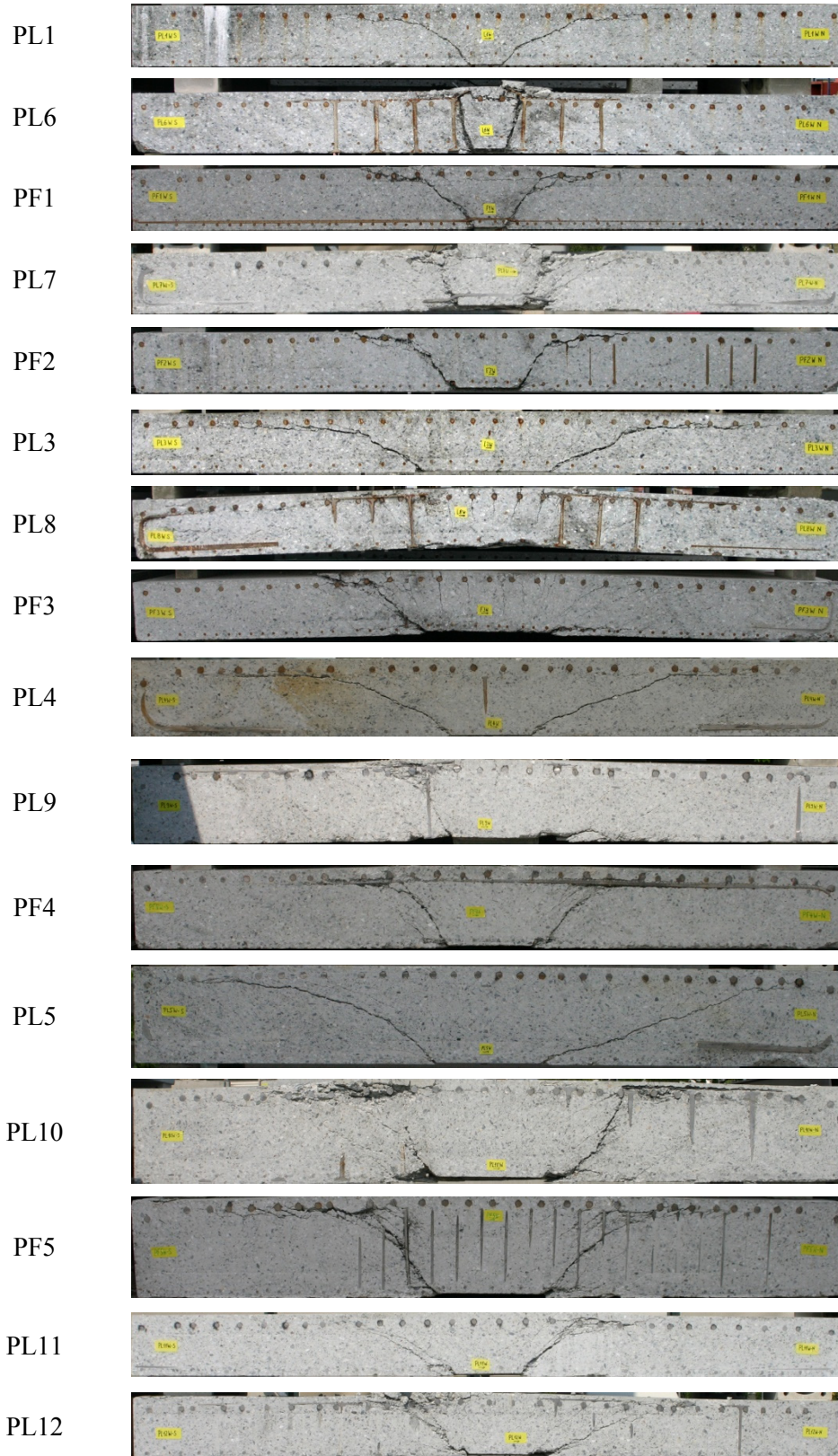


Figure 3.7: Saw-cuts along the weak axis after punching failure

## 3.6. Discussion of the results

### 3.6.1. Performance of the shear reinforcement

Figure 3.8 shows the load-rotation curves of specimens with shear reinforcement and the reference specimens without shear reinforcement. It can be observed that the strength and the rotation capacity significantly increases if shear reinforcement is provided. This significant increase occurred by all slab specimens as it is shown in Figure 3.8a for specimens with a small  $c/d$  ratio, in Figure 3.8b for the standard specimens, and in Figure 3.8c for specimens with large thickness. Additionally, it can be observed that the performance of a slab specimen depends somewhat on the shear reinforcement system. The slabs with studs showed a higher strength and a larger rotation capacity than slabs with stirrups. This difference can be seen in all the investigated cases such as in the case of small columns (Figure 3.8a), in the case of the standard specimen (Figure 3.8b), as well as in the case of increased thickness (Figure 3.8c).

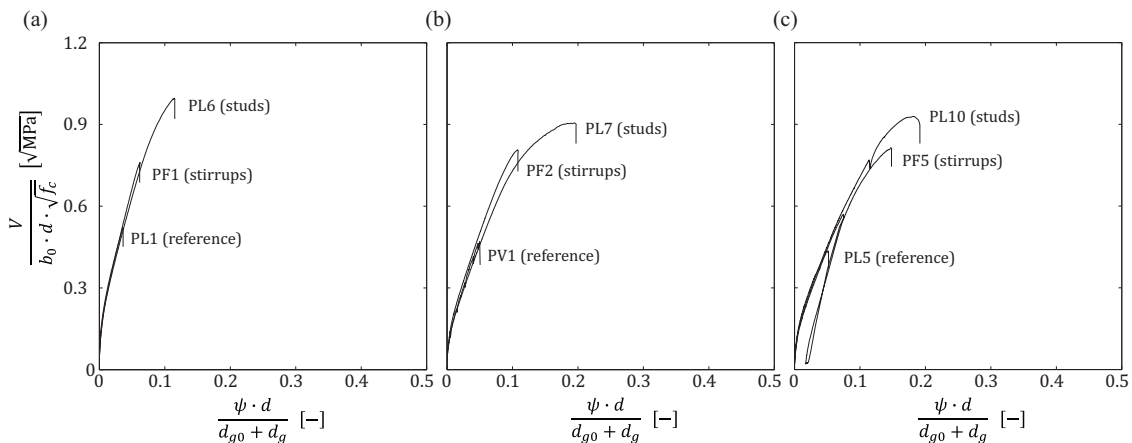


Figure 3.8: Load-rotation curves for slab specimens with and without shear reinforcement: (a)  $c = 130 \text{ mm} / h = 250 \text{ mm}$ ; (b)  $c = 260 \text{ mm} / h = 250 \text{ mm}$ ; (c)  $c = 440 \text{ mm} / h = 400 \text{ mm}$

### 3.6.2. Column size

Figure 3.9 shows the load-rotation curves for specimens supported by various column sizes. In the case of slabs without shear reinforcement the test results follow a clear tendency. The strength and the rotation capacity increase with larger column sizes. However, due to the larger perimeter  $b_0$ , the normalized strength is smaller in the case of larger columns (Figure 3.9a). A similar tendency can be observed for the test specimens with studs (Figure 3.9c). However, whereas in the case of slabs without shear reinforcement the normalized strength increases more by decreasing column sizes, in the case of slabs with studs the increase for smaller columns is smaller. This is even more significant in the case of stirrups, for which the normalized strength even decreases for small columns (PF1).

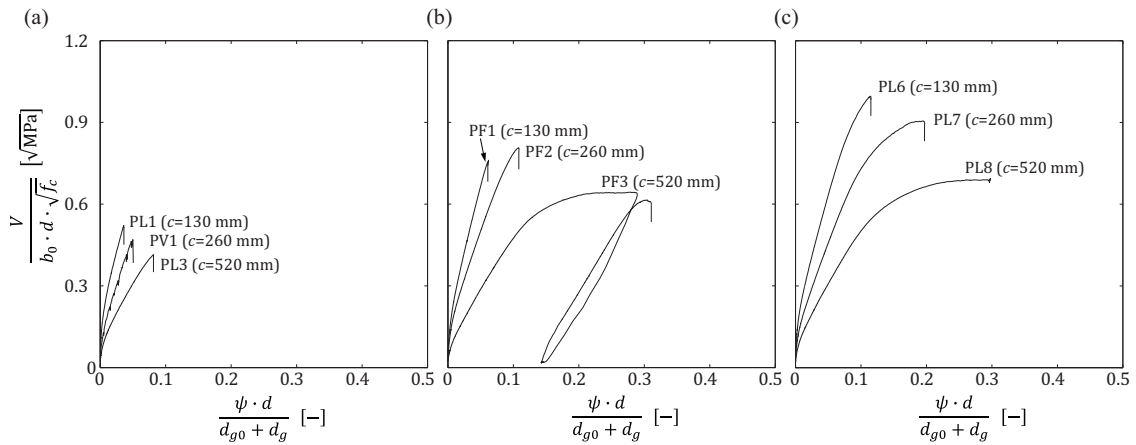


Figure 3.9: Load-rotation curves for slab specimens with various column sizes: (a) without shear reinforcement; (b) with stirrups; (c) with studs

### 3.6.3. Slab thickness

Figure 3.10 shows the load-rotation curve for specimens with various thicknesses. It can be seen that since the three normalized load-rotation curves nearly coincide, the strength develops approximately proportional to the normalization parameter  $b_0 \cdot d$  and the rotation capacity inversely proportional to the normalization parameter  $d$ . This indicates a similar influence of size for specimens without shear reinforcement, for specimens with stirrups, and for specimens with studs.

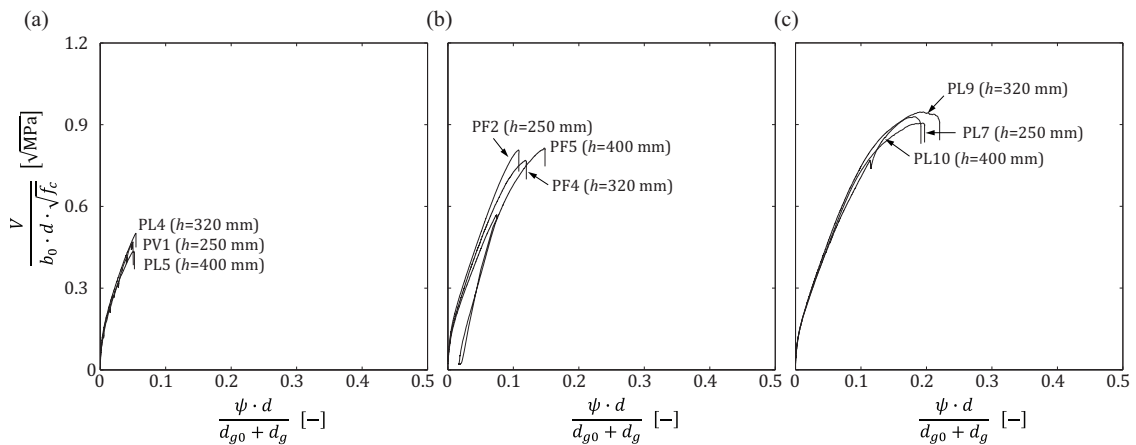


Figure 3.10: Load-rotation curves for specimens with various thicknesses for (a) specimens without shear reinforcement, (b) specimens with stirrups, and (c) specimens with studs

### 3.6.4. Amount of shear reinforcement

Figure 3.11 shows the load-rotation curves for specimens with different amount of shear reinforcement. It can be seen that the load-rotation curves of all the specimens coincide. Thus, the flexural stiffness is not influenced by the shear reinforcement. However, the amount of shear reinforcement has an influence on the strength and rotation capacity. Even a rather small amount of shear reinforcement increases the strength and the rotation capacity (PL11). By doubling the amount of shear reinforcement the punching strength and the rotation capacity can be further increased. However, if even more shear reinforcement is added, the punching strength does not significantly increase. This can be explained by the change in failure mode between specimens PL12 and PL7. While PL12 had a failure within the shear-reinforced area, PL7 had a failure due to crushing of the concrete strut close to the column. Consequently, further increase of the amount of shear reinforcement would also lead to crushing of the concrete strut so that it will not result in a significant higher punching strength or in a significant larger rotation capacity. In addition, it seems that in the case of PL7 the flexural reinforcement is yielding since the curve shows the beginning of a plateau. Therefore, the maximum punching strength is reached and cannot be further increased without increasing the flexural capacity.

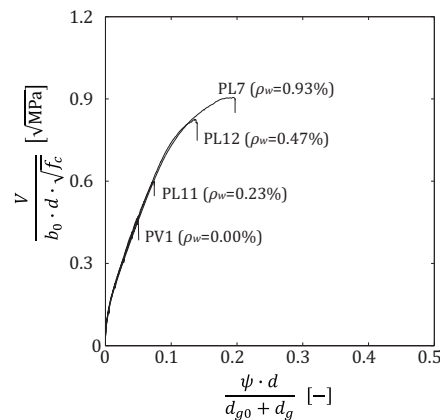


Figure 3.11: Load-rotation curve for specimens with various amount of shear reinforcement

### 3.6.5. Shear deformations at column face

The shear deformations at the column face cannot be measured directly. However, they can be estimated by using certain assumptions. Firstly, it has to be assumed that all the shear deformations occur at the column face, thus no shear deformation occurs between point B and C shown in Figure 3.12. Additionally, the rotation is assumed to be constant between point B and C. Both assumptions are supported by the measured displacements between point B and C. Another assumption is that the rotation occurs within a small region at the column face so that the extrapolated displacements at the column face calculated by the rotations are approximately zero.



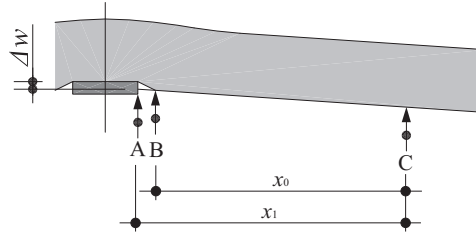


Figure 3.12: Calculation of the shear deformations at the column face

Using these assumption, the shear deformations at the column face can be estimated from the measured displacement at the bottom side of the slab (Figure 3.12). By an extrapolation of these displacements, one can obtain the shear deformations at the column face:

$$\Delta w = (w_C - w_A) - \frac{(w_C - w_B)}{x_0} \cdot x_1 \quad (3.1)$$

Figure 3.13 shows the normalized load-deformation curves for shear deformations near the column face. By comparing the slabs with shear reinforcement (PL7 and PF2) to the reference slab (PV1), it can be noted that large shear deformations occur only if shear reinforcement is present. Similar to the measured load-rotation behavior, the slab with studs (PL7) leads to larger shear deformations than the slab with stirrups (PF2). With respect to the column size, Figure 3.13b shows that the smaller the column is the larger the shear deformations are. In comparison to specimen PL6 ( $c = 130$  mm;  $c/d = 0.66$ ), which had rather large shear deformations, specimen PL8 ( $c = 520$  mm;  $c/d = 2.60$ ), by which no punching failure occurred, had significantly smaller shear deformations. A difference in shear deformation occurs also for slab specimens with different thicknesses. However, the differences are rather small. Nevertheless, it can be noted that the stiffer the slab is the smaller the normalized shear deformations are. This is again similar to the observed load-rotation behavior.

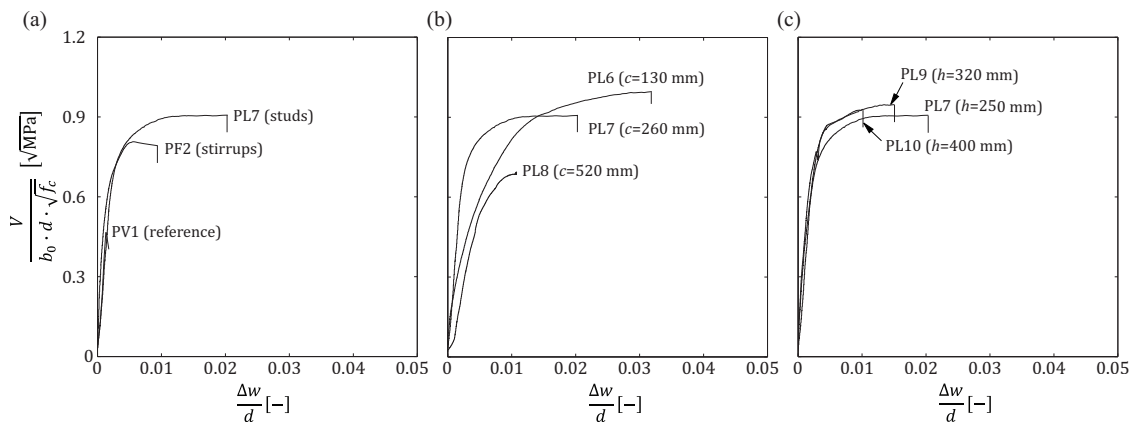


Figure 3.13: Normalized shear deformations at the column face as a function of the normalized shear force of selected specimens: (a) varying shear reinforcement system, (b) varying column size, and (c) varying slab thickness

### 3.6.6. Opening of the shear cracks

The measurement of the change in slab thickness close to the column can be interpreted as an indirect measurement of the opening of the shear cracks. Figure 3.14a shows the location of the thickness measurements whereby the exact location depends on the slab thickness. Generally, it can be said that distance  $x$  is approximately  $d/2$  and  $y$  between 0 and 35 mm depending on the reinforcement layout. The exact distances for each specimen can be found in the test reports (Lips et al. 2012a) and (Lips et al. 2010). The change in slab thickness has been measured by using a small rod that was fixed on the bottom side, crossed the slab vertically through a hole in the slab, and was connected to a LVDT on the top side of the slab.

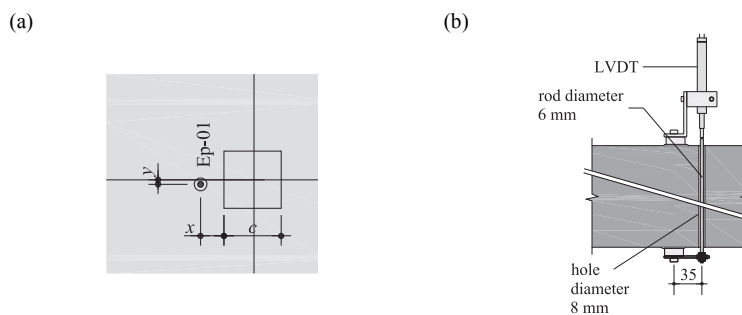


Figure 3.14: Measurement of change in slab thickness: (a) location in plan view and (b) detail of the measurement installation (dimensions in mm)

Figure 3.15 shows the curve of the change in slab thickness, or the vertical shear crack opening, as a function of the normalized applied load. Generally, it can be noted that specimens without shear reinforcement (PL1-PL5) experience as soon as the first shear crack opens significant changes in thickness. In contrast, the shear reinforcement present in specimens PL6-PL12 controls the crack opening of the first shear crack, leading to a higher strength and larger crack openings. With respect to the column size, Figure 3.15a shows that in the case of specimens without shear reinforcement the crack opening is larger for larger column sizes. In the case of specimens with shear reinforcement the crack opening is nearly the same for all column sizes. With respect to the slab thickness (Figure 3.15b), it can be generally noted that the thicker the slab is the larger the crack openings are. However, the difference between the specimens PL4 / PL5 and PL9 / PL10 is rather small. With respect to the amount of shear reinforcement (Figure 3.15c), it can be seen that an increase in crack opening occurs between specimen PL11 and PL12. A further increase in shear reinforcement does not seem to influence the crack opening as it can be seen by comparing specimen PL12 and PL7. Additionally, it can be noted that the specimen with stirrups (PF2) experiences less change in thickness than the specimen with studs (PL7).



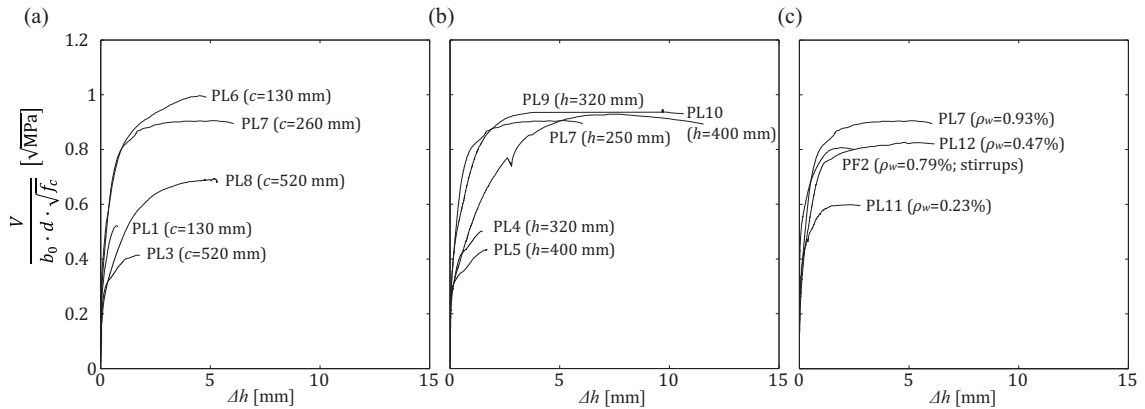


Figure 3.15: Normalized shear deformations at the column face as a function of the normalized shear force of selected specimens: (a) varying column size, (b) varying slab thickness, and (c) varying the amount of shear reinforcement

### 3.6.7. Strains in the studs

Strain gauges measured the strain in the shear reinforcement. They were placed on the first three vertical branches at the top and bottom side of the shear reinforcement in axial and diagonal direction (Figure 3.16a and Figure 3.18a). In order to show the different behavior of the shear reinforcement for failure due to crushing of the concrete strut and for failure within the shear-reinforced area, two different specimens were further analyzed. Specimen PL7, which had a large amount of shear reinforcement ( $\rho_w = 0.93\%$ ), exhibit crushing of the concrete strut and specimen PL12, which had only half of the amount of shear reinforcement of the first specimen ( $\rho_w = 0.46\%$ ), showed a failure within the shear-reinforced area. The illustration of the strains in the studs for each specimen at different load levels and the load-deformation curves reveal the difference in behavior of the two investigated specimens.

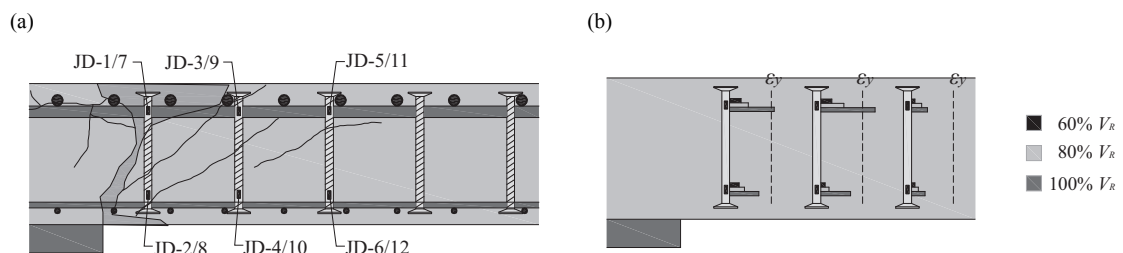


Figure 3.16: Strain measurements on the shear studs of slab specimen PL7: (a) instrumentation and crack pattern and (b) measured strain for load levels of 60%, 80%, and 100% of failure load

Figure 3.16 shows the average of the axial and diagonal strain measurements in the studs for several load levels and Figure 3.17 shows the load-strain curves for the studs in axial and diagonal direction for slab specimen PL7. It can be seen that yielding only occurs at the top end of the first and second stud at load levels close to the failure load. Additionally, it can be noted

that the strains in the second row of studs are generally higher than in the first one. This leads to the conclusion that load must have been transferred from the second row of studs directly to the column.

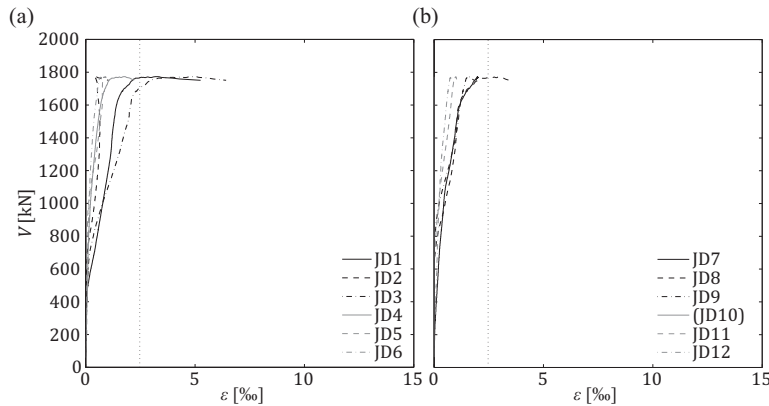


Figure 3.17: Strain measurements as a function of the applied load of studs (a) in axial direction and (b) in diagonal direction for slab specimen PL7

In comparison to specimen PL7, specimen PL12, which exhibited a failure within the shear reinforced area, behaved slightly different. The second row of studs started yielding on the top end of the stud whereas the strain measurements in the first row of studs on top and on the bottom showed lower strains.

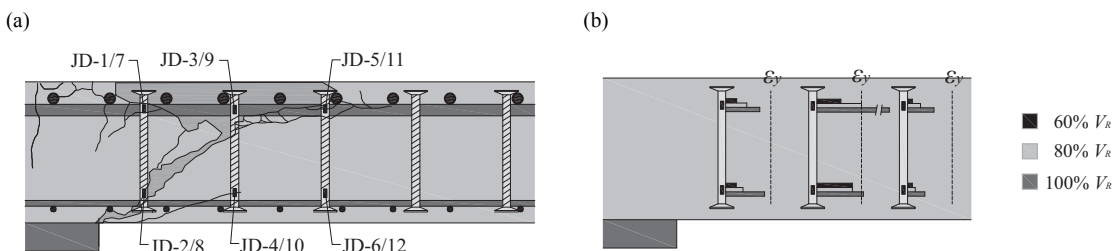


Figure 3.18: Strain measurements on the shear studs of slab specimen PL12: (a) instrumentation and crack pattern and (b) measured strain for load levels of 60%, 80%, and 100% of failure load

With respect to the strain development in the studs, Figure 3.19 shows that specimen PL12 performs similarly to specimen PL7. Generally, the strains in the studs of specimen PL12 are larger in the second row of studs. In fact, the strains measured in that row started to increase significantly at the load level at which the reference specimen punched (PV1:  $V_R = 974$  kN). Afterwards, the strains in the studs further increased and the second row of studs started yielding just before reaching the failure load (JD-3).

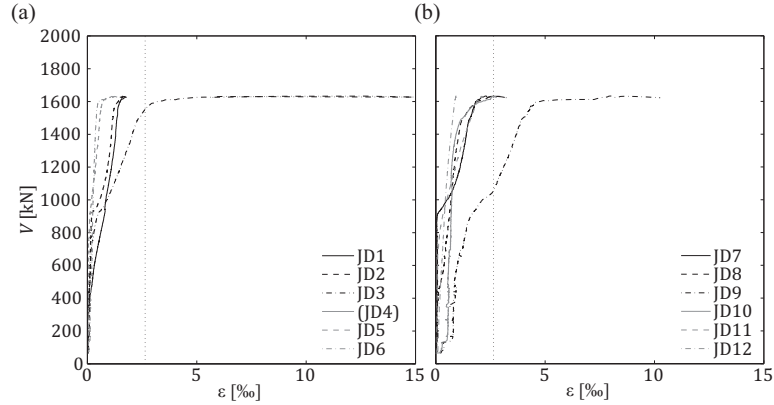


Figure 3.19: Strain measurements as a function of the applied load of studs in (a) axial direction and (b) in diagonal direction for slab specimen PL12

In order to analyze the contribution of each row of studs and the concrete, the force inside the studs was estimated and compared to the total shear force. Assuming that the force in the studs is proportional to the strains, thus no influence of bond at the measured location are assumed, the force in one stud can be estimated by multiplying the strain by the Young's modulus and the cross sectional area of the stud. Additionally, assuming that the slab behaves in a perfectly symmetric manner, the total shear force can be calculated by multiplying the force in one stud by the number of studs in one perimeter. Therefore, the contribution of the shear reinforcement can be estimated by:

$$V_{w,i} = n_r \cdot A_{sw,i} \cdot E_s \cdot \varepsilon_i \quad (3.2)$$

Based on Figure 3.16 and Figure 3.18, it can be assumed that only the force in the first two rows of studs is directly transferred to the column. Forces from studs further away will be first transferred to another stud closer to the column. Therefore, the total shear force contribution of the shear reinforcement can be described as the sum of the shear force in the first two rows of studs, whereby it has to be noted that for the sum the force calculated at the bottom end of the studs of the first row and the force calculated at the top surface were used. This can be explained by the fact that it is assumed that a portion of the load of the second stud will be introduced to the first stud through bond stresses. In addition to the shear forces in the studs, it is assumed that a portion of the load will be transferred by the concrete. Therefore, it can be stated that:

$$V = V_{w,1,bot} + V_{w,2,top} + V_c \quad (3.3)$$

Using Equation 3.3, the contribution of the concrete can be estimated as a function of the rotation. Despite the rather coarse assumptions, a general behavior can be presented. Figure 3.20 shows the normalized load-rotation curve with the estimated contribution of the studs and the

concrete. Generally, it can be noted that for low rotations the estimated contribution of the concrete is dominant up to a certain point at which the concrete contribution starts to decrease. In the case of specimen PL7 (Figure 3.20a) the point at which the concrete contribution starts to decrease is approximately at the rotation at which the reference specimens without shear reinforcement (PV1) punched. Additionally, it can be noted that after a first decay, the contribution of concrete stays constant before it descends again with increasing rotation until failure occurs.

A different behavior can be observed in the case of specimen PL8, which did not fail in punching. The changes in the concrete contribution are less dominant than for specimen PL7. However, again it can be noted that the rotation at which the contribution of the concrete is maximal is close to the rotation at failure of the reference specimen (PL3). After the peak, the concrete contribution decreases slowly until the point at which the test was stopped. Specimen PL10 shows a similar behavior to specimen PL7, although the estimation shows a certain stabilization at the level of the maximum of the estimated concrete contribution. This maximum is again near the failure of the reference specimen.

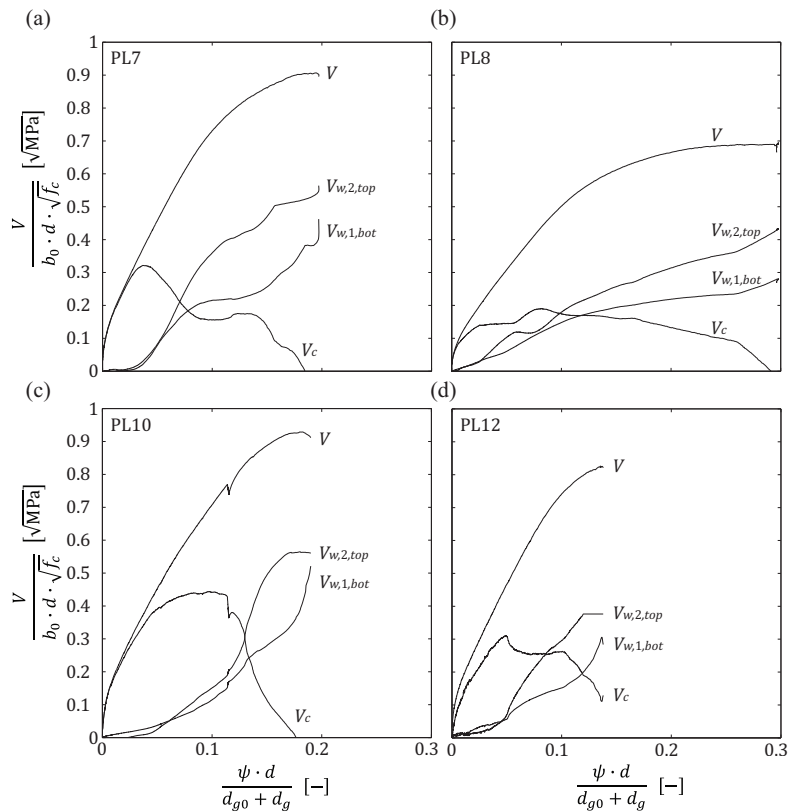


Figure 3.20: Contribution of the first to rows of studs and the concrete to the normalized strength as a function of the normalized slab rotation for slab specimen (a) PL7, (b) PL8, (c) PL10, and (d) PL12

The results obtained for specimen PL12 also follows the same tendency as specimen PL7. Again, it can be noted that the peak of the concrete contribution occurs at the rotation at which the reference specimen reaches its punching strength. Similar to specimen PL7, specimen PL12 shows stabilization of the concrete contribution after a certain decay of concrete contribution. At a certain rotation, the contribution of the concrete starts to decrease until punching failure occurs.

Interesting to note is that in the case of PL12, which had a failure within the shear reinforced area, the contribution of concrete is still at a rather high level compared to the contribution of the shear reinforcement, unlike in the case of specimen PL7 that had a failure of the concrete strut. This leads to the conclusion that the contribution of the concrete should not be neglected for the failure within the shear-reinforced area. Additionally, it can be noted that the concrete contribution is not constant and thus is influenced by the slab rotation. These observations are in agreement with the hypotheses of the CSCT, which considers these effects in its mechanical model.

Using the same assumption as for Equation 3.2, one can calculate the force in the studs based on the strain measurements on the top side of the first and second row of studs. Figure 3.21 shows the shear force at the top side of the first and second stud with respect to the total shear force as a function of the normalized slab rotation for slab specimen PL7 and PL9. It can be seen that after a first increase the shear force ratio is nearly constant before it increases shortly before failure. Another interesting fact is that the sum of the calculated shear force in each stud is larger than the total shear force. Thus, a part of the force is transferred from the second row of studs to the first row of studs.

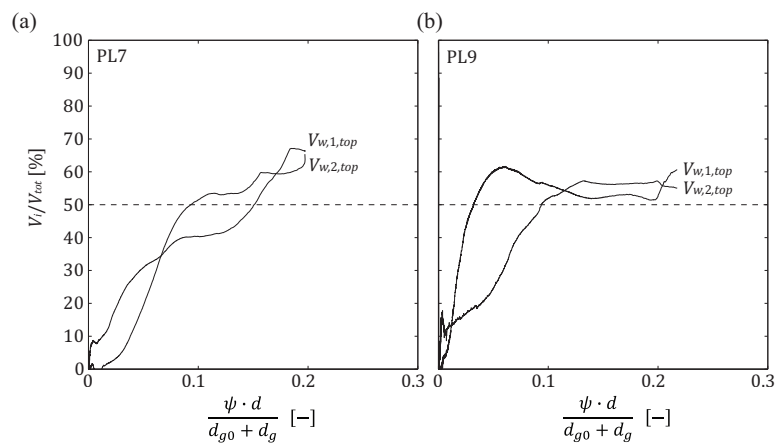


Figure 3.21: Shear force at the top side of the first and second stud with respect to the total shear force as a function of the normalized slab rotation for slab specimen (a) PL7 and (b) PL9

### 3.6.8. Deformations at the shear-critical region

On the top and bottom surface of the slab specimens, omega-shaped extensometers were placed to measure the surface deformations. The location of each measurements device and all the results of the measurements can be found in the test reports (Lips et al. 2010; Lips et al. 2012a). Selected results of deformation measurements on the bottom side of the slab specimens PL1, PL6, and PF1 show the general behavior observed in all specimens with respect to the radial and tangential direction. The shown measurements were taken by the measurement devices placed according to Figure 3.22.

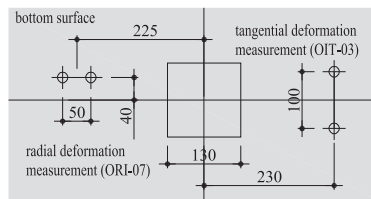


Figure 3.22: Location of the surface deformation measurements (dimensions in mm)

Figure 3.23 shows the normalized load-deformation curve of the surface deformation at the bottom surface of specimens without shear reinforcement (PL1), with studs (PL6), and with stirrups (PF1). All specimens experienced similar radial deformation at the beginning with stabilized or even decreasing strains at the load level where the reference specimens (PL1) punched. Afterwards, the strains of the other two specimens remained approximately constant until a load level close to punching. Just before punching failure occurred, the radial strains increased significantly. With respect to the tangential deformation, it can be noted that the specimens with and without shear reinforcement show the same behavior. The three curves nearly coincide until each specimen reaches its punching strength. Interesting to note is that PL6 reached strains above 4‰, which could lead to softening and further on to spalling of the concrete.

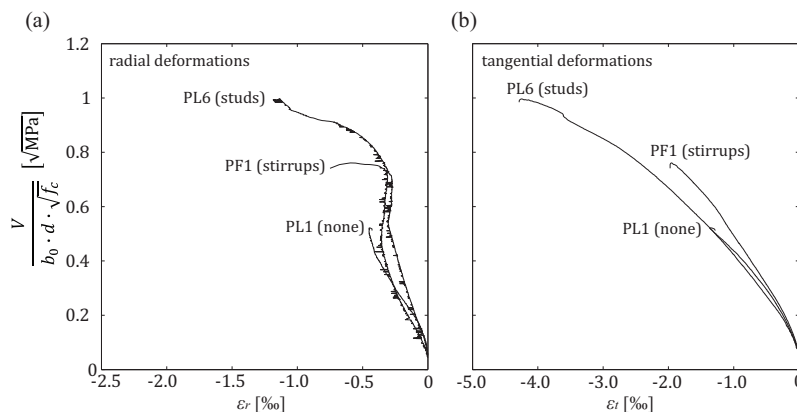


Figure 3.23: Normalized load-deformation curve of the bottom surface deformations (a) in radial direction and (b) in tangential direction

## 4. Validation of Code Provisions and the CSCT

The results from the experimental campaign presented in the previous chapter were compared to current code provisions (ACI 318 2011; EC2 2004; NAD 2011; SIA 262 2003; MC 2011) and to the CSCT (Muttoni 2008; Fernández Ruiz and Muttoni 2009) to investigate the performance of these models. The used formulations of the code provisions and the CSCT are presented in Chapter 2. The code provisions were investigated with respect to the predicted punching strength and the influence of several different parameters such as the slab thickness, the column size, and the shear reinforcement ratio. For this, the punching strength was calculated accordingly to the provisions of the previously mentioned codes as a function of the investigated parameter. These calculations were performed using the following assumptions: the concrete compression strength was chosen as 33.5 MPa (average of the tests), the yielding strength of the flexural reinforcement as 575 MPa (average of the tests), the yielding strength of the shear reinforcement as 550 MPa (average of the tests), the shear reinforcement as 0.9% if not varied, the effective depth as 210 mm if not varied, and the ratio of the column size to the effective depth as 1.24 if not varied. Additionally, the predicted punching strength was compared with the experimentally obtained strength of punching tests from literature in order to investigate the general performance of the investigated models.

## 4.1. ACI 318-11 (ACI 318 2011)

### 4.1.1. Punching strength

In comparison to the results from the tests performed within this research project, it can be noted that ACI 318-11 predicts somewhat conservative punching strength. Although it is a rather simple approach, the coefficient of variation is relatively small leading to a 5%-fractile of 1.10. Figure 4.1 shows the ratio of the punching strength of the tests to the one predicted by ACI 318-11 as a function of the shear reinforcement ratio. All points are above 1.0 showing that ACI 318-11 leads to safe estimates of the punching strength for the performed tests.

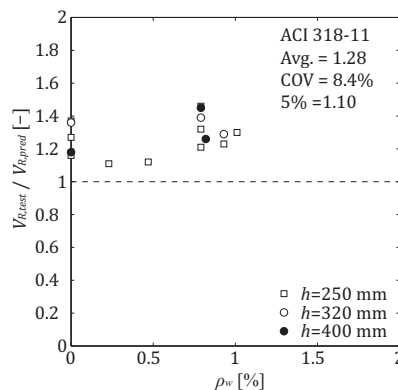


Figure 4.1: Ratio of the experimentally obtained punching strength to the punching strength predicted according to ACI 318-11 (ACI 318 2011)

### 4.1.2. Slab thickness

Figure 4.2a shows the normalized predicted punching strength as a function of the effective depth  $d$ . Due to the specified parameter, mainly due to the large shear reinforcement ratio, only crushing of the concrete strut (maximum punching strength) is governing. ACI 318-11 does not account for influences of the effective depth on the normalized punching strength. Therefore, the calculation leads to a horizontal line for slabs without shear reinforcement and slabs with shear reinforcement since a proportional increase is used. The distinction between studs and stirrups using an increasing factor of 2 instead of 1.5 seems to be reasonable.



#### 4.1.3. Column size

Figure 4.2b shows the normalized predicted punching strength as a function of the ratio of the column size to the effective depth  $c/d$ . Again the predicted failure mode is crushing of the concrete strut. ACI 318-11 predicts smaller normalized punching strength for larger  $c/d$  ratios, which is in good agreement with the test results although this tendency does not seem to apply to specimens with small column sizes and stirrups (PF1:  $c/d = 0.62$ , stirrups). However, the safety margin is large enough so that the predicted strength is still lower than the experimentally obtained punching strength.

#### 4.1.4. Shear reinforcement ratio

Figure 4.2c shows the normalized predicted punching strength as a function of the shear reinforcement ratio. The failure modes are well addressed although in the case of specimen PL12 ( $\rho_w = 0.47\%$ ) the experimentally obtained failure mode seems to be failure within the shear-reinforced area, whereas the predicted failure mode is crushing of the concrete strut. Again, the larger increase of the strength in the case of double headed studs compared to stirrups complies with the test results.

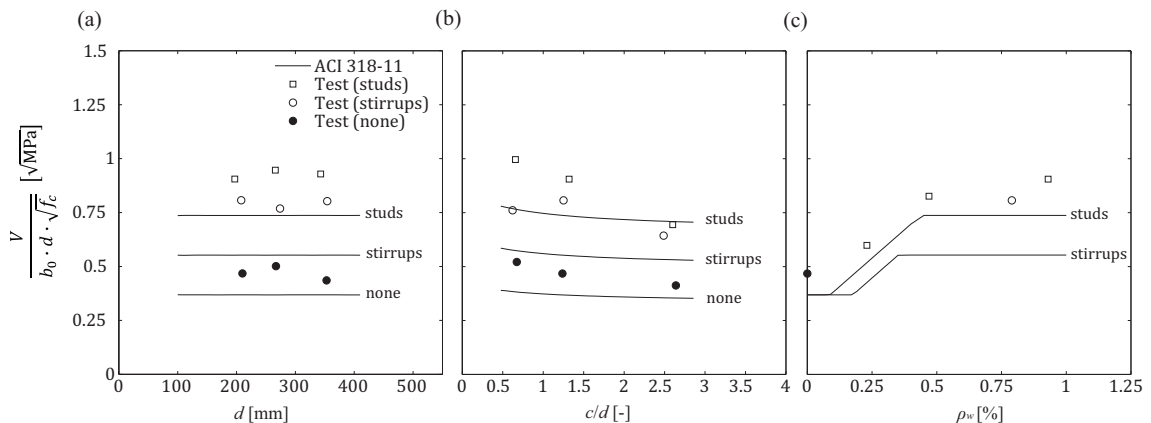


Figure 4.2: Punching strength according to ACI 318-11 (ACI 318 2011) as a function of (a) the effective depth, (b) the column size to effective depth ratio, and (c) the shear reinforcement ratio

## 4.2. Eurocode 2 (EC2 2004)

### 4.2.1. Strength prediction

In comparison to the tests performed within this research project, it can be noted that EC2 2004 may lead to unsafe design. Due to the rather low average and a large coefficient of variation, the 5%-fractile is only 0.76. Several factors contribute to this rather low value. Firstly, EC2 2004 does not distinguish between the different shear reinforcement systems since the provision applies implicitly only for shear links. This fact leads to scattered results. Secondly, as it is explained later, the provision regarding the maximum punching strength is not well addressed, which can lead to an overestimation of the punching strength.

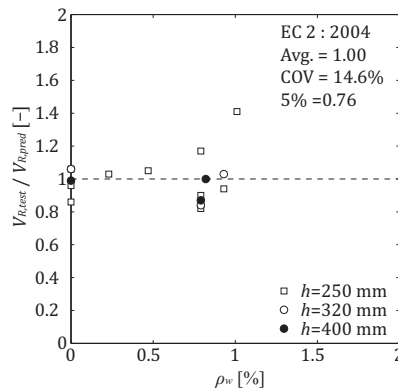


Figure 4.3: Ratio of the experimentally obtained punching strength to the punching strength predicted according to EC2 2004

### 4.2.2. Slab thickness

Figure 4.4a shows the normalized predicted punching strength as a function of the effective depth  $d$ . While the strength is well predicted for specimens without shear reinforcement and for specimens with studs, the provision overestimates the strength for specimens with stirrups. This is even more pertinent considering the fact that EC2 2004 implicitly applies only for shear links and not for studs. It clearly shows that a distinction between double headed studs and stirrups could increase the accuracy of the strength predictions. Another interesting fact is that EC2 2004 accounts for size effects in the case of slabs without shear reinforcement (decrease of normalized strength with increase of the effective depth) but not in the case of slabs with shear reinforcement that fail due to crushing of the concrete strut.

### 4.2.3. Column size

Figure 4.4b shows the normalized predicted punching strength as a function of the ratio of the column size to the effective depth  $c/d$ . In the case of specimens without shear reinforcement, the strength is generally well predicted. However, it overestimates the strength for small column

sizes, which could lead to unsafe design. In the case of specimens with shear reinforcement, it can be clearly seen that the beam analogy used in the EC2 2004 provision does not work. It underestimates the strength for small column sizes and the strength increases rapidly with increasing column size so that it overestimates the strength for  $c/d$  ratio of 1.5. With further increase of the column size, the predicted strength would increase even more, if it was not limited by other predicted failure modes such as failure within the shear-reinforced area or as in this case by the flexural strength. Consequently, this could lead to unsafe design, especially in the case of large column sizes and slabs with large flexural and shear reinforcement ratios.

#### 4.2.4. Shear reinforcement ratio

Figure 4.4c shows the normalized predicted punching strength as a function of the shear reinforcement ratio. For the failure within the shear-reinforced area, the strength is well predicted. However, again in the case of failure of the concrete strut and the specimen with stirrups, the strength is overestimated.

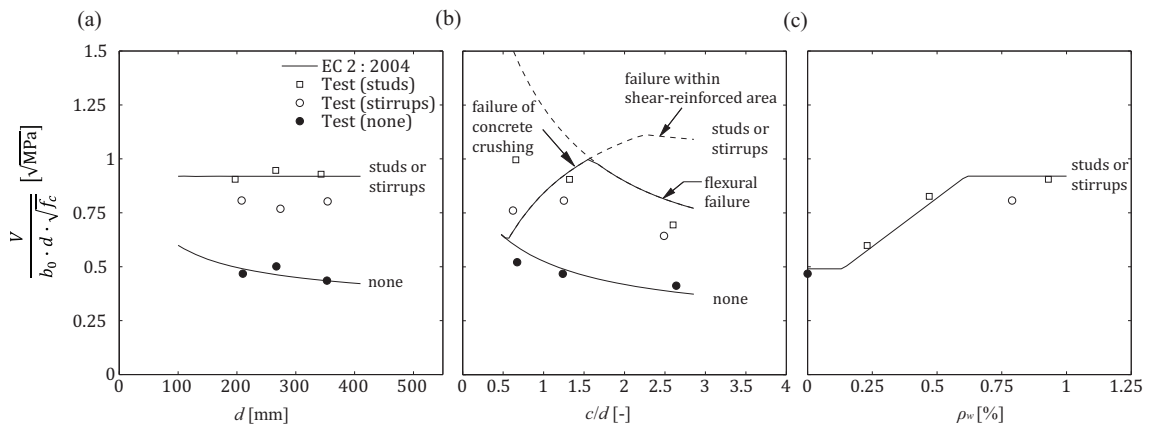


Figure 4.4: Punching strength according to EC2 2004 as a function of (a) the effective depth, (b) the column size to effective depth ratio, and (c) the shear reinforcement ratio

### 4.3. German National Annex to Eurocode 2 (NAD 2011)

#### 4.3.1. Strength prediction

The approach adapted by NAD 2011 for the calculation of the maximum punching strength leads to a higher average of the ratio of the experimentally to the predicted strength than EC2 2004 does. However, the coefficient of variation is around 15% leading to a 5%-fractile below 1.0. One reason for the coefficient of variation of around 15% is again that no distinction between different shear reinforcement systems was made since the code provision applies implicitly only for shear links. Another reason for this variation is that the average of specimens without shear reinforcement is 1.01 and the average of the specimens with shear reinforcement is 1.25. Therefore, the scatter results from the different safety margins of the approaches used for slabs with and without shear reinforcement. The statistical values will show better results if the specimens with and the specimens without shear reinforcement are analyzed separately. This would lead to a coefficient of variation of only 4% for specimens without shear reinforcement and 12% for specimens with shear reinforcement, whereby the 5%-fractile increases to 0.94 and 1.01, respectively. A further improvement can be obtained, by using different factors relating the punching strength of slabs without shear reinforcement to the maximum punching strength for double headed studs and for stirrups as it is used in practice. Figure 4.5 shows the comparison to the test results for a constant factor of 1.4 (Figure 4.5a) and by using a factor of 1.4 for stirrups and 1.9 for double headed studs (Figure 4.5b).

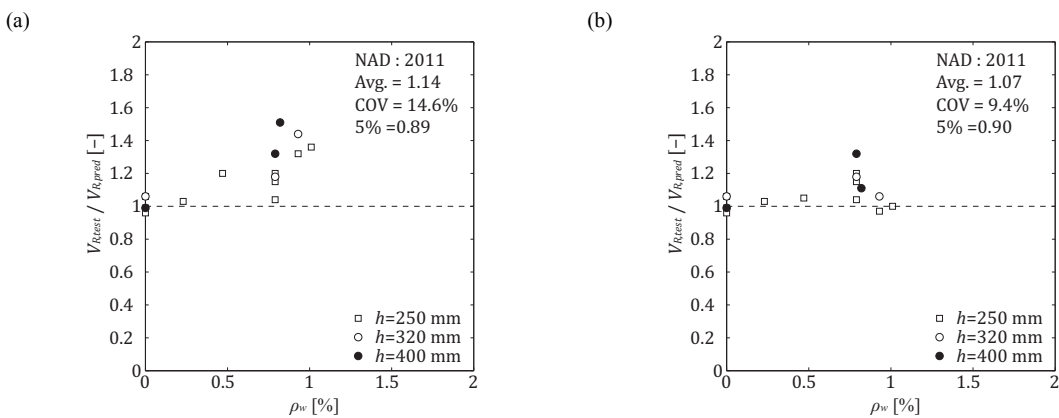


Figure 4.5: Ratio of the experimentally obtained punching strength to the punching strength predicted (a) according to NAD 2011 and (b) according to NAD 2011 with adjusted factor for double headed studs (stirrups: 1.4 / double headed studs: 1.9)

#### 4.3.2. Slab thickness

Figure 4.6a shows the normalized predicted punching strength as a function of the effective depth  $d$ . Since the formulation for specimens without shear reinforcement is the same as in EC2 2004, the prediction of the strength corresponds well to the experimentally obtained

strength as it was already shown previously. Due to the adjusted approach for the failure of the concrete strut, the predictions are always on the safe side for specimens with shear reinforcement. However, especially when studs are used and the prediction of the strength is calculated with the factor used in the code (factor: 1.4), the predictions are rather conservative as it can be seen by comparing the test results of the studs to the predicted strength curve for stirrups. Again, it can be noted that using a larger factor for double headed studs (factor: 1.9) improves the predictions as it can be seen by comparing the test results of the studs to the predicted strength curve for studs.

### 4.3.3. Column size

Figure 4.6b shows the normalized predicted punching strength as a function of the ratio of the column size to the effective depth  $c/d$ . In comparison to the approach of EC2 2004, it can be seen that the adapted provision in NAD 2011 for the maximum punching strength leads to better predictions of the punching strength. The predictions are always on the safe side. Moreover, due to the adjusted  $C$  factor for small  $c/d$  ratios, the provision accounts for the lower normalized strength in the case of small column sizes.

### 4.3.4. Shear reinforcement ratio

Figure 4.6b shows the normalized predicted punching strength as a function of the shear reinforcement ratio. For low amounts of shear reinforcement the predictions are the same as for EC2 2004 since the same formulations were used. However, the change in failure mode is predicted at lower shear reinforcement ratios as other codes (ACI 318 2011; EC2 2004) do. This may lead to a different prediction of the failure mode and thus to more conservative predictions.

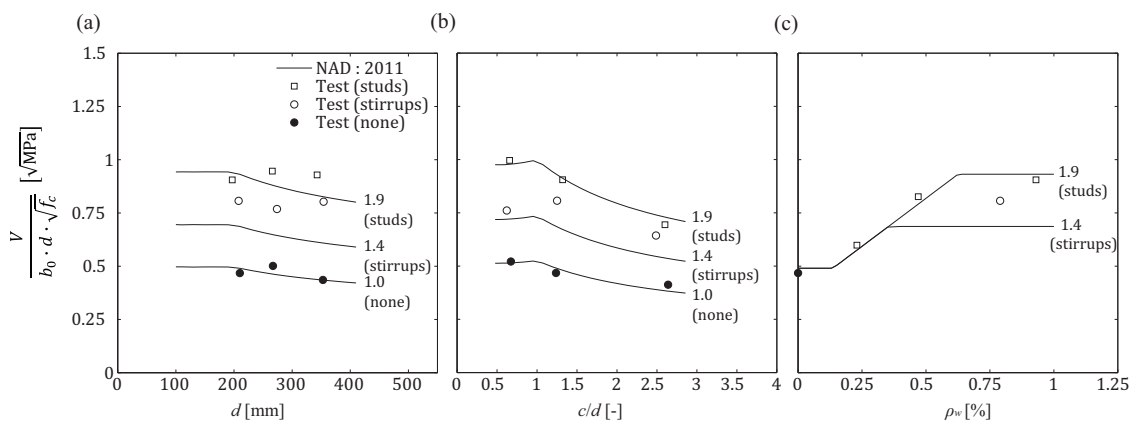


Figure 4.6: Punching strength according to NAD 2011 (including the predictions calculated with the adjusted factor for studs) as a function of (a) the effective depth, (b) the column size to effective depth ratio, and (c) the shear reinforcement ratio

## 4.4. SIA 262 (SIA 262 2003)

### 4.4.1. Strength prediction

In comparison to the results from the tests performed within this research project, it can be noted that SIA262 2003 predicts a somewhat conservative punching strength. Additionally, SIA262 2003 leads to scattered results, mainly due to the fact that it does not distinguish between different shear reinforcement systems and that it uses a relatively low increasing factor of 2.0. Furthermore, SIA262 2003 neglects any concrete contribution for the provision regarding failure within the shear-reinforced area leading to enormously conservative values for slabs with low amounts of shear reinforcement. These two conditions lead to a rather large scatter and thus to a rather large coefficient of variation of 15% resulting in a 5%-fractile around 1.0 despite the large average value of 1.31.

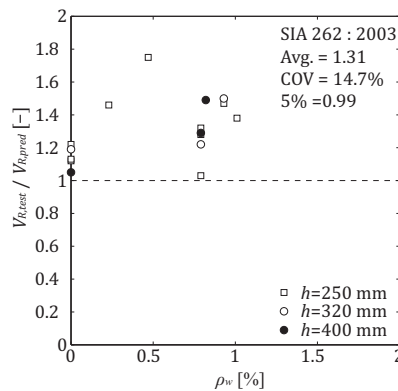


Figure 4.7: Ratio of the experimentally obtained punching strength to the punching strength predicted according to SIA262 2003

### 4.4.2. Slab thickness

Figure 4.8a shows the normalized predicted punching strength as a function of the effective depth  $d$ . While the provision for slabs without shear reinforcement leads to a good agreement with the test results, the provision of the maximum punching strength leads to rather conservative results. Since no distinction between different shear reinforcement systems is made, the difference between the predicted and measured values is, especially in the case of slabs with studs, relatively large.

#### 4.4.3. Column size

Figure 4.8b shows the normalized predicted punching strength as a function of the ratio of the column size to the effective depth  $c/d$ . Again, the provision for slabs without shear reinforcement leads to a good agreement with the test results. As noted previously, the provision of the maximum punching strength leads generally to conservative predictions. However, in the case of stirrups and small column sizes, the low factor relating the punching strength of slabs without shear reinforcement to the maximum punching strength of 2.0 is justified and can thus be seen as a lower limit.

#### 4.4.4. Shear reinforcement ratio

Figure 4.8c shows the normalized predicted punching strength as a function of the shear reinforcement ratio. For the failure within the shear-reinforced area, SIA262 2003 neglects the concrete contribution leading to low estimates of strength for slabs with low amounts of shear reinforcement. In this case, the punching strength calculated with the formulation for slabs without shear reinforcement needs to be considered. Furthermore, since the maximum punching strength is rather low when using a factor of 2.0 relating the punching strength of slabs without shear reinforcement to the maximum punching strength, the prediction of failure within the shear-reinforced area is restricted to a small range of shear reinforcement ratios ( $\rho_w = 0.40\%$ - $0.65\%$ ). This clearly leads to an underestimation of the punching strength.

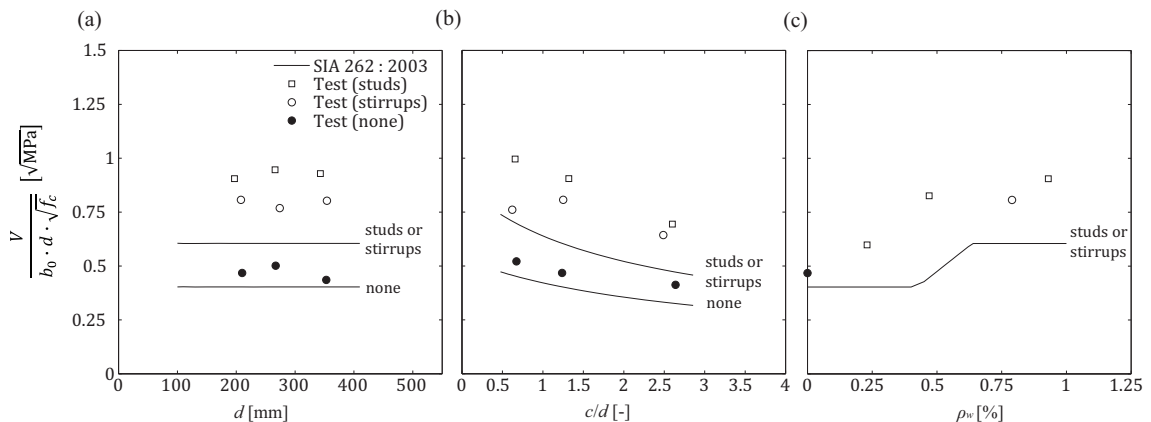


Figure 4.8: Punching strength according to SIA262 2003 as a function of (a) the effective depth, (b) the column size to effective depth ratio, and (c) the shear reinforcement ratio

## 4.5. fib Model code (MC 2011)

### 4.5.1. Strength prediction

Regarding the results from the tests performed within this research project, it can be noted that MC 2010 predicts safe estimates of the punching strength. The ratios between the experimentally obtained and the predicted values are somewhat scattered. The scatter results mainly from the rather low estimates of the punching strength for failure within the shear-reinforced area. This failure mode is also predicted in the cases, for which a failure due to the crushing of the concrete strut was observed (e.g. PL6). This effect is observed for a Level II and a Level III calculation. Generally, it can be noted that a Level II and a Level III calculation lead to nearly the same results for all the test specimens.

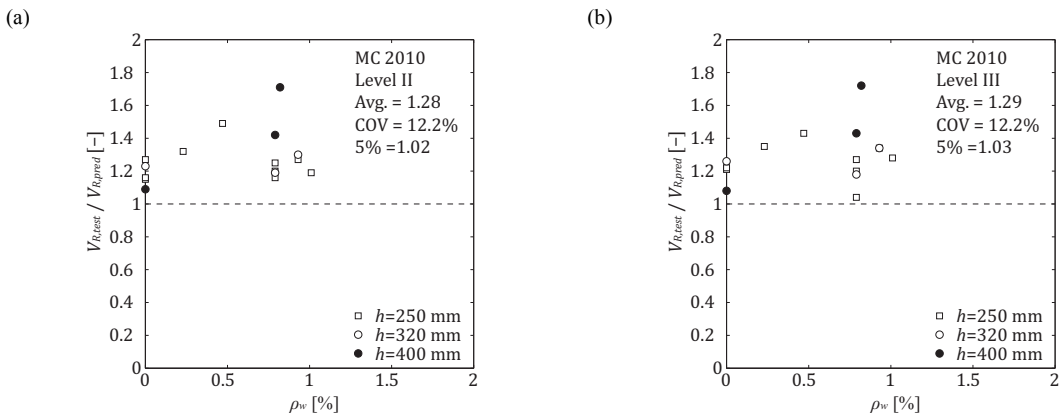


Figure 4.9: Ratio of the experimentally obtained punching strength to the punching strength predicted according to MC 2010 (a) Level II and (b) Level III

### 4.5.2. Slab thickness

Figure 4.10a and Figure 4.11a show the normalized predicted punching strength as a function of the effective depth  $d$  for a MC 2010 Level II and Level III calculation, respectively. It can be noted that both calculation methods show good agreement with the test results for specimens without shear reinforcement. In the case of specimens with shear reinforcement, both calculation methods show good agreement for effective depth smaller than 300 mm. However, for effective depths larger than 300 mm the predicted failure modes changes from crushing of the concrete strut to failure within the shear-reinforced area leading clearly to an underestimation of the punching strength. This is mainly due to the formulation regarding the activation of the shear reinforcement. For thicker and thus stiffer slabs, the stresses, which depend on the slab rotation, are relatively small in the shear reinforcement according to the provision since it assumes that the shear reinforcement is not fully activated. This assumption permits only the consideration of small stresses in the shear reinforcements and thus leads to a minor increase of strength due to the shear reinforcement ( $V_{R,s}$ ).



### 4.5.3. Column size

Figure 4.10b and Figure 4.11b show the normalized predicted punching strength as a function of the ratio of the column size to the effective depth  $c/d$  for a MC 2010 Level II and Level III calculation, respectively. Generally, the Level II and the Level III calculations show good agreement with the experimentally obtained punching strength for specimens with and without shear reinforcement. Similar to thick slabs, the predicted failure mode changes in the case of slabs with smaller  $c/d$  ratios. This change limits the normalized strength for smaller columns, which correspond to the test results for specimens with stirrups. For slabs with studs it may lead to an underestimation of the punching strength.

### 4.5.4. Shear reinforcement ratio

Figure 4.10c and Figure 4.11c show the normalized predicted punching strength as a function of the shear reinforcement ratio for a MC 2010 Level II and Level III calculation, respectively. It can be seen that the provision for failure within the shear-reinforced area leads to conservative estimates of the punching strength. This is mainly due to the fact that only shear reinforcement within a band between  $0.35d$  to  $d$  around the column is considered. In the performed tests only one perimeter of studs is within this zone and is thus considered in the calculation. A calculation with a shear reinforcement ratio (smeared shear reinforcement) would clearly increase the predicted strength and therefore would correspond better to the test results.

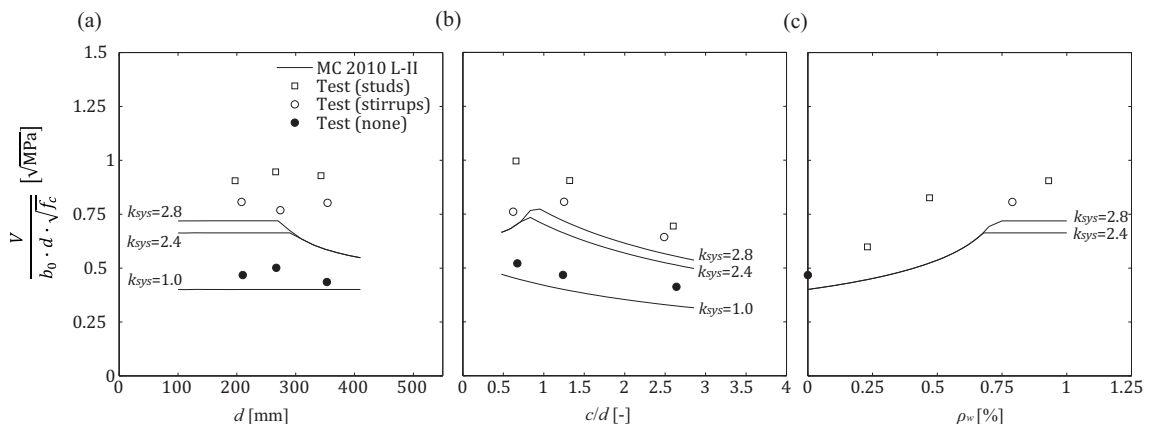


Figure 4.10: Normalized punching strength according to MC 2010 Level II as a function of (a) the effective depth, (b) the column size to effective depth ratio, and (c) the shear reinforcement ratio

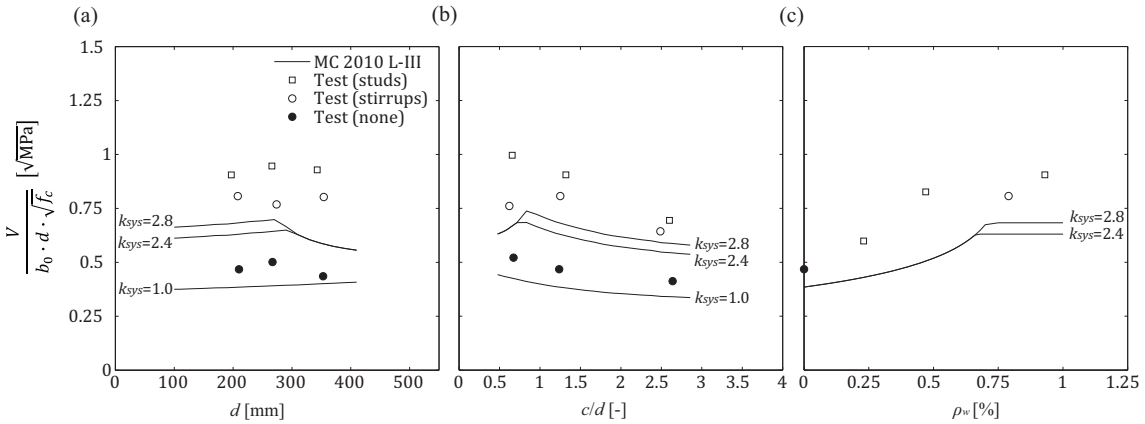


Figure 4.11: Normalized punching strength according to MC 2010 Level III as a function of (a) the effective depth, (b) the column size to effective depth ratio, and (c) the shear reinforcement ratio

## 4.6. Critical shear crack theory (CSCT)

### 4.6.1. Strength prediction

In comparison to the tests performed within this research project, it can be noted that the CSCT predicted strength agree very well with the experimentally obtained strength (Figure 4.12a). The average is close to 1.0 and the coefficient of variation is small (6.8%). Only the strength of the specimen with stirrups and a small column size (PF1) is somewhat overestimated. However, with respect to the rotation, it can be seen that the CSCT generally underestimates the rotations (Figure 4.12b). Additionally, it can be noted that the ratio between the predicted and the experimentally obtained rotation lead to scattered results. In order to address this observation, the predicted and the measured load-rotation curves will be further analyzed subsequently.

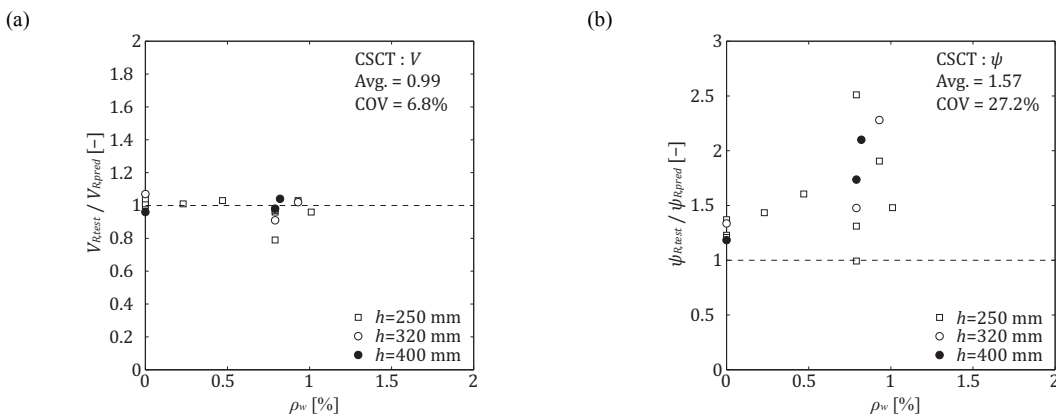


Figure 4.12: Ratio of (a) the experimentally obtained punching strength to the punching strength predicted according to the CSCT and (b) the experimentally obtained rotation at failure to the rotation at failure predicted according to the CSCT

#### 4.6.2. Slab thickness

Figure 4.13a shows the predicted punching strength as a function of the effective depth  $d$ . It can be seen that the CSCT predicts the strength very well for specimens with and without shear reinforcement. Moreover, the difference in strength between specimens with studs and with stirrups is well addressed. It is interesting to note that for specimens without shear reinforcement the predicted normalized strength slightly increases with decreasing thickness, which corresponds to the test results. On the other hand, in the case of specimens with shear reinforcement, the predicted normalized strength slightly increases with decreasing thickness for large column sizes until a certain thickness, at which the predicted normalized strength decreases with decreasing thickness. This can be explained by the fact that in the case of smaller slab thicknesses, and thus lower stiffness, the model predicts yielding of the flexural reinforcement leading to a smaller normalized strength.

#### 4.6.3. Column size

Figure 4.13b shows the predicted punching strength as a function of the ratio of the column size to the effective depth  $c/d$ . Generally, the CSCT leads to good agreement with the test results. It accounts for the increase in normalized strength with decreasing column size for slabs with and without shear reinforcement. However, for extremely small column sizes the normalized strength may decrease in certain cases. For example, for specimen PF1 with stirrups and a column size of  $c = 130$  mm, the experimentally obtained normalized strength is considerably lower than the predicted one.

#### 4.6.4. Shear reinforcement ratio

Figure 4.13c shows the normalized predicted punching strength as a function of the shear reinforcement ratio. Again, the normalized strength predicted by the CSCT shows good agreement with the test results. The increase in strength with increasing shear reinforcement ratio is well predicted as it corresponds very well with the experimental results. Moreover, the change in failure mode is accurately predicted. Again, the distinction between the different shear reinforcement systems is properly addressed.

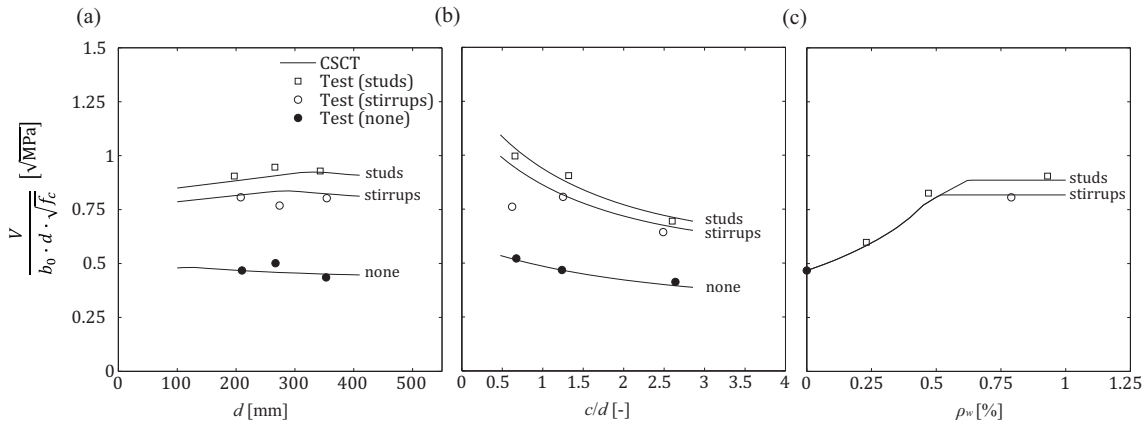


Figure 4.13: Normalized punching strength according to the CSCT as a function of (a) the effective depth, (b) the column size to effective depth ratio, and (c) the shear reinforcement ratio

#### 4.6.5. Prediction of the slab response and failure criteria

As discussed previously, while the punching strength is well predicted with a low coefficient of variation (Figure 4.12a), the predicted rotations are not only generally lower than the experimentally obtained rotation but lead also to scattered results compared to the experimentally obtained rotations (Figure 4.12b). This indicates an overestimation of the stiffness of the slab specimens by the CSCT. In order to address this issue, the measured load-rotation curves are compared to the predicted load-rotation curves and the failure criteria.

Figure 4.14 illustrates the normalized load-rotation curves for specimens without shear reinforcement. Although the predicted load-rotation curve behaves slightly stiffer than the measured load-rotation curve, they generally correspond well. It can be noted that the difference of the predicted and measured curves are larger for specimens for which higher strength is obtained, thus for specimens with larger column sizes (PL3) or larger thicknesses (PL4 and PL5). However, even for larger strength, the agreement to the test results is still acceptable. This corresponds also to Figure 4.12b which shows that for specimens without shear reinforcement the ratios between the predicted to the experimentally obtained rotation are within a small range. In fact, if only the specimens without shear reinforcement are considered, one can obtain an average value of 1.27 and a coefficient of variation of only 7%. This leads to the conclusion that this issue needs only be addressed in the case of large shear forces as it is the case of slab specimens with shear reinforcement.

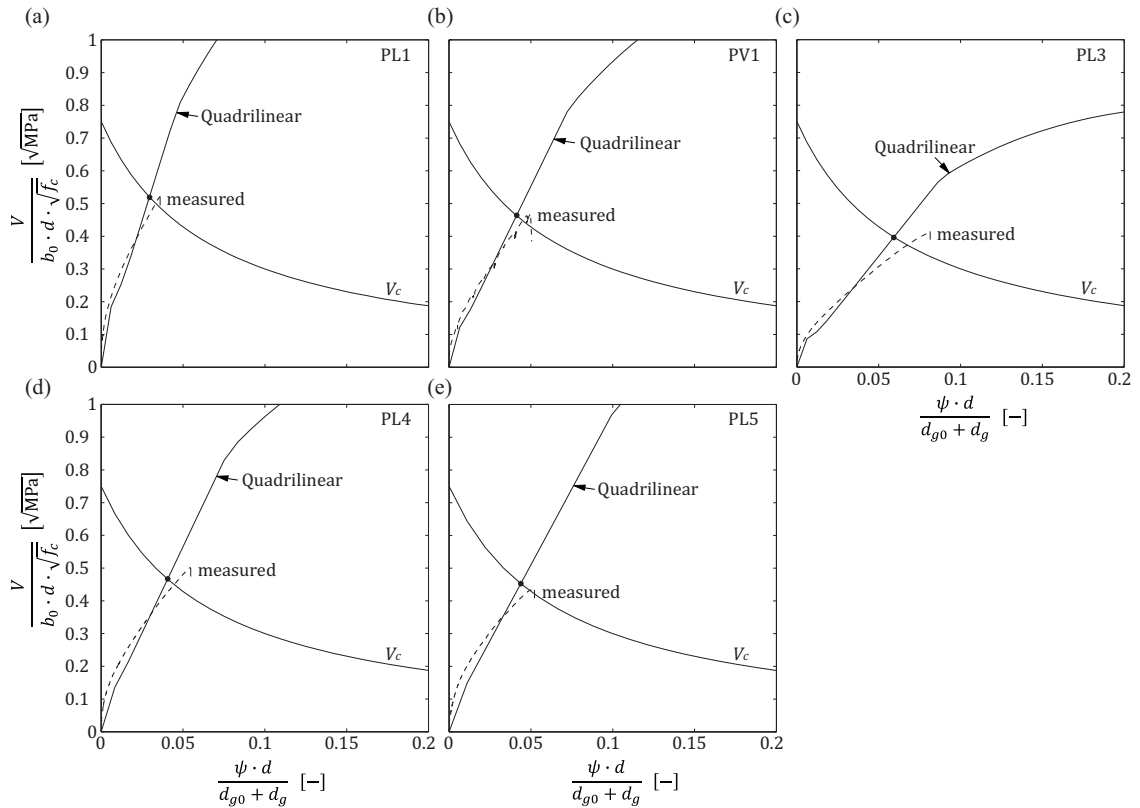


Figure 4.14: Measured normalized strength, calculated normalized strength (Quadrilinear), and failure criterion ( $V_c$ ) as a function of the normalized rotation for specimens without shear reinforcement (a-e)

Figure 4.15 illustrates the load-rotation curves for specimens with shear reinforcement. The trend mentioned previously is clearly visible. The slab specimens with shear reinforcement show not only a less stiff behavior than predicted but also reach their flexural strength much below the theoretical flexural capacity. This reduced stiffness leads to the underestimated rotations and to the scattered results as shown in Figure 4.12b. Another aspect of the difference in the load-rotation behavior of the test specimens compared to the predictions is that the intersection point between the slab behavior and the failure criterion is far from being close to the actual measured failure. However, due to the fit of the value  $\lambda$  that was chosen as 3 for studs and 2.5 for stirrups, the strength can be predicted accurately. Nevertheless, it has to be reminded that neither the predicted load-rotation curve nor the failure criterion represents the actual slab behavior accurately.

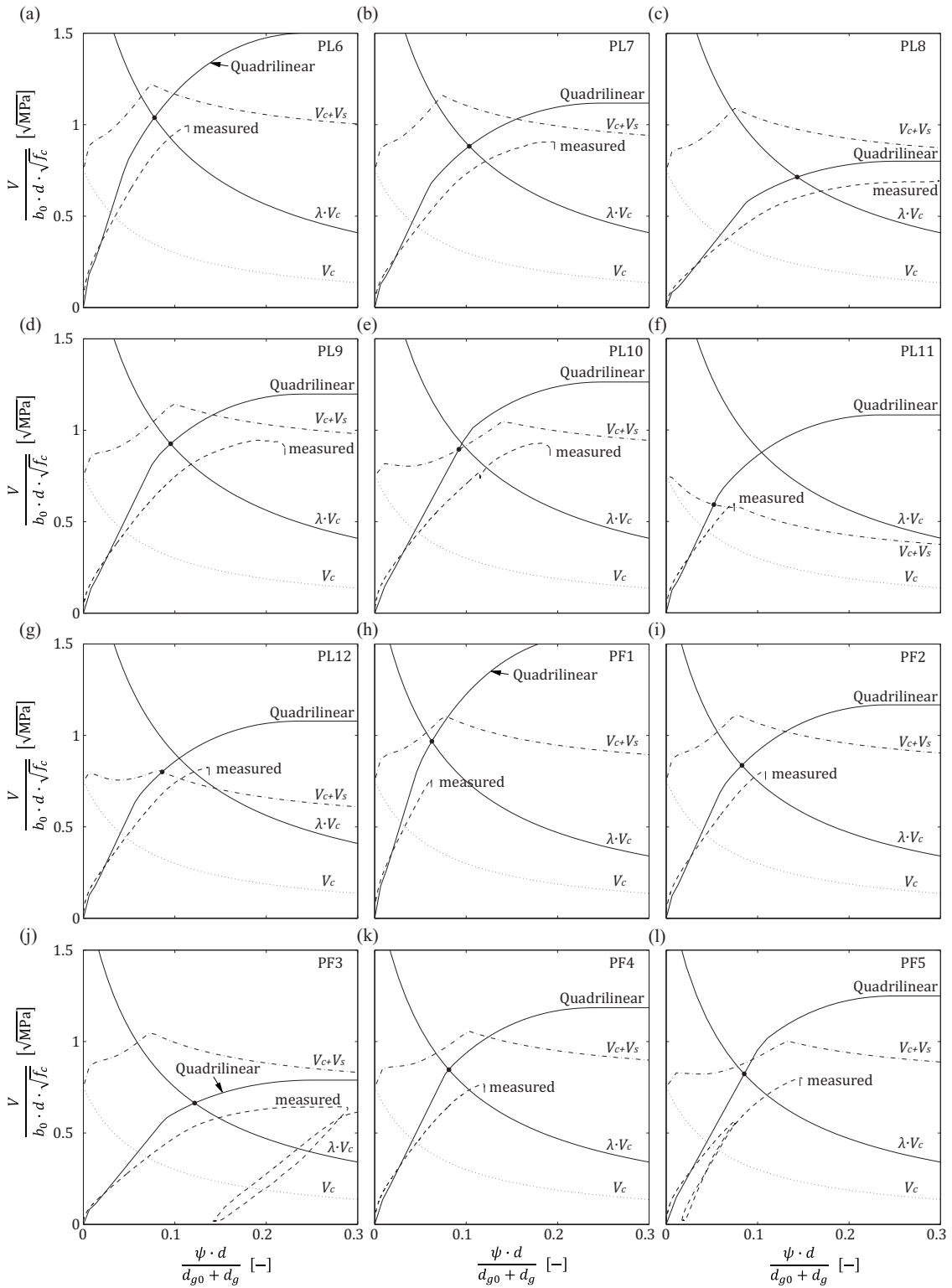


Figure 4.15: Measured normalized strength, calculated normalized strength (Quadrilinear), concrete contribution for failure criterion ( $V_c$ ), failure criterion for failure within the shear-reinforced area ( $V_c + V_s$ ), and failure criterion for crushing of the concrete strut ( $\lambda \cdot V_c$ ) as a function of the normalized rotation for specimens with studs (a-g) and stirrups (h-l)

## 4.7. Overview of the performance of the codes

In order to give an overview of the general performance of the code provisions and the CSCT, the results obtained by them were compared to the results from 132 tests found in literature whereby the selection consists of 28 tests of specimens without shear reinforcement and 104 tests of specimens with shear reinforcement. The selection of test specimens without shear reinforcement consists only of specimens that were used as reference specimens in series investigating slabs with shear reinforcement. More details of the test specimens used in this investigation and the results of the calculations can be found in Appendix A.

For the comparison of the different approaches, the ratio of the experimentally obtained punching strength to the predicted strength was calculated with each approach. From these results, statistical values such as the average and the coefficient of variation (COV) were determined for different sets of specimens. Additionally, the 5%-fractile for an assumed normal distribution with corresponding average and standard deviation was determined for the code provisions. Since the CSCT is not a code provision and thus does not have any safety margin in its formulation, the 5%-fractile has no meaning and is therefore not shown. After the statistical analysis, the ratios of the experimentally obtained punching strength to the predicted strength will be illustrated with respect to different parameters namely the shear reinforcement ratio, the effective depth, the column size to effective depth ratio, the flexural reinforcement ratio, and the concrete compressive strength. These comparisons reveal the advantages and the drawbacks of each code provision and the CSCT.

If all specimens are considered, all the codes except MC 2010 and the mechanical model of the CSCT lead to similar results as it can be seen in Table 4.1. Only EC2 2004 has due to the low average a rather low 5%-fractile value of only 0.82. In contrast, MC 2010 is the only code that has a 5%-fractile close to 1.0 mainly due to the low coefficient of variation of 11.6%, which is by far the lowest of all investigated code provisions. Since MC 2010 is based on the CSCT, the CSCT shows a similar low coefficient of variation of 10.8%. Additionally, the CSCT agrees well with the test results leading to an average value close to 1.0. Although this statistical analysis gives a good general overview of the performance of the different approaches, a differentiation of specimens with and without shear reinforcement will lead to a more detailed overview of the performance of each code and the CSCT.

Table 4.1: Statistical analysis of all investigated tests from literature

	ACI <sup>2011</sup>	EC <sup>2004</sup>	NAD <sup>2011</sup>	SIA <sup>2003</sup>	MC <sup>2010</sup>	CSCT
# specimens	132	132	132	132	132	132
Average	1.37	1.09	1.22 / 1.18 <sup>1</sup>	1.37	1.24	0.98
COV	19.7%	14.8%	15.2% / 16.1% <sup>1</sup>	20.3%	11.6%	10.8%
5% fractile	0.93	0.82	0.92 / 0.87 <sup>1</sup>	0.91	1.00	-

<sup>1</sup> with consideration of the increased factor for specimens with studs (1.9 instead of 1.4)

Table 4.2 shows the statistical analysis for the investigated tests divided into specimens with and without shear reinforcement. In the case of specimens without shear reinforcement, it can be noted that all the models lead to similar scatter except ACI 318-11 that shows much more scatter. This is mainly due to the fact that it does not consider the influence of the flexural reinforcement ratio. Although this simplified design approach leads to scatter compared to test results, it was reasonably justified by Alexander and Hawkins (Alexander and Hawkins 2005) who noted that the code should not predict the punching strength accurately but define a lower limit. In comparison to ACI 318-11, EC2 2004 and NAD 2011 have a much smaller coefficient of variation. However, due to the average close to 1.0, the 5%-fractile for EC2 2004 and NAD 2011 is smaller than the one for ACI 318-11. It has to be noted that EC2 2004 and NAD 2011 have nearly the same formulation for specimens without shear reinforcement except for coefficient  $C$ , which is constant in EC2 2004 whereas it depends on the column size in NAD 2011. SIA262 2003 and MC 2010 have nearly the same average and coefficient of variation since they both are based on the CSCT.

Table 4.2: Statistical analysis of tests from literature for specimens with and without shear reinforcement

Specimens considered		ACI <sup>2011</sup>	EC <sup>2004</sup>	NAD <sup>2011</sup>	SIA <sup>2003</sup>	MC <sup>2010</sup>	CSCT
Specimens without shear reinforcement	# specimens	28	28	28	28	28	28
	Average	1.25	1.03	1.03	1.12	1.17	0.95
	COV	16.7%	12.0%	11.7%	7.9%	7.8%	8.4%
	5% fractile	0.91	0.82	0.84	0.98	1.02	-
Specimens with shear reinforcement	# specimens	104	104	104	104	104	104
	Average	1.40	1.10	1.27 / 1.22 <sup>1</sup>	1.44	1.25	0.99
	COV	19.7%	15.1%	13.1% / 15.2% <sup>1</sup>	19.1%	12.0%	11.1%
	5% fractile	0.95	0.83	1.00 / 0.91 <sup>1</sup>	0.99	1.01	-

<sup>1</sup> with consideration of the increased factor for specimens with studs (1.9 instead of 1.4)

With respect to the specimens with shear reinforcement, it can be noted that while MC 2010 and CSCT show approximately a small coefficient of variation, the other codes show a rather large scatter of the results. However, due to a sufficient high average, ACI 318-11, SIA262 2003, and NAD 2011 lead to a 5%-fractile close to 1.0. In contrast, EC2 2004 has a low average leading together with a rather high coefficient of variation to a 5%-fractile well below 1.0. The difference between EC2 2004 and NAD 2011 is significant although they use nearly the same formulations. The main modification of NAD 2011 compared to EC2 2004 is the approach for the calculation of the punching strength for the failure of the concrete strut. Interesting to note is that the calculation according to NAD 2011 with consideration of a larger factor for the increase in the punching strength for specimens with studs (factor = 1.9), the statistical values seem to be worse compared to the calculations according to NAD 2011 with the standard factor (factor = 1.4). However, this can be explained by the fact that the change in the factor lead only to an improvement of the prediction for specimens with studs that have a prediction of failure



due to crushing of the concrete strut whereas the prediction of slabs with other shear reinforcement systems and failure modes do not change. Therefore, the average of a certain set of tests is reduced which leads to a larger scatter of the results when all specimens are considered. If the different failure modes are considered, this scatter in the results is less apparent. In order to address the predictions for the different failure modes in more detail, the statistical values were calculated for each model with respect to the predicted failure mode.

Table 4.3 presents the average, the coefficient of variation, and the 5%-fractile for each approach depending on the failure mode predicted by the corresponding model. Therefore, the number of specimens with a certain predicted failure mode is different for each approach. It can be noted that generally one failure mode dominates. This dominant failure mode has the largest average and in most cases the largest coefficient of variation. For example, ACI 318-11 has for failure modes crushing of concrete strut and failure within the shear-reinforced area an average of around 1.3 and a coefficient of variation of around 13%. For failure outside the shear-reinforced area however, the average is nearly 1.5 and the coefficient of variation at 20%. This raises the question if the ACI 318-11 provisions address this failure mode correctly.

In the case of SIA262 2003 the dominant failure mode is failure within the shear-reinforced area. While the averages of the other failure modes are around 1.25, the average for failure within the shear-reinforced area is above 1.5. This can be explained by the fact that SIA262 2003 considers solely the contribution of the shear reinforcement in the formulation of this failure mode leading to conservative estimates. Consequently, this failure mode becomes dominant with a rather large average value.

In contrast to ACI 318-11 and SIA262 2003, EC2 2004 shows the opposite tendency. The critical failure mode is in the case of crushing of the concrete strut although it has the lowest average. However, while the coefficient of variation is 11% and 14% for the other failure modes, it is 18% for failure of the concrete strut, leading to a 5%-fractile of only 0.78. Therefore, it can be concluded that this code provision may overestimate the punching strength for this mode of failure. In contrast, the statistical values for this failure mode are significantly improved using NAD 2011 resulting in a 5%-fractile above 1.0 due to the modified formulation for crushing of the concrete strut. Moreover, the consideration of a reduced effective depth for the calculation of the punching strength for failure outside the shear-reinforced area leads to a larger average resulting in a 5%-fractile above 1.0.

MC 2010 and CSCT show similar results. The slightly more dominant failure mode is for both approaches failure within the shear-reinforced area. The average and the coefficient of variation are slightly larger than the ones for the other two failure modes. However, the coefficient of variation is still small leading together with a sufficient large average to a 5%-fractile above 1.0 for all failure modes. It can be noted that MC 2010 has in comparison to the other code provisions not only the lowest coefficient of variation but is also the most balanced approach with respect to the different failure modes.

Table 4.3: Statistical analysis of tests from literature according to the predicted failure mode

Predicted failure mode		ACI <sup>2011</sup>	EC <sup>2004</sup>	NAD <sup>2011</sup>	SIA <sup>2003</sup>	MC <sup>2010</sup>	CSCT
crushing of the concrete strut	# specimens	32	22	37 / 34 <sup>1</sup>	28	14	22
	Average	1.29	1.11	1.25 / 1.11 <sup>1</sup>	1.28	1.21	0.92
	COV	13.6%	17.9%	11.4% / 12.8% <sup>1</sup>	9.6%	7.5%	7.7%
	5% fractile	1.00	0.78	1.02 / 0.87 <sup>1</sup>	1.08	1.06	-
within shear-reinforced area	# specimens	8	17	7 / 8 <sup>1</sup>	65	43	46
	Average	1.27	1.11	1.14 / 1.13 <sup>1</sup>	1.55	1.32	1.03
	COV	12.6%	11.0%	11.2% / 10.8% <sup>1</sup>	17.3%	11.7%	12.1%
	5% fractile	1.01	0.91	0.93 / 0.93 <sup>1</sup>	1.11	1.07	-
outside shear-reinforced area	# specimens	63	61	60 / 62 <sup>1</sup>	9	45	36
	Average	1.48	1.11	1.30 / 1.29 <sup>1</sup>	1.22	1.23	1.00
	COV	20.3%	14.5%	13.7% / 13.8% <sup>1</sup>	8.8%	10.1%	8.8%
	5% fractile	0.99	0.85	1.01 / 1.00 <sup>1</sup>	1.04	1.02	-

<sup>1</sup> with consideration of the increased factor for specimens with studs (1.9 instead of 1.4)

All the conclusions drawn on the basis of the statistical values can be additionally supported by the detailed analysis of the ratio of the experimentally obtained punching strength to the predicted strength as a function of several parameters such as the shear reinforcement ratio, the effective depth, the column size to effective depth ratio, the flexural reinforcement ratio, and the concrete compressive strength.

#### 4.7.1. Shear reinforcement ratio

Figure 4.16 shows the ratio of the experimentally obtained punching strength of the tests from literature to the predicted strength as a function of the shear reinforcement ratio. ACI 318-11 shows scattered but safe results for all shear reinforcement ratios. Additionally, it can be noted that for larger amounts of shear reinforcement only crushing of the concrete and failure outside the shear-reinforced area is predicted. In contrast, EC2 2004 predicts even for large amount of shear reinforcement a failure within the shear-reinforced area. This effect results from the overestimation of the crushing failure load as already discussed previously in this chapter. Consequently, EC2 2004 has a tendency that the larger the shear reinforcement ratio is the lower the ratio of the experimentally obtained strength to the predicted strength is. NAD 2011 avoids these drawbacks of EC2 2004 and thus leads to safe estimates even for large amounts of shear reinforcement. SIA262 2003 shows a clear underestimation of the strength in the case of low amount of shear reinforcement. Due to the fact that SIA262 2003 neglects any concrete contribution if shear reinforcement is present and thus the punching strength of slabs without shear reinforcement is governing for low amounts of shear reinforcement (Figure 4.8c), the punching strength is largely underestimated for these cases. MC 2010 as well as the CSCT shows good agreement to the test results for all shear reinforcement ratios. No tendency occurs in both cases.

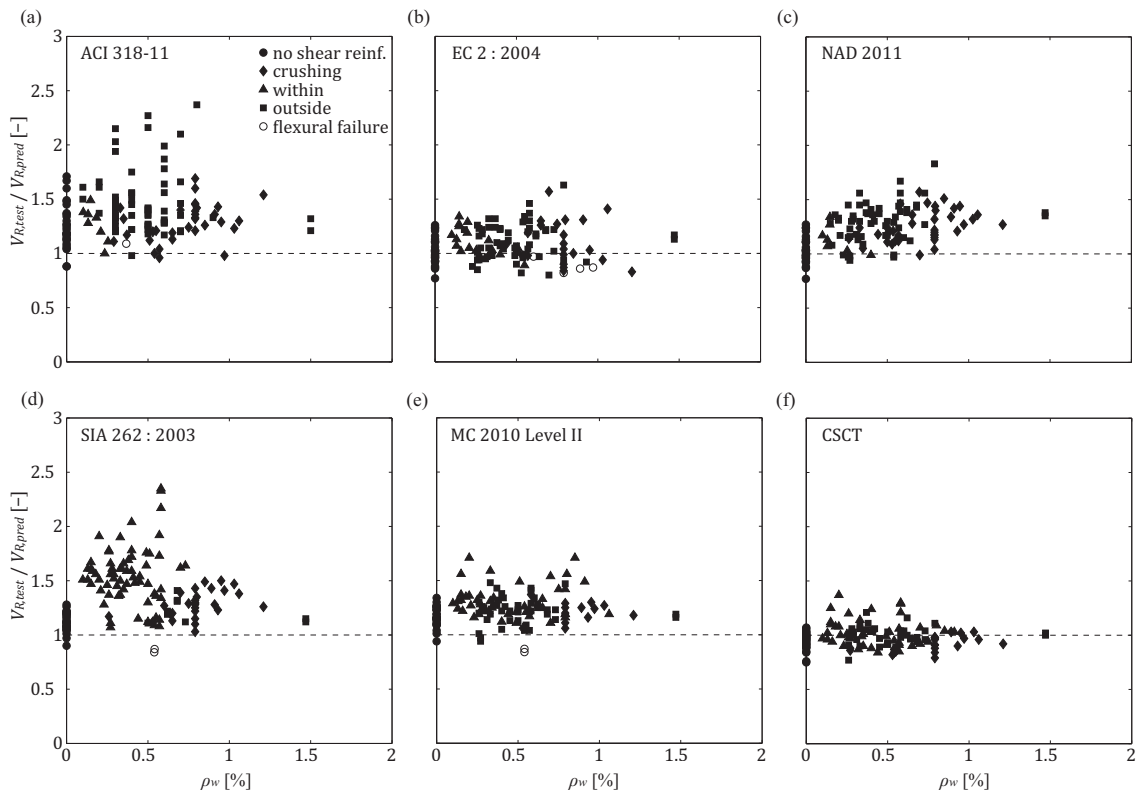


Figure 4.16: Ratio of the experimentally obtained punching strength of tests from literature to the predicted strength as a function of the shear reinforcement ratio

### 4.7.2. Effective depth

Figure 4.17 shows the ratio of the experimentally obtained punching strength of the tests from literature to the predicted strength as a function of the effective depth. ACI 318-11 shows scattered but safe results without any particular tendency. EC2 2004 shows somewhat scattered results without any clear tendency. However, it seems that EC2 2004 slightly overestimates the strength in the case of thicker slabs but due to the scarce set of tests with effective depths larger than 300 mm, no explicit conclusion can be drawn. Again, NAD 2011 improves the provisions of EC2 2004 and thus leads to safer estimates of the strength for specimen with shear reinforcement. Similar to ACI 318-11, SIA262 2003 shows scattered results, mainly due to the negligence of the concrete contribution, for all thicknesses without showing any tendency. Also no tendency occurs for MC 2010 and the CSCT, which both show good agreement for all effective depths. Interesting to note is that unlike the other codes, MC 2010 as well as the CSCT predicts failure within the shear-reinforced area for large effective depths. This can be explained by the fact that the stresses in the shear reinforcement depend in both models on the slab rotation. For small rotations such as it is the case for thick slabs, it is assumed that the shear reinforcement is not fully activated, thus the yielding strength is not reached, leading to a predicted failure within the shear-reinforced area.

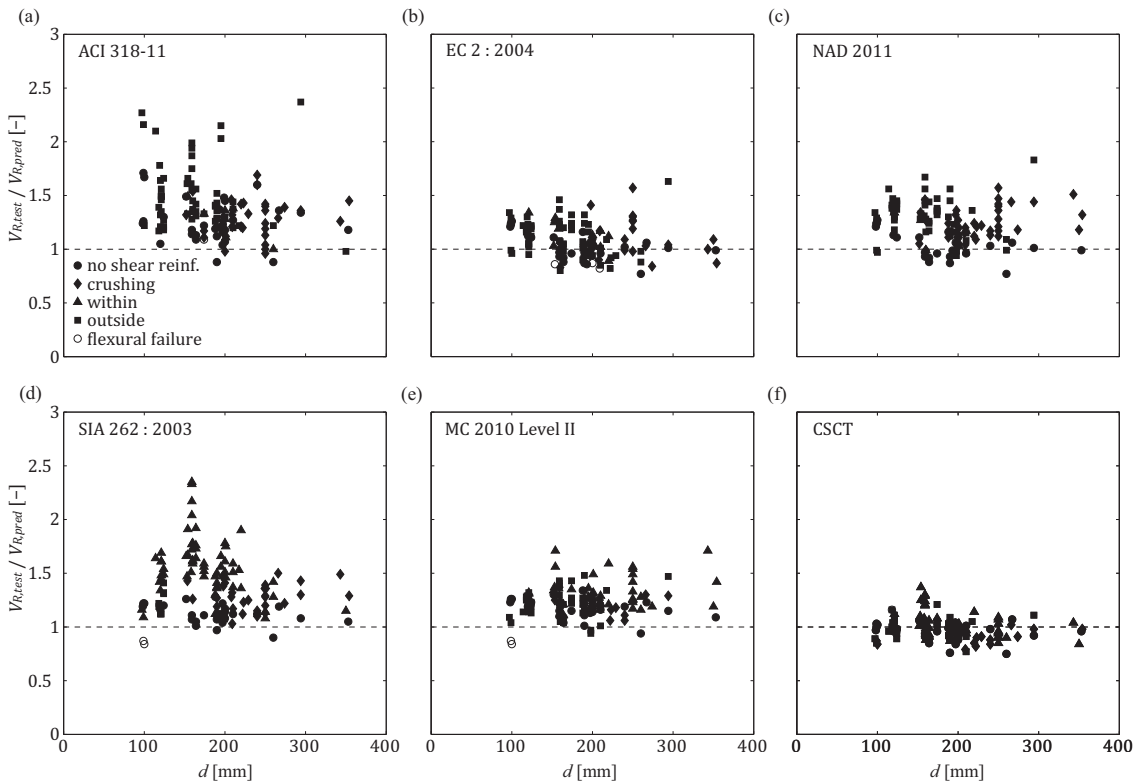


Figure 4.17: Ratio of the experimentally obtained punching strength of tests from literature to the predicted strength as a function of the effective depth

### 4.7.3. Column size

Figure 4.18 shows the ratio of the experimentally obtained punching strength of the tests from literature to the predicted strength as a function of the column size to the effective depth ratio. As for the previously investigated parameters, ACI 318-11 does not show any tendency with respect to the  $c/d$  ratio. EC2 2004 shows no tendency as one would expect according to Figure 4.4b. In fact, the estimates are not worse for large  $c/d$  ratios than for smaller ones. However, it is interesting to note that unlike the other codes, EC2 2004 predicts only once a failure of the concrete strut for specimens with moderate to large  $c/d$  ratios ( $c/d > 1.5$ ). This observation corresponds well to Figure 4.4b that shows a large increase in strength for larger  $c/d$  ratios for failure of the concrete strut. Again, NAD 2011 overcomes this deficiency by using a different formulation for failure of the concrete strut leading to larger ratios for larger column sizes. Neither SIA262 2003, MC 2010, nor the CSCT show a clear trend with respect to the  $c/d$  ratio. However, an interesting aspect is that MC 2010 predicts no failure of the concrete strut for small  $c/d$  ratios unlike the predictions of the other codes. This is due to the fact that in the case of small columns the punching strength for failure of the concrete strut might be overestimated as shown in Figure 4.10b and Figure 4.11b. Although this strength might be overestimated, MC 2010 provides still safe estimates since the considered cross sectional area of shear reinforcement decreases significantly with smaller  $c/d$  ratios so that failure within the shear-reinforced area is predicted (refer to Figure 4.10b). Similar to MC 2010, the CSCT predicts larger normalized strength for smaller column sizes as it can be seen by comparing Figure 4.10b and Figure 4.13b. However, in contrast to MC 2010, the CSCT may also predict failure of the concrete strut for smaller column sizes as it is the case for the calculations shown in Figure 4.13b. This difference can mainly be explained by the fact that the CSCT allows more cross sectional area of shear reinforcement for the calculation (compare subchapter 2.6.2 and 2.7.2) leading to the prediction of larger punching strength for failure within the shear-reinforced area. Consequently, the punching strength might be overestimated in the case of small column sizes as it can be seen in Figure 4.18f.

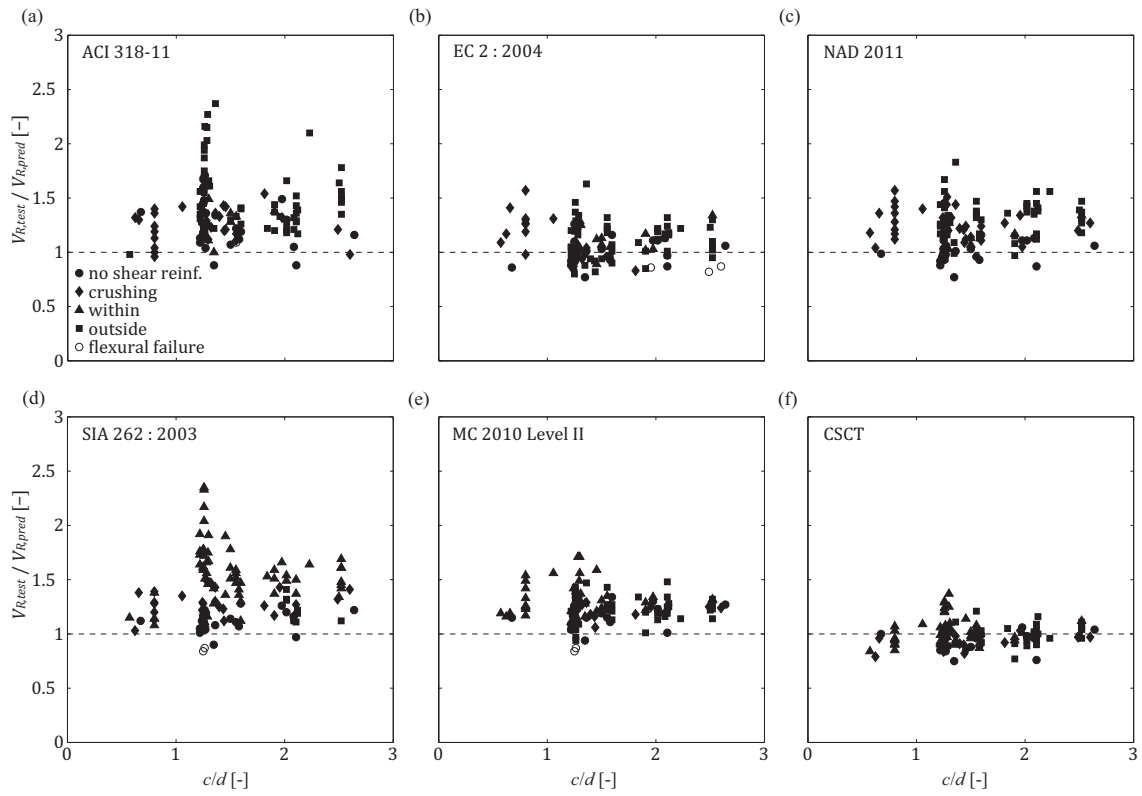


Figure 4.18: Ratio of the experimentally obtained punching strength of tests from literature to the predicted strength as a function of the column size to effective depth ( $c/d$ ) ratio

#### 4.7.4. Flexural reinforcement ratio

Figure 4.19 shows the ratio of the experimentally obtained punching strength of the tests from literature to the predicted strength as a function of the flexural reinforcement ratio. It can be noted that all the codes predict a punching failure even for low flexural reinforcement ratios, which correspond to the experimental observations. Generally, none of the models leads to an obvious trend with respect to the flexural reinforcement ratio. Nevertheless, ACI 318-11 seems to lead to lower ratios of experimentally obtained and predicted strength for lower flexural reinforcement ratios than in the case of higher flexural reinforcement ratios.

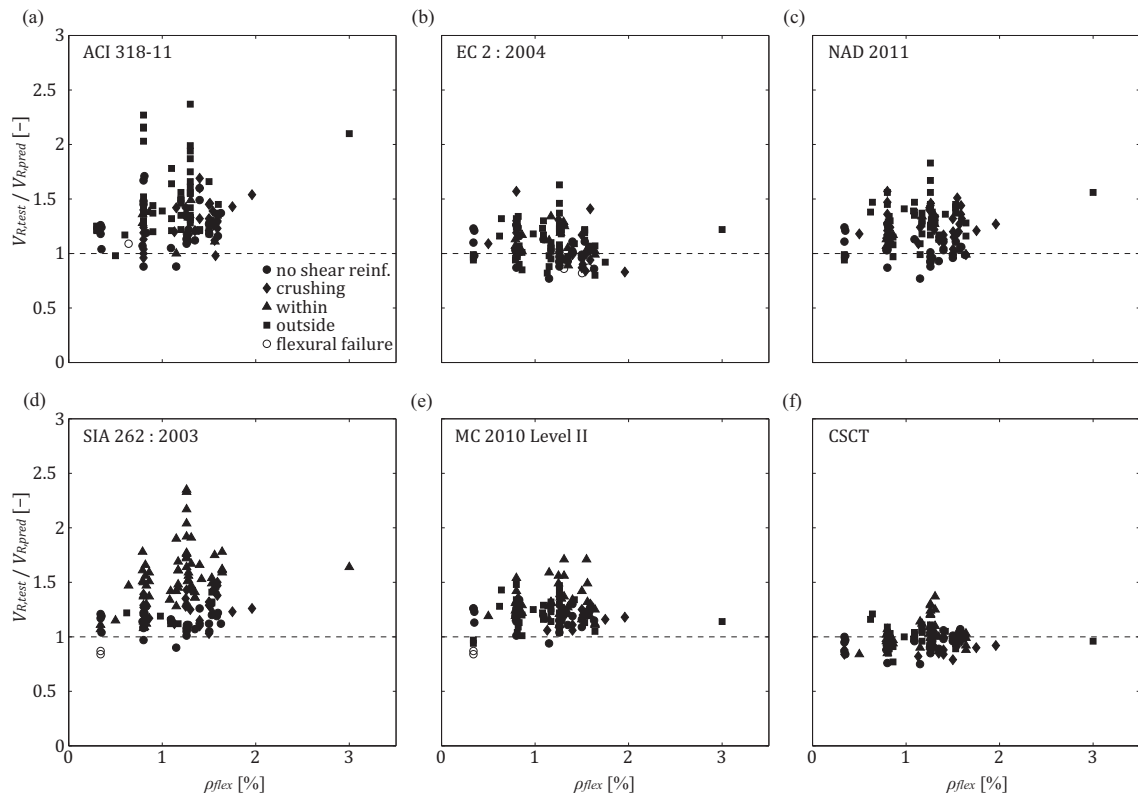


Figure 4.19: Ratio of the experimentally obtained punching strength of tests from literature to the predicted strength as a function of the flexural reinforcement ratio

### 4.7.5. Concrete compressive Strength

Figure 4.20 shows the ratio of the experimentally obtained punching strength of the tests from literature to the predicted strength as a function of the concrete compressive strength. Since most tests were performed with normal strength concrete with a compressive strength between 20 MPa and 40 MPa, the comparison lead to a cloud of points and no clear conclusions can be drawn. However, it can be noted that no approach shows obvious deficiencies for tests with concrete with compressive strength larger than 40MPa. Nevertheless, more test data is desired in order to analyze the trend of each approach with respect to the compressive strength.

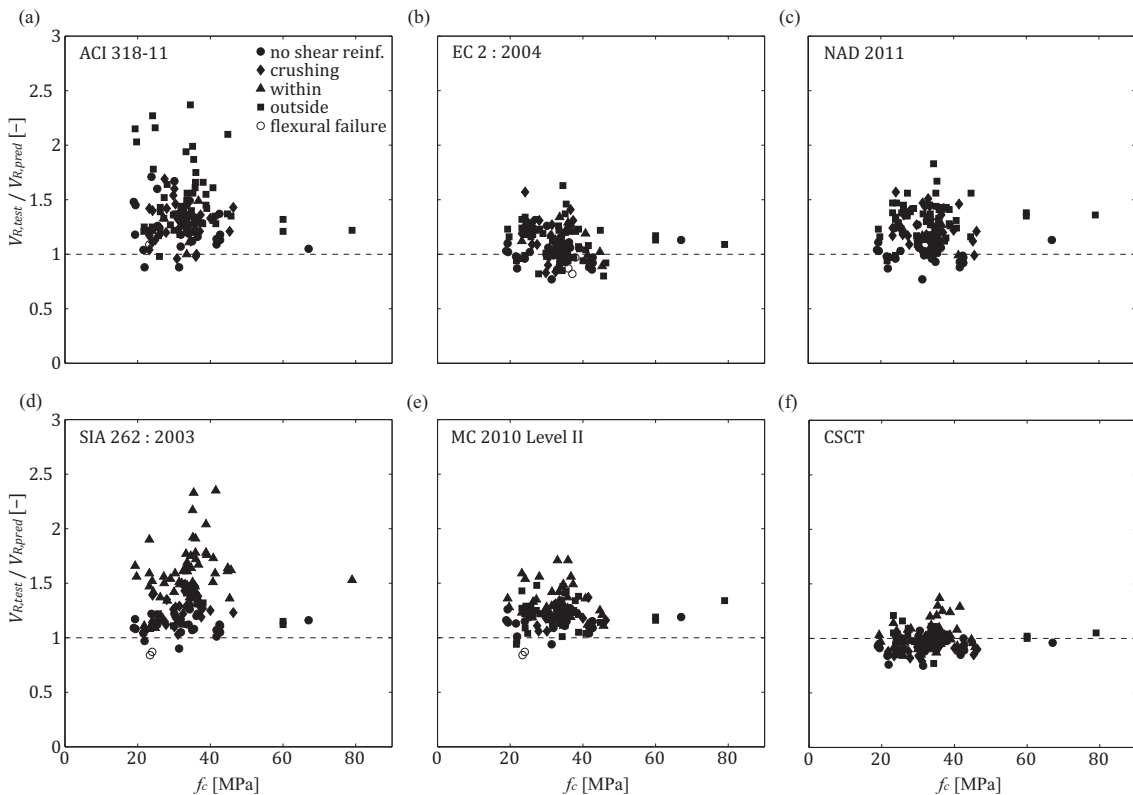


Figure 4.20: Ratio of the experimentally obtained punching strength of tests from literature to the predicted strength as a function of the concrete compressive strength



## 5. Development of a Nonlinear Finite Element Approach

In order to study the load-deformation behavior of the slab specimens, a finite element approach was developed. Since the nonlinearity in the behavior of cracked reinforced concrete has to be considered in the calculation of the deformation, the calculation requires a sophisticated model. Generally, two possible finite element methods seemed to be suitable: a two dimensional approach with plate or shell elements or a three dimensional analysis with solid elements. Since the complexity of a three dimensional model increases the number of (mostly unknown) input parameters as well as generates problems in detailing the interaction of concrete and reinforcing steel, the two dimensional approach was chosen. In order to implement the nonlinear behavior, a “modified stiffness” approach was chosen by which the secant stiffness is calculated using a plane stress field method.

Figure 5.1 shows the calculation procedure of the application in a flow chart. The approach is based on a linear finite element analysis with modified stiffness for each element. For this, the secant stiffness is calculated by the moment-curvature response of a single reinforced concrete element (Figure 5.2) whereby the response is determined by the integration of the forces of several plane stress field layers. Using this secant stiffness a linear finite element calculation will be performed. The thereby calculated curvatures lead to a new set of stiffness parameters for each element. This calculation is repeated until the difference of the reaction force and the maximum rotation between two calculation steps is smaller than a certain tolerance. Afterwards, the reaction force and the maximum rotation will be stored and the imposed displacement will be increased. One of the advantages of this calculation is that all input parameters are well defined and physically sound. Additionally, since the moment-curvature calculation is performed only once, the calculation is less time consuming than other methods. However, this procedure is only possible by using certain assumptions that are further explained in subchapter 5.3 in which the analysis is explained.

Before the analysis is described, the calculation of the moment-curvature curves is presented including the explanation of the input parameters and the used material properties. Finally, this chapter presents a comparison of the nonlinear finite element approach to experimentally obtained results from tests found in literature and from tests within this research project.

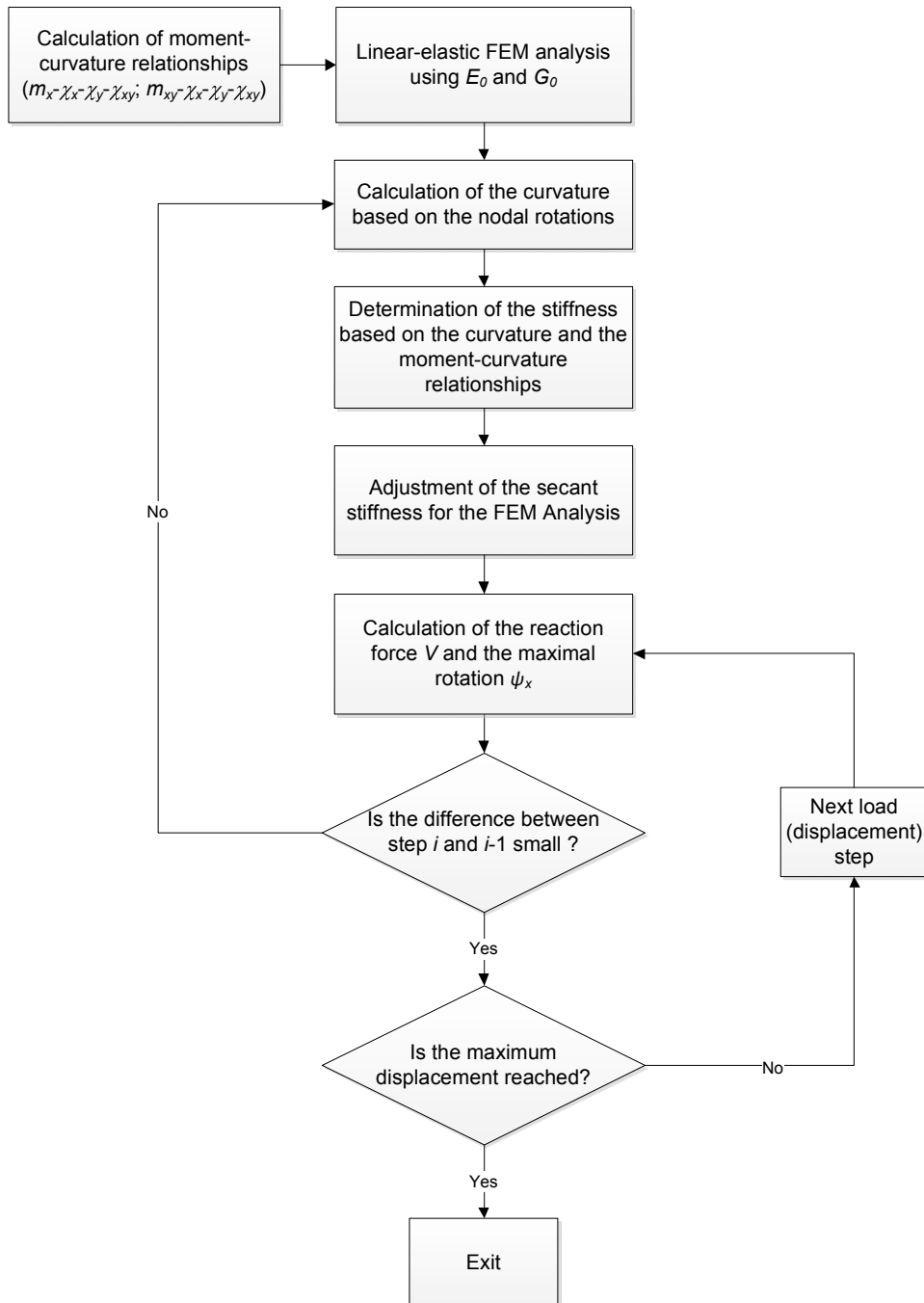


Figure 5.1: Flowchart of the NLFEA

## 5.1. Flexural stiffness

### 5.1.1. Compatibility conditions

Since it is assumed for the calculation of the flexural and torsional stiffness that normals to the median plane of a slab remain straight and orthogonal to the median surface during deformations, the strain at each level can be described as a linear function of the strains at mid-height of the cross section ( $\varepsilon_{0,x}$ ,  $\varepsilon_{0,y}$ ,  $\gamma_{0,xy}$ ) and the curvatures ( $\chi_x$ ,  $\chi_y$ ,  $\chi_{xy}$ ):

$$\begin{aligned}\varepsilon_x(z) &= \varepsilon_{0,x} + \chi_x z \\ \varepsilon_y(z) &= \varepsilon_{0,y} + \chi_y z \\ \gamma_{xy}(z) &= \gamma_{0,xy} + 2\chi_{xy} z\end{aligned}\quad (5.1)$$

Based on this, a strain profile can be determined from the given strains at mid-height of the section and the curvatures.

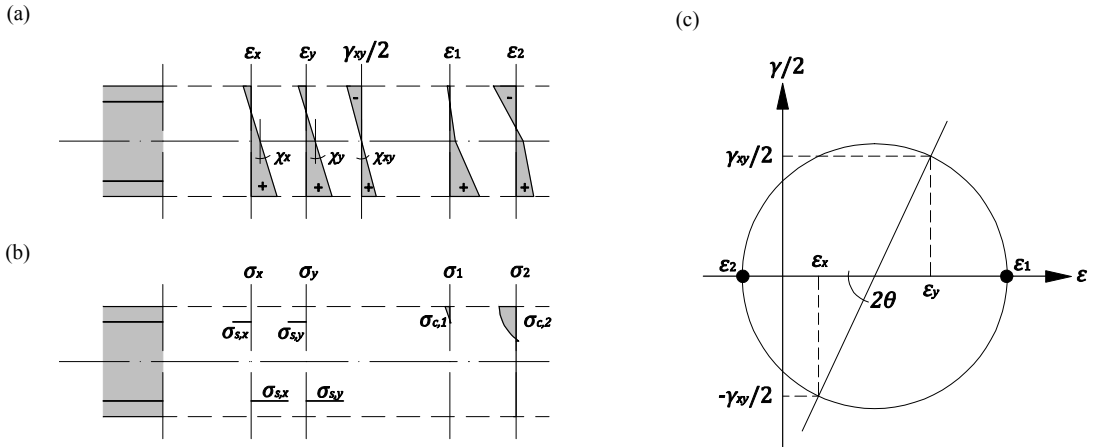


Figure 5.2: Stress and strain distribution

From Mohr's circle of strains, one can calculate the principal strains ( $\varepsilon_1$ ,  $\varepsilon_2$ ) and the direction of the principal strains ( $\theta$ ).

$$\begin{aligned}\varepsilon_1 &= \frac{\varepsilon_x(z) + \varepsilon_y(z)}{2} + \sqrt{\left(\frac{\varepsilon_x(z) - \varepsilon_y(z)}{2}\right)^2 + \left(\frac{\gamma_{xy}(z)}{2}\right)^2} \\ \varepsilon_2 &= \frac{\varepsilon_x(z) + \varepsilon_y(z)}{2} - \sqrt{\left(\frac{\varepsilon_x(z) - \varepsilon_y(z)}{2}\right)^2 + \left(\frac{\gamma_{xy}(z)}{2}\right)^2}\end{aligned}\quad (5.2)$$

where  $z$  is the distance to the mid-height of the cross section.

$$\theta(z) = \frac{1}{2} \cdot \arctan\left(\frac{2\chi_{xy}z}{\varepsilon_x(z) - \varepsilon_y(z)}\right) \quad (5.3)$$

By assuming that the directions of the principle strains coincide with the directions of the principle stresses, one can calculate the stresses in the element based on the constitutive model.

### 5.1.2. Material behavior

#### *Concrete*

The concrete behavior is modeled on the basis of the approach of (Vecchio and Collins 1986). The stress-strain relationship is described by a parabolic function, whereby the maximum strength is determined by the transverse tensile strains (Equation 5.4). However, the parabolic function was more generalized (Equation 5.5), so that adjustments could be easily made. This modification allows implementing confinement or a residual strength.

$$f_{c,max}(z) = \frac{-f_c}{0.8 + 0.34 \frac{\varepsilon_1(z)}{\varepsilon_p}} \geq -f_c \quad (5.4)$$

where  $f_c$  is the compressive strength,  $\varepsilon_1$  the transverse tensile stain, and  $\varepsilon_p$  the strain at the peak compression stress.

$$\begin{aligned} 0 \leq \varepsilon(z) \leq \varepsilon_{ct} &\rightarrow \sigma_{c,1}(z) = \varepsilon(z) \cdot E_{c,0} \\ \varepsilon_r \leq \varepsilon(z) \leq 0 &\rightarrow \sigma_{c,1}(z) = f_{c,max}(z) \cdot a \cdot (\varepsilon(z) - \varepsilon_r)^2 + \sigma_r \end{aligned}$$

where

$$a = \frac{\varepsilon_p - \varepsilon_q}{\varepsilon_p^2 (\varepsilon_q - \varepsilon_r)} \quad (5.5)$$

and

$$\varepsilon_q = \frac{\varepsilon_p \left( \varepsilon_r - \frac{\sigma_r}{f_{c,max}(z)} \varepsilon_p \right)}{\varepsilon_r - \varepsilon_p}$$

The parabolic function is defined by the maximum compressive strength  $f_c$ , which is reduced in presence of transverse tensile stains  $\varepsilon_1$ , by the strain at the peak  $\varepsilon_p$ , and by the maximum strain  $\varepsilon_r$ , at which a certain residual stress is obtained  $\sigma_r$ . For the calculations herein, a peak strain of  $\varepsilon_p = -0.002$ , a maximum strain of  $\varepsilon_r = -0.006$ , and a residual stress of  $\sigma_r = 0$  MPa were set (Figure 5.3).

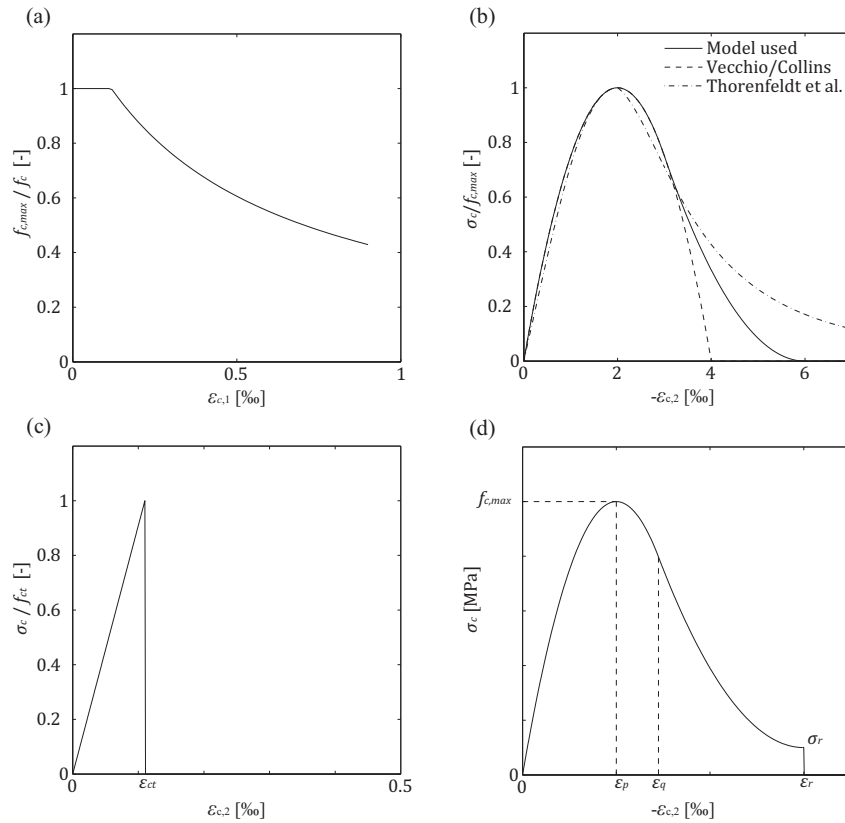


Figure 5.3: Concrete stresses as a function of the principal (a) lateral tensile strains and (b) compressive strains (Vecchio and Collins 1986; Thorenfeldt et al. 1987); (c) tension model and (d) parameters for the implemented compressive stress-strain function

## Steel

The stress-strain behavior of the reinforcing steel is modeled as a bilinear function. The behavior in tension and compression is assumed to be the same. The stresses increase linearly with increase of the strain until the yielding strength  $f_y$  is reached. After the yielding strength is reached the stresses increase linearly until the ultimate strain  $\varepsilon_u$  and the ultimate strength defined as  $k_{sh} \cdot f_y$  are reached. It has to be noted that this bilinear function was chosen in order to provide numerical stability when the reinforcing bars are yielding. It is not supposed to model the strain hardening accurately.

$$\begin{aligned}
 0 \leq \varepsilon_{s,i} \leq \varepsilon_y &\rightarrow \sigma_{s,i} = \varepsilon_{s,i} \cdot E_s \\
 \varepsilon_y < \varepsilon_{s,i} \leq \varepsilon_u &\rightarrow \sigma_{s,i} = \varepsilon_{x,y} + (\varepsilon_{s,i} - \varepsilon_y) \cdot E_{sh} \\
 \varepsilon_u < \varepsilon_{s,i} &\rightarrow \sigma_{s,i} = 0
 \end{aligned}
 \tag{5.6}$$

with

$$E_{sh} = f_y \cdot \frac{(k_{sh} - 1)}{(\varepsilon_u - \varepsilon_y)}$$

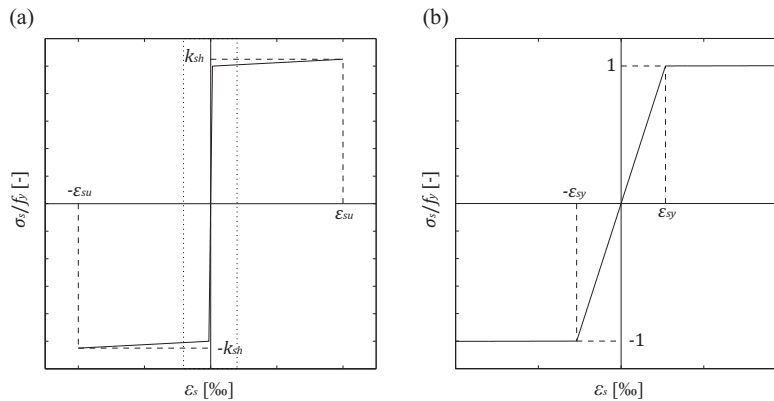


Figure 5.4: Stress-strain relationship for the reinforcing steel: (a) general view and (b) detailed view of pre-yield behavior

## Tension stiffening

The tension stiffening effect is the increase of the rigidity due to the tensile stresses in the concrete between cracks transferred by bond of reinforcing bars at stabilized cracking of the section ( $F_t > F_{cr}$ ). Various research has been performed in the past on this subject. However, in the case of slabs subjected to bending, most formulations rely on rather coarse simplifications or empirical adjustments. The difficulty lies mostly in defining the crack spacing, the bond stresses, and the area of concrete contributing to the tension stiffening. For numerical analyses, mostly two approaches are used in order to consider tension stiffening. The first one uses a modified pseudo-behavior of concrete under tension (Vecchio and Collins 1986; Vecchio 1989;

Polak 1992; Polak and Vecchio 1993) and the second one uses a pseudo-behavior of the reinforcing steel under tension (Sigrist 1995; Marti et al. 1998; Kaufmann and Marti 1998; Alvarez et al. 2000). Within this research, the second approach was used.

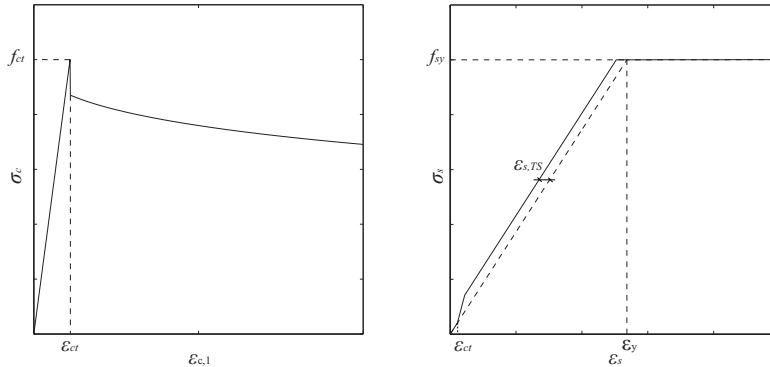


Figure 5.5: Considering tension stiffening by using (a) a modified concrete model (Vecchio and Collins 1986) or (b) a modified steel behavior (Sigrist 1995)

Assuming a rigid perfectly-plastic bond law, the stresses in the reinforcement bar reduce linearly along the length. This assumption is valid as long as the reinforcing steel does not yield. However, since the behavior of steel after yielding, steel hardening, is not modeled the tension stiffening in the post-yield phase is neglected. On the basis of these assumptions the reduced strain due to tension stiffening can be expressed as (Sigrist 1995):

$$\varepsilon_{sm} = \frac{1}{E_s} \cdot \left( \sigma_{smax} - \frac{\tau_b \cdot s_{cr}}{\phi} \right) \quad (5.7)$$

where  $\sigma_{smax}$  is the stress in the rebar at the crack,  $\tau_b$  is the bond strength,  $s_{cr}$  is the crack spacing,  $\phi$  is the diameter of the rebar, and  $E_s$  is the Young's modulus of the reinforcing steel.

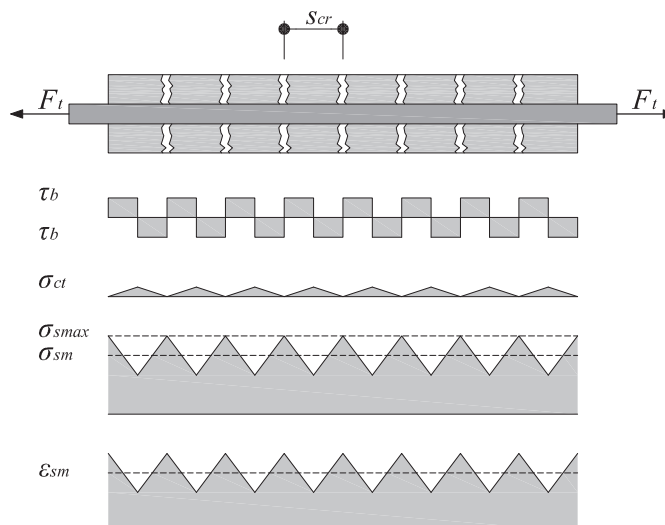


Figure 5.6: Stresses and strains in a tension member considering tension stiffening

The crack spacing is assumed to be the spacing of the flexural reinforcing bars. This rather simple hypothesis can be supported by several considerations. Firstly, although several researchers developed different approaches to express the crack spacing analytically, the calculation methods are in most cases based on empirical simplifications and the variation of the results from different research is rather high. Consequently, it seems more reasonable to use one coarse but physically sound simplification than to use a more sophisticated formulation, which uses several assumptions. Additionally, this basic assumption shows a good agreement with the experimentally observed average crack spacing.

### 5.1.3. Equilibrium conditions

By using the stress-strain relationship for concrete and steel the internal forces can be calculated. Because the concrete stresses (principal directions) and the steel stresses (direction of the global coordinate system) are not equivalent, the stresses have to be transformed to the same direction. Since in the NLFEA the stiffness will be defined in the direction of the global coordinate system, the stresses need to be transformed into these directions. Generally, the transformation of stresses ( $\sigma_x, \sigma_y, \tau_{xy}$ ) can be performed by using the inverse of the transformed strain transformation matrix [T] in order to obtain the stresses in another direction ( $\sigma'_x, \sigma'_y, \tau'_{xy}$ ).

The strain transformation matrix is defined as (Cook et al. 2002):

$$\{\varepsilon'\} = [T]\{\varepsilon\} \quad (5.8)$$

where for two dimensional problems, the transformation matrix can be expressed as:

$$[T] = \begin{bmatrix} \cos^2(\theta) & \sin^2(\theta) & \sin(\theta) \cdot \cos(\theta) \\ \sin^2(\theta) & \cos^2(\theta) & -\sin(\theta) \cdot \cos(\theta) \\ -2 \cdot \sin(\theta) \cdot \cos(\theta) & 2 \cdot \sin(\theta) \cdot \cos(\theta) & \cos^2(\theta) - \sin^2(\theta) \end{bmatrix} \quad (5.9)$$

Similarly, the strain transformation matrix can be used to obtain the stress transformation relations (Cook et al. 2002):

$$\{\sigma'\} = [T]^{-T}\{\sigma\} \quad (5.10)$$

where  $[T]^{-T}$  has the form

$$[T]^{-T} = \begin{bmatrix} \cos^2(\theta) & \sin^2(\theta) & -2 \cdot \sin(\theta) \cdot \cos(\theta) \\ \sin^2(\theta) & \cos^2(\theta) & 2 \cdot \sin(\theta) \cdot \cos(\theta) \\ \sin(\theta) \cdot \cos(\theta) & -\sin(\theta) \cdot \cos(\theta) & \cos^2(\theta) - \sin^2(\theta) \end{bmatrix} \quad (5.11)$$



It can be noted that the same relationship can be stated for curvatures:

$$\{\chi'\} = [T]\{\chi\} \quad (5.12)$$

and for moments:

$$\{m'\} = [T]^T\{m\} \quad (5.13)$$

Since the calculation of the concrete stresses is performed in the principal direction, one has to transform them into the direction of the reinforcement to form the equilibrium condition. Thus, if the existing stresses are the principal stresses and  $\theta$  is the principal direction (Equation 5.3), Equation 5.10 becomes:

$$\begin{Bmatrix} \sigma_x \\ \sigma_y \\ \tau_{xy} \end{Bmatrix} = [T]^T \begin{Bmatrix} \sigma_2 \\ \sigma_1 \\ 0 \end{Bmatrix} \quad (5.14)$$

By integrating the concrete stresses, one can obtain the concrete forces in the global directions. Thus,

$$\begin{Bmatrix} F_{c,x} \\ F_{c,y} \\ F_{c,xy} \end{Bmatrix} = \int_{-h/2}^{h/2} [T]^T \cdot \begin{Bmatrix} \sigma_{c,2} \\ \sigma_{c,1} \\ 0 \end{Bmatrix} \cdot dz \quad (5.15)$$

The steel forces can be obtained by the summation of the forces in each rebar. Thus,

$$\begin{aligned} F_{s,x} &= \sum_{i=1}^n \sigma_{sx,i} \cdot a_{sx,i} \\ F_{s,y} &= \sum_{i=1}^n \sigma_{sy,i} \cdot a_{sy,i} \end{aligned} \quad (5.16)$$

The first set of equilibrium conditions can be described as the sum of the internal and external membrane forces in each direction. Thus,

$$\begin{aligned} \sum F_x &= 0 \rightarrow F_{c,x} + F_{s,x} + n_x = 0 \\ \sum F_y &= 0 \rightarrow F_{c,y} + F_{s,y} + n_y = 0 \\ \sum F_{xy} &= 0 \rightarrow F_{c,xy} + n_{xy} = 0 \end{aligned} \quad (5.17)$$

Similarly, the moments due to the concrete stresses can be defined as:

$$\begin{Bmatrix} m_{c,x} \\ m_{c,y} \\ m_{c,xy} \end{Bmatrix} = \int_{-h/2}^{h/2} [\mathbf{T}]^{-T} \cdot \begin{Bmatrix} \sigma_{c,2} \\ \sigma_{c,1} \\ 0 \end{Bmatrix} \cdot z \cdot dz \quad (5.18)$$

and the moments due to the steel stresses:

$$\begin{aligned} m_{s,x} &= \sum_{i=1}^n \sigma_{sx,i} \cdot z_{x,i} \cdot a_{sx,i} \\ m_{s,y} &= \sum_{i=1}^n \sigma_{sy,i} \cdot z_{y,i} \cdot a_{sy,i} \end{aligned} \quad (5.19)$$

leading to the second set of equilibrium conditions, which equals the sum of the internal and external moments in each direction to zero. Thus,

$$\begin{aligned} \sum m_x &= 0 \rightarrow m_{c,x} + m_{s,x} + m_x = 0 \\ \sum m_y &= 0 \rightarrow m_{c,y} + m_{s,y} + m_y = 0 \\ \sum m_{xy} &= 0 \rightarrow m_{c,xy} + m_{xy} = 0 \end{aligned} \quad (5.20)$$

Hence, for each state of deformation ( $\varepsilon_{0,x}$ ,  $\varepsilon_{0,y}$ ,  $\gamma_{0,xy}$ ,  $\chi_x$ ,  $\chi_y$ ,  $\chi_{xy}$ ) the external forces ( $n_x$ ,  $n_y$ ,  $n_{xy}$ ,  $m_x$ ,  $m_y$ ,  $m_{xy}$ ) can be calculated. Assuming that the membrane forces ( $n_x$ ,  $n_y$ ,  $n_{xy}$ ) are equal to zero, one can calculate the moment-curvature relationship for each state of deformation. Figure 5.7 illustrates the moment  $m_x$  and  $m_{xy}$  as a function of the curvature  $\chi_x$  and  $\chi_{xy}$  for a lateral curvature  $\chi_y$  equal to zero. The calculated surfaces in Figure 5.7 clearly show the change in the slab behavior depending on the different state of deformation. For example, the flexural stiffness decreases if the torsional curvature increases. Even more pertinent is the change of the torsional stiffness due to the flexural curvature.

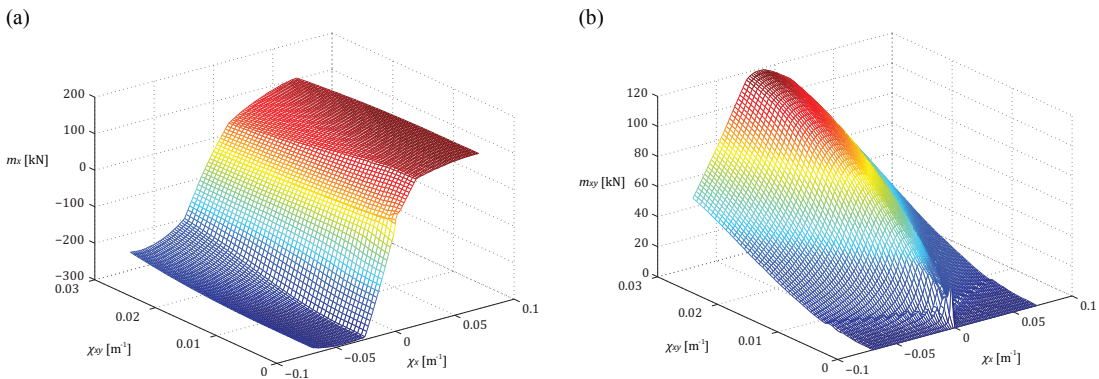


Figure 5.7: Moment as a function of the curvatures  $\chi_x$  and  $\chi_{xy}$  for (a)  $m_x$  and (b)  $m_{xy}$

The dependence of the stiffness on the different curvatures can also be seen in Figure 5.8 that shows the moment  $m_x$  as a function of the curvature  $\chi_x$  for different levels of  $\chi_{xy}$  and the moment  $m_{xy}$  as a function of the curvature  $\chi_{xy}$  for different levels of  $\chi_x$ . Again, it can be seen that while a difference in the flexural stiffness due to a torsional curvature only marginally occurs, the difference in the torsional stiffness due to a flexural curvature is significant. Therefore, these effects clearly need to be considered for an accurate analysis of a slab in which torsional moments occur.

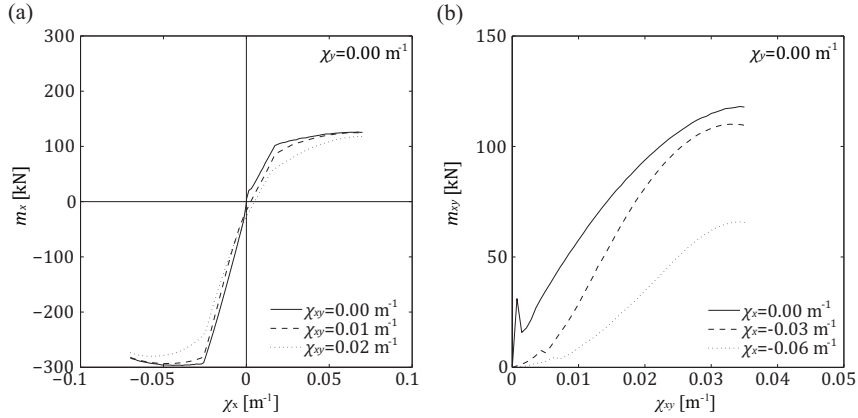


Figure 5.8: Interaction of the curvatures  $\chi_x$  and  $\chi_{xy}$ : (a) bending moment-curvature diagram in x-direction and (b) torsional moment-curvature diagram

Based on the calculated moment-curvature response of the element, the secant stiffness matrix  $K$  can be determined, which is afterwards used for the linear-elastic finite element analysis. The secant stiffness matrix becomes:

$$\begin{Bmatrix} m_x \\ m_y \\ m_{xy} \end{Bmatrix} = \begin{bmatrix} K_x & 0 & 0 \\ 0 & K_y & 0 \\ 0 & 0 & K_{xy} \end{bmatrix} \cdot \begin{Bmatrix} \chi_x \\ \chi_y \\ \chi_{xy} \end{Bmatrix} \quad (5.21)$$

Although this diagonal matrix does not seem to account for the interaction between the different curvatures, each stiffness ( $K_x$ ,  $K_y$ , and  $K_{xy}$ ) is determined as a function of all the curvatures ( $\chi_x$ ,  $\chi_y$ , and  $\chi_{xy}$ ). Thus, the interaction between the different curvatures is accounted in the calculation of each stiffness.

## 5.2. Shear stiffness

Flat slabs are generally thin structures. Thus, the shear deformations are relatively small and are usually neglected in FEM calculations of slabs (e.g. by using Kirchhoff elements). In this case the shear deformations are considered (based on the Mindlin theory) but with an uncracked shear stiffness ( $G_{xz} = G_{yz} = G_{c0}$ ). This assumption is valid for regions where the shear deformations are small and thus for regions where no shear reinforcement is used. In regions

with shear reinforcement, in the vicinity of the columns, the shear deformations can be significant as it was presented in Chapter 3. As it will be discussed in Chapter 7, these large shear deformations result from the compression strut close to the column and thus it is assumed that they lead to a rigid body shift of the slab element outside the supported area. Therefore, it is assumed that the load-rotation response of the slab is only slightly influenced by these shear deformations.

### 5.3. Analysis

The analysis procedure consists of certain simplifications in order to reduce the demand of resources and to increase the calculation speed. The first assumption concerns the calculation of the flexural stiffness. The flexural stiffness is regarded as independent from the actions perpendicular to the investigated direction. For example, it is assumed that the curvature  $\chi_y$ , which acts perpendicular to the moment  $m_x$ , does not influence the stiffness in  $x$ -direction. Thus, only the curvatures  $\chi_x$  and  $\chi_{xy}$  are considered for the calculation of the stiffness  $EI_x$ . This assumption can be supported by the moment-curvature ( $m_x$ - $\chi_x$ ) curves for different levels of lateral  $\chi_y$  and torsional curvatures  $\chi_{xy}$ . Figure 5.9 illustrates the moment-curvature curves for different levels of lateral and torsional curvatures. It can be seen that the discrepancy between the different curves are relatively small leading to only small differences in the secant stiffness. Therefore, this minor error resulting from the assumption can be accepted. However, it has to be noted that this assumption can only be made as long as the curvatures in  $x$ - and  $y$ -direction have the same sign. In this case the concrete is influenced only by lateral compression, which would slightly increase the strength (Kupfer and Gerstle 1973). In the case of lateral tension due to an opposite signed flexural moment, the compression zone will be drastically softened. Consequently, the rigidity would be largely decreased and thus the assumption would not be valid.

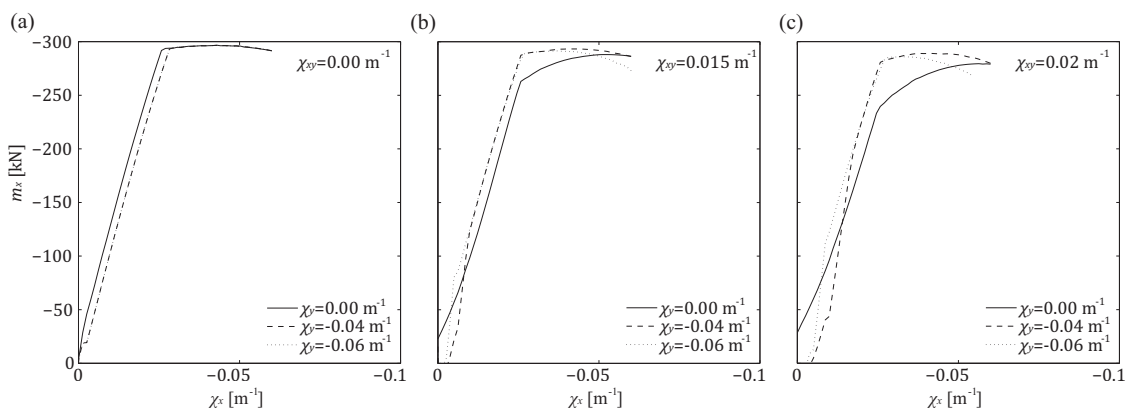


Figure 5.9: Moment-curvature diagram in  $x$ -direction for different lateral curvatures  $\chi_y$  and for twisting curvatures of (a)  $\chi_{xy} = 0.00 \text{ m}^{-1}$ , (b)  $\chi_{xy} = 0.015 \text{ m}^{-1}$ , and (c)  $\chi_{xy} = 0.02 \text{ m}^{-1}$

The torsional stiffness however cannot be assumed as independent of the moments in  $x$ - and  $y$ -direction. In order to address this influence, the moment  $m_{xy}$  needs to be calculated by a variation of  $\chi_{xy}$  and a pair of  $\chi_x$  and  $\chi_y$ . Figure 5.10 shows the moment-curvature ( $m_{xy}$ -  $\chi_{xy}$ ) curve for different flexural curvatures  $\chi_x$  and  $\chi_y$  whereby the curvature  $\chi_y$  is shown as a function of  $\chi_{xy}$ . Unlike the flexural curvature ( $\chi_x$ ), the torsional stiffness depends largely on the flexural curvatures as the discrepancies between the different curves show. Another interesting aspect to note is that in the case of lateral curvature ( $\chi_y$ ) the stiffness is low until a certain point at which the slab starts to behave more rigid. This can be explained in the change of the state of stress. At first a large depth of the slab is cracked due to the dominance of the curvature  $\chi_x$ . However, at a certain point some cracks will be closed due to compression resulting from the twisting moments, leading finally to an increase in stiffness. This explanation is of course only based on a pure theoretical point of view since the actual behavior may depend as well on the effective loading and thus the cracking history of the slab element. Nevertheless, since the load history is neglected in the NLFEA, the theoretically obtained behavior is assumed to be accurate enough. Another assumption was made in order to decrease the calculation time and data volume. Since the stiffness is within two boundaries, only one calculation with the lateral curvature equal to zero ( $\chi_{xy} \neq 0$ ;  $\chi_x \neq 0$ ;  $\chi_y = 0$ ) and one calculation with the lateral curvature equal to the main curvature ( $\chi_{xy} \neq 0$ ;  $\chi_x = \chi_y \neq 0$ ) are performed whereby values of the stiffness between these two boundaries will be linearly interpolated.

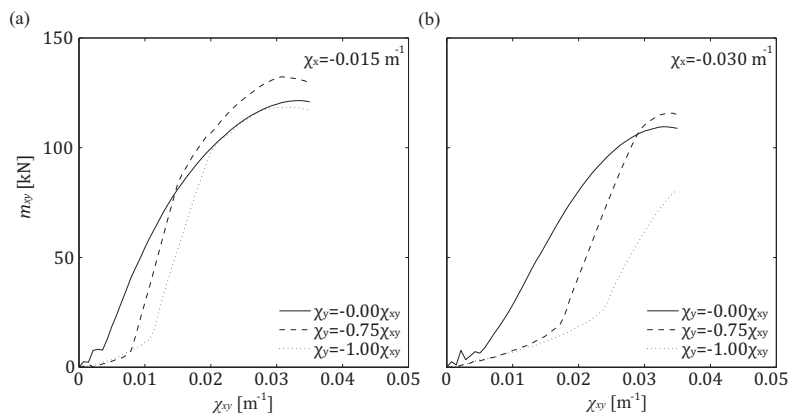


Figure 5.10: Moment-curvature diagram for torsional moments

## 5.4. Comparison

The analysis of the stiffness in combination with the finite element method is independent of the geometry and the boundary conditions of the slab. Therefore, any slab test could be used in order to verify the proposed model. However, since the main objective is to obtain the load-rotation curve of punching tests performed within this research, similar punching tests from literature were used in addition to the tests performed within this research in order to verify the numerical model. Additionally, the two boundary case regarding the flexural behavior, pure

bending and pure torsion, were investigated. Therefore, tests found in literature were used to compare the response of the tests specimens to the response predicted by the numerical model.

### 5.4.1. Pure bending

The first boundary case that was analyzed was pure bending. The investigated specimens were slab elements with dimensions of 4.00 m x 1.00 m tested by (Kenel and Marti 2001). The slab specimens were loaded symmetrically at each end and supported on two bearings at a distance of 0.60 m away from the center axis. Figure 5.11 shows the principal dimensions of the test set-up and the loading. The measurements that were compared are the force  $Q$ , which was applied at each side, and the displacement  $w$  that was measured at the load introduction point.

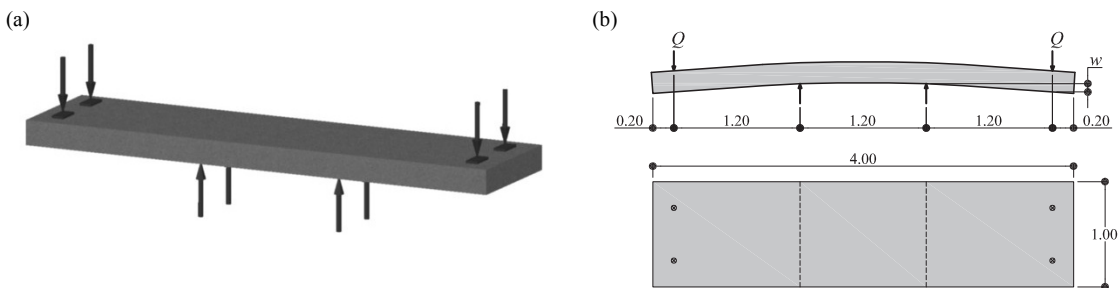


Figure 5.11: Dimensions and loading of the bending test specimens

Table 5.1 summarizes the main parameters of the test specimens. For all the slabs, the slab dimensions were constant (4.00 m x 1.00 m x 0.20 m). The investigated parameters were the compressive strength of the concrete (Specimen B3), the reinforcement ratio (Specimen B4) and the bar diameter of the reinforcement (Specimen B5). Since the test program treated main input parameters of the NLFEA such as the reinforcement ratio and the concrete strength, this test series is well suited for a comparison to the finite element calculations. Additionally, the measured crack spacing can be used to verify the assumed tension stiffening approach. For this, the measured crack spacing, as indicated in Table 5.1, was used for the comparison of these tests. In addition, the measured tensile strength was used instead of the calculated one.

Table 5.1: Parameters of bending test specimens from literature

Specimen	$h$ [mm]	$\rho_x$ [%]; ([mm])	$f_y$ [MPa]	$f_c$ [MPa]	$f_{ct}$ [MPa]	$s_{rm}$ [mm]
B1	200	0.31 (8 $\phi$ 10)	563	41.5	3.2	150
B3	200	0.31 (8 $\phi$ 10)	563	81.4	4.8	140
B4	200	0.16 (4 $\phi$ 10)	563	37.3	3.1	280
B5	200	0.31 (4 $\phi$ 14)	508	39.4	2.7	150

Figure 5.12 shows the measured and the calculated load-displacement curves of the four specimens. The two curves of the measured values correspond to the values obtained when the loading was halted to take measurements (higher load value) and when the manually performed deformation measurements were completed (lower load value). The comparison shows good agreement between the calculated and the experimentally obtained curves. Generally, the NLFEA predicts a slightly stiffer behavior before the yielding moment. After yielding, it somewhat underestimates the strength. This can be explained by the fact that it does not consider the strain hardening of the reinforcing steel properly (a small strain-hardening is implemented but only to prevent numerical problems) and that it neglects tension stiffening after yielding of the reinforcement. Despite these small differences, it can be noted that the behavior is calculated accurately for specimen B1, B3, and B4. The inaccuracy for specimen B5 is due to the asymmetry of the test performed. In fact, the displacements at one side were significantly larger than at the other side. Since the NLFEA uses a displacement controlled analysis with equal displacements at each side, the strength at yielding will be overestimated. However, the ultimate strength should be the same. This can also be seen in the diagram, at which for large displacements the experimentally obtained curves and the calculated curves converge.

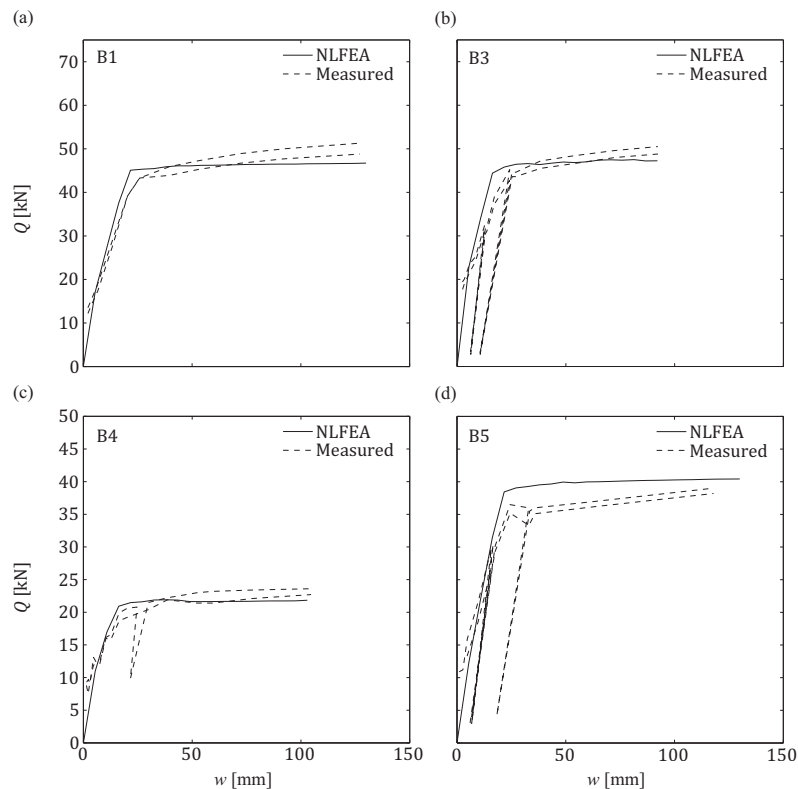


Figure 5.12: Measured and calculated load-displacement curves of the bending test specimens: (a) B1, (b) B3, (c) B4, and (d) B5

### 5.4.2. Pure torsion

The second boundary case investigated is pure torsion. The investigated specimens were square slab elements with a side length of 1.70 m, which were tested by Marti et al. (Marti et al. 1987). The forces were applied downwards on opposite corners of the slab. The slab was supported by two spherical bearings at the other two opposite corners. The introduced load as well as the reaction forces was distributed by a steel plate with dimensions of 0.150 m x 0.150 m x 0.025 m leading to a distance of 1.55 m between the load introduction point and the reaction point. The vertical displacement was measured at the load introduction and the reaction points. The measurements of the vertical displacements lead to the relative vertical displacement  $w$  of the slab, which relates to the non-displaced axis as shown in Figure 5.13.

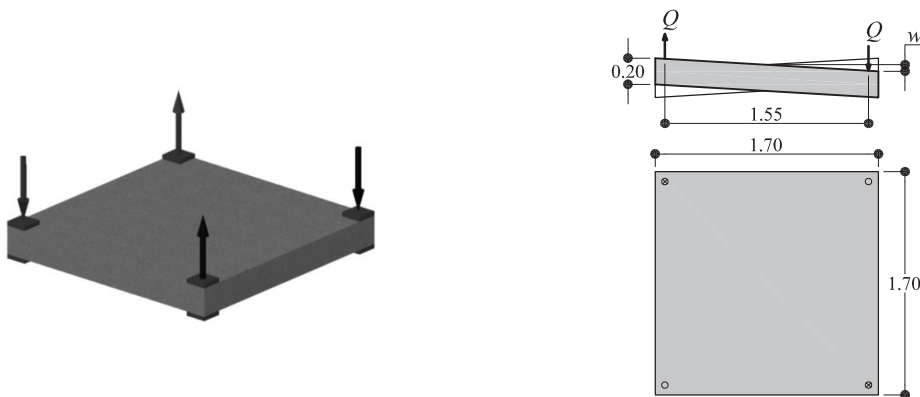


Figure 5.13: Dimensions and loading of the torsion test specimens

The investigated parameter was the reinforcement ratio whereas all the other parameters such as the slab dimensions were kept constant. Table 5.2 shows the main parameters of the test specimens. For the crack spacing, a value of half of the bar spacing was chosen, which corresponds to 50 mm for specimen ML2, ML3, and ML9 and 100 mm for specimen ML1 and ML7. These values were chosen in accordance to the picture of the specimens shown in the reference (Marti et al. 1987).

Table 5.2: Parameters of torsion test specimens from literature

Specimen	$h$ [mm]	$\rho_x = \rho_y$ [%]	$f_y$ [MPa]	$f_c$ [MPa]
ML1	200	0.25	551	46.7
ML2	200	0.50	551	36.2
ML3	200	1.00	481	37.5
ML7	200	0.25	479	44.4
ML9	200	1.00	479	44.4



Figure 5.14 shows the moment-displacement curves for the torsion tests. The NLFEA shows good agreement with the test results. The small difference in the slab response between the calculated and the measured values can be attributed to shear deformations that were not considered in the numerical calculation. Additionally, larger differences can be observed at the uncracked state. However, this can be explained by the step width of the calculation. Since the peak, at which the cracking moment is reached, lies between two calculation points, it is not accurately displayed. This problem could be overcome by using more dense calculation steps. Nevertheless, this part was neglected and the step width was kept as it is because the principal interest lies in the cracked behavior.

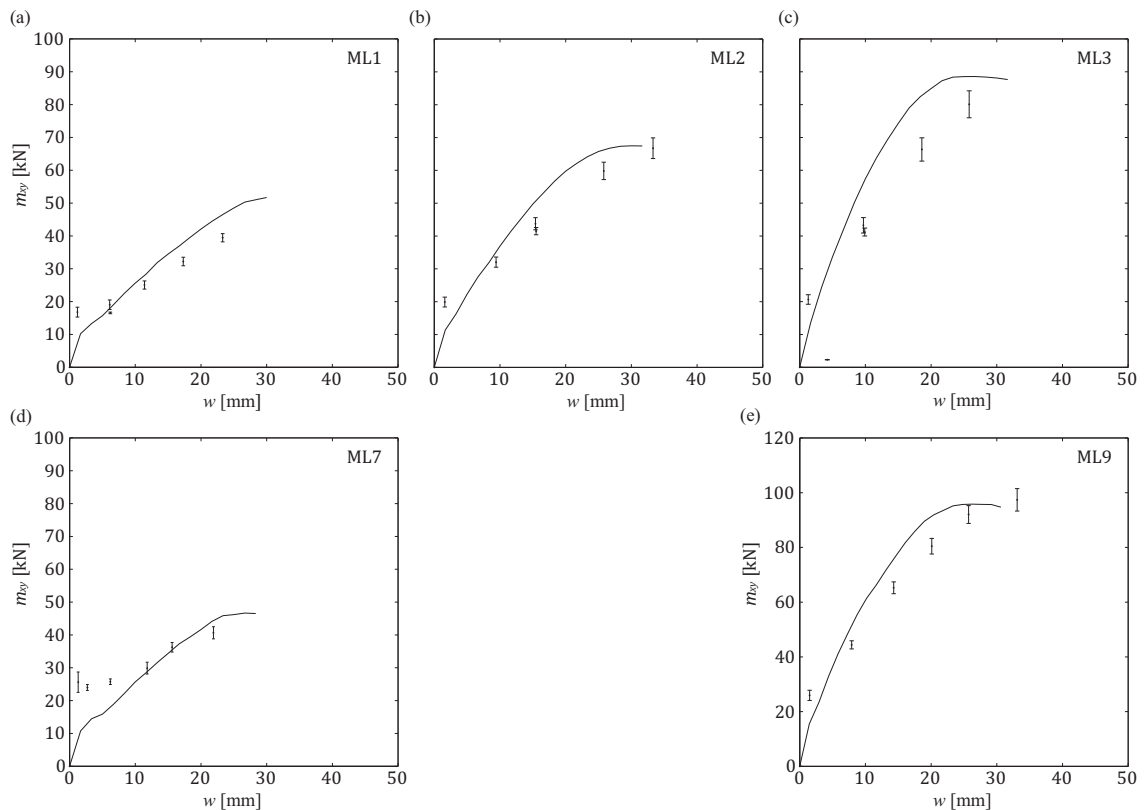


Figure 5.14: Measured (peak and end value of each load step) and calculated (continuous curve) moment-displacement curves of the torsion test specimens: (a) ML1, (b) ML2, (c) ML3, (d) ML7, and (e) ML9

### 5.4.3. Punching of slabs without shear reinforcement

From the two investigated boundary cases, it can be seen that the NLFEA delivers results that are in good agreement with the experimentally measured ones. This leads to the conclusion that the NLFEA should predict the behavior of punching tests accurately. In order to verify this expectation, punching tests of slab specimens without shear reinforcement found in literature (Guandalini and Muttoni 2004; Guidotti et al. 2009) and from tests within this research project were analyzed. Figure 5.15 illustrates the dimensions and the loading of the punching test specimens from literature.

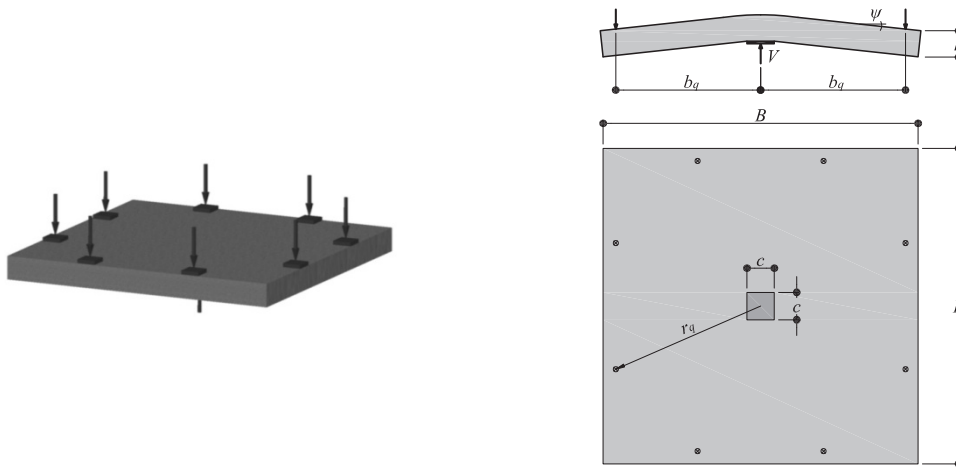


Figure 5.15: Dimensions and loading of the punching test specimens

Except for specimen PG3 (double in size), all test specimens had the same dimensions (3.00 m x 3.00 m x 0.25 m) and were supported by the same column size ( $c = 0.26$  m). The variable parameter is the flexural reinforcement ratio, which ranges from a rather low ratio of  $\rho = 0.25\%$  to a reinforcement ratio of  $\rho = 1.5\%$ . Table 5.3 presents the main parameters of the punching test specimens without shear reinforcement from the literature. All parameters as well as loading conditions of the punching test specimens within this research project (PL1-PL5) can be found in Chapter 3.

Table 5.3: Parameters of specimens without shear reinforcement of punching tests from literature

Specimen	$b$ [mm]	$h$ [mm]	$c$ [mm]	$b_q$ [mm]	$r_q$ [mm]	$\rho_x = \rho_y$ [%]	$f_y$ [MPa]	$f_c$ [MPa]
PG1 <sup>1</sup>	3000	250	260	1380	1505	1.50	573	27.7
PG2b <sup>1</sup>	3000	250	260	1380	1505	0.25	552	40.5
PG3 <sup>1</sup>	6000	500	520	2590	2846	0.33	520	32.4
PG4 <sup>1</sup>	3000	250	260	1380	1505	0.25	541	32.2
PG5 <sup>1</sup>	3000	250	260	1380	1505	0.33	555	29.3
PG19 <sup>2</sup>	3000	250	260	1380	1505	0.78	510	46.2

<sup>1</sup> (Guandalini and Muttoni 2004); <sup>2</sup> (Guidotti et al. 2009)

Figure 5.16 shows the measured and the calculated load-rotation curve of tests from literature. The calculations of all specimens show good agreement with the measured behavior. Only for low rotations, the stiffness will be slightly underestimated. This could be improved by using a finer mesh of the constitutive surfaces. However, since this phase is of less interest in this research, no further analysis of this phenomenon was performed. Additionally, one has to note that the loads in most cases are relatively small. Thus, the influence of shear deformation is small too.

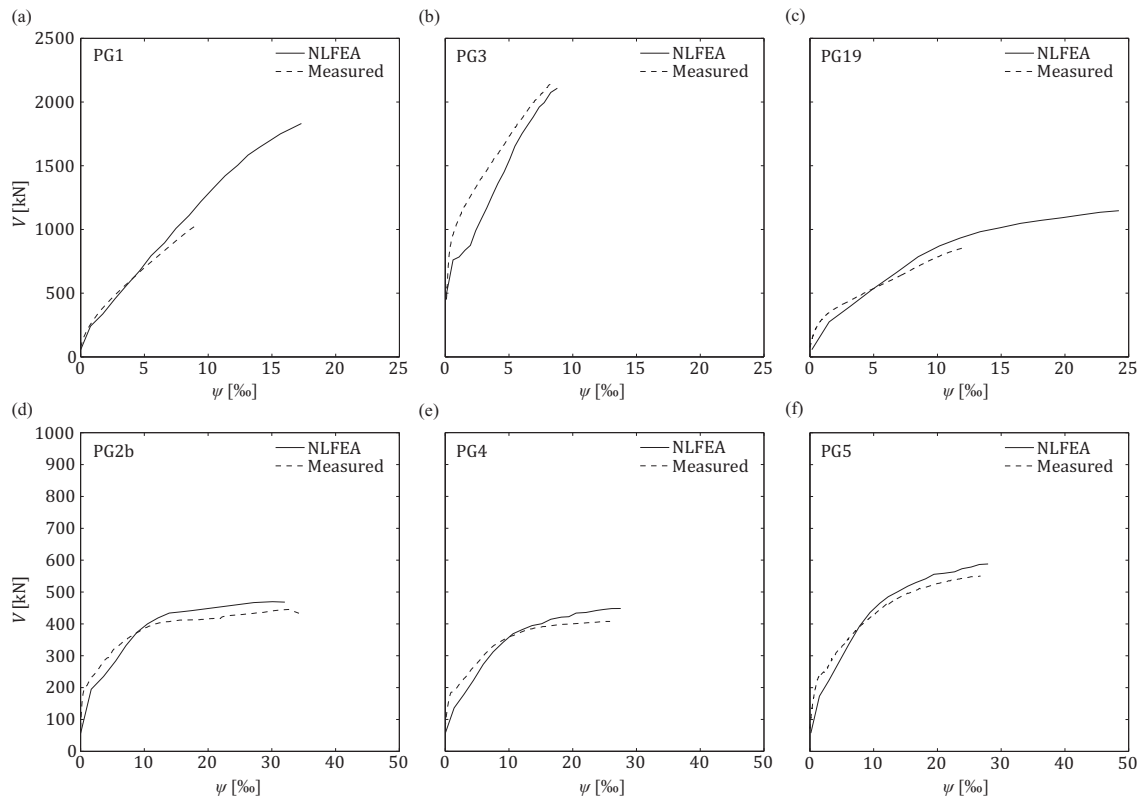


Figure 5.16: Measured and calculated load-rotation curves of the punching test specimens: (a) PG1, (b) PG3, (c) PG19, (d) PG2b, (e) PG4, and (f) PG5

Figure 5.17 shows the measured and the calculated load-rotation curve of tests within this research project of the specimens without shear reinforcement. Generally, the slab specimens behave similarly as the tests from literature presented previously and thus the calculated and measured behavior show a good agreement. However, due to the flexural reinforcement ratio of  $\rho_L = 1.5\%$ , they reach higher punching strengths than the tests from literature presented previously. This higher load level seem to influence the stiffness of the slab. Especially, in the cases with large shear forces (Specimens PL4 and PL5), the behavior predicted by the NLFEA is stiffer than the measured one.

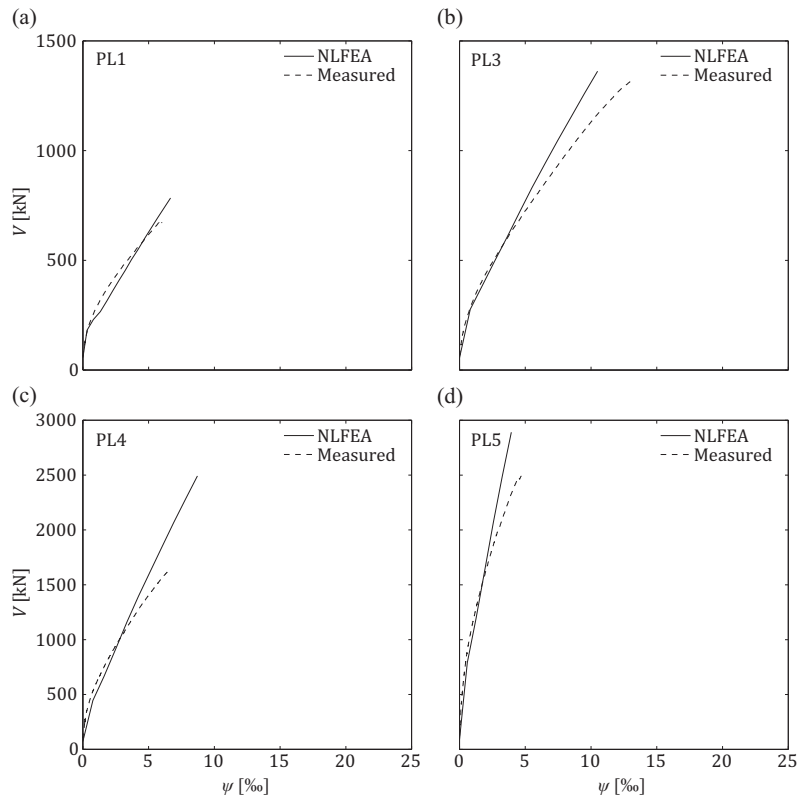


Figure 5.17: Measured and calculated load-rotation curves of the punching test specimens: (a) PL1, (b) PL3, (c) PL4, and (d) PL5

#### 5.4.4. Punching of slabs with shear reinforcement

Figure 5.18 and Figure 5.19 show the measured and the calculated load-rotation curve of tests within this research project of the specimens with studs and stirrups, respectively. As already seen for the specimens without shear reinforcement, the curves correspond well for lower shear forces. However, in the case of larger shear forces the slabs show a lower stiffness as already shown in Figure 5.17. Whereas the difference between the measured and calculated behavior for slabs without shear reinforcement is rather small, it becomes significant for slabs with shear reinforcement. Consequently, it is necessary to consider in the analysis the reduction in stiffness due to concentrated shear forces.

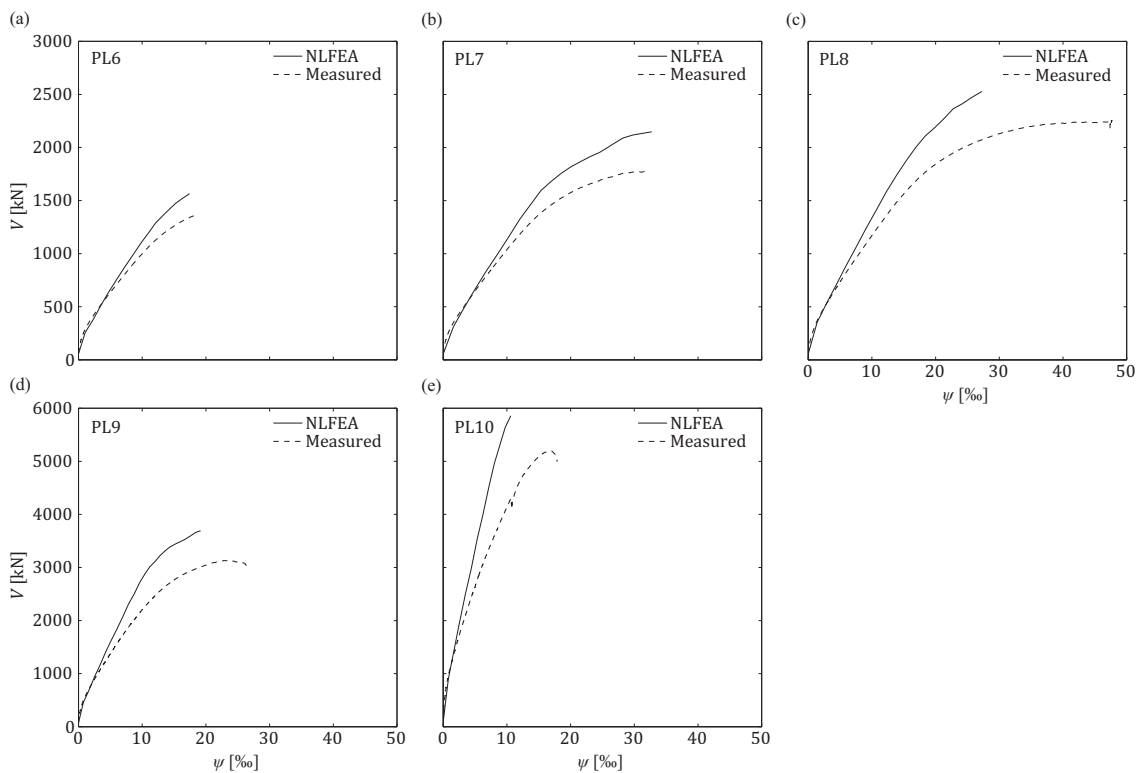


Figure 5.18: Measured and calculated load-rotation curves of the punching test specimens: (a) PL6, (b) PL7, (c) PL8, (c) PL9, and (e) PL10

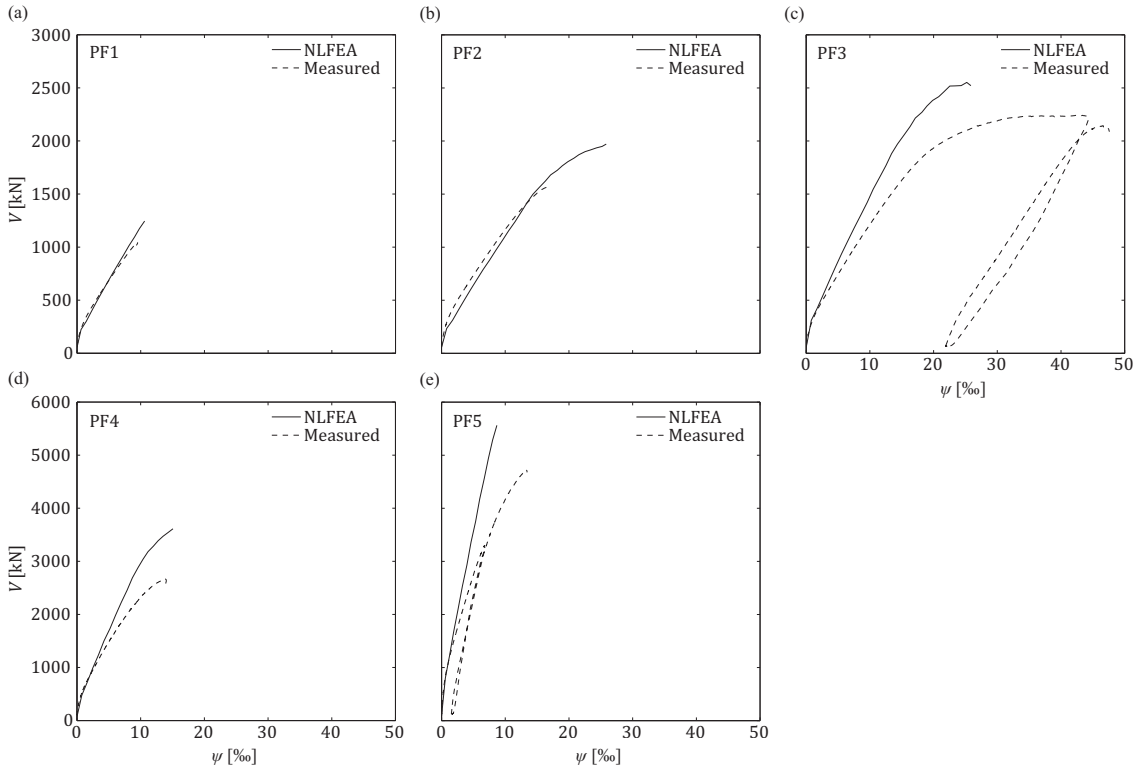


Figure 5.19: Measured and calculated load-rotation curves of the punching test specimens: (a) PF1, (b) PF2, (c) PF3, (d) PF4, and (e) PF5

As already illustrated in Chapter 4, the difference of the load-rotation curves for large shear forces is not only a problem of the NLFEA. Since other models such as the analytical Quadrilinear model (Muttoni 2008) neglect the influence of the shear forces on the flexural behavior, the same discrepancies occur (see Chapter 4). In fact, the calculated curves of the NLFEA and the Quadrilinear model (Muttoni 2008) show nearly the same behavior (Figure 5.20). Therefore, it is crucial to analyze the influence of the shear forces on the flexural stiffness in order to improve the existing models and the NLFEA.

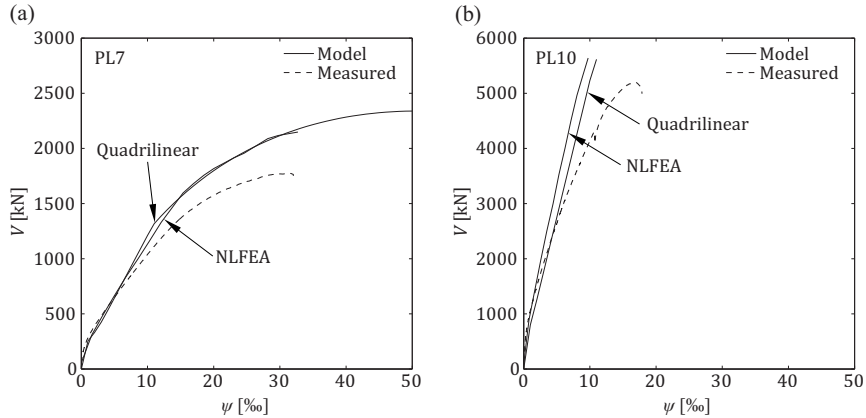


Figure 5.20: Comparison of the calculation model Quadrilinear (Muttoni 2008) and the NLFEA to the experimentally obtained load-rotation curve of specimens (a) PL7 and (b) PL10

In order to see whether the nonlinear finite element model is capable to predict the load-deformation response of the slab correctly when the influence of the shear force on the reduction of the stiffness is known, the longitudinal reinforcement ratio was reduced by the ratio of the measured flexural strength ( $V_{R,measured}$ ) to the calculated flexural strength ( $V_{flex,calc}$ ). By using a reduced flexural reinforcement ratio, a good agreement with the test results was obtained (Figure 5.21). Therefore, it is possible to estimate the global behavior of the slab accurately with the NLFEA, if local effects such as the reduction of the flexural stiffness due to the concentrated shear forces in the vicinity of columns are considered. However, it has to be noted that this is only applicable for the analysis of tested slab specimens by which the load-rotation response is known.

$$\rho_{red} = \frac{V_{R,measured}}{V_{flex,calc}} \cdot \rho \quad (5.22)$$

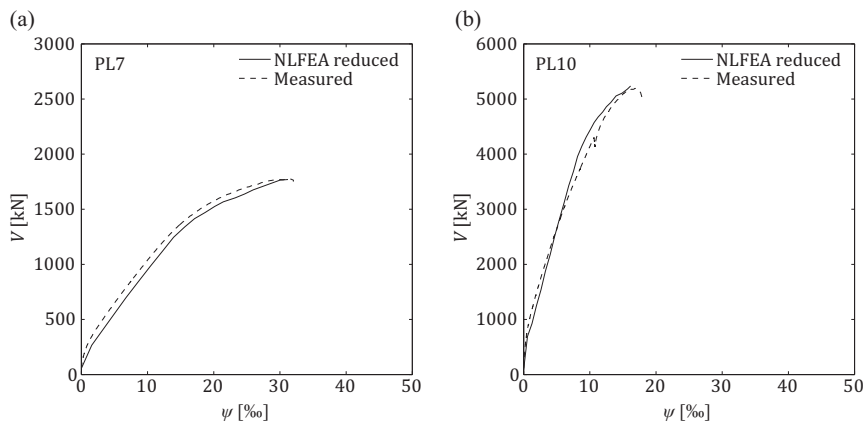


Figure 5.21: Load-rotation curve for specimen (a) PL7 and (b) PL10 calculated with a reduced flexural reinforcement ratio





## 6. Analysis of the Slab Response

As discussed in the previous chapter, the shear concentration at the vicinity of the column has a significant influence on the flexural behavior of the slab. Consequently, the interaction of moment and shear influences the slab behavior and thus needs to be considered in the analysis of the punching test specimens. In order to account for the influence of shear in the numerical model, the nonlinear finite element analysis (subsequently referred to as NLFEA) described in the previous chapter was combined with an existing finite element software which calculates in-plane deformations due to in-plane forces (subsequently referred to as jconc). It has to be noted that this method explained in this chapter is used to analyze the global and local behavior of the slab specimens separately. Neither one of this program is able to model the slab specimens correctly on its own. However, by combining the two programs, a good agreement with the actual measured behavior can be achieved with respect to the displacements and deformations leading to valuable insights in the slab behavior. Nevertheless, one has to distinguish between a global and a local slab behavior. Therefore, the comparison to the experimentally obtained measurements and the results of the analysis is divided into a global and a local part. Before these results are shown, the basis of the in-plane analysis tool will be briefly explained. For a more detailed description it is referred to literature (Fernández Ruiz and Muttoni 2007; Kostic 2009; Muttoni et al. 2011).

## 6.1. Analysis procedure

As mentioned previously, the NLFEA explained in Chapter 5 was combined with *jconc*, which is a two dimensional non-linear finite element analysis program that is used to analyse structure with respect to the in-plane forces. The program uses an elastic-plastic material behavior for steel and concrete whereby the maximum concrete strength is reduced to account for lateral tensile strains. Due to the fact that the program uses several assumptions such as that the principal strain directions coincide with the principle stress directions, it requires only few and well defined input parameter leading to a rather straightforward calculation. Despite its ease of application, it provides good predictions of the response of beams with shear reinforcements and walls (Muttoni et al. 2011).

The separate calculations of the global and local response were combined by certain input parameters as explained subsequently. Besides the geometrical and the material parameters, an additional parameter was introduced into the NLFEA in order to reduce the flexural stiffness. In fact, this introduced factor multiplies the amount of flexural reinforcement so that the stiffness changes. With this adjusted stiffness, the program calculates the global slab behavior leading to the slab deformations and to the internal forces. These forces serve as input parameter for the *jconc* analysis. Since *jconc* performs only in-plane calculation it is not capable to analyze a slab accurately. However, if only a short, thin cut of the slab along the axis is taken, the influence of out-of plane actions can be reduced. Therefore, a cut along the axis in the vicinity of the column was taken.

The length of the cut  $l_{cut}$  was chosen so that the slab portion between the center of the slab and the third row of shear reinforcement is modeled. This distance was chosen based on the assumption that after the third row of studs the influence of the shear forces is small, which corresponds to the experimental observations. The width of the cut  $w_{cut}$  was chosen as 100 mm at the column face and stepwise increased at the outer part accounting for the distribution of the shear forces. This leads to a slight overestimation in stiffness but since the main deformations in radial direction occur close to the column, this effect can be neglected. The moment and the shear force that were introduced at the end of the cut could be obtained by the NLFEA. The moment was determined at the end of the cut length and was introduced by a force-couple. The shear forces were determined near the column face at a distance of  $0.375d$  in order to avoid regions with numerical distortions resulting from the boundary conditions of the support, which was modeled using four point supports at the corner of the column. These shear forces were also applied at the end of the cut model.

Figure 6.1 presents the calculation method in more detail for the calculation at one applied displacement level. In a first step, the response of a slab element is calculated with the actual flexural reinforcement ratio. With the obtained stiffness, a nonlinear finite element analysis is performed. From the NLFEA, the shear force and the moment are extracted and introduced in the *jconc* (in-plane) analysis. The shear force and the moment are scaled by a factor  $\beta$ , which will be adjusted until the rotation obtained from the *jconc* analysis corresponds to the rotations

obtained by the NLFEA. This factor  $\beta$  defines the stiffness reduction factor  $\alpha$ , which describes the reduction in the stiffness by adjusting the flexural reinforcement ratio. Afterwards, a new NLFEA with the adjusted stiffness was performed. This procedure is repeated for certain times. For the calculations performed herein, the maximum number of iteration was set to  $i_{max} = 3$  leading to an acceptable convergence. Finally, the applied displacement is increased and the procedure starts from the beginning.

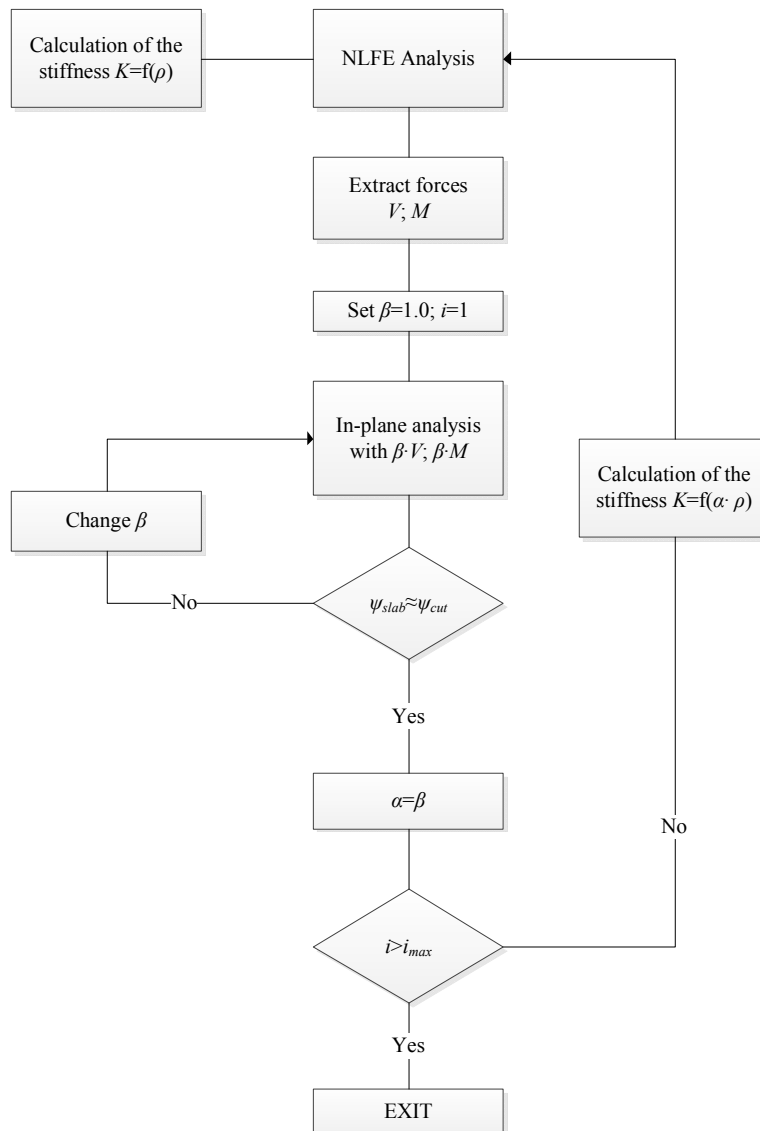


Figure 6.1: Flowchart of the interaction of the NLFEA and the in-plane analysis tool for the calculation at a certain load / displacement level

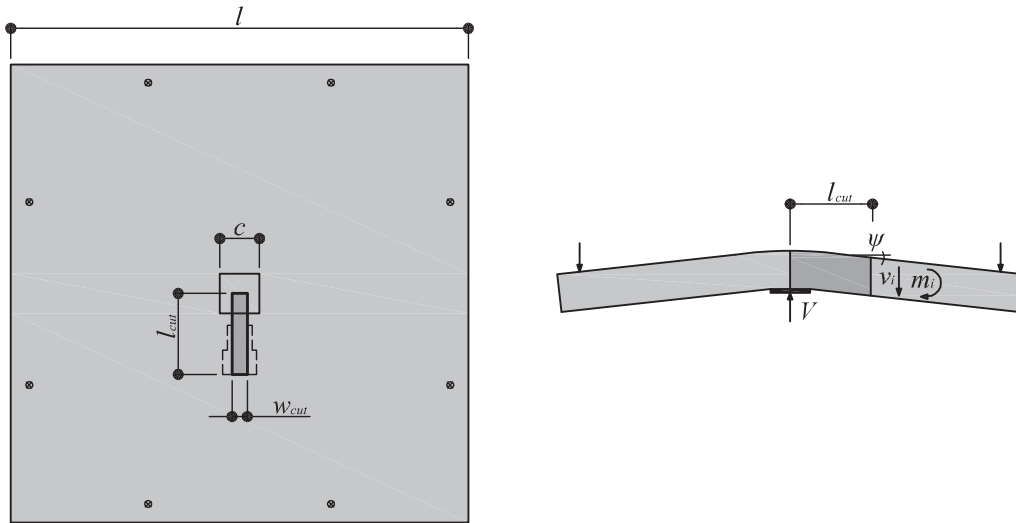


Figure 6.2: Plan view and section of the slab cut modeled in an in-plane analysis tool (jconc)

This method allows modeling the behavior of the slab near the column leading to the vertical in-plane stresses within the cut plane and the vertical deformations. By using the results from the calculation of the cut, one can calculate the rotation of the slab at the end of the cut. Since this rotation has to be the same as the one of the NLFEA at this point, the stiffness factor used in the NLFEA can be adjusted until both rotations are the same. If this calculation is performed for different applied displacements, one can obtain the global load-rotation relationship. Although this approach uses coarse simplifications and thus the results should be viewed with caution, it provides results that correspond well to the measurements from tests leading to valuable information regarding the global and local slab response.

Figure 6.3 shows the calculated and the measured load-rotation curve for specimens PL7, PL8, and PL9. It can be seen that the prediction of the load-rotation curve are in good agreement with the experimentally obtained behavior. However, it has to be noted that the stiffness reduction factor can only be calculated until yielding of the flexural reinforcement otherwise no equilibrium can be found for the cut model. Therefore, the factor was chosen constant for the calculation after yielding of the flexural reinforcement occurs. Generally, the adjustment factor is close to 1.0 for low load levels, thus nearly no change in stiffness exists. Afterwards, this factor decreases and reaches the minimal value when yielding occurs leading to a smaller stiffness and thus to a change in the behavior of the slab.

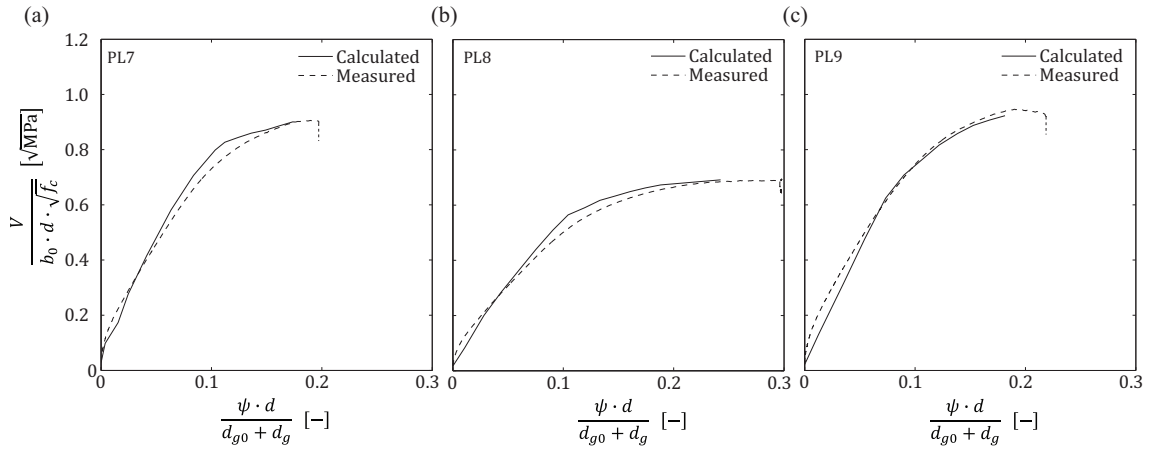


Figure 6.3: Measured and calculated load-rotation curve for specimen (a) PL7, (b) PL8, and (c) PL9

## 6.2. Global slab behavior

The global slab behavior was analyzed by the adjusted NLFEA. From these calculations, one obtained the state of deformations and the internal forces. These results were validated by the comparison to the experimentally obtained values. For this, the global behavior of slab PL7 was analyzed and is presented in detail subsequently. The calculations were performed at three states of deformation corresponding to the measured load of 60%, 75%, and 90% of the failure load. It has to be noted that the analysis was not performed at the same load level as the measured load but at the corresponding rotation in order to achieve the same state of deformation.

Table 6.1: Shear force, rotation, and vertical displacement at each investigated load level

Load Level	60%	75%	90%
Measured shear force $V$ [kN]	1060	1334	1585
Rotation $\psi$ [-]	0.103	0.144	0.20
Applied displacement $d_z$ [m]	-0.012	-0.017	-0.025

The comparison of the calculated to the experimentally measured deformations shows the performance of the NLFEA approach. For this comparison, the vertical displacements as well as the strains in radial and tangential direction on the bottom surface and in radial direction on the top surface were investigated for the three load cases. Figure 6.4 shows the calculated and measured values for the load stage of 60%  $V_R$ . The vertical displacements calculated with the NLFEA and Jconc correspond well to the experimentally obtained values. Differences occur only in the prediction of the shear deformations at the column face since they are not modeled in the NLFEA. With respect to the radial strains at the top surface of the slab (tension side), it can be noted that the measurements clearly depend on the crack opening and crack spacing. Since the NLFEA uses a smeared crack approach, these local strains cannot be modeled properly. However, if the average strains are considered, the NLFEA shows a good agreement. On the bottom surface of the slab (compression side), the NLFEA leads to a good agreement with the experimentally measured values. For this load case, the maximal strains are at around 2‰, thus close to the value of the peak strain of the assumed stress-strain relationship of the concrete.

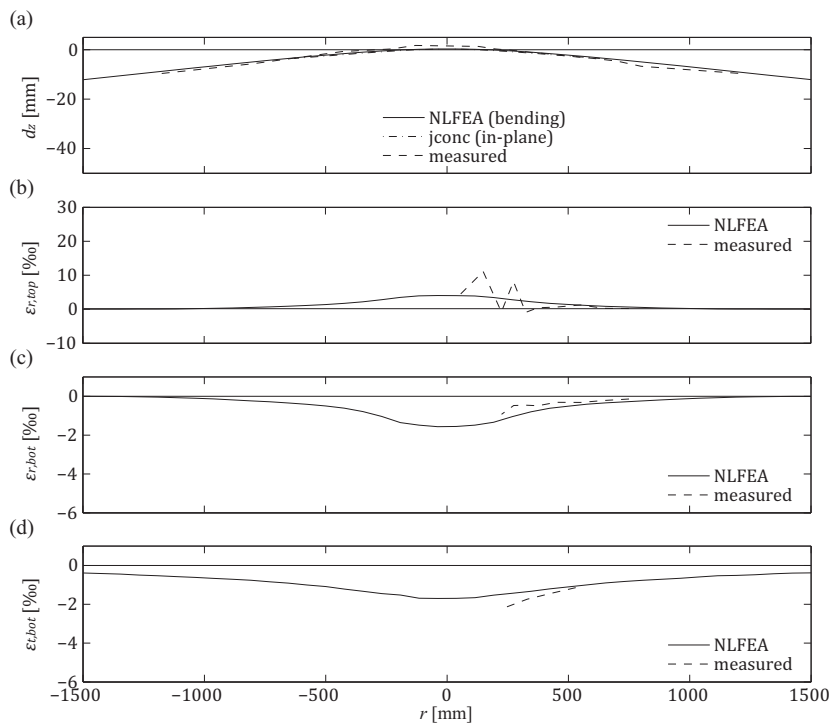


Figure 6.4: Comparison of the modeled and measured deformations along the axis for a load level of 60%  $V_R$ : (a) vertical displacements, (b) radial strains on the top surface, (c) radial strains at the bottom surface, and (d) tangential strains at the bottom surface

For the load case of  $75\%V_R$ , the calculated vertical displacements are again in a good agreement with the experimentally measured values (Figure 6.5). Although the measured radial strains on the top surface depend again on the cracking, the trend is well predicted by the NLFEA. On the bottom side, the predictions in radial and tangential direction correspond well with the measurements. It can be noted that at this load level the radial strains are stabilized, thus they do not increase with increasing load until failure occurs (see Chapter 3 and Figure 6.7). This stabilization is also well predicted by the NLFEA as it can be seen for the load level of  $90\% V_R$ .

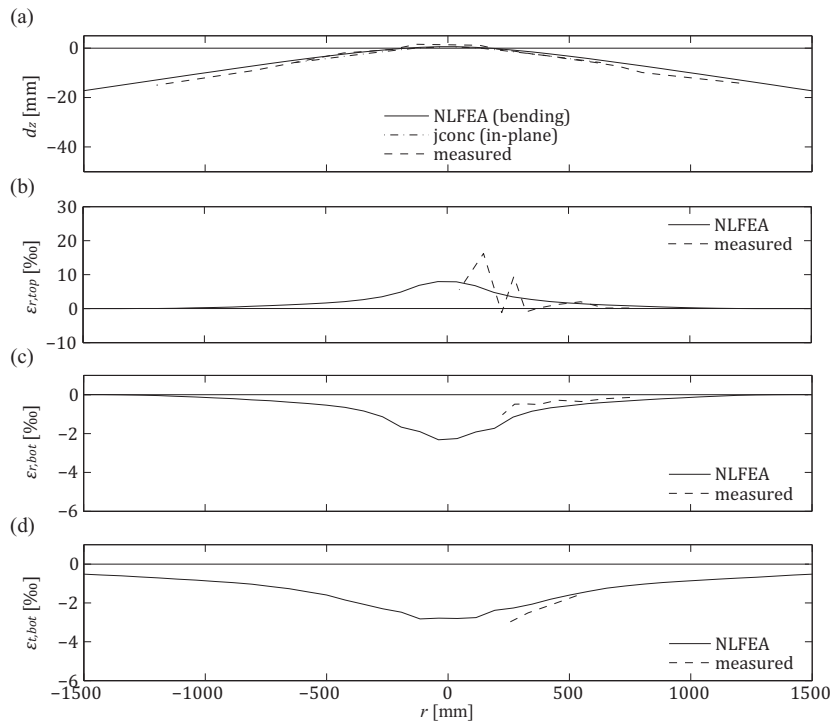


Figure 6.5: Comparison of the modeled and measured deformations along the axis for a load level of  $75\% V_R$ : (a) vertical displacements, (b) radial strains on the top surface, (c) radial strains at the bottom surface, and (d) tangential strains at the bottom surface

Similar to the previous load levels, the predicted and the experimentally obtained displacements and strains at the load level of  $90\%V_R$  are in good agreement (Figure 6.6). The calculated tensile strains in radial direction on the top surface correspond to the tendency of the measurements. However, due to the cracking, no definite conclusion can be drawn. The calculated compressive strains on the bottom side in radial, and especially in tangential direction, show an excellent agreement with the measurements. It has to be noted that the tangential strains are beyond the peak strain of the assumed stress-strain relationship of the concrete. Thus, it can be concluded that the softening of the concrete is properly modeled.

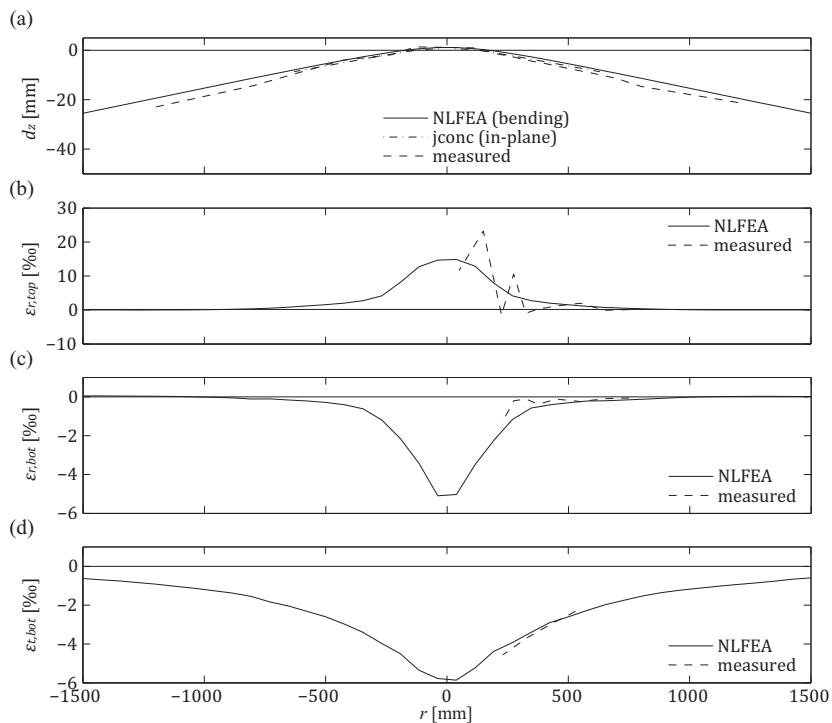


Figure 6.6: Comparison of the modeled and measured deformations along the axis for a load level of  $90\%V_R$ : (a) vertical displacements, (b) radial strains on the top surface, (c) radial strains at the bottom surface, and (d) tangential strains at the bottom surface



Figure 6.4 to Figure 6.6 showed that the calculated strains at the bottom side are generally in good agreement with the measured strains for the investigated load levels. In order to analyze the radial and tangential strains at the bottom surface in more detail, the load-deformation curves were calculated at the locations of the measurements and compared to the measured values. Figure 6.7a shows the radial strains measured at two locations at the bottom surface of the slab. It can be seen that the behavior of the strains can be accurately modeled. It is interesting to note that the numerical model, which considers only flexural behavior (bending and torsion), follows the curve of the strain measurements in radial direction ORI-00 although the strains decrease with increasing load at a certain load level. This stabilization and the decrease afterwards of the radial strain can thus be explained by the distribution of the radial curvature and radial moment. In other words, at a certain load level, the radial moment reaches its maximum value at this location and does not increase furthermore. The load level at which the change in behavior occurs is assumed to be at the point at which the yielding moment is reached at the column face. Afterwards, the moment cannot further increase at the column face. Additionally, due to the shear forces that define the difference in moment in radial direction, the moment distribution is given. This provides valuable information for the development of the analytical model presented in Chapter 7. Figure 6.7b shows the tangential strains at two locations at the bottom surface of the slab. It can be seen that the strains increase with increasing load. The same behavior is predicted by the numerical analysis. Although small differences between the measured and the calculated strains occur for strains near the column (OIT-03), the general behavior is well captured by the numerical model.

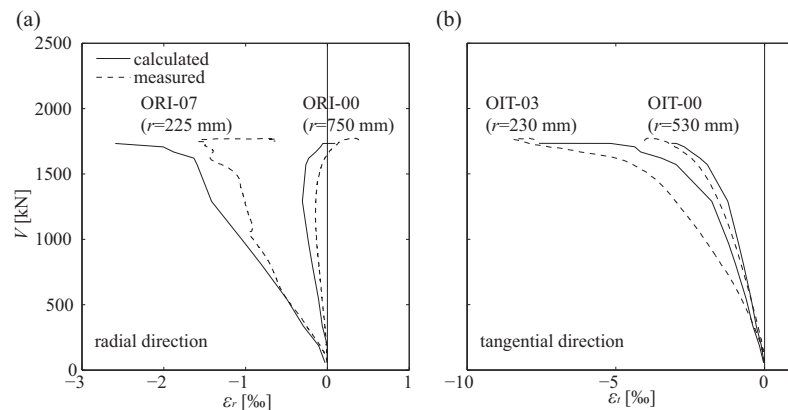


Figure 6.7: Calculated and measured load-deformation curves for specimen PL7 of surface deformations in (a) radial direction and (b) in tangential direction ( $r$ : distance to the center of the slab)

Since the calculated strains show generally a good agreement with the measurements, they were used to calculate the curvatures. Figure 6.8 illustrates the curvature in  $x$ -direction  $\chi_x$  for the three investigated load levels. As expected, the curvatures are the largest at the column face. With increasing load, the curvatures increase and are more distributed along the  $y$ -axis (tangential curvatures). In the  $x$ -direction (radial direction), the curvature decreases rapidly at the column face and are already at low levels at the mid-distance between the column and the slab edge.

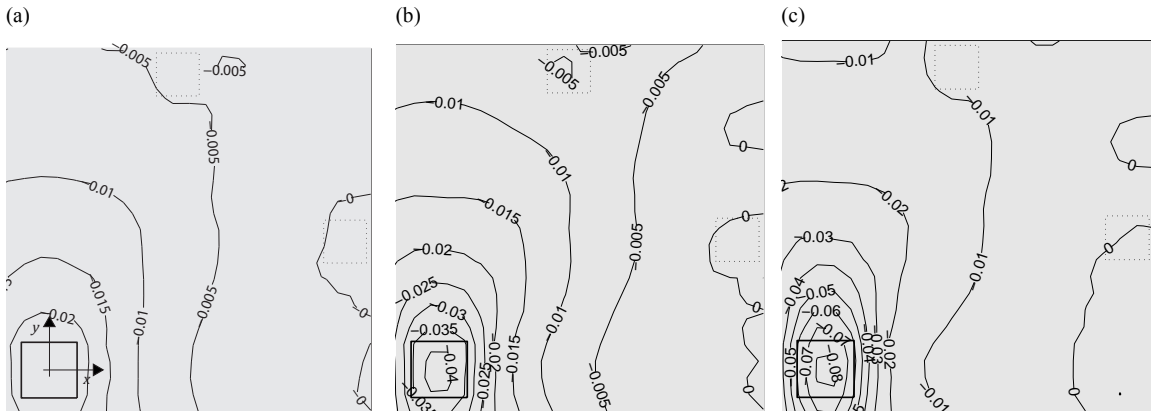


Figure 6.8: Distribution of the flexural curvature  $\chi_x$  (in  $\text{m}^{-1}$ ) for load levels of: (a) 60%  $V_R$ , (b) 75%  $V_R$ , and (c) 90%  $V_R$

Figure 6.9 illustrates the distribution of the twisting curvature  $\chi_{xy}$  for the three investigated load levels. As one can expect, the twisting curvature is the largest at the point between the load introduction points and the column and zero along the  $x$  and  $y$  axis. With increasing load, the curvature increases at the corners of the column. The presence of twisting curvatures close to the slab edge leads to the conclusion that this part of the slab somewhat stiffens the overall slab behavior.

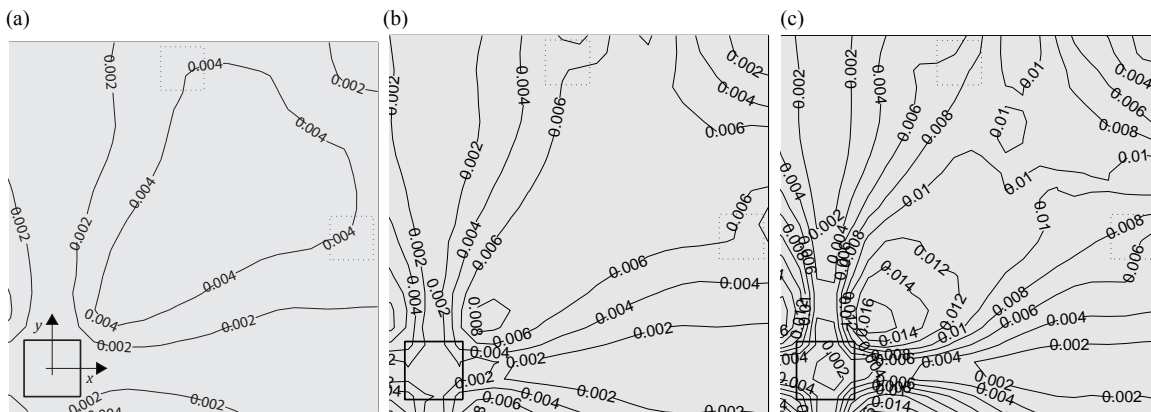


Figure 6.9: Distribution of the torsional curvature  $\chi_{xy}$  (in  $\text{m}^{-1}$ ) for load levels of: (a) 60%  $V_R$ , (b) 75%  $V_R$ , and (c) 90%  $V_R$

A cut along the x-axis provides more detailed information about the development of the radial and tangential curvatures and moments. Thus, Figure 6.10 shows the radial and the tangential curvatures and moments along the axis for the three investigated load levels (60%  $V_R$ , 75%  $V_R$ , and 90%  $V_R$ ). Generally, it can be noted that the radial curvature is maximal close to the column face and it decreases rapidly until it reaches the value zero at the slab edge. In contrast, the axial distribution of the tangential curvature is somewhat flatter. Especially, for the lowest investigated load level, the tangential curvatures are nearly evenly distributed. This is mainly due to the fact that the yielding strength was not obtained at a load level of 60%  $V_R$ . At the load level of 75%  $V_R$ , the radial as well as the tangential moments reached the flexural strength. Although plastic redistribution of the moments took place in tangential direction, the curvatures were still at moderate levels. The radial moment distribution is similar to that of the previously shown load level of 60%  $V_R$ . However, due to the yielding of the flexural reinforcement, the radial curvature has increased. At the load level of 90%  $V_R$ , it can be noted that while the radial moment distribution does not significantly change in comparison to the lower load levels, the tangential moment reaches the flexural strength at a large portion of the slab. Additionally, the radial and tangential curvatures increase significantly due to the yielding of the reinforcement.

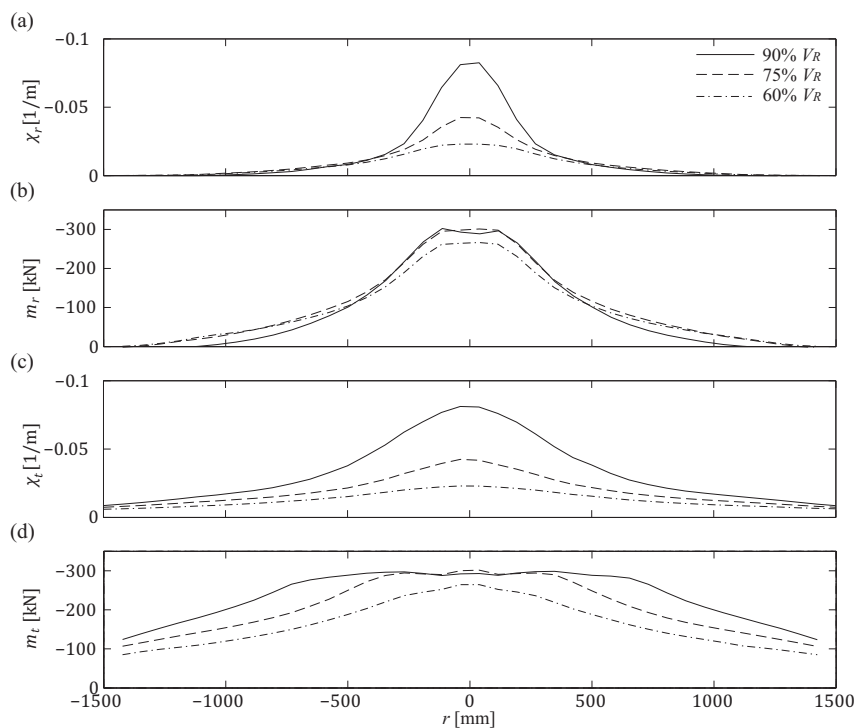


Figure 6.10: Calculated curvatures along the axis for a load level of 60%  $V_R$ : (a) radial curvature, (b) radial moment, (c) tangential curvature, and (d) tangential moment

The axial sections clearly show the plastic moment distribution and thus they indicate the difference between a linear-elastic and a nonlinear analysis. This difference can also be seen by comparing the curvature and the moment distribution in the first principal (tangential) direction as well as from the comparison of the shear fields of a linear-elastic and a nonlinear analysis. Figure 6.11 illustrates the results of a linear-elastic and nonlinear calculation. Since the calculations were performed at the same shear force level ( $90\% V_R$ ), the curvatures are much smaller in case of the linear-elastic calculation than in the case of a non-linear calculation. The linear-elastic calculation leads to evenly distributed moments and curvatures with a decrease in the direction of the slab corners. In contrast, the non-linear calculation leads to a distribution of the moments that is largely influenced by the layout of the orthogonal reinforcement. The tangential moments concentrate along the axis of the slab where the slab reaches its flexural strength. This moment distribution leads also to a difference in the curvature distribution compared to the linear-elastic analysis. The same phenomenon can be seen in the analysis of the shear fields. The shear forces follow much more the orthogonal reinforcement layout in the case of a nonlinear calculation than in the case of a linear-elastic calculation.

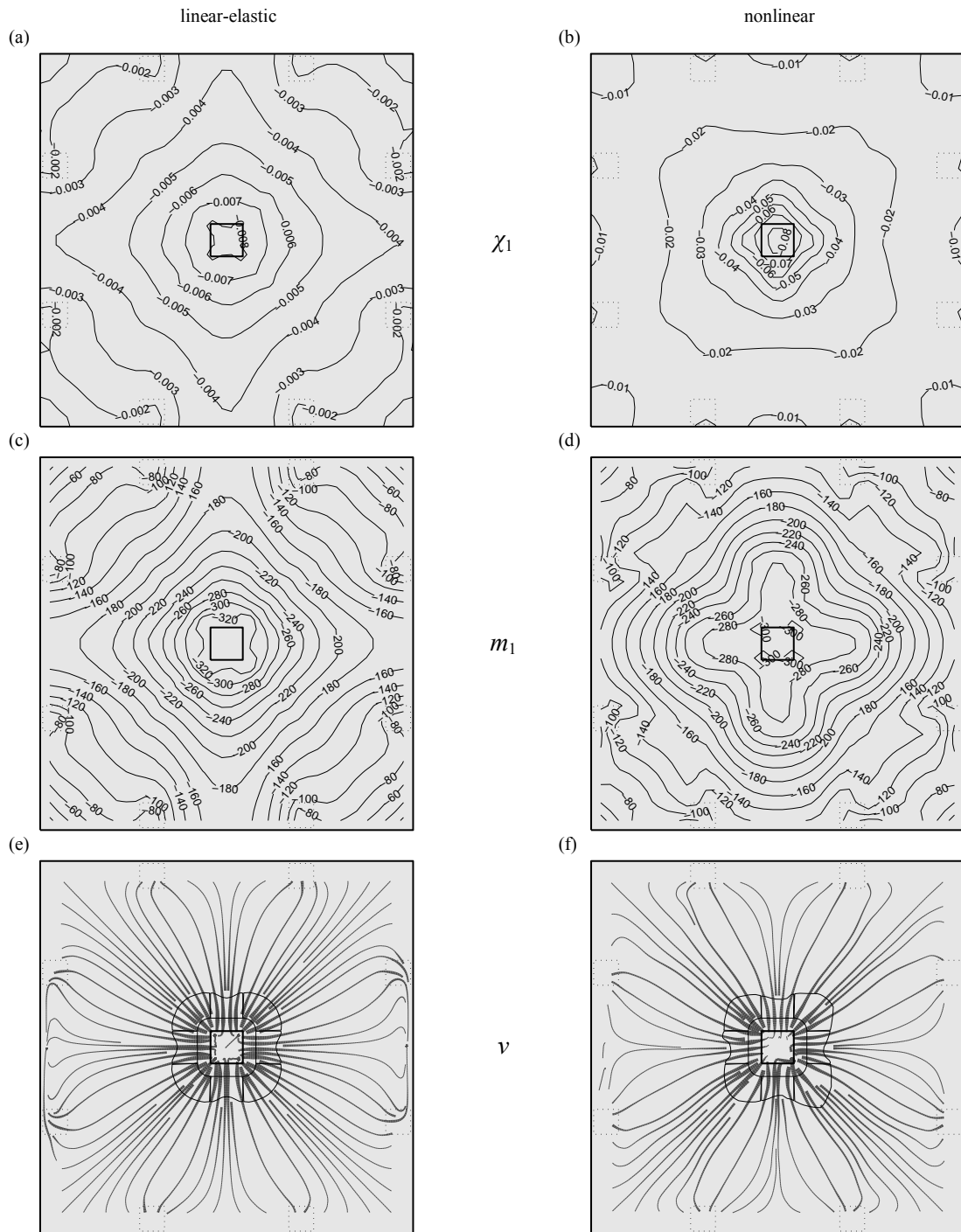


Figure 6.11: Distribution of the curvature  $\chi_1$  (a,b) and the moment  $m_1$  (c,d) in the first principal (tangential) direction and shear fields including shear distribution along the control perimeter (e,f) for a linear-elastic (a,c,e) and a nonlinear calculation (b,d,f)

### 6.3. Local slab behavior

By using the results of the jconc calculations, one can analyze the local slab behavior at the vicinity of the support area. Besides the in-plane stresses obtained by jconc, the moment was calculated by the integration of the horizontal stresses along several vertical sections. Additionally, the stresses in the flexural reinforcement and the strains in the shear reinforcement were analyzed. Figure 6.12 to Figure 6.14 show the analysis of the local slab behavior for load levels of 60%  $V_R$ , 75%  $V_R$ , and 90%  $V_R$ .

With respect to the general behavior it can be noted that at the load level of 60%  $V_R$ , the stresses are generally low, only at the outermost fiber at the compression zone and at the anchorage zone of the first and second stud the stresses are close to the concrete strength. With further increase of the load, the stresses at these zones grow. Additionally, a clear path of the load transfer can be seen. A portion of the load is taken by the first stud and directly transferred to the column face. The load transfer of the second row of studs can be described as a compression strut that is deviated at the first row of studs. In other words, the load descends from the second row in a rather steep angle to the first row of studs. At this point, a portion of the load is transferred to the first row of studs. The rest of the load is transferred by a slightly inclined compression strut to the column face. This is in agreement with the strain measurements in the studs discussed in Chapter 3. It was presented that the sum of the forces calculated based on the strain measurements on the top part of first and second row of studs exceeds the total measured shear force. This indicates that a certain amount of the load in the second row of studs has to be transferred to the first row of studs.

At the load levels of 75%  $V_R$  and 90%  $V_R$ , the general behavior does not significantly change. However, the plot of the relative stresses clearly shows the development of the failure zone at the compression strut between the first stud and the column. The maximum relative stresses are first reached at the intersection of the first stud and the flexural reinforcement before the failure zone propagates towards the column face. Additionally, large compressive stresses occur at the bottom side of the slab near the column face.

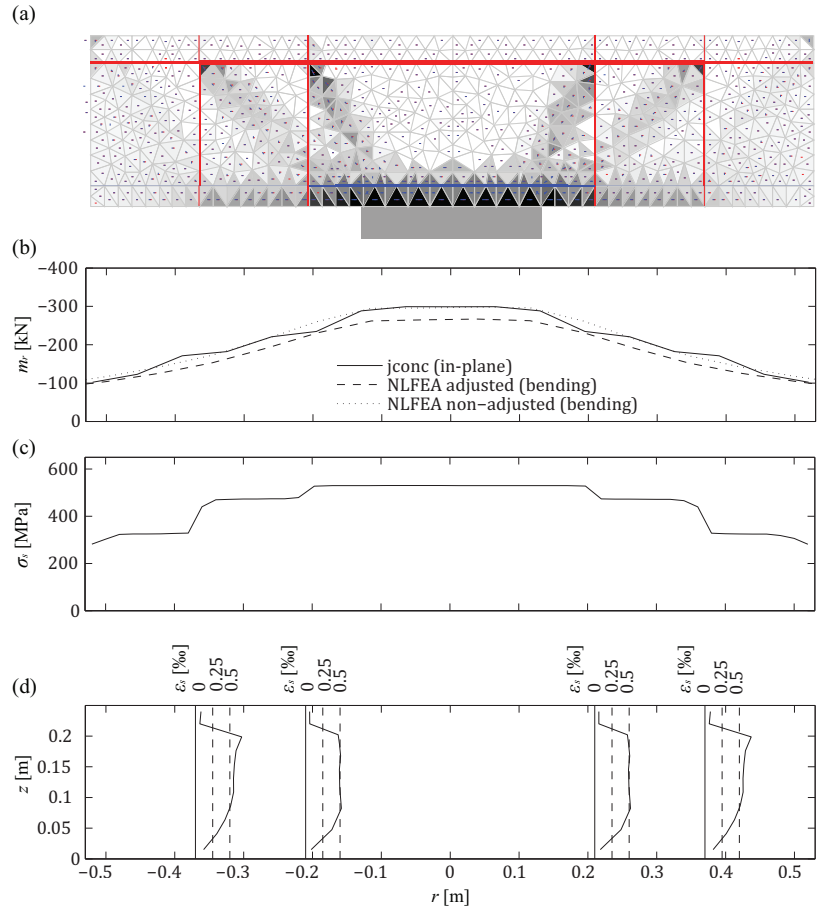


Figure 6.12: Local behavior at the load level of 60%  $V_R$ : (a) shear transfer, (b) radial moment, (c) stresses in the flexural reinforcement, and (d) strains in the shear reinforcement

With respect to the stresses in the top reinforcement and to the moment calculated by the horizontal concrete stresses and the forces in the bottom reinforcement, it can be noted that the yielding strength of the flexural reinforcement is reached between load level 60% and 75%. However, more interesting to note is that yielding of the flexural reinforcement occurs only between the studs in the first row. Since the compression strut is rather steep, the moment decreases rapidly between the column face and the first stud. This effect is not considered in the NLFEA leading to a flatter moment curve. At the intersection point of the first stud and the flexural reinforcement, the stresses in the flexural reinforcement decrease. This effect can be explained by the compression strut that adds forces to the inner part of the reinforcement. Therefore, the stresses outside the first row of stud are reduced.

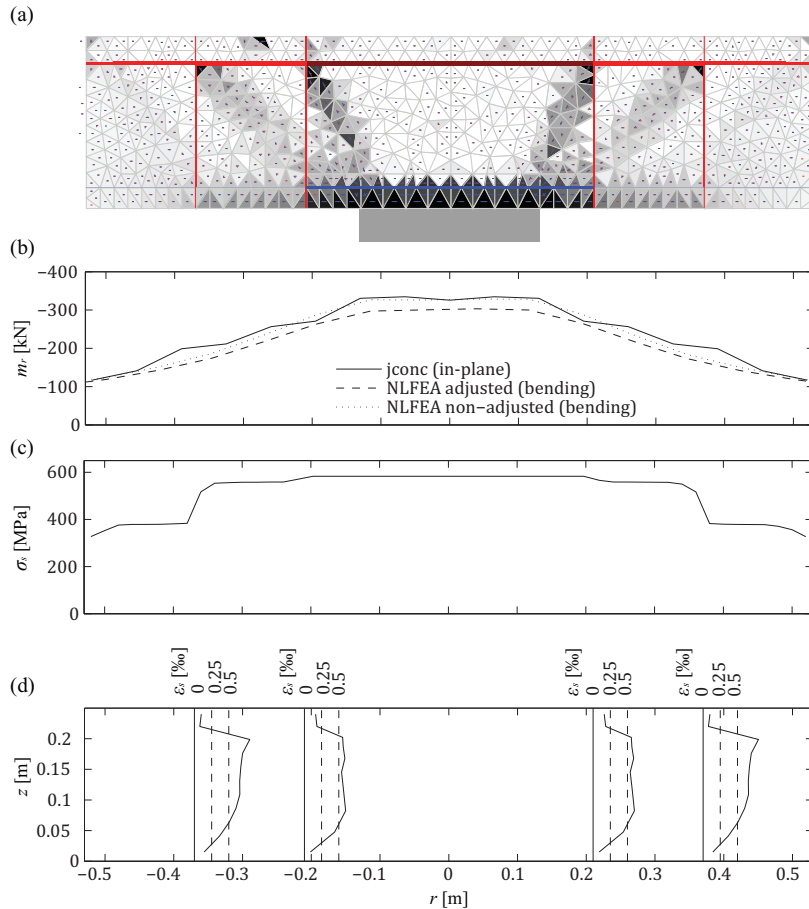


Figure 6.13: Local behavior at the load level of 75%  $V_R$ : (a) shear transfer, (b) radial moment, (c) stresses in the flexural reinforcement, and (d) strains in the shear reinforcement

Unlike the analysis of the flexural reinforcement, the calculated strains of the transverse reinforcement have to be regarded with reservations. Since the strains in the studs mainly depend on the shear cracks and the bond conditions, which both are not properly considered in the calculation, the results do not resemble the effective strain distribution accurately. Nevertheless, the calculated values show a qualitative behavior leading to certain general conclusions. It can be noted that the calculated average strains are much less than the yielding strains ( $\epsilon_y \approx 2.5\%$ ). Additionally, it can be seen that the first and the second row of studs exhibit nearly the same strains. Thus, they transfer nearly the same amount of force. This corresponds to the strain measurements on the top end of the first and second row of studs (refer to Figure 3.20).



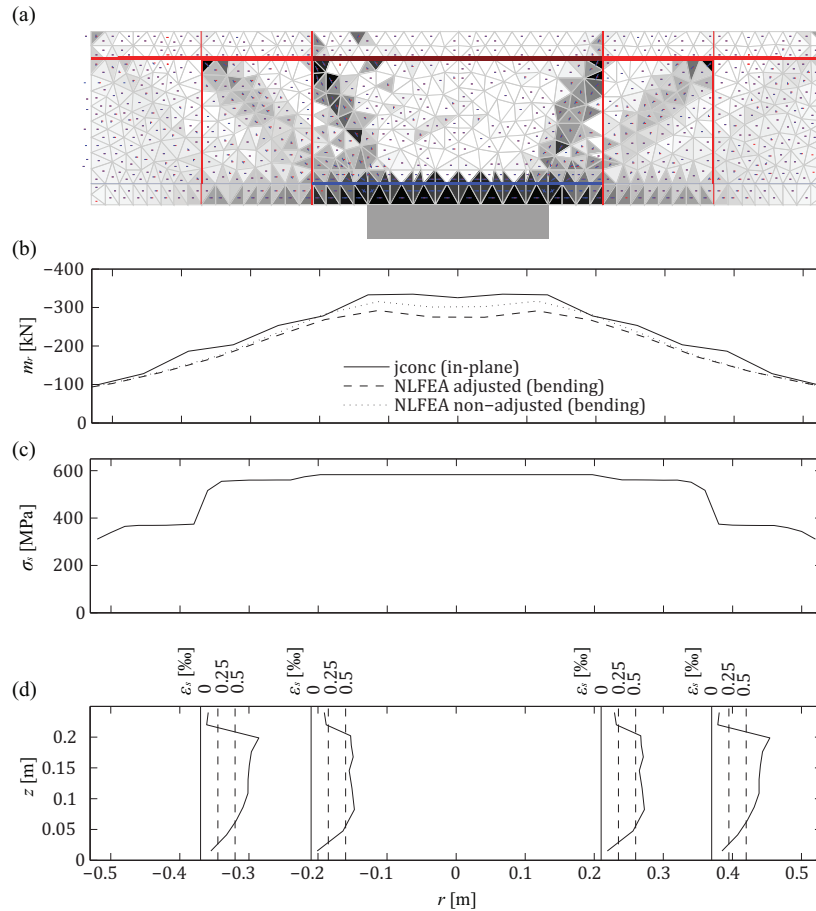


Figure 6.14: Local behavior at the load level of 90%  $V_R$ : (a) shear transfer, (b) radial moment, (c) stresses in the flexural reinforcement, and (d) strains in the shear reinforcement

The herein discussed shear transfer at the column vicinity shows also a good agreement with the experimentally obtained cracking pattern. Figure 6.15 illustrates the cracking pattern observed at the saw-cut after failure overlaid by the results of the calculation at a load level of 90%  $V_R$ . Especially at the right-hand side, the cracks indicate a similar behavior as predicted by the numerical calculation. The calculated compression strut from the second row of studs seems to follow the cracks in this area. Similarly, the calculated concrete strut from the first stud to the column face corresponds to the experimentally observed cracking pattern. Moreover, the numerical analysis predicts basically two failure areas: one at the bottom surface close to the column and one close to the top surface at the intersection of the stud and the flexural reinforcement. Again, both failure zones can be seen at the cracking pattern. At the bottom surface, the concrete is spalling. However, it has to be noted that although the calculated radial strains are not small, the spalling seen in the test results from the large tangential strains near the column face, which are not modeled in jconc. At the intersection between the flexural reinforcement and the first stud, crushing of concrete occurs at a large area due to lateral tensile strains. This corresponds to the predicted behavior of the numerical calculation. Thus, the local model helps to understand qualitatively the behavior of the slab in the vicinity of the column.

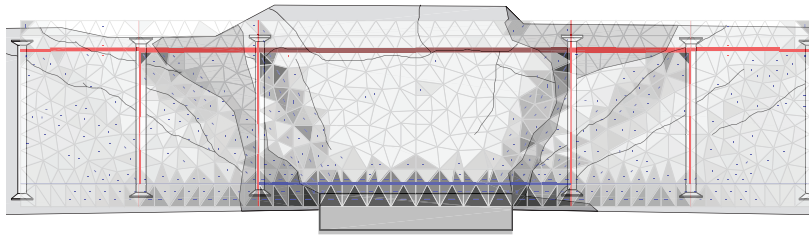


Figure 6.15: Calculated stresses at a load level of 90%  $V_R$  overlaid by the experimentally observed cracking pattern

Since the global and the local model showed good agreement to the experimentally observed and measured behavior, the results help to understand the actual response of the slab. However, the calculations are based on rather coarse simplification and thus the application of this approach is limited to the investigation of tested slab specimens. For the prediction of the slab response, a more applicable approach is desired. In the following chapter, an analytical model will be presented with which the load-rotation response of slabs can be easily predicted. Additionally, formulations for failure criteria enable the estimation of the punching strength and rotation capacity.

## 7. Development of an Analytical Model

The experimental observation and the results of the numerical analysis of the tests performed within this research provide valuable information regarding the slab behavior and failure mode. Based on these findings, an analytical model was developed allowing a simplified calculation. Since the punching strength strongly depends on the state of deformation, the analytical model should consider the load as well as the slab deformation. Thus, the model is based on the CSCT which defines the punching strength as a function of the slab rotation. However, the experimental and numerical investigation revealed that several additional aspects should be considered in the analytical model. With respect to the load-rotation response of the slab, it was shown that the current Quadrilinear model (Muttoni 2008) predicts a stiffer load-rotation response compared to the experimentally observed behavior. Thus, the model should enable more accurate predictions of the load-rotation response of slabs.

An improved load-rotation prediction necessitates also a change of the failure criteria in order to provide similar or even better predictions for the punching strength and rotation capacity than the existing formulation. With respect to the failure within the shear-reinforced area, the model should be based on the mechanical approach of the CSCT (Fernández Ruiz and Muttoni 2009) since it showed good agreement with test results. However, the calculations for validation were performed using a smeared shear reinforcement approach. Therefore, the proposed model should enhance the applicability of calculations using the actual location of the shear reinforcement by considering the load transfer path in the column vicinity. With respect to the failure of the concrete strut, the basic hypothesis of the CSCT that the strength of the compression strut depend on the transverse strains and thus are related to the state of deformation should also be applied in the new model. However, additional parameter such as the amount of compression at the column face or the spacing of the shear reinforcement should be implemented to improve the prediction for example in the case of small column sizes.

The development of the analytical model presented within this chapter begins with the assumed slab behavior and the kinematics in the vicinity of the column. Afterwards, equations will be derived to estimate the slab behavior and to determine the failure mechanism. Finally, several parameters required for the calculation will be derived and discussed. A numerical example of the calculation procedure is shown in Appendix B.

## 7.1. General slab behavior

As already discussed in Chapter 2, an analytical approach necessitates an axisymmetric slab specimen. Therefore, the derivation of the slab behavior was performed for an axisymmetric case. The required parameters for the transformation from an axisymmetric to a square slab identical to the tested specimens are presented in the next chapter. Additionally, it can be noted that the proposed approach is based on the CSCT (Fernández Ruiz and Muttoni 2009) and the Quadrilinear model (Muttoni 2008). Thus, the model considers that the punching failure depends on the deformation of the slab. Therefore, a crucial aspect is to define the load-rotation response of the slab.

The basis of such an approach results from the model of Kinnunen and Nylander (Kinnunen and Nylander 1960) in which it is assumed that the slab is divided into two parts separated by a shear crack (Figure 7.1a). Additionally, it is assumed that the outer part deforms following a conical shape with a constant slab rotation. Based on this approach, Muttoni (Muttoni 2008) derived a formulation to obtain the shear force as a function of the slab rotation by defining the equilibrium condition at the outer slab segment and by using a quadrilinear moment-curvature relationship (refer to Chapter 2).

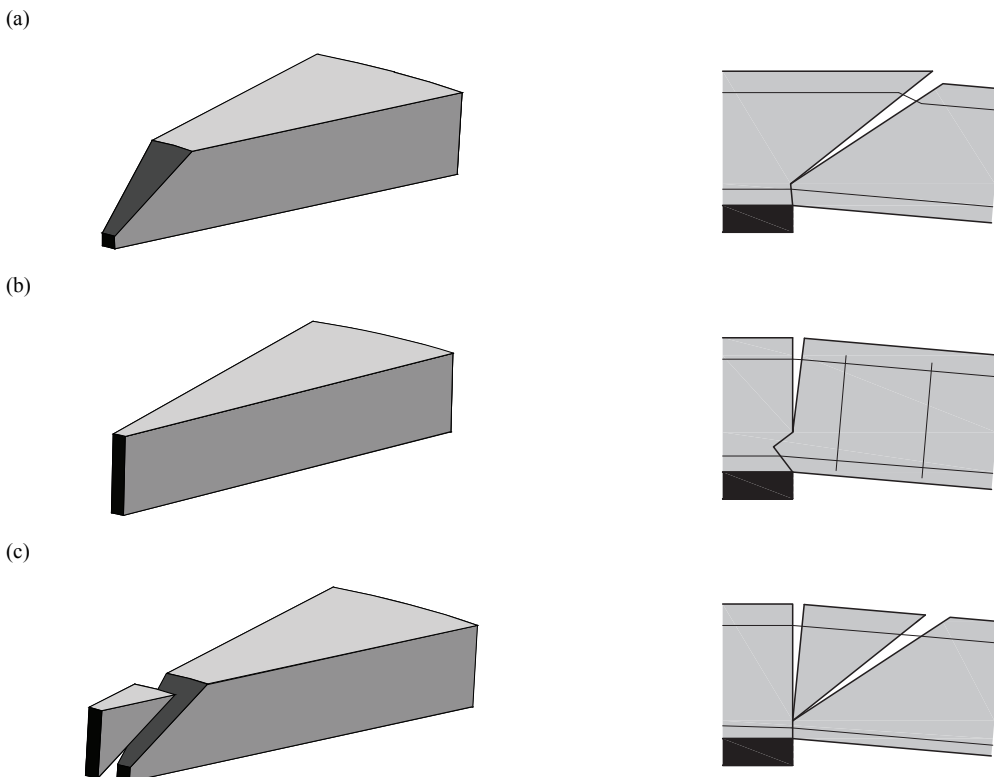


Figure 7.1: Simplified slab behavior proposed by previous research: (a) Kinnunen and Nylander (Kinnunen and Nylander 1960), (b) Andersson (Andersson 1963), and (c) Shehata and Regan (Shehata and Regan 1989)

In presence of shear reinforcement, this general approach has to be somewhat changed. Andersson (Andersson 1963) proposed to change the shear crack to a flexural crack that opens at the column face (Figure 7.1b). This approach was adopted and further developed by Gomes (Gomes and Regan 1999a). He used an approach for slabs without punching shear reinforcement proposed by Shehata (Shehata and Regan 1989) who introduced an additional shear crack dividing the slab into three parts namely a column part, a wedge, and an outer segment. However, Gomes (Gomes and Regan 1999a) assumed that the whole slab except the column part rotates as a rigid body leading to a similar global slab model as the model proposed by Andersson (Andersson 1963).

The model proposed within this research project and presented subsequently relies on similar principles as the aforementioned models. The main concept of the proposed model is the distinction between a global and a local behavior. The local behavior concerns the shear-critical region in the column vicinity that is separated to the outer slab segment by an outer shear crack. The inner part is itself separated by a step crack leading to a slab element over the column and to a wedge element (Figure 7.2). The global and the local part can be combined by the equilibrium and compatibility conditions at the outer shear crack area (subsequently referred to it as intersection plane).

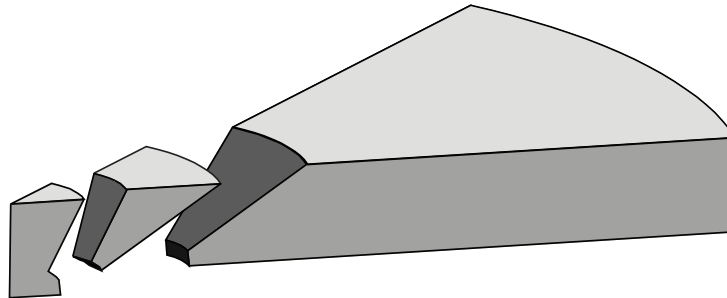


Figure 7.2: Slab divided into three parts: Column part, wedge, and outer slab segment

With respect to the local behavior in the vicinity of the column, the proposed model is based on the experimental observations and the numerical model. Figure 7.3a illustrates the assumed deformed shape in comparison to the undeformed shape. It is assumed that the rotations are performed within an area exceeding the intersection plane whereby large amount of rotation is performed within the shear crack. Besides the rotations, vertical (shear) deformations occur in the wedge due to the inclined compression force introduced by the shear reinforcement. The assumption of such a slab deformation leads to several implications, which can be confirmed either by measurements or visual observations. Figure 7.3 shows principal experimental observations such as the detachment of concrete on the top and the spalling of concrete at the bottom surface, and considerations that are used in the proposed model such as the location of the shear deformations.

For certain test specimens, spalling of the concrete at the bottom surface occurred at large rotations. This spalling results from the large tangential compressive strains acting on the bottom surface near the column. The spalling of concrete on the top surface is more a detachment of the concrete cover as it can be seen in Figure 7.5. The detachment results from the rather large shear deformations that are assumed to be performed in the wedge element. The location of these shear deformations can be determined by the detailed analysis of the vertical measurements in the column vicinity. The vertical displacement measurements along the axis on the bottom surface indicate that large shear deformation occurs (refer to Chapter 3). Additionally, the change in slab thickness measured by the distance between the top and bottom surface of the slab lead to similar deformations as it was obtained based on the vertical displacement measurements. However, the elongation of the shear reinforcement predicts a much smaller displacement.

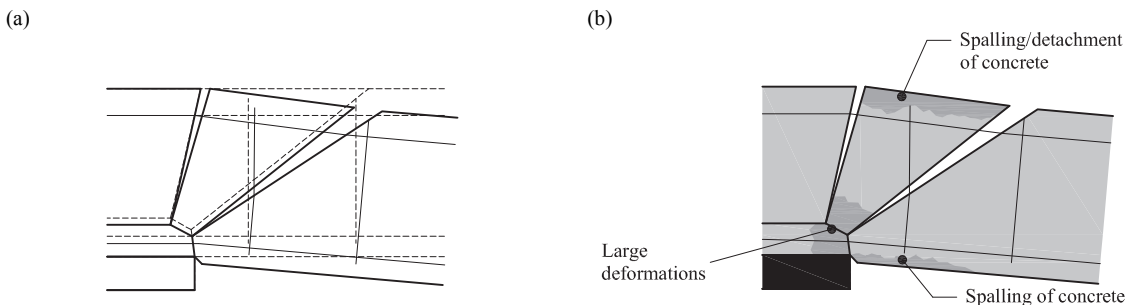


Figure 7.3: Assumed deformed shape of the slab specimen close to failure

Figure 7.4 shows these three vertical deformations as a function of the slab rotation. While the change in thickness corresponds directly to the measured value, the shear deformations were calculated based on the vertical displacement measurements on the bottom surface (Equation 3.1) and the stud elongations were estimated based on the local strain gauge measurements on the top side of the first row of studs. Although all presented graphs represent vertical deformations, each measurement or estimate relies on different influences according to the proposed model. The calculated shear deformations  $\Delta w$  depend solely on the shear forces and are thus independent of the rotations. In contrast, the changes in slab thickness  $\Delta h$  depend not only on the shear deformations, since the top surface detaches due to the dowel action of the flexural reinforcement, but also on the slab rotation that lead to the opening of inclined shear cracks. Therefore, the measurements of the change in thickness should be larger than the shear deformations. This statement is confirmed by Figure 7.4.

Although it has to be noted that the estimations of the stud elongations are based on coarse assumptions such as that the strains are constant along the stud and that they are equal to the measurement on top, they provide valuable information. It can be seen that the estimated stud elongation are much smaller than the calculated shear deformations at the column face. This observation is especially noteworthy if one considers that the stud elongation results from the combination of the shear deformations within the shear cracks that cross the shear reinforcement and the opening of inclined shear cracks resulting from the slab rotation. Additionally, it can be noted that the deformation in the studs increases nearly linearly with increasing rotations. These observations lead to the conclusion that only few shear deformations occurred within the shear crack. Therefore, it can be concluded that the main deformations in the shear reinforcement result from the rotation of the slab confirming a principal hypothesis of the proposed model.

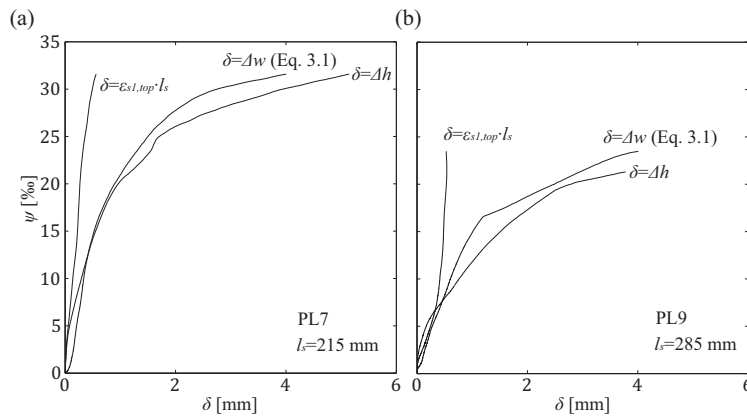


Figure 7.4: Rotation-deformation curve for specimens (a) PL7 and (b) PL9 of deformations calculated based on the strain measurements in the shear reinforcement  $\varepsilon_s$ , assuming a constant strain along the stud length  $l_s$  and for shear deformations  $\Delta w$  calculated based on the vertical displacement measurements (see Eq. 3.1), and the change in slab thickness  $\Delta h$

Generally, unconfined concrete shows a limited deformation capacity. In contrast, well confined concrete has not only an increased compressive strength but also an increased deformation capacity so that even strains in the range between 0.01 and 0.02 can occur. Such strains are required to obtain the measured shear deformations. Thus, it can be concluded that these deformations occur, without visible failure, at a location where confinement exists. The only possible location for this is at the bottom side over the column where a triaxial state of compressive stresses exists leading to an active confinement of the concrete. The rather large deformations at this area result in a rigid vertical displacement of the outer slab segment and cause a shortening of the wedge element, which leads to the detachment of the top cover concrete as it is visible in Figure 7.5.

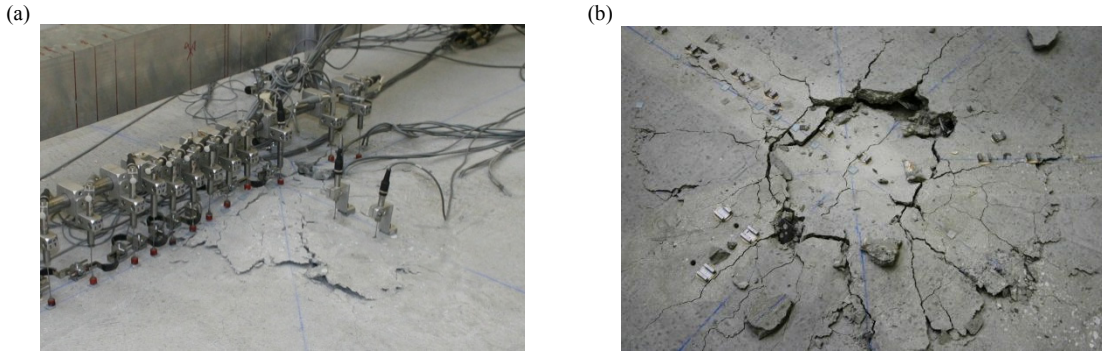


Figure 7.5: Top view after failure of (a) specimen PL6 and (b) specimen PL7

As mentioned previously, it is assumed that the rotations cause the opening of the cracks separating the three slab elements. The assumption of such a mechanical model leads to several possible failure locations. With respect to failure, the most critical aspects regarding the assumed load transfer path are the shear reinforcement crossing the crack, the transverse (tensile) deformations close to the top surface in the wedge, and the direct shear transfer of the outer slab segment to the column. The direct shear transfer can be considered as concrete contribution to the total punching shear strength, similar to the CSCT approach, and as the contribution of the shear reinforcement in the outer segment that transfers load directly to the support (Figure 7.6). Besides the shear force that is directly transferred from the outer segment to the support, a fraction of the shear force is transferred to the wedge by the shear reinforcement crossing the outer shear crack. This force is either limited by the amount of shear reinforcement crossing the crack or by the strength of the compression strut transferring the force to the support. If the sum of the contribution of the concrete, the contribution of the shear reinforcement outside the outer shear crack, and the contribution of the shear reinforcement crossed by the outer shear crack is exceeded, the slab fails in punching. The failure mode will be determined by whether the shear reinforcement (failure within) or the compression strut (crushing of concrete) reaches its limit first.

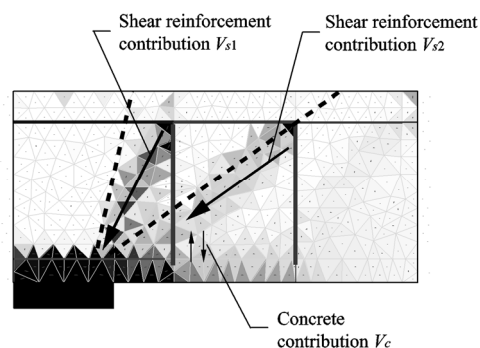


Figure 7.6: Load transfer to the support by the shear reinforcement crossing the crack, by the shear reinforcement outside the crack and by the concrete



## 7.2. Load-rotation response

In the case of slabs without shear reinforcement, the Quadrilinear approach proposed by Muttoni (Muttoni 2008) presented in Chapter 2, in which the shear force can be calculated using the equilibrium conditions at the outer slab segment, leads to a good agreement with test results. The equilibrium condition is given by:

$$V \cdot \frac{\Delta\varphi}{2\pi} \cdot (r_q - r_c) = -m_r \cdot \Delta\varphi \cdot r_0 - \Delta\varphi \int_{r_0}^{r_s} m_t \cdot dr \quad (7.1)$$

where  $\Delta\varphi$  is the angle of the slab segment,  $V$  is the shear force,  $r_q$  the load application radius,  $r_c$  is the radius of the column,  $m_r$  is the moment acting radially at a distance  $r_0$ ,  $r_0$  is the radius of the shear crack,  $r_s$  is the radius of the slab, and  $m_t$  is the tangential moment at a certain position  $r$ .

However, in presence of shear reinforcement additional aspects need to be considered. The Quadrilinear approach assumes that all the force is directly transferred from the outer slab segment to the column and thus no shear force occurs at the slab portion within a radius  $r_0$ . This assumption is valid for slabs without shear reinforcement. If shear reinforcement is present, one has to account for shear forces within the zone between the column face  $r_c$  and radius  $r_0$ . Moreover, the load transfer in the column vicinity has to be fully considered. Consequently, the column region can be defined as a discontinuity region and thus needs to be treated differently than the outer slab portion. Therefore, the slab behavior is divided into a global and local part. The outer slab segment can be treated as a slab subjected to bending. In other words, the assumptions that plane sections remain plane can be applied. In contrast, the response in the column vicinity is highly influenced by the shear forces. In this area the response is determined by rigid-plastic stress fields. The change in the calculation is assumed to be at the outer shear crack at radius  $r_2$ . The state of deformation at this intersection plane defines the stresses in the reinforcement at the shear crack and thus the compression forces acting at the outer slab segment.

### 7.2.1. Global slab behavior

#### *Assumed rotation*

The distribution of the slab rotation is simplified by describing three different regions. The part over the column has a linear increase in rotation leading to a constant radial and tangential curvature. The outermost part of the slab starting at a radius  $r_0$  is assumed to have a constant rotation assuming that the outer part undergoes a rigid body displacement in radial direction. Between the column face and the outer slab segment (between  $r_c$  and  $r_0$ ), a transition part exists. In this area, the variation of the rotation is described as a quadratic function. The quadratic function leads to a linear variation in radial curvature and thus describes the actual behavior

poorly. However, a polynomial function of higher order has not been considered for simplicity. Nevertheless, for a more accurate calculation, the curvature at radius  $r_2$  can be determined numerically using a more sophisticated rotation function.

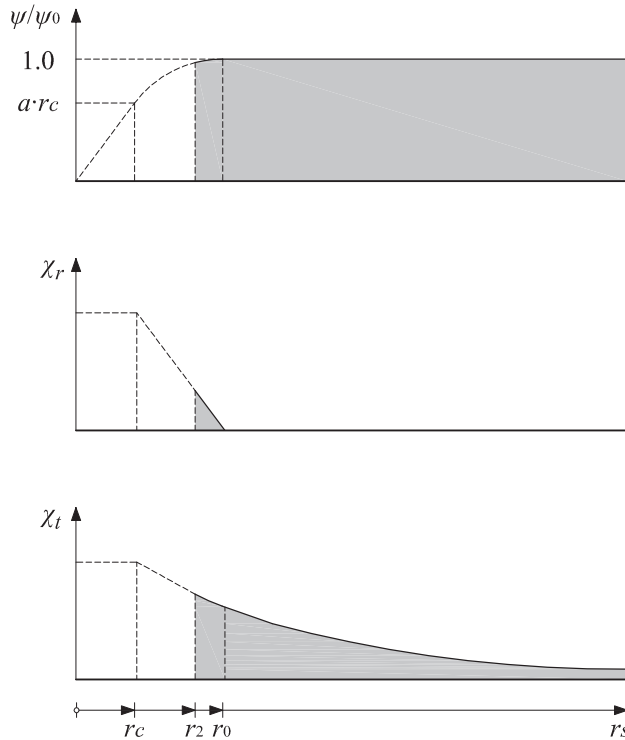


Figure 7.7: Assumed simplified slab behavior for the outer slab segment: (a) rotations, (b) radial curvatures, and (c) tangential curvatures

As mentioned previously, the rotations are defined by a linear relationship over the column, by a quadratic relationship at a transition zone between the column face  $r_c$  and  $r_0$ , and by a constant value  $\psi_0$  at the outer segment. The quadratic function can be defined as:

$$\begin{aligned}
 r < r_c &\rightarrow \psi(r) = a \cdot r \cdot \psi_0 \\
 r_c < r < r_0 &\rightarrow \psi(r) = [c(r - r_c)^2 + a \cdot (r - r_c) + a \cdot r_c] \cdot \psi_0 \\
 r_0 < r &\rightarrow \psi(r) = \psi_0
 \end{aligned}
 \tag{7.2}$$

where parameter  $a$  and  $c$  can be determined so that the values of the function and the derivatives are equal at the boundaries leading to the parameter  $a$  equal to:

$$a = \frac{2}{r_c + r_0}
 \tag{7.3}$$

and to the parameter  $c$  equal to

$$c = -\frac{a}{2(r_0 - r_c)}
 \tag{7.4}$$

Based on the assumed rotation, one can calculate the curvatures. It has to be noted that for the global behavior only the curvatures in tangential direction are of interest. In axisymmetric cases, the tangential curvature is defined by the fact that the curvature is equal to the rotation at a certain location divided by the radius of this location leading to following expressions:

$$\begin{aligned}
 r < r_c &\rightarrow \chi_t(r) = -a \cdot \psi_0 \\
 r_c < r < r_0 &\rightarrow \chi_t(r) = -[c(r - r_c)^2 + a \cdot (r - r_c) + a \cdot r_c] \cdot \frac{\psi_0}{r} \\
 r_0 < r &\rightarrow \chi_t(r) = -\frac{\psi_0}{r}
 \end{aligned} \tag{7.5}$$

where  $\psi_0$  is the constant rotation at the outer slab segment.

### Flexural relationships

Generally, the pure flexural relationship can be calculated numerically using a similar approach as it was used for the NLFEA described in Chapter 5. For the analytical calculation of the slab response, a simplified moment-curvature relationship proposed by Muttoni was used (Muttoni 2008). The relationship is defined by four phases: an uncracked stage, a cracking stage, a stabilized cracking stage, and a yielded stage. Figure 7.8 shows the different phases in the moment curvature diagram.

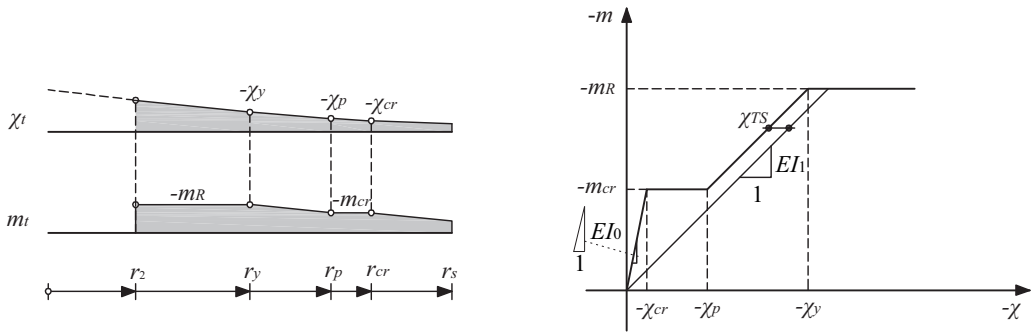


Figure 7.8: Moment and curvature distribution (adapted from (Muttoni 2008))

Assuming that the influence of the reinforcement can be neglected for the phase before cracking, the cracking moment can be estimated as:

$$m_{cr} = \frac{f_{ct} \cdot h^2}{6} \tag{7.6}$$

The cracking moment and the stiffness before cracking can be expressed as:

$$EI_0 = \frac{E_c \cdot h^3}{12} \tag{7.7}$$

leading to the cracking curvature of:

$$-\chi_{cr} = \frac{m_{cr}}{EI_0} = \frac{2 \cdot f_{ct}}{h \cdot E_c} \quad (7.8)$$

After cracking, the stiffness of the reinforced slab specimen decreases. If a linear-elastic behavior of the concrete and the reinforcing steel is assumed, the stiffness after cracking can be estimated as:

$$EI_1 = \rho \cdot \beta \cdot E_s \cdot d^3 \cdot \left(1 - \frac{x_{el}}{d}\right) \cdot \left(1 - \frac{x_{el}}{3d}\right) \quad (7.9)$$

where  $x_{el}$  is the height of the compression zone calculated with linear-elastic material behavior given by:

$$x_{el} = \rho \cdot \beta \cdot \frac{E_s}{E_c} \cdot d \cdot \left( \sqrt{1 + \frac{2 \cdot E_c}{\rho \cdot \beta \cdot E_s}} - 1 \right) \quad (7.10)$$

where  $E_s$  is the Young's modulus of the reinforcing steel,  $E_c$  is the Young's modulus of the concrete,  $\rho$  is the flexural reinforcement ratio,  $d$  is the effective depth and  $\beta$  is an efficiency factor that accounts for the orthogonal reinforcement layout.

If one assumes a rigid-plastic concrete behavior, the flexural strength can be determined by:

$$m_R = \rho \cdot f_y \cdot d^2 \cdot \left(1 - \frac{\rho \cdot f_y}{2 \cdot f_c}\right) \quad (7.11)$$

where  $\rho$  is the flexural reinforcement ratio,  $d$  is the effective depth,  $f_y$  is the yielding strength of the reinforcement, and  $f_c$  is the compressive strength of the concrete.

The consideration of a constant influence of the tension stiffening estimated as:

$$\chi_{TS} = \frac{f_{ct}}{\rho \cdot \beta \cdot E_s} \cdot \frac{1}{6 \cdot h} \quad (7.12)$$

leads to the curvature in the beginning of the stabilized cracking phase of:

$$-\chi_p = \frac{m_{cr}}{EI_1} - \chi_{TS} \quad (7.13)$$

and to the curvature at yielding of:

$$-\chi_y = \frac{m_R}{EI_1} - \chi_{TS} \quad (7.14)$$

### 7.2.2. Local slab behavior

The local slab behavior near the support is defined by the state of deformation at section  $r_2$  (Figure 7.9) and by the shear forces. Therefore, the first step is to calculate the curvature in radial direction at the intersection plane  $r_2$ . The curvature in radial direction can be calculated as a function of the rotation based on the global slab behavior. However, the numerical analysis showed that at a certain rotation, the radial curvature at radius  $r_2$  stays approximately constant (refer to Chapter 6). Therefore, the curvature is limited by a value  $\chi_{r,lim}$ . A formulation for the estimation and a further discussion of this curvature will be presented subsequently in the section of model parameters. Thus, the curvature in radial direction at the intersection plane  $r_2$  can be estimated as:

$$\chi_{r,r_2} = -[2 \cdot c \cdot (r_2 - r_c) + a] \cdot \psi_0 \leq \chi_{r,lim} \quad (7.15)$$

where  $r_2$  is the radius of the intersection plane,  $r_c$  is the radius of the column,  $a$  and  $c$  are calculation parameter determined according to Equation 7.3 and Equation 7.4, respectively, and  $\psi_0$  is the rotation at the outer slab segment.

From the state of deformation, one can obtain the stresses in the reinforcement at the intersection plane  $r_2$ . Using linear-elastic material relationships, one can obtain the stresses in the reinforcement based on the curvatures in radial direction  $\chi_r$ :

$$\begin{aligned} \chi_r < \chi_{cr} &\rightarrow \sigma_s \cong \chi_r \cdot \left(d - \frac{h}{2}\right) \cdot E_s \\ \chi_{cr} < \chi_r < \chi_p &\rightarrow \sigma_s \cong \chi_p \cdot \left(d - \frac{h}{2}\right) \cdot E_s \\ \chi_p < \chi_r &\rightarrow \sigma_s = (\chi_p + \chi_{TS}) \cdot (d - x_{el}) \cdot E_s \cdot \beta \leq f_y \end{aligned} \quad (7.16)$$

where  $\chi_{cr}$  is the curvature at cracking (Equation 7.8),  $\chi_p$  is the curvature at crack stabilization (Equation 7.13),  $\chi_{TS}$  is the difference in curvature due to tension stiffening (Equation 7.12),  $d$  is the effective depth,  $h$  is the slab thickness,  $E_s$  is the Young's modulus of steel,  $x_{el}$  is the height of the compression zone based on a linear-elastic calculation (Equation 7.10),  $\beta$  is an efficiency factor that accounts for the orthogonal reinforcement layout, and  $f_y$  is the yielding strength of the reinforcement.

From the equilibrium condition regarding horizontal forces at the intersection plane, it can be noted that the sum of the compression and the tensile forces is equal to zero at the intersection plane for a segment of  $\Delta\varphi$  (Figure 7.9). Thus, it can be noted that:

$$C_{r_2} = -\rho \cdot d \cdot \sigma_s \cdot r_2 \cdot \Delta\varphi \quad (7.17)$$

where  $C_{r_2}$  is the compression force acting at the intersection plane at a slab segment of  $\Delta\varphi$ .

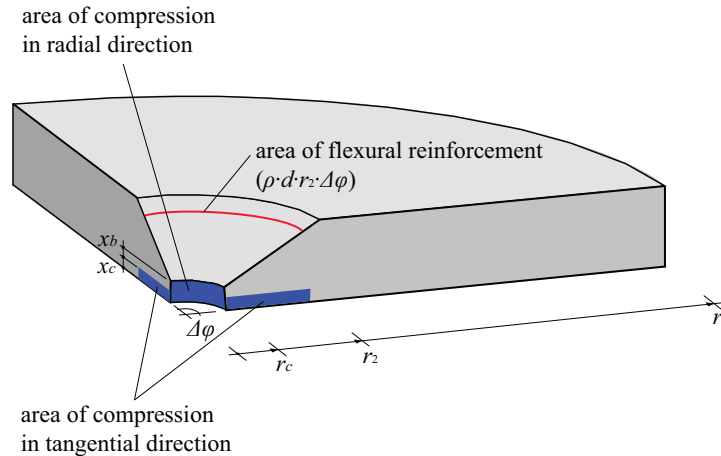


Figure 7.9: Area of tensile and compression forces acting at the intersection plane  $r_2$

The total compression forces acting at the intersection plane can be divided into a horizontal part  $C_b$  of an inclined compression strut due to the shear force ( $F_{c,b}$  in Figure 7.10b) and a horizontal part  $C_c$  due to bending ( $F_{c,c}$  in Figure 7.10b). The horizontal component of the compression force  $C_b$  depends on the amount of shear force, which is directly transferred from the outer slab segment to the column, and on the inclination angle of the compression strut. Thus, it can be expressed as:

$$C_b = -(1 - \lambda) \cdot V \cdot \cot \alpha_b \quad (7.18)$$

where  $\lambda$  is the load distribution factor (Equation 7.70) and  $\alpha_b$  is the inclination angle of the compression strut. Angle  $\alpha_b$  defines only the ratio between the compression force  $C_b$  and the compression force  $C_c$ . In other words, it does not affect the sum of the compression forces  $C_b$  and  $C_c$ . Therefore, the variation of angle  $\alpha_b$  has nearly negligible influence on the overall response of the slab. Thus, a constant value of  $26.6^\circ$  ( $\cot(\alpha_b) = 2$ ) was chosen based on the numerical analysis which indicated generally an angle around  $20^\circ$ .

The compression force  $C_c$  due to bending is defined as the difference of the total compression force acting at the intersection plane and the compression force  $C_b$ . Thus, it is given by:

$$C_c = C_{r2} - C_b \quad (7.19)$$

However, it has to be checked that the total compression force acting at the column face does not lead to tensile stresses in the reinforcement that exceed the yielding strength. Therefore, the following condition needs to be ensured:

$$\sigma_s = \frac{-(C_a + C_b + C_c)}{\rho \cdot d \cdot 2\pi r_2} \leq f_y \quad (7.20)$$

where  $C_a$  is the horizontal component of the compression strut in the wedge element. It can be calculated by the amount of shear force transferred to the wedge element and the inclination of the compression strut. Thus, the horizontal component of the compression strut in the wedge can be calculated by:

$$C_a = -\lambda \cdot V \cdot \frac{r_1 - r_c}{d - x_1/2} \quad (7.21)$$

where  $\lambda$  is the load distribution factor,  $V$  is the applied shear force,  $r_1$  the radius of the resultant force that is transferred across the outer shear crack by the shear reinforcement,  $r_c$  is the radius of the column,  $d$  is the effective depth, and  $x_1$  is height of the compression zone at the column face.

While the compression force due to bending acts along the whole intersection plane, the compression force due to the compression strut acts only along the column face. This fact leads to the different distribution of the compression force in radial and tangential direction (Figure 7.9).

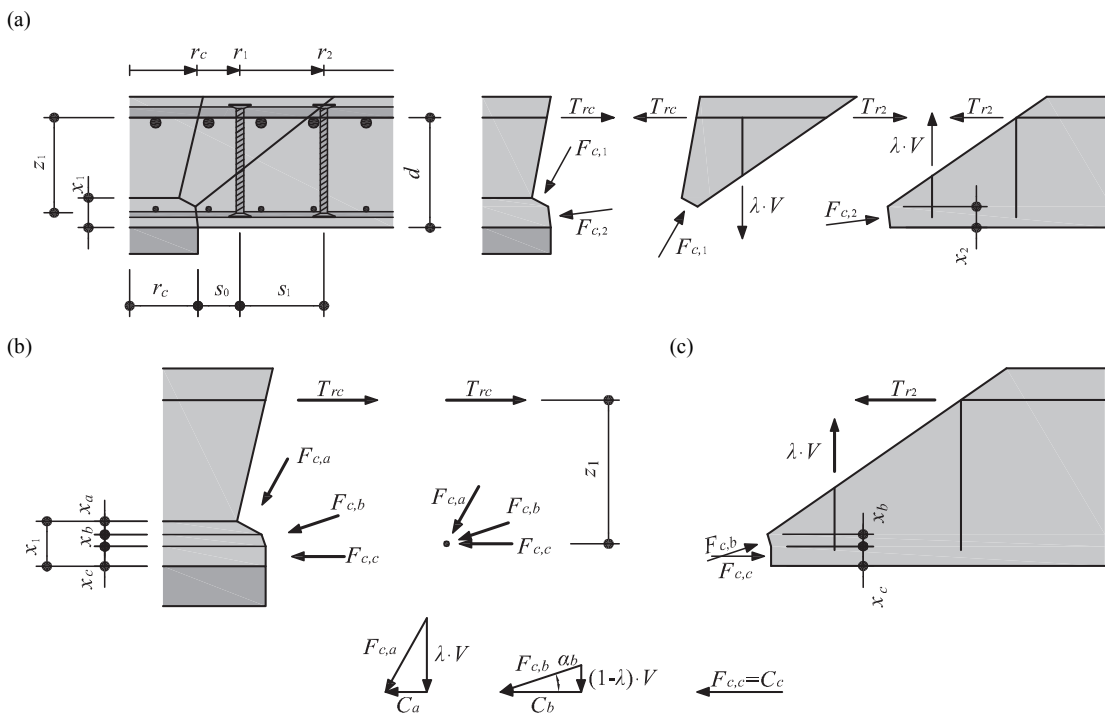


Figure 7.10: Forces acting at each slab element: (a) overview; (b) detailed view of forces acting at the column face; (c) detailed view of forces acting at the intersection plane at  $r_2$

Based on the compression forces, the moments in radial and tangential direction (per unit length) can be determined by:

$$m_r = \frac{(C_a + C_b + C_c)}{2\pi r_2} \cdot \left(d - \frac{x_1}{2}\right) \quad (7.22)$$

and

$$m_t = \frac{C_c}{2\pi r_2} \cdot \left(d - \frac{x_c}{2}\right) \quad (7.23)$$

where the heights of the compression zones ( $x_1$  and  $x_c$ ) can be approximated by using a rigid-plastic stress distribution.

Thus, the height of the compression zone  $x_1$  can be estimated as:

$$x_1 = \frac{-C_b - C_a}{f_c \cdot 2\pi r_c} + x_c \quad (7.24)$$

and the height of the compression zone  $x_c$  by:

$$x_c = \frac{-C_c}{f_c \cdot 2\pi r_2} \quad (7.25)$$

### 7.2.3. Equilibrium conditions

The moment equilibrium condition at a free body enables the calculation of the acting shear forces. Using the column face for defining the equilibrium condition, one can equilibrate the moment due to the shear force acting at a distance  $r_q$  and the radial and tangential moments acting at the free body (Figure 7.11). The moment in tangential direction can be further separated into the force that acts within the outer shear crack and the moment that acts exterior the outer shear crack. Therefore, it can be stated:

$$V \cdot \frac{\Delta\varphi}{2\pi} \cdot (r_q - r_c) = -\Delta\varphi \cdot m_r \cdot r_c - \Delta\varphi \cdot m_{t,int}(r_2 - r_c) - \Delta\varphi \int_{r_2}^{r_s} m_{t,ext} \cdot dr \quad (7.26)$$



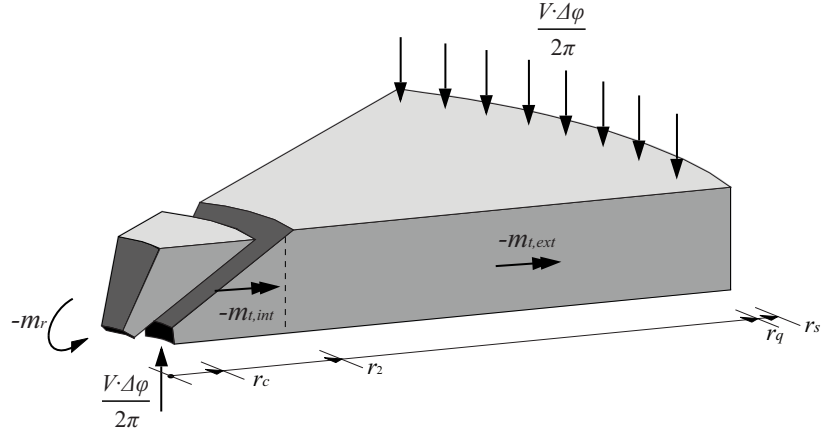


Figure 7.11: Forces and moments acting on a free body segment of the slab

The moment in radial direction acting at the column face is rather straightforward and can be stated according to Equation 7.22. The tangential part within the shear crack is assumed to be uniformly distributed between the boundaries  $r_2$  that defines the location of the outer shear crack (intersection plane) and the column face  $r_c$ .

The integration of the moment in tangential direction exterior the shear crack has to be separated to the part with a constant rotation ( $r_0$ - $r_s$ ) and the part with a quadratic rotation function ( $r_2$ - $r_0$ ). Thus, the integral of the moment in tangential direction outside the shear crack can be evaluated from:

$$\Delta\varphi \int_{r_2}^{r_s} m_t \cdot dr = \Delta\varphi \int_{r_0}^{r_s} m_t \cdot dr + \Delta\varphi \int_{r_2}^{r_0} m_t \cdot dr \quad (7.27)$$

The moment acting at the part with constant rotation ( $r_0$ - $r_s$ ) can be solved using the constitutive relationship defined previously (see Figure 7.8). The integral of the tangential moment at the part with constant rotation can be expressed as:

$$\Delta\varphi \int_{r_0}^{r_s} m_t \cdot dr = \Delta\varphi \left[ \begin{array}{l} m_R(r_y - r_0) + EI_1\psi[\ln(r_p) - \ln(r_y)] \\ +EI_1\chi_{TS}(r_p - r_y) + m_{cr}(r_{cr} - r_p) + EI_0\psi[\ln(r_s) - \ln(r_{cr})] \end{array} \right] \quad (7.28)$$

where the following condition applies:

$$\text{if } \{r_y, r_p, r_{cr}\} < r_0 \rightarrow \{r_y, r_p, r_{cr}\} = r_0 \quad (7.29)$$

The constitute relationship defines three different regions at the part with constant rotation. These regions are:

The region in which the reinforcement is yielding defined by

$$r_y = -\frac{\psi}{\chi_y} = \frac{\psi}{\frac{m_R}{EI_1} - \chi_{TS}} \leq r_s, \quad (7.30)$$

the region where the cracking is stabilized defined by

$$r_p = -\frac{\psi}{\chi_1} = \frac{\psi}{\frac{m_{cr}}{EI_1} - \chi_{TS}} \leq r_s, \quad (7.31)$$

and the region where the concrete is cracked defined by

$$r_{cr} = -\frac{\psi}{\chi_{cr}} = \frac{\psi \cdot EI_0}{m_{cr}} \leq r_s \quad (7.32)$$

The tangential moment in the part where it is assumed that the rotation corresponds to a quadratic function ( $r_2-r_0$ ) can be integrated as follows:

$$\int_{r_2}^{r_0} m_t \cdot dr = \int_{r_2}^{r_y} m_t \cdot dr + \int_{r_y}^{r_p} m_t \cdot dr + \int_{r_p}^{r_{cr}} m_t \cdot dr + \int_{r_{cr}}^{r_0} m_t \cdot dr \quad (7.33)$$

where following conditions apply:

$$\text{if } \{r_y, r_p, r_{cr}\} < r_2 \rightarrow \{r_y, r_p, r_{cr}\} = r_2 \quad (7.34)$$

and

$$\text{if } \{r_y, r_p, r_{cr}\} > r_0 \rightarrow \{r_y, r_p, r_{cr}\} = r_0 \quad (7.35)$$

The distances  $r_i$  can be calculated by:

$$r_i = -\frac{-\left[-2r_c \cdot c + a - \frac{\chi_{t,i}}{\psi_0}\right] - \sqrt{\left(-2r_c \cdot c + a - \frac{\chi_{t,i}}{\psi_0}\right)^2 - 4c^2 \cdot r_c^2}}{2c} \quad (7.36)$$

where  $a$  and  $c$  are calculation parameter determined according to Equation 7.3 and Equation 7.4, respectively,  $\psi_0$  is the rotation at the outer slab segment, and  $\chi_{t,i}$  is the tangential curvature for which radius  $r_i$  is searched ( $\chi_y, \chi_p, \chi_{cr}$ ).

Knowing the radius  $r_i$  for each change in phase, the integral can be solved independently. Leading to the expressions:

$$\int_{r_2}^{r_y} m_t \cdot dr = m_{R,t} \cdot (r_2 - r_y), \quad (7.37)$$

$$\int_{r_y}^{r_p} m_t \cdot dr = \left[ \frac{c}{2} (r_y^2 - r_p^2) - 2c \cdot r_c (r_y - r_p) \right] \psi_0 \cdot EI_1 + \chi_{TS} \cdot EI_1 (r_y - r_p), \quad (7.38)$$

$$+ a(r_y - r_p) + c \cdot r_c \cdot \ln \left( \frac{r_y}{r_p} \right)$$

$$\int_{r_p}^{r_{cr}} m_t \cdot dr = m_{cr} \cdot (r_p - r_{cr}), \quad (7.39)$$

and

$$\int_{r_{cr}}^{r_0} m_t \cdot dr = \left[ \frac{c}{2} (r_0^2 - r_{cr}^2) - 2c \cdot r_c (r_0 - r_{cr}) \right] \psi_0 \cdot EI_1 \quad (7.40)$$

$$+ a(r_0 - r_{cr}) + c \cdot r_c \cdot \ln \left( \frac{r_0}{r_{cr}} \right)$$

### 7.3. Failure criteria

Within the research presented herein, two failure modes were investigated: failure within the shear-reinforced area and failure due to crushing of the compression strut. Thus, for each of this two failure modes a failure criterion was developed. With respect to the failure within the shear-reinforced area, codes such as ACI 318-11, EC2 2004, or MC 2010 and the CSCT use generally the sum of a certain contribution of the concrete and a certain contribution of the shear reinforcement to the punching strength. While ACI 318-11 and EC2 2004 uses a fixed parameter for the concrete contribution, MC 2010 and the CSCT uses a contribution of the concrete as a function of the slab rotation. Generally, the proposed model uses the same approach as the CSCT proposed by Fernández Ruiz and Muttoni (Fernández Ruiz and Muttoni 2009) for failure within the shear-reinforced area. However, certain modifications were made mainly for the calculation of the crack width and the amount of the shear reinforcement that is contributing to the punching strength. Both modifications can be attributed to the different assumption regarding the location and the inclination of the shear crack crossing the shear reinforcement. The used assumptions of the location and the inclination of the shear crack are discussed in detail in subchapter 7.4.2.

If large amount of shear reinforcement is present, failure due to crushing of the concrete strut may occur. Generally, codes such as ACI 318-11, NAD 2011, or MC 2010 and the CSCT increase the punching strength of slabs without shear reinforcement, in the case of MC 2010 and the CSCT defined as a function of the rotation, by a certain factor. However, the different provisions have different justifications for the use of such an approach. In the case of NAD 2011, the approach is based on the conclusion that the resistance is defined by the strength of the concrete compression zone at the column face (Beutel 2003; Häusler 2009). The main parameters defining the strength of the concrete compression zone are the effective depth, the flexural reinforcement ratio and the compressive strength of concrete. These parameters are all considered in the formulation of punching of slabs without shear reinforcement so that the increase of the punching strength of slabs without shear reinforcement by a certain factor was justified.

In the case of the CSCT and MC 2010, the approach is based on the main assumption that the crushing strength of the concrete depends on the state of transverse strains in the compression strut (Fernández Ruiz and Muttoni 2009; Muttoni and Fernández Ruiz 2010). Since the state of transverse strains can be described as a function of the opening of cracks in the shear-critical region, which corresponds to the hypothesis of the formulation of the CSCT for slabs without shear reinforcement, the use of the same formulation is proposed as basis for the failure criterion for crushing of concrete. Additionally, the width of the crushing zone is assumed to depend on the aggregate size (Muttoni and Fernández Ruiz 2010), for which the formulation of the CSCT for slabs without shear reinforcement also accounts for. The multiplication factor used to increase the punching strength of slabs without shear reinforcement takes into account of the performance of the anchorage and the distribution of the shear reinforcement system.

The failure criterion for crushing of the concrete strut proposed within this research relies basically on the assumed load transfer path in the vicinity of the column. The assumed load transfer corresponds to the load transfer proposed for failure within the shear-reinforced area, by which the concrete, the shear reinforcement outside the shear crack, and the shear reinforcement crossing the shear crack contributes to the punching strength. In other words, the proposed model considers that only a portion of the force is transferred by the compression strut close to the column whereby this force is directly supported by the column (Figure 7.12c,d). With increasing load, the force in the compression strut increases until it becomes too large and the concrete starts crushing at the anchorage zone of the shear reinforcement. At this moment, the direct support of the force is interrupted so that the compression strut has to be deviated (Figure 7.12e,f). However, this deviation leads to large tensile forces transverse to the compression strut leading immediately to failure. This explains the immediate loss of strength that was experimentally observed without any softening which one would expect in the case of a compression failure.

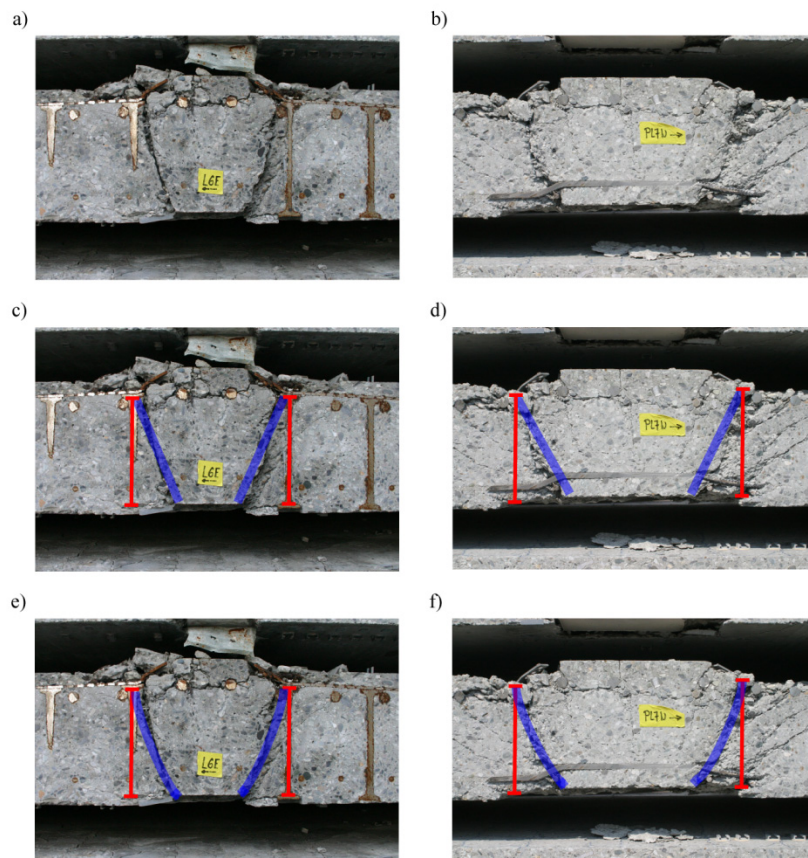


Figure 7.12: Load transfer and failure mechanism shown for PL6 (a, c, e) and PL7 (b, d, f): (a, b) Detailed view of the crack pattern, (c, d) load transfer until failure, and (e, f) change in load transfer at failure

As discussed previously, the total shear force can be defined as the sum of the contribution of the shear reinforcement crossing the crack, the contribution of the shear reinforcement outside the crack, and the contribution of the concrete. Therefore, it can be stated that:

$$V_R = \Sigma V_{Rs} + V_{Rc} \quad (7.41)$$

The concrete contribution is assumed to be the same as for slabs without shear reinforcement as proposed by the CSCT approach (Muttoni 2008; Fernández Ruiz and Muttoni 2009). Therefore, the maximum concrete contribution can be expressed as:

$$V_{Rc} = \frac{\frac{3}{4} \cdot b_0 \cdot d \cdot \sqrt{f_c}}{1 + \frac{15 \cdot \psi \cdot d}{d_{g0} + d_g}} \quad (7.42)$$

where  $\psi$  is the slab rotation,  $d$  is the effective depth,  $d_{g0}$  is a reference aggregate size equal to 16 mm,  $d_g$  is the aggregate size,  $f_c$  is the compressive strength of concrete, and  $b_0$  is the control perimeter set at a distance of  $0.5d$  from the support region with circular corners.

The sum of the contribution of the shear reinforcement can be defined by the load distribution factor for the shear reinforcement  $\lambda_s$ , which defines the portion of the shear force that is transferred across the crack by the shear reinforcement and afterwards transferred to the column by the compression strut. The use of this factor leads to the following expression:

$$\Sigma V_s = \frac{V_{s1}}{\lambda_s} \quad (7.43)$$

where  $V_{s1}$  is the shear force transferred across the crack.

Failure occurs when the applied shear force  $V$  is larger than the shear strength defined by:

$$V > V_R = \frac{V_{Rs}}{\lambda_s} + V_{Rc} \quad (7.44)$$

The maximum concrete contribution is defined by Equation 7.42 and the maximum shear force transferred across the crack ( $V_{Rs}$ ) is either limited by the amount of shear reinforcement (failure within) or by the compression strut (crushing of concrete).

For a failure within the shear-reinforced area, an approach similar to the CSCT (Fernández Ruiz and Muttoni 2009) is used. Therefore, the maximum shear force transferred across the crack  $V_{Rs}$  is calculated by the product of the area of shear reinforcement crossed by the crack ( $A_{sw}$ ) and the stresses in the shear reinforcement as a function of the rotation  $\sigma_w(\psi)$ . Thus, the maximum shear force transferred through the crack  $V_{Rs,1}$  is given by:

$$V_{Rs,1} = A_{sw} \cdot \sigma_w(\psi) \quad (7.45)$$

For the calculation of the stresses in the shear reinforcement, one requires the crack width at the location of the shear reinforcement. According to Figure 7.13a, the crack width  $w_1$  can be estimated as:

$$w_1 = \kappa \cdot \psi \cdot \frac{s_0}{\cos(\alpha_{cr})} \cdot \cos(\alpha_{cr}) = \kappa \cdot \psi \cdot s_0 \quad (7.46)$$

where  $\kappa$  defines the ratio of the rotation performed at this crack to the total slab rotation. Assuming that approximately one third of the total rotation is performed within this crack,  $\kappa$  can be estimated as:

$$\kappa = 0.35 \quad (7.47)$$

This factor  $\kappa$  can be associated to the factor  $\kappa$  used in the CSCT (Fernández Ruiz and Muttoni 2009) that was empirically determined to be  $\kappa_{CSCT} = 0.5$ . However, a difference in the value exists since the CSCT approach defines the crack width as:

$$w_1 = \kappa_{CSCT} \cdot \psi \cdot h_1 \cdot \cos\left(\frac{\pi}{4}\right) \quad (7.48)$$

where  $\psi$  is the rotation of the slab and  $h_1$  is the vertical distance from the crack tip to the point where the crack crosses the shear reinforcement.

Assuming a crack inclination of  $45^\circ$  ( $\pi/4$ ),  $s_0$  can be stated as:

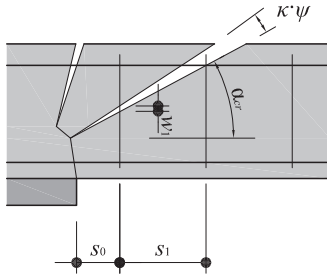
$$s_0 = h_1 \cdot \tan\left(\frac{\pi}{4}\right) = h_1 \quad (7.49)$$

leading to the expression:

$$\kappa \cong \kappa_{CSCT} \cdot \cos\left(\frac{\pi}{4}\right) = 0.5 \cdot \cos\left(\frac{\pi}{4}\right) = 0.35 \quad (7.50)$$

If more than one vertical branch of shear reinforcement crosses the crack, the crack opening can be determined similarly at each intersection point (Figure 7.13b). This can occur if the spacing of the shear reinforcement is rather close as it was the case of the tests with continuous stirrups (PF1-PF5).

(a)



(b)

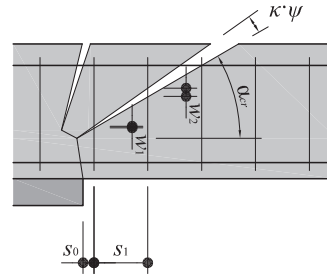


Figure 7.13: Estimation of the crack width at the location of the shear reinforcement for (a) cases by which only one vertical branch of the shear reinforcement crosses the crack and (b) cases by which more than one vertical branch of the shear reinforcement crosses the crack.

The crack width at the location of the shear reinforcement leads to the stresses in the reinforcement. These stresses can be calculated using the approach of the CSCT (Fernández Ruiz and Muttoni 2009) that distinguishes between three cases (described in detail in Chapter 2).

Case 1: If

$$w_i \leq \frac{4 \cdot \tau_b}{E_s \cdot d_w} \cdot l_{ai}^2 \quad (7.51)$$

where  $E_s$  is the Young's modulus,  $\tau_b$  is the bond strength,  $d_w$  is the diameter of the shear reinforcement, and  $l_{ai}$  is the shorter distance between the crack and one end of the shear reinforcement ( $l_{ai} = \min(l_{bi}; l_{bs})$ )

then

$$\sigma_{wi} = \sqrt{\frac{4 \cdot \tau_b \cdot E_s \cdot w_i}{d_w}} \leq f_{yw} \quad (7.52)$$

where  $E_s$  is the Young's modulus,  $\tau_b$  is the bond strength,  $d_w$  is the diameter of the shear reinforcement,  $w_i$  is the crack opening, and  $f_{yw}$  is the yielding strength of the shear reinforcement.



Case 2: If

$$\frac{4 \cdot \tau_b}{E_s \cdot d_w} \cdot l_{ai}^2 < w_i < \frac{2 \cdot \tau_b}{E_s \cdot d_w} \cdot [(l_{as} + l_{ai})^2 - 2 \cdot l_{ai}^2] \quad (7.53)$$

where  $E_s$  is the Young's modulus,  $\tau_b$  is the bond strength,  $d_w$  is the diameter of the shear reinforcement,  $l_{ai}$  is the shorter distance between the crack and one end of the shear reinforcement ( $l_{ai} = \min(l_{bi}, l_{bs})$ ), and  $l_{as}$  is the longer distance between the crack and one end of the shear reinforcement ( $l_{as} = \max(l_{bi}, l_{bs})$ )

then

$$\sigma_{wi} = \frac{-l_{ai} + \sqrt{2 \cdot l_{ai}^2 + \frac{d_w \cdot E_s \cdot w_i}{2 \cdot \tau_b}}}{\frac{d_w}{4 \cdot \tau_b}} \leq f_{yw} \quad (7.54)$$

where  $E_s$  is the Young's modulus,  $\tau_b$  is the bond strength,  $d_w$  is the diameter of the shear reinforcement,  $w_i$  is the crack opening,  $l_{ai}$  is the shorter distance between the crack and one end of the shear reinforcement, and  $l_{as}$  is the longer distance between the crack and one end of the shear reinforcement, and  $f_{yw}$  is the yielding strength of the shear reinforcement.

Case 3: If

$$w_i \geq \frac{2 \cdot \tau_b}{E_s \cdot d_w} \cdot [(l_{as} + l_{ai})^2 - 2 \cdot l_{ai}^2] \quad (7.55)$$

where  $E_s$  is the Young's modulus,  $\tau_b$  is the bond strength,  $d_w$  is the diameter of the shear reinforcement,  $l_{ai}$  is the shorter distance between the crack and one end of the shear reinforcement ( $l_{ai} = \min(l_{bi}, l_{bs})$ ), and  $l_{as}$  is the longer distance between the crack and one end of the shear reinforcement ( $l_{as} = \max(l_{bi}, l_{bs})$ )

then

$$\sigma_{wi} = \frac{E_s \cdot w_i}{l_{as} + l_{ai}} + \frac{2 \cdot \tau_b}{d_w} \cdot \frac{l_{as}^2 + l_{ai}^2}{l_{as} + l_{ai}} \leq f_{yw} \quad (7.56)$$

where  $E_s$  is the Young's modulus,  $\tau_b$  is the bond strength,  $d_w$  is the diameter of the shear reinforcement,  $w_i$  is the crack opening,  $l_{ai}$  is the shorter distance between the crack and one end of the shear reinforcement, and  $l_{as}$  is the longer distance between the crack and one end of the shear reinforcement, and  $f_{yw}$  is the yielding strength of the shear reinforcement.

For failure due to crushing of the concrete strut, the assumed failure mechanism leads to a set of parameters that must be considered. The main parameters to consider are the transverse strain in the compression strut, the area of the compression strut, and the anchorage conditions. Thus, the strength of the compression strut can generally be expressed as:

$$V_{Rs,II} = k_1 \cdot k_2 \cdot f_c \cdot A_c \cdot \sin(\alpha_1) \quad (7.57)$$

where  $k_1$  is a factor accounting for the reduction of the strength due to transverse strains,  $k_2$  is a factor accounting for the stress distribution within the compression strut depending on the anchorage of the shear reinforcement,  $f_c$  is the compressive strength,  $A_c$  is the sectional area of the compression strut.

Factor  $k_1$  that accounts for the transverse strains can be calculated based on the approach proposed by Vecchio and Collins (Vecchio and Collins 1986), which is given by:

$$f_{c,max} = \frac{f_c}{0.8 + 170\varepsilon_1} \leq f_c \quad (7.58)$$

where  $\varepsilon_1$  is the tensile strain transverse to the compression strut.

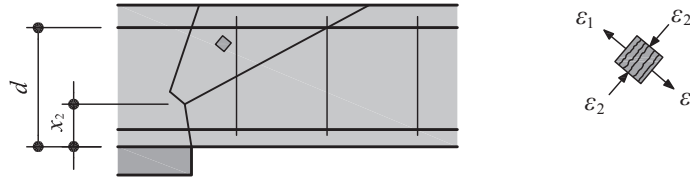


Figure 7.14: Strains acting on an element within the compression strut

Based on Equation 7.58, the reduction factor accounting for the softening due to tensile strains transverse to the compression strut can be expressed as:

$$k_1 = \frac{1}{\xi_1 + \xi_2 \cdot \varepsilon_1} \quad (7.59)$$

where  $\varepsilon_1$  is the average tensile strain transverse to the compression strut within the outer shear crack and  $\xi_1$  and  $\xi_2$  are constant parameters.

The average tensile strains transverse to the compression strut mainly depends on the opening of cracks within the outer shear crack. Thus, it can be assumed that the average tensile strains are proportional to the rotation of the slab at the location of the compression strut, which is assumed to be proportional to the rotation at the outer slab segment, leading to following expression:

$$\varepsilon_1 \propto \frac{\psi_0 \cdot (d - x_2)}{r_2} \quad (7.60)$$

where  $\psi_0$  is the rotation at the outer slab segment,  $d$  is the effective depth,  $x_2$  is the height of the compression zone at the outer slab segment (Figure 7.14), and  $r_2$  is the radius of the outer shear crack.

By combining Equation 7.59 and 7.60 and estimating the constants  $\zeta_1$  and  $\zeta_2$ , one can express the reduction factor  $k_1$  as:

$$k_1 = \frac{1}{1 + 135 \frac{\psi_0 \cdot (d - x_2)}{r_2}} \quad (7.61)$$

where  $\psi_0$  is the rotation at the outer slab segment,  $d$  is the effective depth,  $x_2$  is the height of the compression zone at the outer slab segment (Figure 7.14), and  $r_2$  is the radius of the outer shear crack.

The strength of the compressive strength depends not only on the softening of the concrete due to transverse strains but also on the maximum area of the compression strut and the stress distribution within the strut. The cross-sectional area of the compression strut is given by the perimeter and the width of the compression strut. While the perimeter is geometrically defined for each location along the compression strut, the maximum width of the compression strut cannot be directly determined. The maximum width of the compression strut may be defined considering material properties such as the maximum aggregate size or geometrical conditions such as the spacing of the shear reinforcement. For example, the CSCT defines the width of the crushing zone as a function of the aggregate size (Muttoni and Fernández Ruiz 2010). In contrast, the model proposed herein considers the location of the shear reinforcement as the principal parameter defining the maximum width of the compression strut.

Generally, the maximum width of the compression strut can be expressed by the horizontal width and the inclination angle of the strut. Thus, one can define the maximum width of the compression strut as:

$$b_w = \frac{s_c}{\sin(\alpha_1)} \quad (7.62)$$

where  $s_c$  is the horizontal width of the compression strut and  $\alpha_1$  the inclination angle of the strut (Figure 7.15).

The horizontal width of the compression strut is defined by the location and the inclination of the compression strut as well as by the location and the inclination of the shear crack. Generally, two cases can occur, the width of the compression strut is limited by the outermost vertical branch of shear reinforcement crossing the shear crack (Figure 7.15a) or by the shear crack (Figure 7.15b). The first case occurs if the inclination angle is rather steep, as it is the case if only one vertical branch crosses the shear crack, and the compression zone is moderate. If more

than one vertical branch crosses the shear crack, the width is generally limited by the shear crack. Similarly, if the compression zone becomes large as it is the case of small columns the width of the compression strut is also limited by the shear crack. Thus, the proposed model also accounts for the amount of compression acting along the column perimeter.

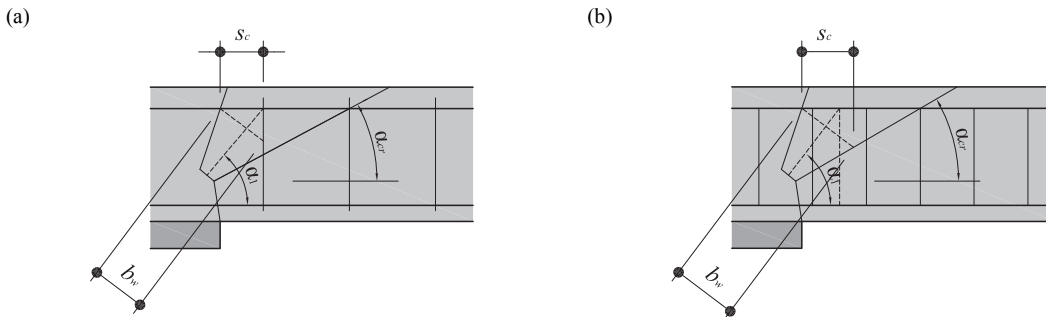


Figure 7.15: Failure of the compression strut in the case of (a) one row of shear reinforcement crossing the crack and (b) in the case of multiple rows of shear reinforcement crosses the crack

The stresses in the compression strut near the anchorage of the shear reinforcement cannot be assumed to be evenly distributed along the width of the strut (Figure 7.16). Thus, the maximum strength is reduced by a factor  $k_2$ . This factor depends on the anchorage conditions of the shear reinforcement system since it is assumed that good anchorage conditions enable a better load distribution for the load introduction into the compression strut. Therefore, the better the anchorage is the higher the value  $k_2$  is. Good agreement with test results can be obtained for a value of  $k_2 = 0.75$  for double headed studs and for a value of  $k_2 = 0.50$  for stirrups.

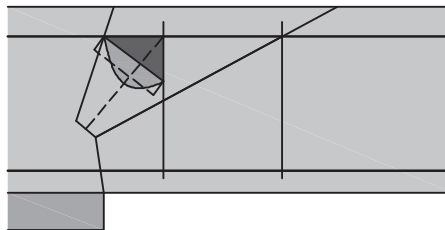


Figure 7.16: Stress distribution near the anchorage zone of the shear reinforcement

Factors  $k_1$  and  $k_2$  as well as the maximum cross-sectional area of the compression strut are not constant along the strut length. Factor  $k_1$  varies due to the variation of the transverse strain  $\varepsilon_1$ . If it is assumed that the transverse strain varies linearly, one can obtain the distribution of factor  $k_1$  (Figure 7.17a). Factor  $k_2$ , representing the variation in stresses along the strut width due to the anchorage condition, is assumed to vary linearly along the compression strut (Figure 7.17b). Thus,  $k_2$  is minimal at the anchorage zone and equal to one at the bottom end of the strut, which means that the stresses are assumed to be evenly distributed along the strut width at this location.

The cross-sectional area of the compression strut is given by the geometry and by the applied shear force. On the bottom end of the strut, the area is defined by the applied shear forces and by the compressive strength of the concrete. The area at this location increases with increasing load since generally no geometrical boundaries occur. Along the compression strut, the area increases up to the height at which the shear reinforcement crosses the crack. Since it is assumed that the compression forces are only deviated within the boundaries of the reinforcement introducing the compression force (flexural reinforcement and shear reinforcement), the area is limited by the shear reinforcement. Therefore, the area is nearly constant above this point (Figure 7.17c).

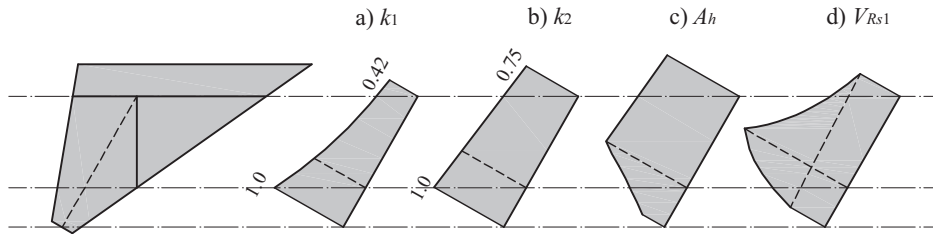


Figure 7.17: Distribution of the shear resistance  $V_{Rs1}$  (d) and its components (a)  $k_1$ , (b)  $k_2$ , and (c)  $A_h$  ( $A_h$ : Area of a horizontal section  $A_c \cdot \sin(\alpha_1)$ ) along the compression strut for specimen PL7

These parameters lead to the shear strength within the compression strut (Figure 7.17d). It has to be noted that the shear strength on the bottom end of the strut was chosen as equal as the applied shear force since no geometrical boundaries occur. In contrast, the shear force on the top end is limited by the parameters  $k_1$  and  $k_2$  and the geometrical conditions. Therefore, the proposed model assumes that the weakest part in the compression strut is at the top end close to the point where the load is introduced by the shear reinforcement.

Based on the previously mentioned considerations, the following failure criterion can be derived:

$$V_{Rs,II} = k_1 \cdot k_2 \cdot f_c \cdot \left( r_c + \frac{b_w \cdot \sin(\alpha_1)}{2} \right) \cdot 2\pi \cdot b_w \cdot \sin(\alpha_1) \quad (7.63)$$

where  $k_1$  is a factor accounting for the reduction of the strength due to transverse strains,  $k_2$  is a factor accounting for the stress distribution within the strut,  $f_c$  is the compressive strength,  $r_c$  is the radius of the column,  $b_w$  is the width of the compression strut, and  $\alpha_1$  is the inclination of the compression strut.

Introducing Equation 7.62 into Equation 7.63, the shear strength  $V_{Rs}$  can be expressed as:

$$V_{Rs,II} = k_1 \cdot k_2 \cdot f_c \cdot \left( r_c + \frac{s_c}{2} \right) \cdot 2\pi \cdot s_c \quad (7.64)$$

where  $k_1$  is a factor accounting for the reduction of the strength due to transverse strains,  $k_2$  is a factor accounting for the stress distribution within the strut,  $f_c$  is the compressive strength,  $r_c$  is the radius of the column, and  $s_c$  is the horizontal width of the compression strut.

## 7.4. Definition of model parameters

### 7.4.1. Limitation of the radial curvature $\chi_{r,lim}$ at radius $r_2$

The numerical analysis presented in Chapters 5 and 6 showed that at a certain rotation, the radial curvature at radius  $r_2$  stays approximately constant (Figure 7.18). In other words, the curvature in radial direction at radius  $r_2$  does not exceed a certain limit  $\chi_{r,lim}$ .

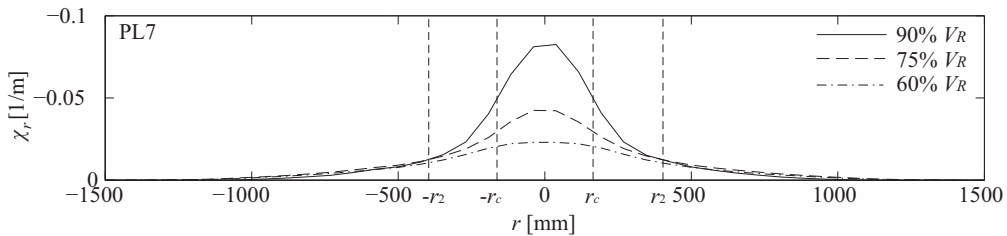


Figure 7.18: Curvature in radial direction for specimen PL7 calculated with the NLFEA approach presented in Chapter 6

This limitation can be explained with the analysis of the equilibrium conditions within this zone. From the equilibrium condition of the moments acting on a discrete slab element (Figure 7.19), one obtains the following expression:

$$[m_r \cdot r - (m_r + \Delta m_r) \cdot (r + \Delta r) + m_t \cdot \Delta r + (v + \Delta v) \cdot (r + \Delta r) \cdot \Delta r] \cdot \Delta \varphi = 0 \quad (7.65)$$

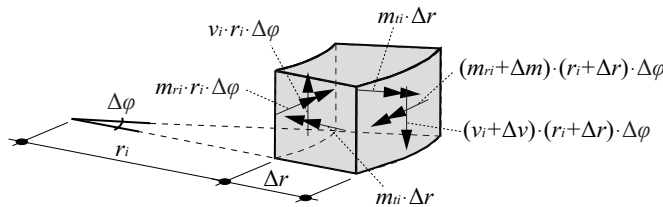


Figure 7.19: Forces acting on a discrete element of an axisymmetric slab

Solving Equation 7.65 for the difference in radial moment leads to the expression:

$$\Delta m_r = \frac{m_t - m_r + (v + \Delta v) \cdot (r + \Delta r)}{\frac{r}{\Delta r} + 1} \quad (7.66)$$

Assuming that the moment in radial  $m_r$  and tangential  $m_t$  direction reached the flexural capacity of the section  $m_R$ , Equation 7.66 can be simplified to:

$$\Delta m_r = \frac{(v + \Delta v) \cdot (r + \Delta r)}{\frac{r}{\Delta r} + 1} \quad (7.67)$$

In order to fulfill Equation 7.67, it can be stated that either the difference in moment is zero and the shear forces are zero as well or shear force is present and the difference in moment is unequal to zero. Assuming that the resultant shear force transferred across the crack acting at radius  $r_1$  (Figure 7.20a) is directly supported by the column, the shear force is equal to zero within a cone of radius  $r_1$ . Thus, within this cone the first statement applies leading to a constant moment in radial direction. On the other hand, outside radius  $r_1$ , shear forces are present and thus the second statement applies. Therefore, the absolute value of the radial moment at radius  $r_2$  is smaller than the absolute value of the radial moment at radius  $r_1$  (Figure 7.20c).

Thus, it is assumed that the limit of the curvature in radial direction  $\chi_{r,lim}$  at location  $r_2$  is reached when the radial curvature at location  $r_1$  exceeds the yielding curvature (Figure 7.20b). The curvature at  $r_1$  can be estimated using the simplified rotation distribution (and thus curvature distribution) used for the analysis of the global slab response. Therefore, the limit of the radial curvature can be expressed as:

$$\chi_{r,lim} = \frac{\chi_y}{[2 \cdot c \cdot (r_1 - r_c) + a]} \cdot [2 \cdot c \cdot (r_2 - r_c) + a] \quad (7.68)$$

where  $\chi_y$  is calculated with Equation 7.14.

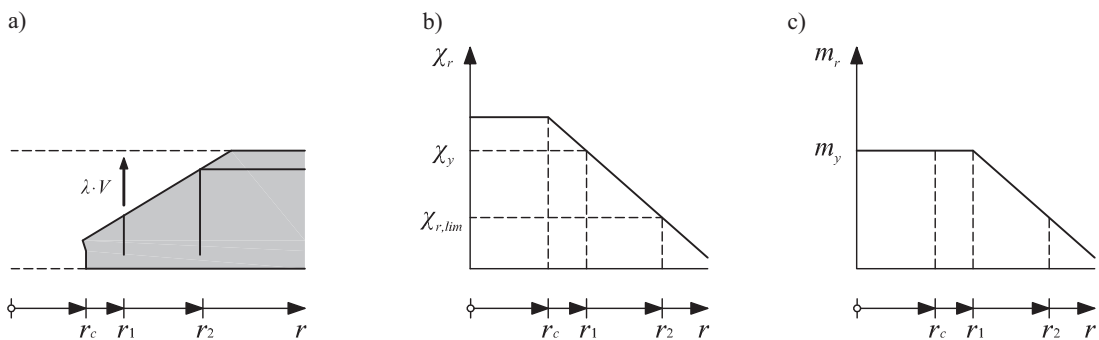


Figure 7.20: Limitation of the radial curvature at position  $r_2$  using the simplified global slab behavior

#### 7.4.2. Radius $r_0$

Generally, radius  $r_0$  can be described as the location beyond which the rotation can be assumed to be constant. Thus, the exact location should be determined at a radius at which the curvature in radial direction becomes small. One possible location could be at a radius at which the section remains uncracked since the curvatures of an uncracked section are very small. However, such a distance would not lead to a good agreement with the actual response since several other conditions of the choice of  $r_0$  need to be considered. One condition is that the simplified rotation function (quadratic function) leads to a linear variation of the curvature in radial direction (Figure 7.7b). Therefore, the radius  $r_0$  need to be chosen so that this simplification represents the distribution of the curvature best. Another condition is that the model should represent the limitation of the curvature in radial direction at position  $r_2$  accurately. In order to fulfill these three conditions most accurately, the radius  $r_0$  was chosen at a distance of  $1.5d$  from the column face but minimal at a distance of  $0.5d$  from the shear crack radius  $r_2$ . Thus, radius  $r_0$  is given by:

$$r_0 = r_c + 1.5d \geq r_2 + 0.5d \quad (7.69)$$

In order to justify this value, it can be noted that this choice of the distance  $r_0$  corresponds also to the experimentally observed principal area of rotations stated in literature (Häusler 2009). Additionally, the analytical approach can be compared to a semi-numerical approach. For the analytical approach, the load-rotation response was calculated using a curvature in radial direction at location  $r_2$  calculated using Equation 7.15 with  $r_0$  according to Equation 7.69. The semi-numerical approach uses the curvature in radial direction at location  $r_2$  calculated by the NLFEA described in Chapter 5 and 6. Figure 7.21 shows the two predicted load-rotation responses of slabs with different column sizes and different thicknesses. It can be seen that for specimens with a thickness of  $h = 250$  mm, the analytical (Equation 7.68) and the semi-numerical (NLFEA) calculations correspond well. Only for the specimen with a large thickness ( $h = 400$  mm), a difference occurs. However, it can be noted that the maximal difference at the yielding plateau is rather small (<10%). Therefore, it can be concluded that the choice of the distance  $r_0$  and the estimation of the limitation in radial curvature  $\chi_{r,lim}$  at radius  $r_2$  is reasonable.



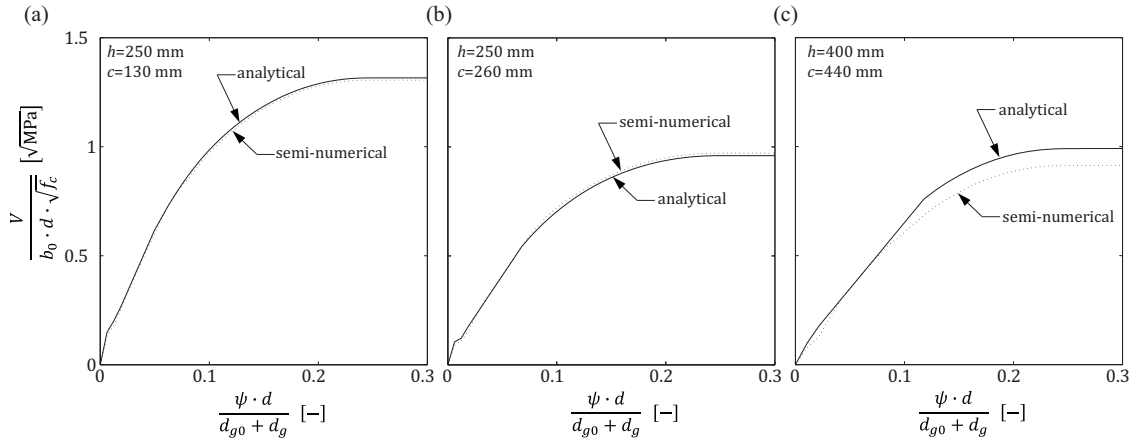


Figure 7.21: Load-rotation curve calculated by the proposed model using the radial curvature determined by Equation 7.15 and determined by the NLFEA for (a) a specimen with  $h = 250$  mm and  $c = 130$  mm (PL6), (b) a specimen with  $h = 250$  mm and  $c = 260$  mm (PL7), and (c) a specimen with  $h = 400$  mm and  $c = 440$  mm (PL10)

### 7.4.3. Shear crack distance $r_2$

The distance  $r_2$  from the center of the slab to the location where the outermost shear crack intersects the flexural reinforcement is another main parameter of the proposed model. Primarily, two assumptions lead to the determination of the distance  $r_2$ . The first assumption is that the outer shear crack starts at the top end of the compression zone  $x_2$  and has an inclination of approximately  $30^\circ$ . The second assumption is that the shear crack passes the intersection point of the flexural reinforcement and a vertical branch of shear reinforcement. This can be explained by the work that has to be performed. Since more work has to be performed to open a crack that crosses shear reinforcement, the crack is supposed to run until a vertical branch of shear reinforcement without crossing them. Based on these assumptions, it can be noted that in the case of studs with commonly used spacing, the crack and thus the distance  $r_2$  arrives at the second row of studs without crossing them (Figure 7.22a). In the case of continuous stirrups with relatively close spacing, the crack may cross one or more rows of vertical branches (Figure 7.22b and c).

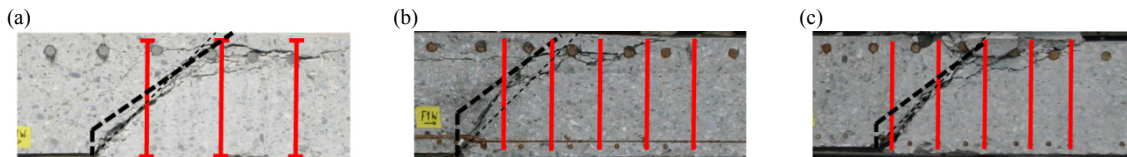


Figure 7.22: Comparison of the assumed outer shear crack and the experimentally obtained crack pattern for (a) specimen PL11, (b) specimen PF1, and (c) specimen PF2

Radius  $r_2$  basically influences the load-rotation curve and both failure criteria of the proposed model. While the load-rotation response is only slightly influenced by the distance  $r_2$ , the influence of the failure criteria especially for failure within the shear-reinforced area may be significant. This can be explained by the fact that radius  $r_2$  defines in conjunction with the spacing of the shear reinforcement the amount of shear reinforcement crossing the shear crack. Thus, the prediction of the punching strength is strongly dependent on  $r_2$  and the actual location of the shear reinforcement defined by the spacing.

For the CSCT, the influence of the spacing and the actual location of the shear reinforcement was limited by using a smeared shear reinforcement approach. Thus, a shear reinforcement ratio was determined and used in the calculations. However, the drawback of such an approach is that although the model allows considering the bond condition and the activation of each vertical branch independently, the smeared shear reinforcement approach leads to an average activation. Consequently, a main advantage of the mechanical model, the modeling of an individual activation of each vertical branch of shear reinforcement, is lost.

Using the actual location of the shear reinforcement however is sensitive to the spacing of the shear reinforcement. In fact, the change in the predicted strength is rather large if only one vertical branch is crossed by the assumed shear crack or if the assumed shear crack crosses more than one vertical branch of shear reinforcement. Figure 7.23 shows the normalized punching strength as a function of the shear reinforcement spacing for a specimen corresponding to PL12. The dashed lines show the normalized punching strength calculated with the CSCT using a smeared shear reinforcement approach and using the actual location of shear reinforcement.

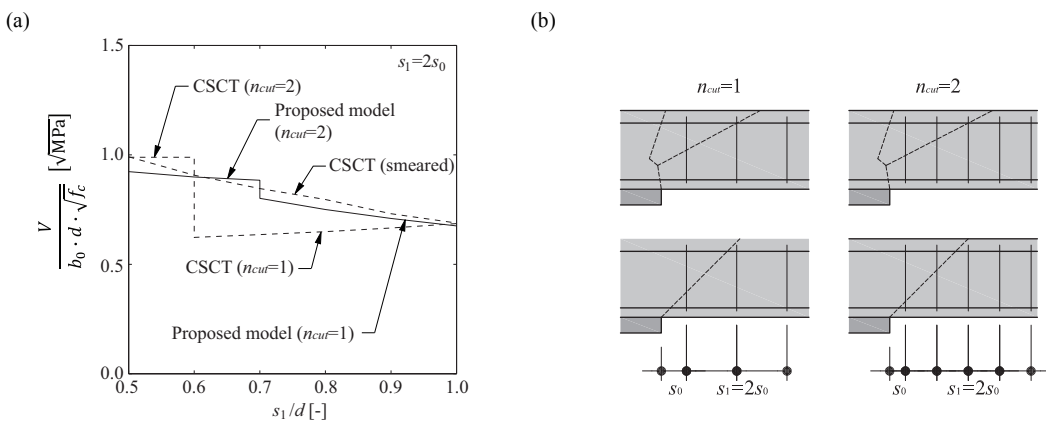


Figure 7.23: (a) Predicted punching strength as a function of the spacing of the shear reinforcement calculated with the proposed model, with the CSCT using a smeared shear reinforcement approach, and with the CSCT using the effective location of the shear reinforcement; (b) One or two vertical branches of shear reinforcement crossing the crack assuming a crack pattern according to the proposed model and the CSCT

The model proposed herein considers the spacing in the calculation of the shear force transferred across the shear crack leading to a variation of the normalized punching strength as a function of the spacing of the shear reinforcement. Furthermore, a variable angle of the shear crack reduces the magnitude of change in strength if an additional row of a vertical branch of shear reinforcement crosses the assumed shear crack (Figure 7.23). Similar to the smeared shear reinforcement approach by the CSCT, the proposed model predicts lower normalized punching strength for larger spacing. The punching strength decreases with increasing spacing since the model assumes that less force is directly transferred from outside the shear crack to the column.

#### 7.4.4. Load distribution factor $\lambda$

The load distribution factor  $\lambda$  depends on several factors such as the shear reinforcement layout, the rotation, or the concrete strength. Therefore, an exact calculation of this value requires a rather complicated approach based on the compatibility conditions in the column vicinity and the anchorage condition of the shear reinforcement. However, although this factor is used for several estimations within this model, the influence on the load-rotation response is fairly limited as shown later. Thus, a rather simple estimation of the load transfer factor is proposed that considers an estimated concrete contribution and the spacing of the studs with respect to the effective depth.

Factor  $\lambda$  is defined as the ratio of the shear force contributed by the shear reinforcement crossing the crack to the total amount of shear force:

$$\lambda = \frac{V_{s1}}{V} \quad (7.70)$$

This factor  $\lambda$  can be expressed as the product of the factors  $\lambda_c$  and  $\lambda_s$ :

$$\lambda = \lambda_c \cdot \lambda_s \quad (7.71)$$

where factor  $\lambda_c$  is the contribution of the shear reinforcement to the total shear force. In other words,  $\lambda_c$  is the ratio of the amount of shear force without the concrete contribution to the total amount of shear force. Thus, it can be expressed as:

$$\lambda_c = \frac{\Sigma V_s}{V} = \frac{V - V_c}{V} \quad (7.72)$$

Factor  $\lambda_s$  is the ratio of the shear force contributed by the shear reinforcement crossing the outer crack to the total amount of shear force contributed by the shear reinforcement. Thus, it can be expressed as:

$$\lambda_s = \frac{V_{s1}}{\Sigma V_s} \quad (7.73)$$

Factor  $\lambda_c$  can be estimated by assuming that it corresponds to the ratio of the predicted to the shear strength at a certain rotation to the predicted total shear strength at this rotation. Thus, factor  $\lambda_c$  can be estimated based on the following expression:

$$\lambda_c = \frac{V_R(\psi) - V_{Rc}(\psi)}{V_R(\psi)} \quad (7.74)$$

where  $V_{Rc}$  is defined by Equation 7.42 and  $V_R$  by Equation 7.44. However, since the maximum strength  $V_R$  depends also on the factor  $\lambda$ , the factor  $\lambda_c$  must be determined iteratively.

The force distribution between the shear reinforcement within and outside the crack can be estimated by accounting for the distances between the shear reinforcement. For general cases by which only one vertical branch of shear reinforcement crosses the outer shear crack ( $n_{cut} = 1$ ), this value can be estimated as:

$$\lambda_s = \frac{s_0 + \frac{s_1}{2}}{d} \leq 1.0 \quad (7.75)$$

where  $s_0$  is the distance between the column face and the first vertical branch of shear reinforcement,  $s_1$  is the distance between two adjacent vertical branches of shear reinforcement of same radius, and  $d$  is the effective depth.

However, if the spacing between the shear reinforcement is small, it is assumed that the shear reinforcement crossing the outer shear crack provides all the contribution of the shear reinforcement. This is proposed to be the case if more than one vertical branch of shear reinforcement crosses the outer shear crack ( $n_{cut} > 1$ ). Thus, in these cases, factor  $\lambda_s$  becomes:

$$\lambda_s = 1.0 \quad (7.76)$$

Figure 7.24 shows the comparison between the calculated load distribution factor  $\lambda$  and the one that was estimated based on the strain measurements on the shear reinforcement according to the method described in Chapter 3. It can be seen that for low load and rotation levels, a difference may occur. However, at failure the calculated factors correspond well with the estimates that are based on the measurements. Nevertheless, it has to be noted that the estimated load distribution factors show only a trend since they are based on local strain measurements on the top end of the first row of shear studs (refer to Subchapter 3.6.7).

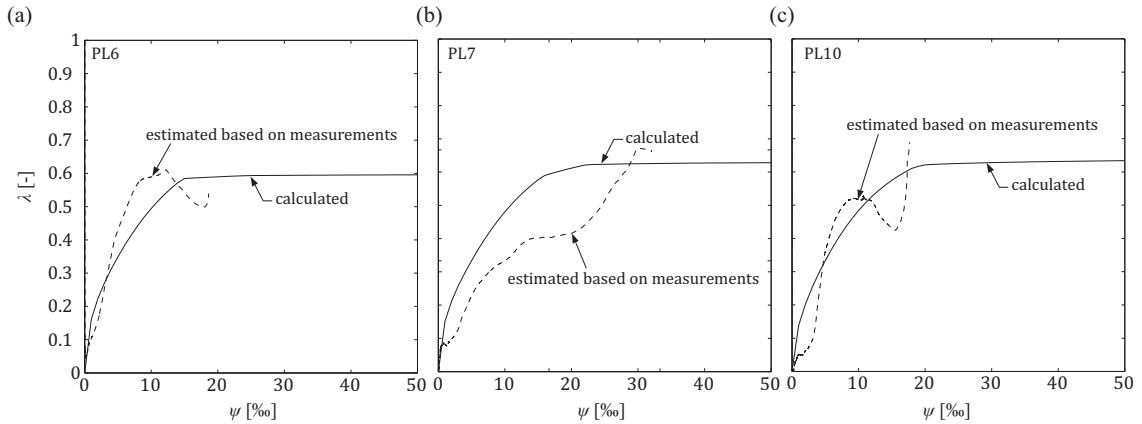


Figure 7.24: Load distribution factor estimations based on the strain measurements on the shear reinforcement and calculated as a function of the slab rotation for specimens (a) PL6, (b) PL7, and (c) PL10

Generally, it can be noted that the influence of value  $\lambda$  on the calculated load-rotation response is rather small. Figure 7.25 shows the calculated load-rotation curve for specimens with different thicknesses and column sizes for values of  $\lambda = 0.60$ ,  $\lambda = 0.75$ , and  $\lambda = 0.90$ . It can be seen that only small differences occur.

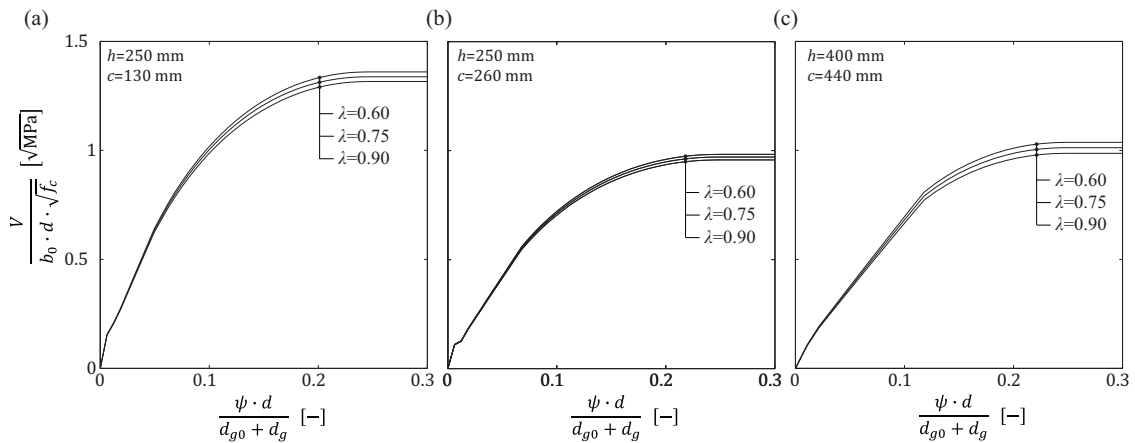


Figure 7.25: Calculated load-rotation curve for different values of  $\lambda$  for (a) a specimen with  $h = 250$  mm and  $c = 130$  mm (PL6), (b) a specimen with  $h = 250$  mm and  $c = 260$  mm (PL7), and (c) a specimen with  $h = 400$  mm and  $c = 440$  mm (PL10)

With respect to the two failure criteria, the partial factor  $\lambda_c$  has a rather limited influence. However, the influence of the partial factor  $\lambda_s$ , which accounts for load distribution between the different rows of shear reinforcement, is significant. Figure 7.26 shows the failure criteria for failure within the shear-reinforced area and failure of the compression strut for different values of  $\lambda_s$ . The different values lead to a rather large bandwidth for both failure criteria especially for failure within the shear-reinforced area. Therefore, the calculation of the punching strength may be sensitive to this value.

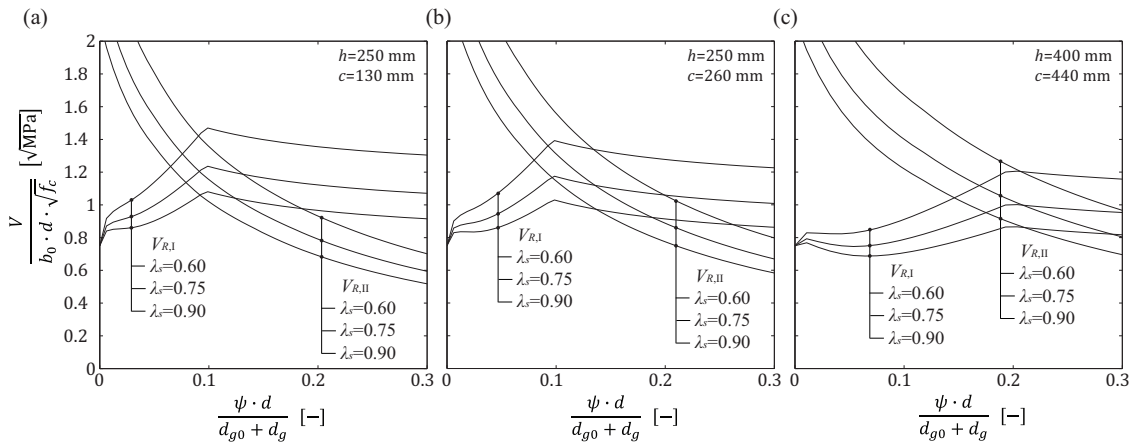


Figure 7.26: Calculated failure criteria for different values of  $\lambda$  for (a) a specimen with  $h = 250$  mm and  $c = 130$  mm (PL6), (b) a specimen with  $h = 250$  mm and  $c = 260$  mm (PL7), and (c) a specimen with  $h = 400$  mm and  $c = 440$  mm (PL10); ( $V_{R,I}$ : failure within shear reinforced area;  $V_{R,II}$ : failure of compression strut)

In order to verify the estimated value used in the calculation, one can compare this value again with the shear force in the stud estimated with the strain measurements. However, this factor cannot be obtained directly from the measurement but it can be validated by the force in the shear reinforcement. Therefore, the value of the force in the first row of studs at failure was calculated based on the local strain measurements in the shear reinforcement and based on the proposed formulations that use factor  $\lambda_s$ .

According to the proposed model, the total force taken by the shear reinforcement is given by:

$$\Sigma V_s(\psi_R) = V_R(\psi_R) - V_{Rc}(\psi_R) \quad (7.77)$$

where  $V_R(\psi_R)$  is the measured punching strength and  $V_{Rc}(\psi_R)$  is defined as:

$$V_{Rc}(\psi_R) = \frac{\frac{3}{4} \cdot b_0 \cdot d \cdot \sqrt{f_c}}{1 + \frac{15 \cdot \psi_R \cdot d}{d_{g0} + d_g}} \quad (7.78)$$

where  $\psi$  is the slab rotation,  $d$  is the effective depth,  $d_{g0}$  is a reference aggregate size equal to 16 mm,  $d_g$  is the aggregate size,  $f_c$  is the compressive strength of concrete, and  $b_0$  is the control perimeter set at a distance of  $0.5d$  from the support region with circular corners.

The forces in the shear reinforcement crossing the outer shear crack at failure can be calculated by:

$$V_{s1}(\psi_R) = \lambda_s(\psi_R) \cdot \Sigma V_s(\psi_R) \quad (7.79)$$

where the calculated value  $V_{s1}(\psi_R)$  can be compared to the value estimated from the strain measurements in the shear reinforcement.

Table 7.1 shows the calculated values and the values estimated based on the measurements for the specimen PL6, PL7, and PL10. It can be seen that generally the calculated forces in the shear reinforcement correspond well to the forces that were estimated based on the strain measurements. However, it has to be considered that the forces from the measurements are obtained indirectly by certain assumptions (see Chapter 3) and thus they involve uncertainties itself.

Table 7.1: Calculated and experimentally obtained forces in the first row of studs at failure

Specimen	$V_R(\psi_R)$ [kN]	$\psi_R$ [‰]	$V_{Rc}(\psi_R)$ [kN]	$\Sigma V_s(\psi_R)$ [kN]	$\lambda_{s,model}$ [-]	$V_{s1,calc}(\psi_R)$ [kN]	$V_{s1,measured}(\psi_R)$ [kN]
PL6	1363	18.6	376	987	0.81	799	697
PL7	1773	32	371	1402	0.81	1135	1124
PL10	5193	18.0	1077	4116	0.76	3128	3424





## **8. Validation of the Analytical Model**

The comparison of the results from the analytical model to the experimentally obtained results enables the verification of the performance of the proposed model. The comparison consists of the tests performed within this research and of tests available in literature. All the test specimens within this research and the selected test specimens from literature have an orthogonal flexural reinforcement layout and most tests specimens are square slab. Therefore, all test specimens in the selection for the validation were non-axisymmetric. However, since the model applies only for fully axisymmetric slabs, the model requires a set of parameters for the slab transformation from a non-axisymmetric to an axisymmetric slab. Therefore, the first part of this chapter covers the transformation of the slab specimens. Afterwards, it presents the performance of the proposed model with respect to the strength and rotation prediction and the influence of different parameter namely the slab thickness, the column size, and the shear reinforcement ratio. Finally, the tests were compared to the same selection of tests used in Chapter 4 to investigate the overall performance of the proposed model. A list of all test specimens considered can be found in Appendix A.

## 8.1. Transformation of the specimen

At first, the transition from the geometry of the test specimens to an axisymmetric model will be discussed. The main critical aspects to investigate are the influences of the orthogonal flexural reinforcement layout, the change from a square to a circular column shape, the change from a square to a circular slab specimen, and the application of the load. Figure 8.1 shows the transition that has to be made from the tested specimens (a,c) to an axisymmetric slab specimens (b,d). Afterwards, this chapter presents an approach to estimate the load-rotation behavior of a non-axisymmetrical slab.

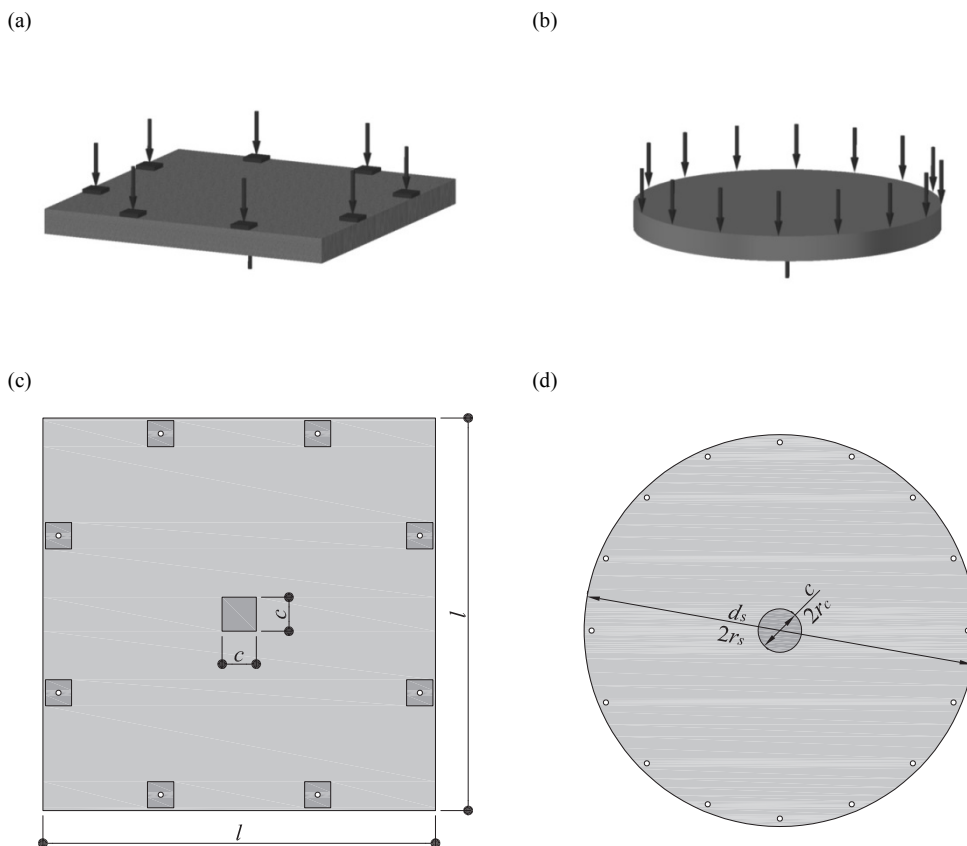


Figure 8.1: Transformation from a square slab as tested (a,c) into an axisymmetric slab (b,d)

Table 8.1 summarizes the geometry and the material properties used for the calculations. The parameters of the square slab correspond to test specimen PL7 with the exception that a flexural reinforcement of 1.0% was used instead of 1.5%. The smaller flexural reinforcement allows the slab to undergo larger deformation so that it is assured that the calculated load-rotation curve reaches the point where yielding of the flexural reinforcement starts to occur. Additionally, Table 8.1 shows the parameters of an equivalent axisymmetric slab. The determination of these parameters will be discussed subsequently.

Table 8.1: Properties of the analyzed specimens unless noted otherwise

Specimen	Square	Axisymmetric
Thickness $h$	250 mm	250 mm
Flexural reinforcement ratio $\rho_L$	1.00%	1.00%
Column size $c$	260 mm	$\varnothing 333$ mm
Effective depth $d$ (average of both directions)	210 mm	210 mm
$c/d$ ratio	1.24	1.59
Slab dimension $l; d_s$	3000 mm	$\varnothing 2992$ mm
Concrete compressive strength $f_c$	30 MPa	30 MPa
Yielding strength $f_{sy}$	500 MPa	500 MPa

### 8.1.1. Influence of the orthogonal reinforcement

A full axisymmetric model necessitates the use of circularly and radially arranged reinforcement. Since such a layout is, due to obvious reasons, not used in practice, the reinforcement is in most experimental tests orthogonally arranged. Therefore, the model should be able to account for a non-axisymmetric reinforcement layout that leads to a softening of the section at locations where the principle directions of the moment are not in the direction of the reinforcement (Figure 8.2). This phenomenon corresponds to the reduced torsional stiffness already discussed in Chapter 5. In order to account for the reduced torsional stiffness, Kinnunen (Kinnunen 1963) introduced a reduction factor. A similar factor was later used by Guandalini (Guandalini 2005) and Muttoni (Muttoni 2008) whereby it was either analytically or empirically obtained. For the analytical determination, the stiffness of a tension chord was calculated as a function of the flexural reinforcement ratio for a reinforcement layout parallel to the applied force and for a reinforcement layout at an angle of  $45^\circ$  to the applied force. Afterwards, the average of the two cases was chosen for the axisymmetric calculation. Other parameters such as the slab geometry and the loading conditions were not included in the derivation of the factor.

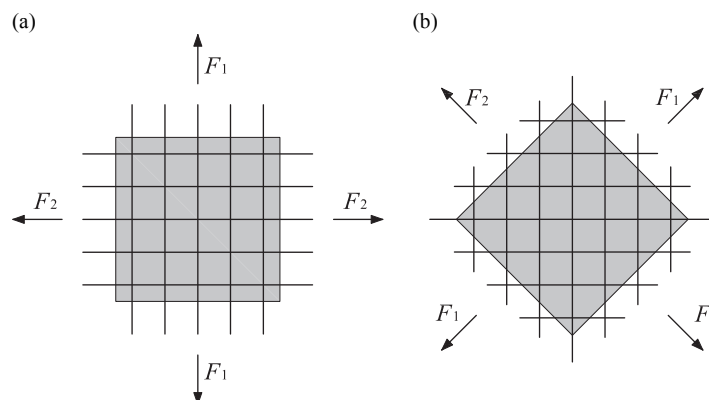


Figure 8.2: Element by which the principal forces act (a) parallel to the reinforcement or (b) at an angle of  $45^\circ$  to the direction of the reinforcement

If one defines the stiffness reduction factor as  $\beta$ -value representing the ratio between the stiffness of an element where the principal forces are acting parallel to the reinforcement and the stiffness of an element where the principal forces are acting in an arbitrary direction, this factor can be expressed as:

$$\beta = \frac{EI_1}{EI_x^{\text{II}}} \quad (8.1)$$

where  $EI_1$  is the secant flexural stiffness in the principal direction (tangential) and  $EI_x^{\text{II}}$  is the stiffness of a cracked section in parallel direction to the reinforcement obtained by using a linear-elastic behavior of steel and concrete. It can be expressed as:

$$EI_x^{\text{II}} = \rho \cdot E_s \cdot d^3 \cdot \left(1 - \frac{x_{el}}{d}\right) \cdot \left(1 - \frac{x_{el}}{3d}\right) \quad (8.2)$$

where  $\rho$  is the flexural reinforcement ratio,  $E_s$  is the Young's modulus of the reinforcing steel,  $d$  is the effective depth and  $x_{el}$  is the height of the compression zone and can be estimated as:

$$x_{el} = \rho \cdot \frac{E_s}{E_c} \cdot d \cdot \left( \sqrt{1 + \frac{2 \cdot E_c}{\rho \cdot E_s}} - 1 \right) \quad (8.3)$$

where  $E_c$  is the Young's modulus of concrete and the other parameters are defined as in Equation 8.2.

The secant flexural stiffness  $EI_1$  was calculated with the NLFEA approach explained in Chapter 5. The value of the flexural stiffness in principal (tangential) direction enables the determination of the  $\beta$ -value at any slab location according to Equation 8.1. Figure 8.3 shows the distribution of the  $\beta$ -value for a square slab specimen with properties according to Table 8.1 for different load levels. One can see that generally the stiffness in tangential direction is larger along the axis (parallel to the reinforcement) than in diagonal direction. For the load level of 60%  $V_{R,flex}$ , the  $\beta$ -value is along the axis approximately 1.0 whereas it is in diagonal direction approximately 0.5. For larger load levels the  $\beta$ -value decreases below 1.0 along the axis due to the fact that the flexural reinforcement starts yielding and thus the secant stiffness is lower than the calculated stiffness based on a linear-elastic material behavior.

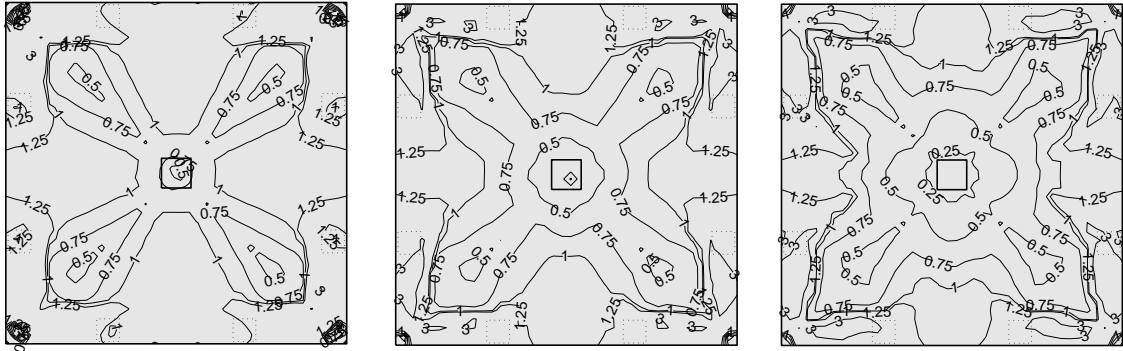


Figure 8.3: Distribution of  $\beta$ -value for load cases of (a) 60%  $V_{R,flex}$ , (b) 75%  $V_{R,flex}$ , and (c) 90%  $V_{R,flex}$

The distribution of the value depends mainly on the geometry of the slab and on the load application. Consequently, each geometry or loading may lead to a different distribution of the stiffness and thus may lead to a different slab response. Figure 8.4 shows the distribution of the  $\beta$ -value for a circular slab with load applied at the slab perimeter. In general, the behavior looks similar to the square slab for which the  $\beta$ -values are smaller in the diagonals. However, due to the equal load around the perimeter, the first principal moments in the diagonal direction are larger and thus the stiffness in the diagonals is smaller than for square slabs with only eight load introduction points.

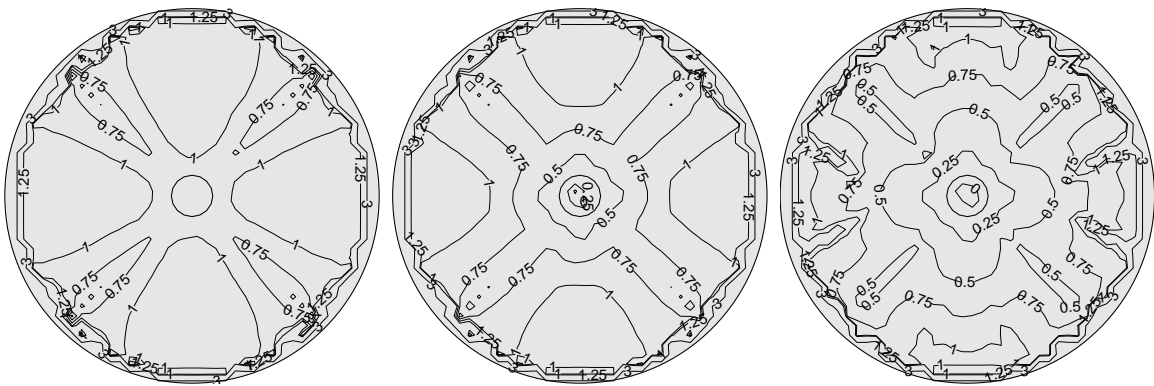


Figure 8.4: Distribution of  $\beta$ -value for load cases of (a) 60%  $V_{R,flex}$ , (b) 75%  $V_{R,flex}$ , and (c) 90%  $V_{R,flex}$

For a simplified calculation, only one average  $\beta$ -value is desired. Therefore, several different parameters and their influence on an average  $\beta$ -value were investigated by comparing the Quadrilinear model to a corresponding NLFEA. The following calculations are performed for slabs corresponding to the specimens tested within this research (square slab with loading at eight points at the perimeter). The investigated parameters were the flexural reinforcement ratio, the column size, and the slab thickness. The comparison of the curve obtained by the NLFEA to the analytical calculations using different  $\beta$ -values leads to an optimal average  $\beta$ -value for the calculation of the tested slab specimens.

### Flexural reinforcement ratio

Figure 8.5 shows the normalized load-rotation curves for slabs with different reinforcement ratios. It can be seen that the larger the reinforcement ratio is the lower the value  $\beta$  is, which corresponds to the observations of Guandalini (Guandalini 2005). However, the differences between the NLFEA calculations and the Quadrilinear curves are relatively small. Therefore, the influence of the flexural reinforcement ratio can be neglected. For all the flexural reinforcement ratio, the best agreement with the NLFEA is obtained by using a value of  $\beta = 0.75$ .

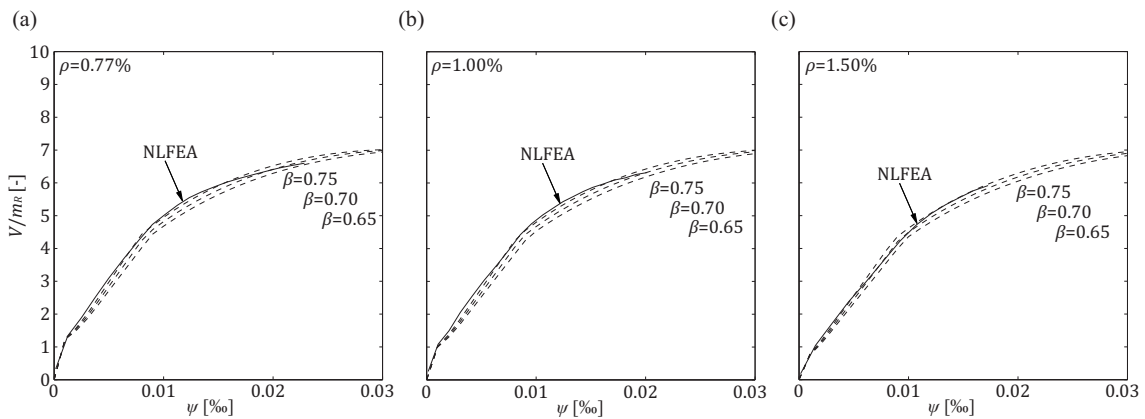


Figure 8.5: Normalized load-rotation curve of the NLFEA and the Quadrilinear approach for reinforcement ratios of: (a) 0.77%, (b) 1.00%, and (c) 1.50%

### Column size

Figure 8.6 shows the normalized load-rotation curves for slabs with different column sizes. It can be seen that the column size does not have a crucial influence on the factor  $\beta$  since the curves of all column sizes follow nearly the same pattern. This can be explained by the fact that the cross-sectional behavior is the same and that the principal direction of the moments do not change. Again, the best agreement with the results of the NLFEA is obtained by using a value of  $\beta = 0.75$ .

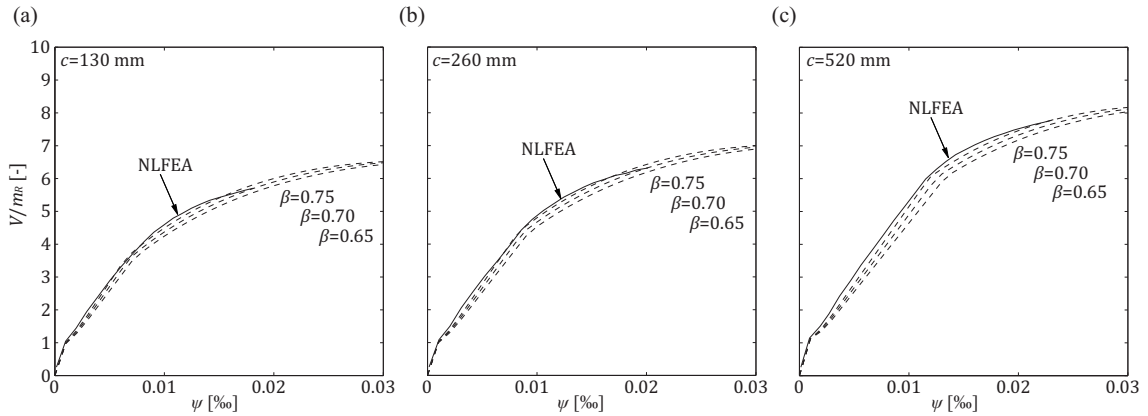


Figure 8.6: Normalized load-rotation curve of the NLFEA and the Quadrilinear approach for column sizes  $c$  of: (a) 130 mm, (b) 260 mm, and (c) 520 mm

### Slab thickness

Figure 8.7 shows the normalized load-rotation curves for slabs with different slab thicknesses. It can be seen that before yielding of the flexural reinforcement the thicker the slab is the larger the factor  $\beta$  is. For these cases a good agreement with the results of the NLFEA is again obtained by using a value of  $\beta = 0.75$ .

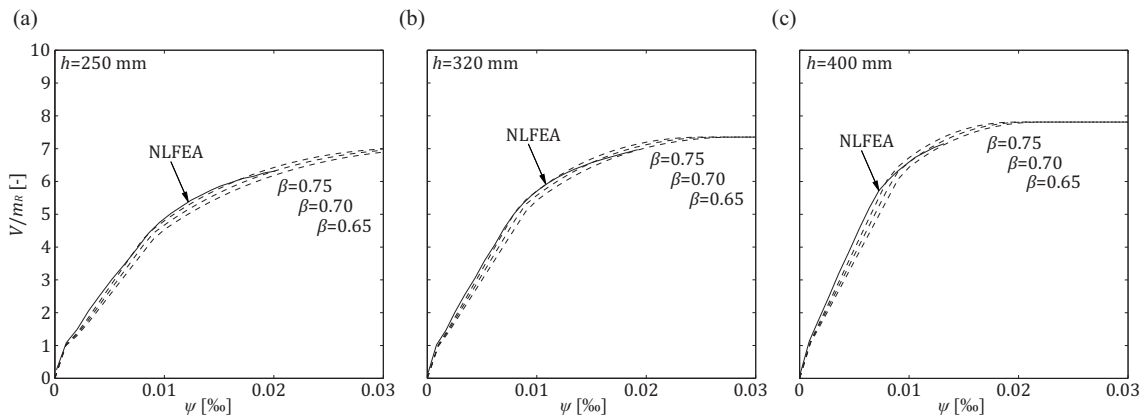


Figure 8.7: Normalized load-rotation curve of the NLFEA and the Quadrilinear approach for slab thicknesses  $h$  of: (a) 250 mm, (b) 320 mm, and (c) 400 mm

Based on this investigation, it can be noted that the influences of the investigated parameters on the  $\beta$ -value are rather small and thus they can be neglected. Thus, the proposed value is  $\beta = 0.75$  since it showed the best agreement with the NLFEA. However, it has to be noted that this value was determined based on calculations of slabs with the geometry and the loading conditions corresponding to the tested specimens. In the case of other slab geometries and loading conditions, this value might be different.

### 8.1.2. Transformation of the column shape

Generally, if symmetrical punching is investigated, two different column shapes were used: circular and square. While for circular columns no further transformation is needed, the square columns have to be transformed to circular columns in order to obtain an axisymmetric case. Guandalini (Guandalini 2005) proposed the use of an equivalent perimeter so that the shear stresses at the column face are the same for both column shapes. Therefore, the radius of the equivalent column  $r_c$  can be calculated by:

$$r_c = \frac{2}{\pi} \cdot c \quad (8.4)$$

where  $c$  is the side length of a square column.

To verify this assumption, NLFEA calculations were performed, in which square and circular column shapes were compared. The radius of the column was calculated according to Equation 8.4 to obtain an equivalent perimeter. The investigated parameters were the reinforcement ratio, the column size, and the slab thickness. For each parameter and column shape, the load-rotation curve was calculated. Additionally, The NLFEA calculations were compared to the results of the Quadrilinear model, for which a  $\beta$  value of 0.75 was used.

#### *Flexural reinforcement ratio*

Figure 8.8 shows the load-rotation curves for different flexural reinforcement ratios. It can be seen that the difference between a calculation with a square column and a circular column are small. Furthermore, it can be noted that the flexural reinforcement does not influence the transformation of the column size.

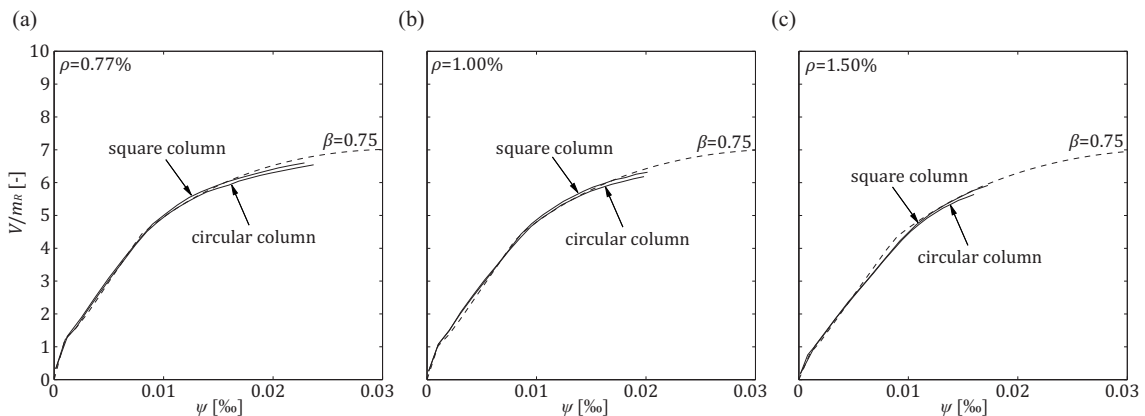


Figure 8.8: Normalized load-rotation curve of the NLFEA and the Quadrilinear approach for reinforcement ratios of: (a) 0.77%, (b) 1.00%, and (c) 1.50%



### Column size

Figure 8.9 shows the load-rotation curve for different column sizes. It can be seen that the hypothesis of an equivalent parameter works well for small column sizes. For larger column sizes the difference are somewhat larger especially after yielding of the flexural reinforcement. However, the differences stay relatively small and are thus in an acceptable range.

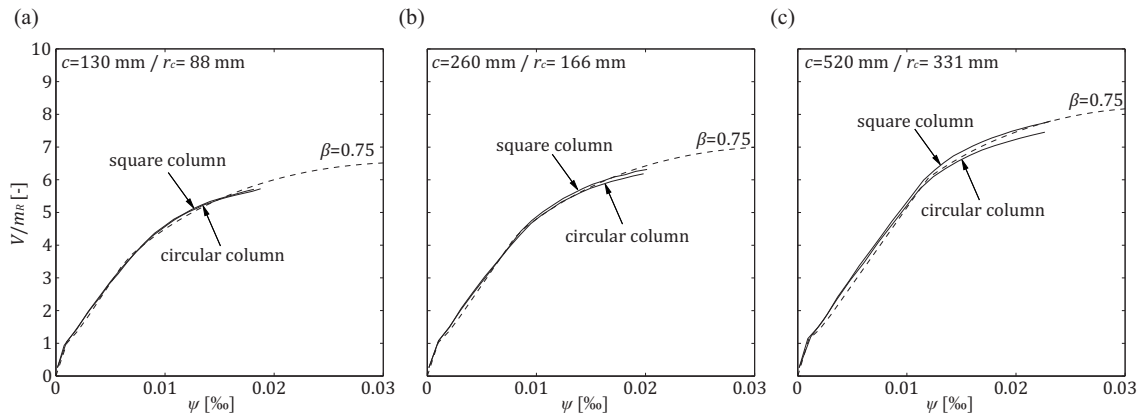


Figure 8.9: Normalized load-rotation curve of the NLFEA and the Quadrilinear approach for column sizes  $c$  of: (a) 130 mm, (b) 260 mm, and (c) 520 mm

### Slab thickness

Figure 8.10 shows the load-rotation curves for different slab thicknesses. It can be seen that again after yielding small differences occurs in the case of thicker slabs. This effect is however not due to the increased thickness but due to the increased column size since the column size to effective depth ratio was kept constant. Therefore, the thicker slabs have larger column sizes and thus the same effect occurs as described in the previous paragraph.

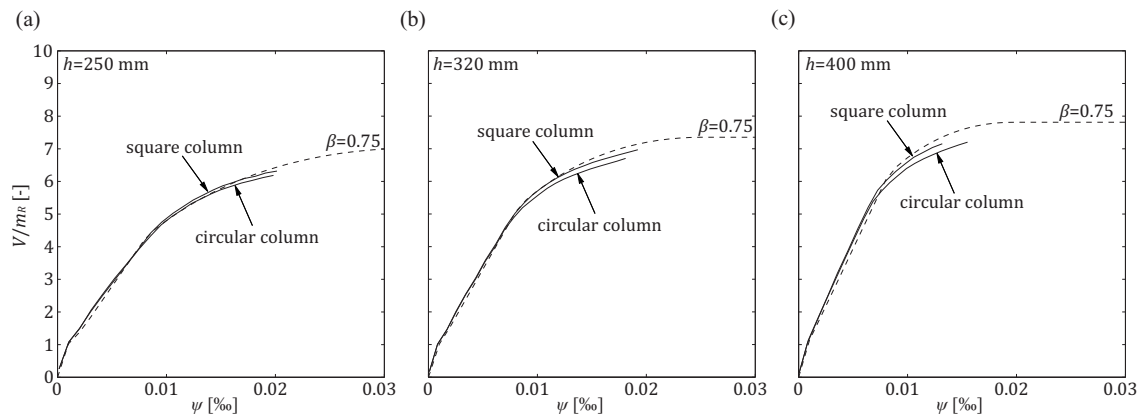


Figure 8.10: Normalized load-rotation curve of the NLFEA and the Quadrilinear approach for slab thicknesses  $h$  of: (a) 250 mm, (b) 320 mm, and (c) 400 mm

Generally, the hypothesis of an equivalent perimeter works well in all the investigated cases. For large columns however, small discrepancies can occur mainly after yielding of the flexural reinforcement. Yet, these differences are for the investigated column sizes in an acceptable range. Thus, it can be concluded that the approach of an equal perimeter is suitable for the analysis.

### 8.1.3. Transformation of slab shape and loading conditions

The transformation of the slab shape from a square slab to a circular slab can be performed by the assumptions that the maximum flexural strength ( $V_{flex}$ ) should be the same for both slab shapes. In the case of a square slab with loading at eight points, the maximum flexural strength can be calculated by assuming a mechanism as shown in Figure 8.11a leading to the following expression (Guidotti 2010):

$$V_{flex} = \frac{8m_{pl}}{l-c} \cdot \frac{l^2 - l \cdot c - \frac{c^2}{4}}{l + b - 2 \cdot (c + b_1)} \quad (8.5)$$

where  $m_{pl}$  is the flexural moment capacity,  $l$  is the side length of the slab,  $c$  is the side length of the column,  $b$  is the distance between the load introduction points, and  $b_1$  is the distance between the load introduction point and the slab edge (see Figure 8.11).

For axisymmetric slabs, the flexural strength can be calculated by assuming a mechanism as shown in Figure 8.11b leading to the expression:

$$V_{flex} = \frac{2\pi \cdot m_{pl} \cdot r_s}{r_q - r_c} \quad (8.6)$$

where  $m_{pl}$  is the flexural moment capacity,  $r_s$  is the radius of the slab,  $r_q$  is the radius of the load introduction points,  $r_c$  is the radius of the column.

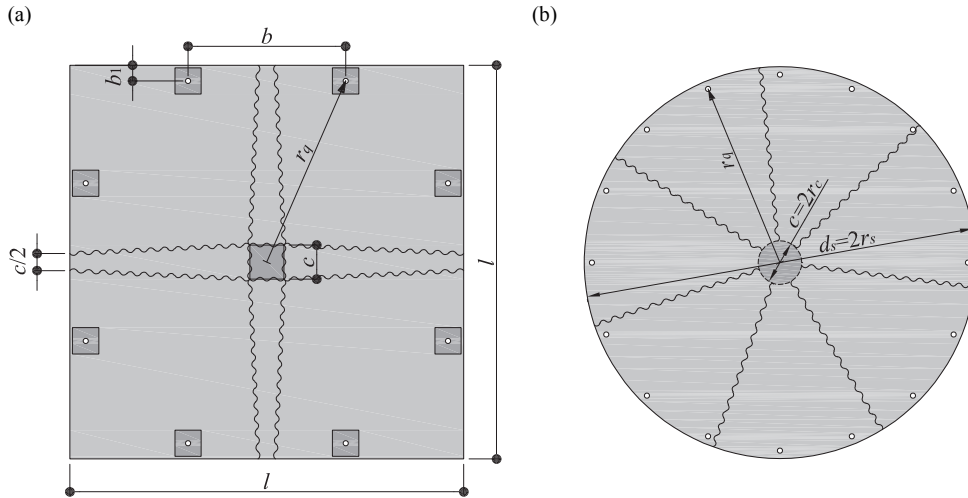


Figure 8.11: Assumed flexural failure mechanism for (a) a square slab and (b) a circular slab

The hypothesis that the flexural strength should be the same for both geometries leads to the size of the corresponding circular slab. Therefore, the radius of the circular slab  $r_s$  can be calculated by:

$$r_s = \frac{8}{l-c} \cdot \frac{\left(l^2 - l \cdot c - \frac{c^2}{4}\right) \cdot (r_q - r_c)}{2\pi \cdot [l + b - 2 \cdot (c + b_1)]} \quad (8.7)$$

where  $r_q$  is the radius of the load introduction point that can be determined by

$$r_q = \sqrt{\left(\frac{l}{2} - b_1\right)^2 + \frac{b^2}{4}} \quad (8.8)$$

In order to verify this hypothesis, calculations with square and circular slabs were performed whereby the following parameters were investigated: the flexural reinforcement ratio, the column size, and the slab thickness.

### ***Flexural reinforcement ratio***

Figure 8.12 shows the normalized load-rotation curves for different flexural reinforcement ratios. It can be seen that generally the response of the square slab and the circular slab correspond well before yielding of the flexural reinforcement occurs. After yielding the square slab behaves stiffer than the axisymmetric slab. Several different influences contribute to the different slab behavior. As seen before, the transformation of the slab geometry contributes somewhat to the softer behavior of the slab. Additionally, the load distribution is different. In the case of the axisymmetric slab the portion of torsional moment is higher than in the case of the square slab as already seen by comparing Figure 8.4 to Figure 8.3. This leads to a softer behavior due to the fact that the torsional stiffness is smaller than the flexural stiffness. However, this change in stiffness is already accounted for by factor  $\beta$ . With respect to the

flexural reinforcement ratio it can be noted that the difference stays always the same. Thus, the transformation of the slab according to the method presented does not depend on the flexural reinforcement ratio.

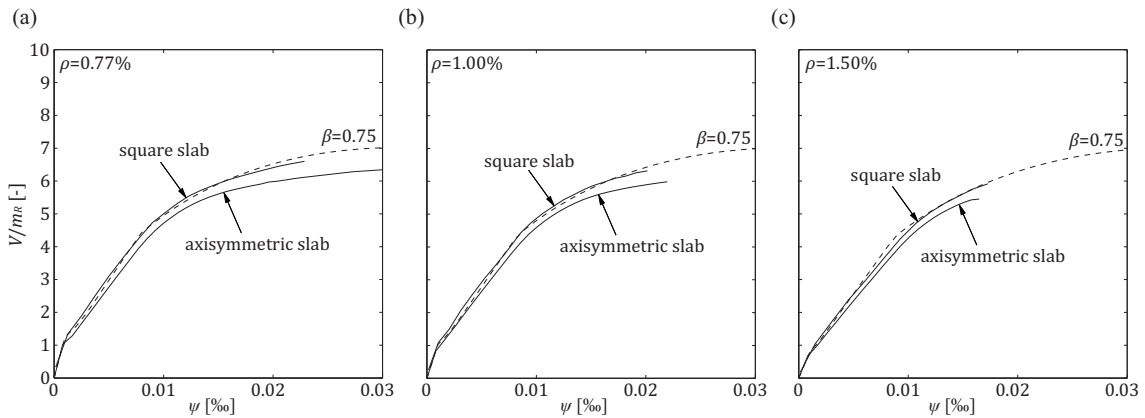


Figure 8.12: Normalized load-rotation curve of the NLFEA and the Quadrilinear approach for reinforcement ratios of: (a) 0.77%, (b) 1.00%, and (c) 1.50%

### Column size

Figure 8.13 shows the load-rotation curve for specimens with different column sizes. The change in the column size influences the difference between a square and a circular slab. The larger the column size is, the larger the difference in behavior between a square and a circular slab is. However, this influence is rather small. The main difference between a square and a circular slab is in all three cases due to the influence of the torsional stiffness as explained previously.

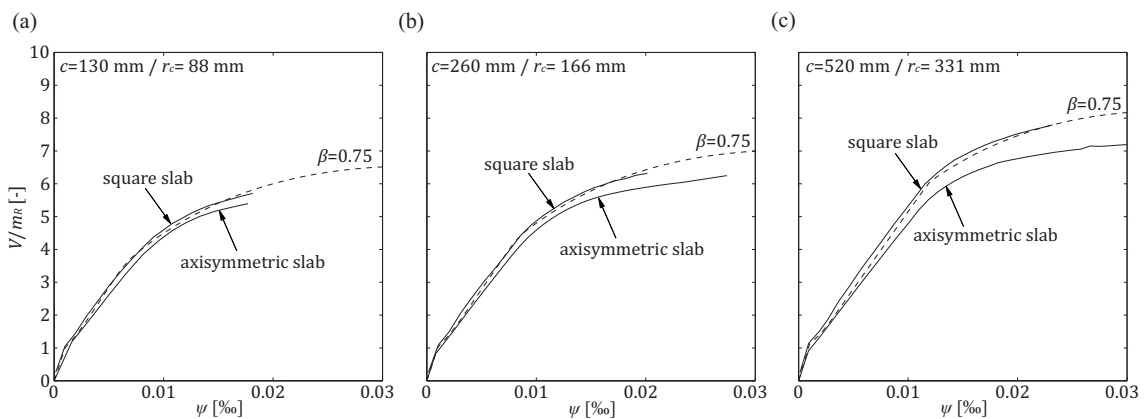


Figure 8.13: Normalized load-rotation curve of the NLFEA and the Quadrilinear approach for column sizes  $c$  of: (a) 130 mm, (b) 260 mm, and (c) 520 mm

### Slab thickness

Figure 8.14 shows the load-rotation curve for specimens with different thicknesses. It can be noted that the slab thickness does not influence the difference in the slab behavior between a square and a circular slab. The main difference is again due to the different torsional behavior as explained previously. This difference is approximately equal for all slab thicknesses. However, it seems that the difference is slightly larger for thicker slabs. This is however not due to the larger slab thickness but to the larger column size since the ratio of the column size to the effective depth ( $c/d$ ) was kept constant for these specimens. Therefore the thicker the slab is, the larger the column is and the larger the differences are (Figure 8.13).

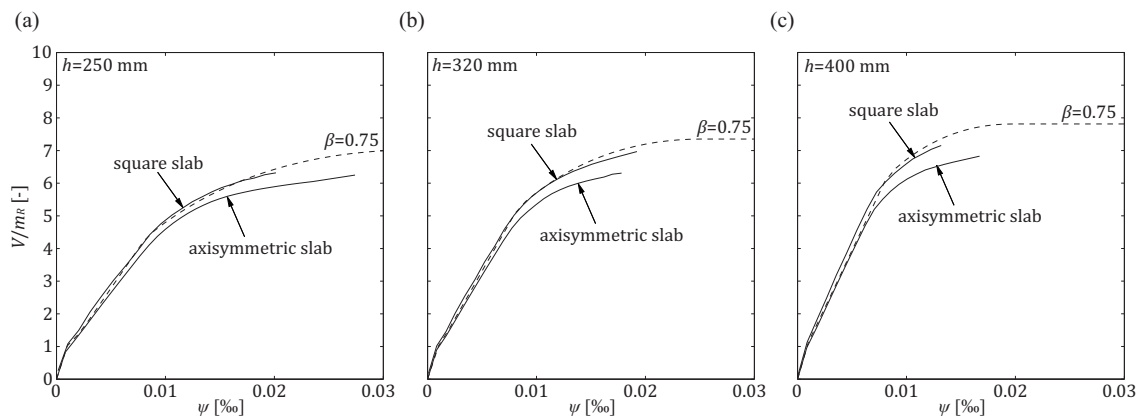


Figure 8.14: Normalized load-rotation curve of the NLFEA and the Quadrilinear approach for slab thicknesses  $h$  of: (a) 250 mm, (b) 320 mm, and (c) 400 mm

#### 8.1.4. Load application

In general, no adjustments are needed regarding the load application since the calculation of the slab dimensions already accounts for the location of the load application. However, another aspect of the load application is to distinguish between equal force applied and equal displacement applied calculations. In the first case, the loading of the specimen will be introduced by applying an equal force, whereas by the latter, loading is provided by the introduction of an equal displacement at the load introduction points. The tests within this research were performed by introducing the same force at each load introduction point. However, as described in Chapter 5, the NLFEA uses an approach in which equal displacements are applied at each load introduction point. This leads to the advantage that the calculations are more robust, especially in the case of yielding of the flexural reinforcement. The drawback of this method is that the behavior of the slab is not modeled accordingly to the experimental test procedure, which could result in wrong predictions. Nevertheless, as Figure 8.15 shows, the difference between the two calculation methods is negligible for the geometry used in the experimental campaign.

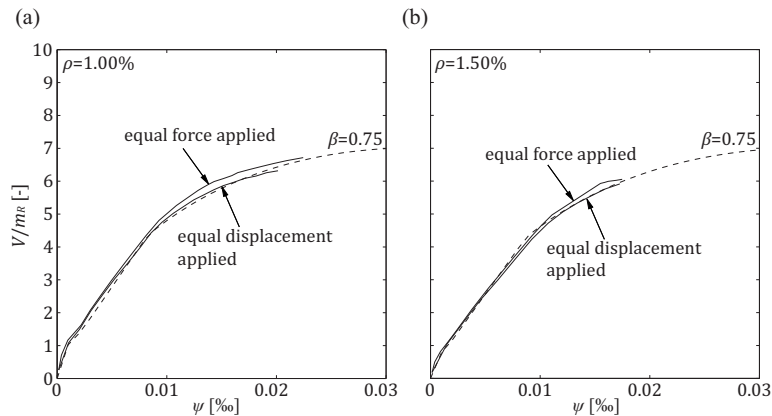


Figure 8.15: Difference between equal force and equal displacement for square slab specimens

The reason for the rather small differences can be further investigated by analyzing the global slab behavior. Figure 8.16 illustrates the behavior of a square slab for an equal displacement applied calculation and the equal force applied calculation with respect to the curvature in the first principal (tangential) direction, the moment in the first principal (tangential) direction, and the shear fields. It can be seen that no significant difference occurs between the displacement and the equal force applied calculation as it was shown by the calculated load-rotation curve presented in Figure 8.15. The curvatures are slightly smaller along the diagonals than along the direction of the load application points. This leads together with the smaller stiffness along the diagonals to larger moment along the axis and smaller moments along diagonals. This moment behavior is approximately the same for the calculation with equally applied displacement and with equally applied force. Same conclusions can be drawn from the stress fields that are similar for both cases. Therefore, in the case of square slabs loaded as the test specimen, nearly no difference in behavior occurs between an equal displacement and an equal load approach. This consideration is also important for the design of punching test set-ups. According to the calculation, no difference occurs if the force is applied at eight points and supported at the center, as it was performed within this research, or if the force is applied at the center and the displacements are kept the same at eight points at the perimeter, which would correspond to an equal displacement approach. Thus, tests performed with either one of these test set-ups are comparable. However, it has to be noted that this is only the case for square slabs with the previously described load application.

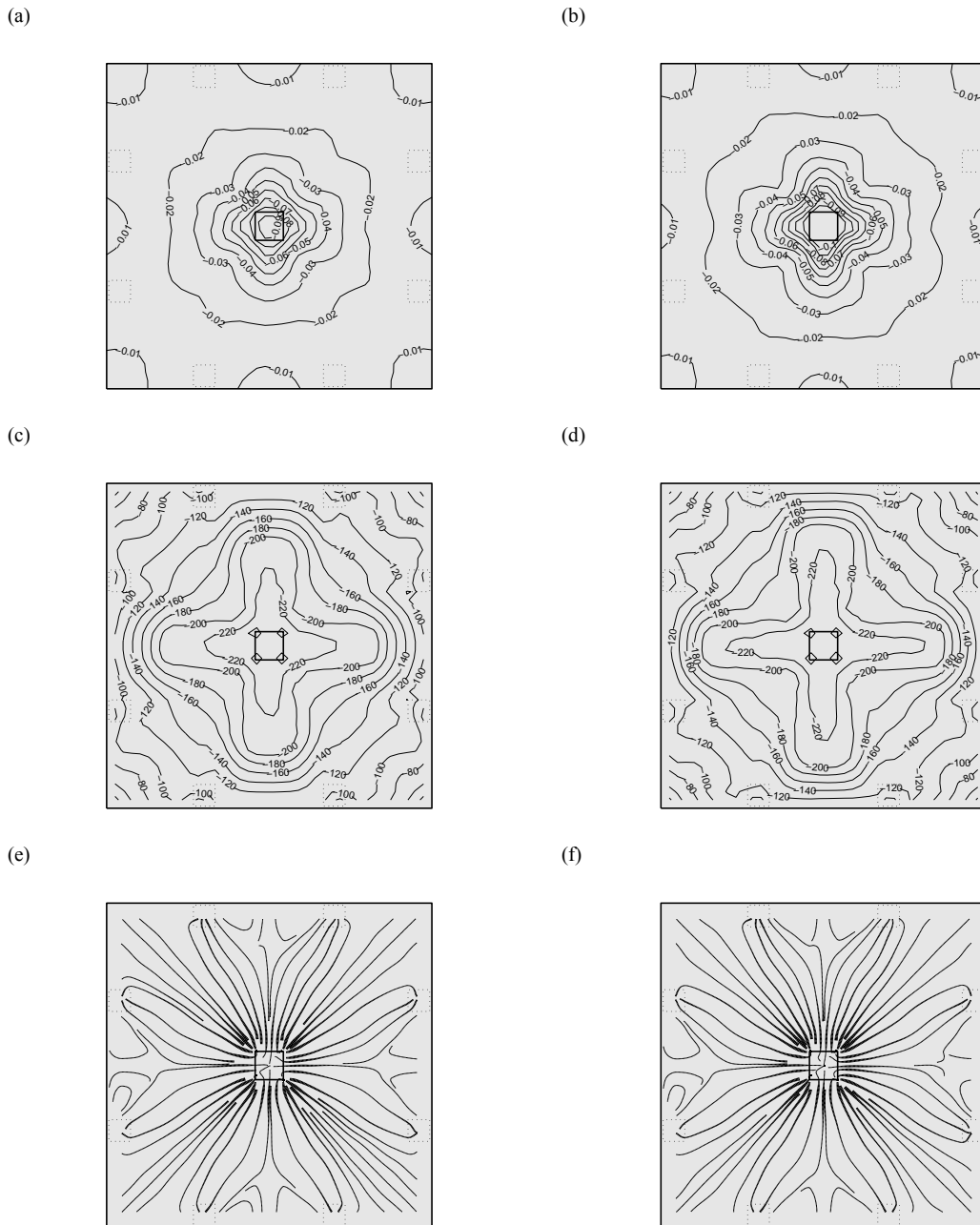


Figure 8.16: Global slab behavior of a square slab with respect to the curvature in the first principal direction  $\chi_1$  (a,b), the moment in the first principal direction  $m_1$  (c,d), and the shear fields (e,f) for an equal displacement applied (a,c,e) and an equal force applied calculation (b,d,f) ( $\rho = 1.00\%$ ;  $V / m_R = 6.0$ )

In the case of other slab geometries or loading conditions, for example for axisymmetric cases, the difference between an equal force applied or an equal displacement applied calculation may become important. Figure 8.17 presents the load-rotation curve for a calculation of a circular slab with equally applied displacement and with equally applied force. Whereas the difference between the equal displacement and equal force curve is small for square slabs, the difference for circular slabs is noticeable.

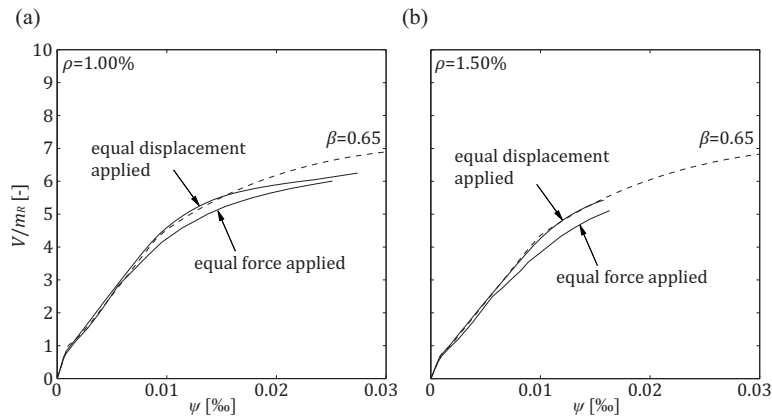


Figure 8.17: Difference between equal force and equal displacement for circular slab specimens

The difference is also clearly visible in the analysis of the slab behavior. Figure 8.18 illustrates the curvature in the first principle direction (tangential), the moment in the first principle direction (tangential), and the shear fields for an equal displacement applied and for an equal force applied calculation. While the behavior of the slab close to the column is similar in both cases, the behavior at the outer part of the slab is clearly different. In the case of the equal displacement applied calculation, the load distributes itself according to the stiffness of the slab. Therefore, the moments are larger in the more rigid direction, thus in the direction of the reinforcement. The curvatures are somewhat larger along the axis than along the diagonals. In the case of the equal force applied calculation, the force is distributed equally along the slab perimeter. Therefore, the moments are also equally distributed. In order to obtain these moments, the curvatures have to be larger along the diagonals than along the axis due to the smaller stiffness in these areas. This increase in curvature along the diagonals leads to a softer slab behavior and thus to a less stiff load-rotation response.



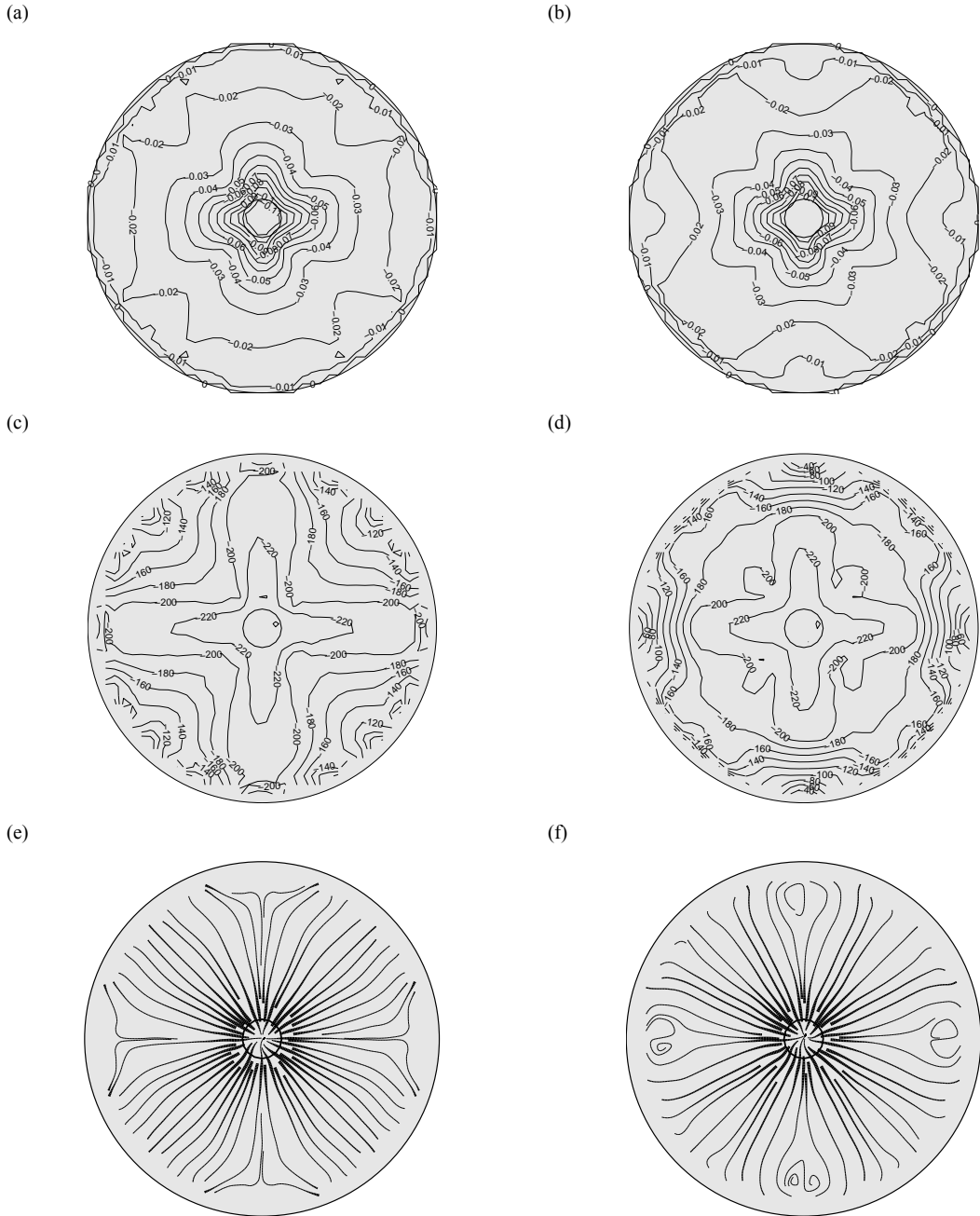


Figure 8.18: Global slab behavior of a circular slab with respect to the curvature in the first principal direction  $\chi_1$  (a,b), the moment in the first principal direction  $m_1$  (c,d), and the shear fields (e,f) for an equal displacement applied (a,c,e) and an equal force applied calculation (b,d,f) ( $\rho = 1.00\%$ ;  $V / m_R = 6.0$ )

## 8.2. Other failure modes considered

The analytical model presented in the previous chapter covers failure within the shear-reinforced area and failure of the concrete strut close to the column. However, for the validation of the proposed model to tests from literature, other failure modes have to be considered as well such as punching of slabs without shear reinforcement and punching outside the shear-reinforced area. Therefore, simplified formulation for cases of punching of slabs without shear reinforcement and for punching outside the shear-reinforced area are presented.

### 8.2.1. Punching of slabs without shear reinforcement

The simplified formulation for cases of punching of slabs without shear reinforcement is based on the CSCT and the Quadrilinear approach proposed by Muttoni (Muttoni 2008). For the load-rotation response of the slab, the only parameter adjusted compared to the proposed model, is the distribution of the rotation and thus the calculation of the curvature at the location of the shear crack  $r_2$ . Similar to the Quadrilinear model, it is assumed that the rotation is constant outside the radius  $r_2$  and that the rotation increases linearly within radius  $r_2$  leading to a constant radial and tangential curvature. Thus, the curvature at location  $r_2$  can be calculated by

$$\chi_r = -\frac{\psi_0}{r_2} \quad (8.9)$$

where  $\psi$  is the slab rotation at the outer slab segment and  $r_2$  is assumed to be at a distance  $d$  (effective depth) from the column face.

The failure criterion for punching of slabs without shear reinforcement corresponds to the formulation of the CSCT (Muttoni 2008; Fernández Ruiz and Muttoni 2009) that is also used for the concrete contribution in the proposed model. Thus, the punching strength as a function of the rotation is given by:

$$V_R = \frac{\frac{3}{4} \cdot b_0 \cdot d \cdot \sqrt{f_c}}{1 + \frac{15 \cdot \psi \cdot d}{d_{g0} + d_g}} \quad (8.10)$$

where  $\psi$  is the slab rotation,  $d$  is the effective depth,  $d_{g0}$  is a reference aggregate size equal to 16 mm,  $d_g$  is the aggregate size,  $f_c$  is the compressive strength of concrete, and  $b_0$  is the control perimeter set at a distance of  $0.5d$  from the support region with circular corners.

### 8.2.2. Punching outside the shear-reinforced area

The investigation of the failure outside the shear-reinforced area is out of scope of this research project. However, in order to compare tests from literature, this failure mode has to be addressed as well. Therefore, a simplified approach is proposed for the use in the comparison. For the prediction of the load-rotation response, the same formulation was applied as for the other failure modes (punching within the shear-reinforced area and failure of the compression strut). Nevertheless, it has to be noted that a shear crack at the outer perimeter may have an influence in the slab response. For the failure criterion, the approach of the CSCT (Fernández Ruiz and Muttoni 2009) was used. This formulation correspond to the failure criterion for punching of slabs without shear reinforcement but with an control perimeter set at a distance of  $0.5d$  from the outermost perimeter of the shear reinforcement. Thus, the punching strength outside the shear reinforcement as a function of the rotation is given by:

$$V_R = \frac{\frac{3}{4} \cdot b_{0,out} \cdot d_{v,ext} \cdot \sqrt{f_c}}{1 + \frac{15 \cdot \psi \cdot d}{d_{g0} + d_g}} \quad (8.11)$$

where  $\psi$  is the slab rotation,  $d$  is the effective depth,  $d_{v,ext}$  is the distance between the flexural reinforcement and the bottom end of the vertical branch of the shear reinforcement,  $d_{g0}$  is a reference aggregate size equal to 16 mm,  $d_g$  is the aggregate size,  $f_c$  is the compressive strength of concrete, and  $b_{0,out}$  is the control perimeter set at a distance of  $0.5d_v$  from the outermost perimeter of the shear reinforcement.

### 8.3. Validation with tests within this research

The proposed model was investigated with respect to the predicted punching strength and the influence of several different parameters namely the slab thickness, the column size, and the shear reinforcement ratio. Thus, the punching strength was calculated according to the proposed model as a function of the investigated parameter. These calculations were performed using the following assumptions: the concrete compression strength was chosen as 33.5 MPa (average of the tests), the yielding strength of the flexural reinforcement as 575 MPa (average of the tests), the yielding strength of the shear reinforcement as 550 MPa (average of the tests), the distance between the column face and the first row of shear reinforcement  $s_0$  as  $0.375d$ , the distance between the shear reinforcement  $s_1$  as  $0.75d$ , the shear reinforcement ratio as 0.9% if not varied, the effective depth as 210 mm if not varied, and the ratio of the column size to the effective depth as 1.24 if not varied. Additionally, the predicted punching strength was compared with the experimentally obtained strength of punching tests from literature in order to investigate the general performance of the proposed model.

### 8.3.1. Strength and rotation predictions

In comparison to the results from the tests performed within this research, it can be noted that the strength predicted by the analytical model is in good agreement with the experimentally obtained punching strength (Figure 8.19a). The average is close to 1.0 (Avg.: 1.01) and the coefficient of variation is rather small (COV: 5.4%). Furthermore, it can be noted that the predictions of the rotations at failure are in good agreement with the measured rotations at failure (Figure 8.19b). The predictions are generally lower than the experimentally obtained rotation at failure leading to an average of 1.17. The scatter is rather low leading to a small coefficient of variation of only 11.3%. This excellent agreement can also be seen subsequently in the comparison of the predicted load-rotation response to the measured one.

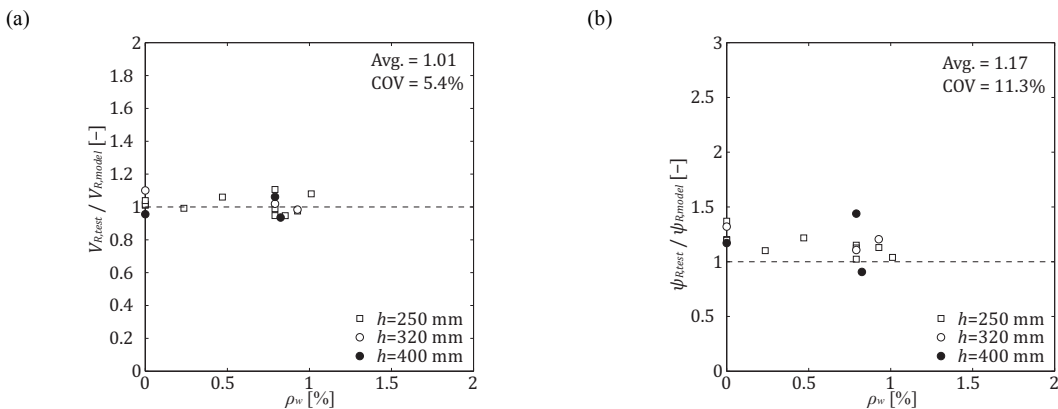


Figure 8.19: Ratio of (a) the experimentally obtained punching strength to the punching strength predicted by the analytical model and (b) the experimentally obtained rotation at failure to the rotation at failure predicted by the analytical model

### 8.3.2. Slab thickness

Figure 8.20a shows the normalized predicted punching strength as a function of the effective depth  $d$ . While the prediction for specimens without shear reinforcement and with studs shows good agreement with the test results, the prediction for specimens with stirrups differ somewhat from the test results. This can be explained by the difference between the properties of the test specimen and the properties used for the calculation. For example, the shear reinforcement ratio was larger for the calculation than the one used in the test specimens. Additionally, the spacing between the column face and the first row of vertical branch of the stirrups were not constant by the test specimens. This led to the prediction of a different failure mode. A detailed analysis of the specimen predicts a failure within the shear-reinforced area (Figure 8.23) whereas by the calculation using a standardized specimen leads to a failure of the concrete strut. Nevertheless, the overall behavior is well predicted by the proposed model for cases with studs and with stirrups. While the model predicts a small decrease in normalized strength for specimen without shear reinforcement, the model predicts a slight increase in the normalized strength with

increasing thickness. This increase in normalized strength reduces with increasing thickness leading to a nearly constant normalized strength for specimens with studs and an effective depth larger than 300 mm.

Figure 8.21a shows the prediction of the normalized rotation at failure as a function of the effective depth  $d$ . For specimens without shear reinforcement, the prediction shows good agreement with the test results. Whereas for slabs without shear reinforcement the product of the rotation at failure and the effective depth is nearly constant, for slabs with shear reinforcement, the product of the rotation at failure and the effective depth is predicted to increase nearly linearly. Thus, the model predicts that the thicker the slab is the larger the deformations at the top surface are. This can be explained by the fact that the slenderness decreases with increasing thickness since the load application radius stays constant. This decrease of slenderness leads to the prediction of larger normalized strength for larger thicknesses.

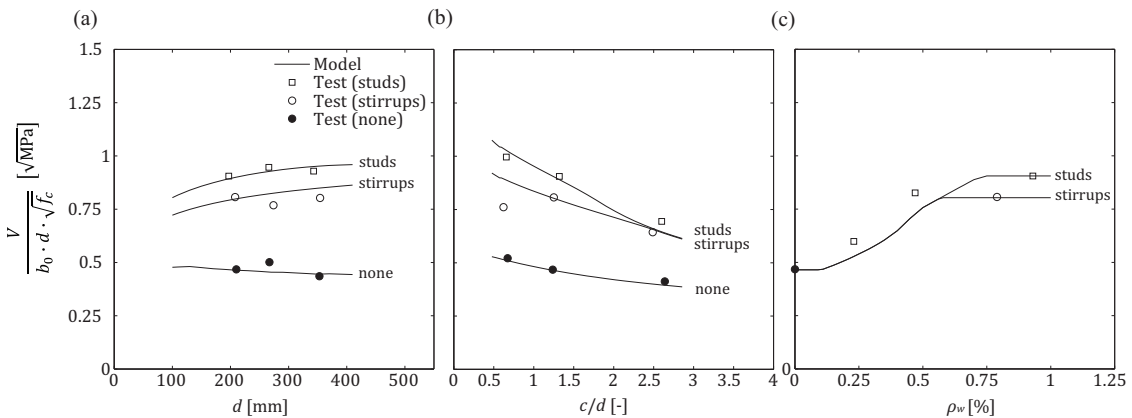


Figure 8.20: Normalized punching strength predicted by the proposed model as a function of (a) the effective depth, (b) the column size to effective depth ratio, and the shear reinforcement ratio

### 8.3.3. Column size

Figure 8.20b shows the normalized predicted punching strength as a function of the ratio of the column size to the effective depth  $c/d$ . For specimens without shear reinforcement, the predicted strength is in good agreement with the experimental results. The normalized strength decreases with increasing  $c/d$  ratio. Similarly, the predicted strength for specimens with studs is in good agreement with the test results. The decrease in normalized strength with increasing  $c/d$  ratio is slightly more dominant than for specimens without shear reinforcement. At a ratio of around 2.5 the flexural capacity is reached and thus the difference between studs and stirrups disappears. Again, the comparison of the predicted normalized strength to the test results of the specimen with stirrups has to be regarded with caution. Due to the difference in the amount and the

arrangement of the calculated and tested specimen, the prediction based on the standard specimen may lead to a different failure mode than a detailed analysis (compare to Figure 8.23h-j). This explains the difference for specimens with small column sizes by which more accurate results can be obtained if the actual amount and arrangement of shear reinforcement are used in the calculation (Figure 8.23h).

Figure 8.21b shows the prediction of the normalized rotation at failure as a function of the ratio of the column size to the effective depth  $c/d$ . For specimens without shear reinforcement, for specimens with stirrups and for specimens with studs, the predictions are in a good agreement with the test results. While the increase in rotation for larger column sizes is rather small for specimens without shear reinforcement, which can be explained by the rather large stiffness of the investigated slab specimens, the increase in rotation is significant for specimens with shear reinforcement. Especially, in the case of studs at a  $c/d$  ratio of around 2.0, the rotations increase rapidly. Thus, it can be noted that for larger  $c/d$  ratios a flexural failure may occur before a punching failure occurs as it was expected to be in the case of specimen PL8 (the test was stopped before failure, thus it is not shown in Figure 8.21b).

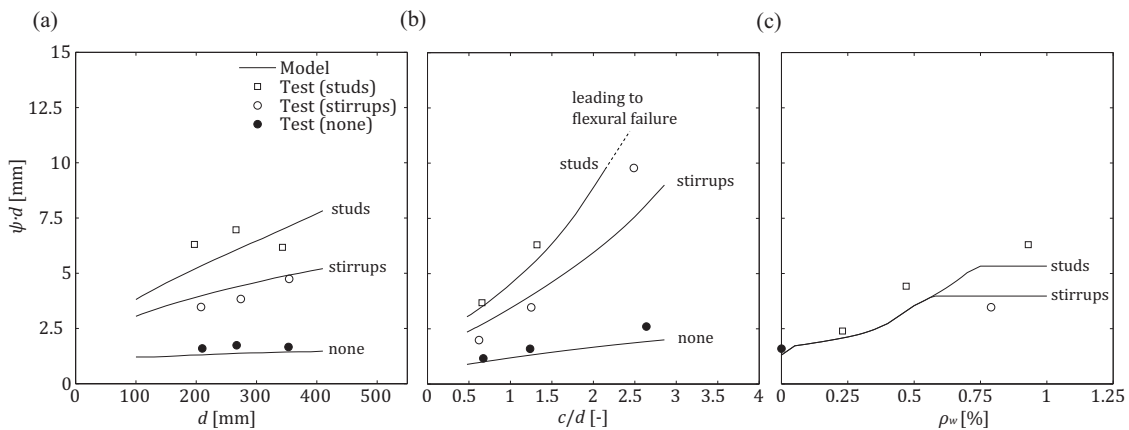


Figure 8.21: Normalized rotation at failure predicted by the proposed model as a function of (a) the effective depth, (b) the column size to effective depth ratio, and the shear reinforcement ratio

### 8.3.4. Shear reinforcement ratio

Figure 8.20c shows the normalized predicted punching strength as a function of the shear reinforcement ratio. Generally, it can be noted that the predicted strength follows the expected trend and the experimental results. The curve can generally be divided into four different parts. In a first part the strength of a calculation for slabs without shear reinforcement was taken since it provides slightly higher loads due to the change in the assumed slab response. In a second phase, the shear reinforcement is starting to contribute to the punching strength but it is not fully activated yet. In other words, the shear reinforcement is not yielding at failure. In a third phase,

the shear reinforcement is fully activated, thus it is yielding at failure. Finally, the maximum punching strength is reached at which a failure of the concrete strut is predicted.

Figure 8.21c shows the prediction of the normalized rotation at failure as a function of the shear reinforcement ratio. Since the amount of shear reinforcement affects, according to the proposed model, mainly the failure criterion and only slightly the load-rotation of the slab, the predicted rotation at failure follows the same trend as the predicted punching strength. This trend is also supported by the experimentally obtained results.

### **8.3.5. Prediction of the slab response and the failure criteria**

The calculation of the punching strength and the rotation at failure led to good agreement with the experimentally obtained results as shown in Figure 8.19. This good performance can also be seen in the comparison of the measured and the predicted load-rotation curves. Figure 8.22 shows the measured and predicted load-rotation response for specimens without shear reinforcement. In addition, Figure 8.22 shows the load-rotation response predicted by the Quadrilinear approach. Both approaches propose nearly the same response since the simplified calculation for slabs without shear reinforcement uses the same curvature at radius  $r_2$  as the Quadrilinear approach. Therefore, the proposed model predicts nearly the same load-rotation response as the Quadrilinear model showing good agreement with the measured response. Additionally, since the failure criterion of the CSCT was adopted, the predicted punching strength corresponds to the predictions obtained from the CSCT leading to a good agreement with the test results.

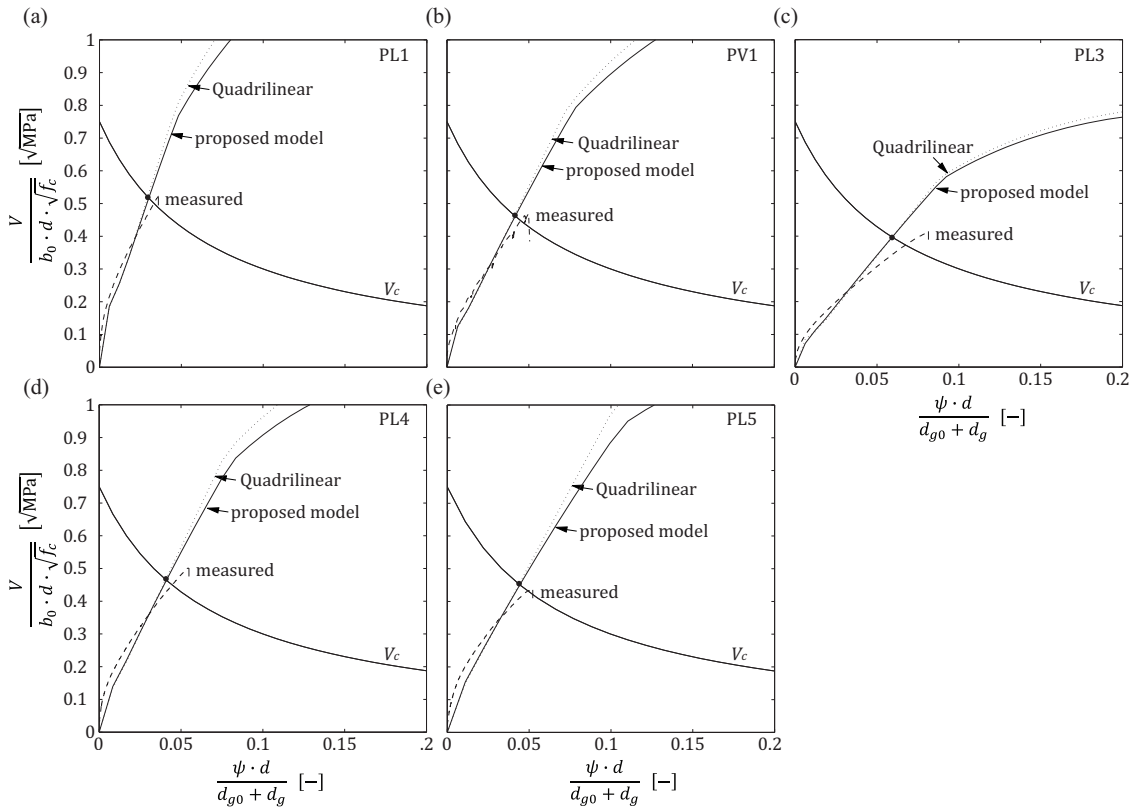


Figure 8.22: Measured and predicted load-rotation curves and failure criterion for specimens without shear reinforcement

Figure 8.23 shows the load-rotation curves for specimens with shear reinforcement. It shows the measured and predicted load-rotation response from the proposed model as well as from the Quadrilinear approach. As previously discussed in Chapter 4, the Quadrilinear approach estimates a stiffer response compared to the experimentally obtained one. In contrast, the proposed model accounts for the less stiff response leading to a good agreement with the experimental measured load-rotation curves.

Additionally, Figure 8.23 shows the failure criteria investigated within this research project: failure within the shear-reinforced area ( $V_{R,I}$ ) and failure of the concrete strut ( $V_{R,II}$ ). Generally, it can be noted that the proposed model predicts for specimens with studs (PL6, PL7, PL9, PL10) failure of the compression strut. On the other hand, for specimens with stirrups (PF2, PF4, PF5), the proposed model predicts failure within the shear-reinforced area but without full activation of all the shear reinforcement that crosses the outer shear crack. Three special cases exist: the specimen with a small column size and stirrups (PF1), the specimens with large column sizes (PL8, PF3) and the specimens with less amounts of shear reinforcement (PL11, PL12).

Due to the small column size of specimen PF1, the model predicts a larger compression zone of the outer slab element ( $x_2$ ) compared to other specimens with stirrups such as specimen PF2. The rather large height of the compression zone reduces the maximum width of the compression



strut in the wedge element used in the calculation. Thus, although less shear reinforcement crosses the shear crack according to the model in the case of specimen PF1 than in the case of specimen PF2, the model predicts nevertheless a failure of the compression strut instead of a failure within the shear-reinforced area as it is predicted for specimen PF2.

For specimens with large column sizes, it can be noted that while the model predicts a failure of the concrete strut at a normalized rotation of 0.27 for specimen PF3, which corresponds well to the normalized measured rotation at failure ( $\psi_{R, test} \cdot d / (d_{g0} + d_g) = 0.31$ ), the model predicts a failure of the concrete strut at a normalized rotation of 0.39 for specimen PL8 (the test was stopped at normalized rotation of  $\psi \cdot d / (d_{g0} + d_g) = 0.31$ ). Therefore, the proposed model predicts not only the punching failure well but also the absence of a punching failure in the case of specimen PL8.

For lower amount of shear reinforcement, the model predicts for both specimens (PL11 and PL12) a failure within the shear-reinforced area. Whereas the model predicts for specimen PL11 a failure without full activation of the shear reinforcement, it predicts for specimen PL12 a failure close to the point at which full activation of the shear reinforcement occurs.

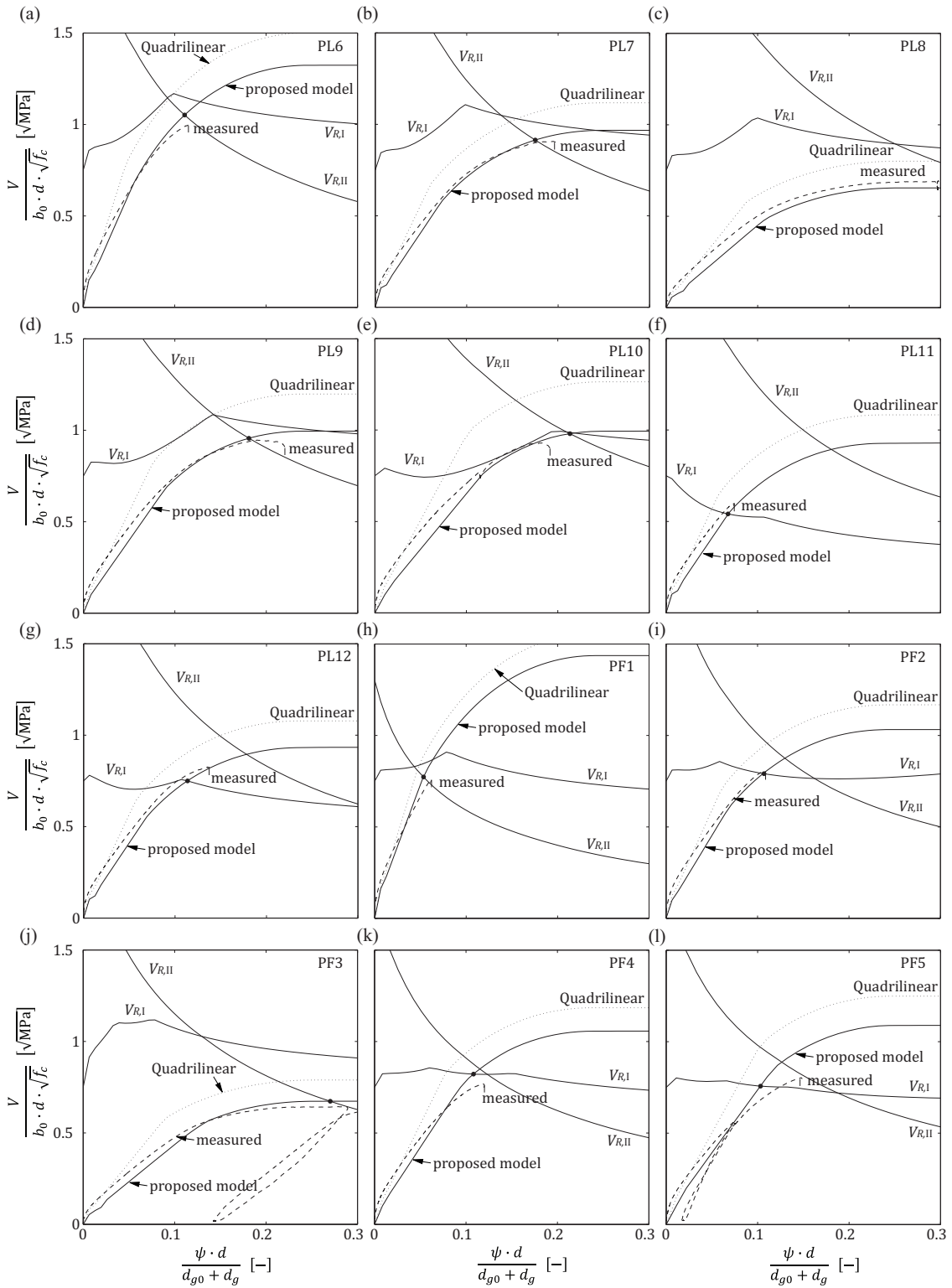


Figure 8.23: Measured and predicted load-rotation curves and failure criteria for specimens with shear reinforcement

## 8.4. Comparison to tests from literature

### 8.4.1. General

In addition to the tests within this research project, the proposed model was compared to a selection of tests from literature which was already used for the validation of the code provision and the CSCT in Chapter 4. The selection consists of 132 test specimens whereby 28 specimens without shear reinforcement and 104 specimens with shear reinforcement were used. More detailed information about the selected test specimens can be found in Appendix A. Since the proposed model is to a certain extent based on the CSCT, the results obtained by the proposed model are directly compared to the results obtained by the CSCT.

Table 8.2 presents the average and the coefficient of variation (COV) for different selections of test specimens. It can be seen that the proposed model shows generally a good agreement with the test results. If all specimens are considered, the average is close to 1.0 and the coefficient of variation is rather low. By the separation of specimens with and without shear reinforcement, it can be noted that the average and the coefficient of variation for specimens without shear reinforcement is the same as for CSCT. This can be explained by the fact that the calculation uses the same failure criterion and similar assumptions for the calculation of the load-rotation response. For specimens with shear reinforcement, it can be seen that despite the different formulation of the load-rotation response and failure criteria compared to the CSCT, the average and the coefficient of variation are nearly the same. In fact, the proposed model achieves also an average that is close to 1.0 and a low coefficient of variation of 10.9% (CSCT: 11.3%). With respect to the predicted failure modes, Table 8.2 shows that for the investigated failure modes (failure within the shear-reinforced area and failure of the concrete strut), the predictions are in good agreement with the test results. The average is for both failure modes close to 1.00. Moreover, the coefficient of variation is only 8.4% and 10.4% (CSCT: 7.8% and 12.1%) for failure of the concrete strut and failure within the shear-reinforced area, respectively. For failure outside the shear-reinforced area, the coefficient of variation is in the same range. However, this failure mode was not investigated and thus the calculation was performed with a simplified approach. Consequently, a more detailed investigation of the load-rotation response and failure criterion for failure outside the shear-reinforced area is desired.

Table 8.2: Statistical analysis of specimens from literature according to the proposed model

Selection		proposed model	CSCT
All specimens	# specimens	132	132
	Average	1.02	0.98
	COV	10.9%	10.8%
Specimens without shear reinforcement	# specimens	28	28
	Average	0.95	0.95
	COV	8.4%	8.4%
Specimens with shear reinforcement	# specimens	104	104
	Average	1.04	0.99
	COV	10.8%	11.3%
Specimens with predicted failure: crushing of concrete strut	# specimens	14	22
	Average	0.99	0.91
	COV	8.4%	7.8%
Specimens with predicted failure: within shear-reinforced area	# specimens	47	46
	Average	1.04	1.03
	COV	10.4%	12.1%
Specimens with predicted failure: outside shear-reinforced area	# specimens	38	36
	Average	1.05	1.00
	COV	11.7%	8.8%

In order to investigate the influence of certain parameters on the agreement of the predictions and the test results, the ratio of the experimentally obtained punching strength and the strength predicted by the proposed model (figures in the center) is shown as a function of several parameters namely the shear reinforcement ratio, the effective depth, the column size, the flexural reinforcement ratio, the concrete compressive strength, and the maximum aggregate size. Again, the results of the proposed model are directly compared to the CSCT. For this, the ratio of the experimentally obtained punching strength and the strength predicted by the CSCT is shown as well (figures on the left). In addition, the ratio of the strength predicted by the CSCT to the strength predicted by the proposed model is shown (figures on the right) to analyze the difference of the two models as a function of the previously mentioned parameters.

#### 8.4.2. Shear reinforcement ratio

Figure 8.24 shows the ratio of the experimentally obtained punching strength and the predicted strength as a function of the shear reinforcement ratio. Basically, the shear reinforcement ratio defines the failure mode and the punching strength for failure within the shear-reinforcement ratio. With respect to the load-rotation response, it can be noted that the load-rotation response calculated with the CSCT is independent of the amount of shear reinforcement. In contrast, the load-rotation response calculated with the proposed model depends somewhat on the amount of shear reinforcement as the amount of shear reinforcement is considered in the calculation of the load-distribution factor  $\lambda$ . However, since the load-distribution factor has only marginal

influence on the load-rotation response, the influence of the amount of shear reinforcement on the response is rather limited.

With respect to the comparison of the test results with the proposed model, it can be noted that specimens without shear reinforcement lead to lower strength ratios than specimens with shear reinforcement. Additionally, it can be seen that the proposed model predicts failure of the concrete strut only for moderate to large shear reinforcement ratios ( $\rho_w > 0.5\%$ ). For lower shear reinforcement ratios, the predicted failure mode is either failure within or failure outside the shear-reinforced area. In comparison to the CSCT, it can be noted that although the approaches are different, the results are rather close. No tendency occurs if the two models are directly compared (Figure 8.24c).

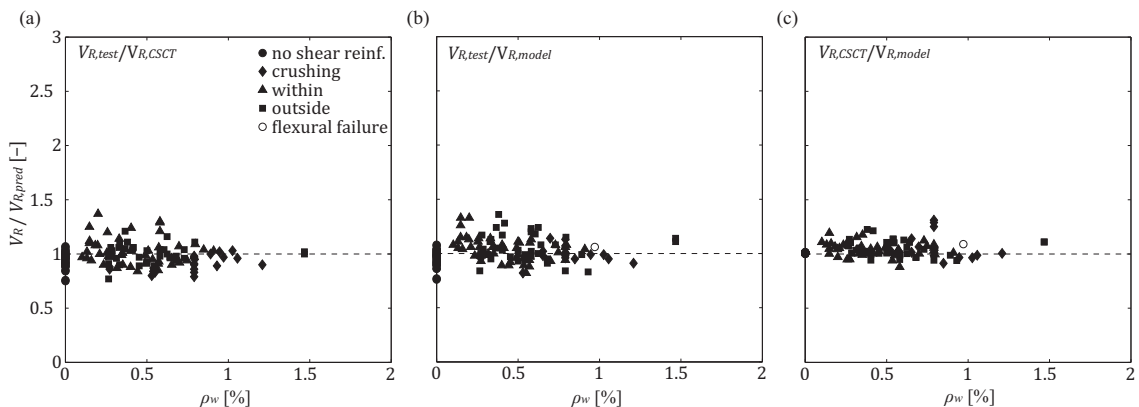


Figure 8.24: Punching strength ratio (a)  $V_{R,test}/V_{R,CSCT}$ , (b)  $V_{R,test}/V_{R,model}$ , and (c)  $V_{R,CSCT}/V_{R,model}$  as a function of the shear reinforcement ratio

### 8.4.3. Effective depth

Figure 8.25 shows the ratio of the experimentally obtained punching strength and the predicted strength as a function of the effective depth. The effective depth is the main parameter defining the slab stiffness and thus the main parameter for the calculation of the load-rotation response. Additionally, the effective depth influences as well the failure criteria in both models. Regarding the concrete contribution, the effective depth defines the shear resisting area ( $d \cdot b_0$ ) and the opening of the shear crack ( $w \propto \psi \cdot d$ ). The crack opening is also the main parameter for the failure criterion for failure within the shear-reinforced area in both approaches (the CSCT and the proposed model). For the failure criterion of crushing of the concrete strut, the effective depth is related to the strains transverse to the concrete strut and thus influences the strength of the compression strut. With respect to the comparison of the test results with the proposed model, it can be noted that no clear tendency exists with respect to the effective depth (Figure 8.25b). Additionally, it can be noted that the prediction of the failure mode does not depend on the effective depth although the proposed model accounts only little for size effects. Moreover,

the comparison to the CSCT reveals that the two models show nearly the same results and the same tendency (Figure 8.25c).

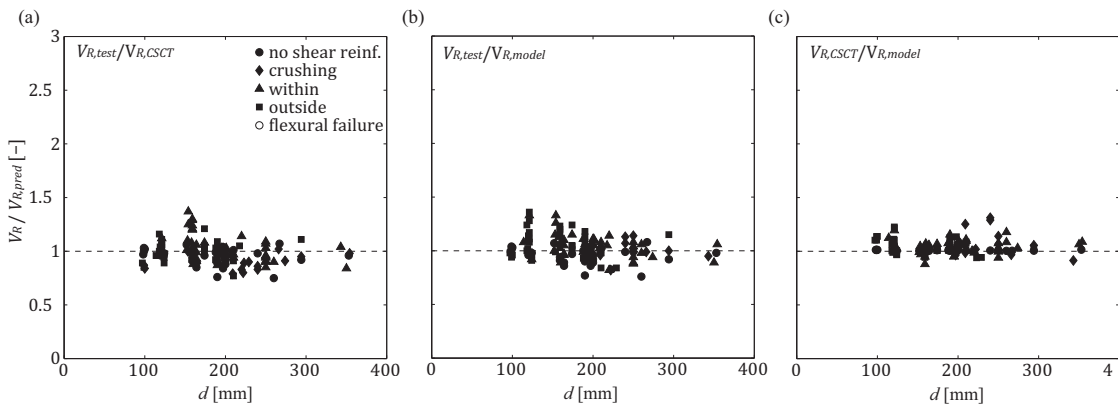


Figure 8.25: Punching strength ratio (a)  $V_{R,test}/V_{R,CSCT}$ , (b)  $V_{R,test}/V_{R,model}$ , and (c)  $V_{R,CSCT}/V_{R,model}$  as a function of the effective depth

#### 8.4.4. Column size

Figure 8.26 shows the ratio of the experimentally obtained punching strength and the predicted strength as a function of the column size. The column size influences the load-rotation response by defining the distribution of the rotation and by the flexural capacity. Additionally, in the case of the proposed model the column perimeter defines directly the height of the compression zone. Generally, it can be noted that smaller column sizes lead to larger compression zones and vice versa. Since the proposed model defines the location of the outer shear crack depending on the height of the compression zone, it has an influence on the width of the compression strut and to certain extent on the amount of shear reinforcement crossing the shear crack. Thus, both failure criteria depend on the height of the compression zone and thus on the column size. In contrast, the failure criteria of the CSCT account for the column size generally in the expression of the control perimeter  $b_0$ . Regarding the comparison to the test results, it can be noted that the predictions of the proposed model show no clear tendency with respect to the column size to effective depth ratio (Figure 8.26b). The comparison with the CSCT shows that the proposed model lead generally to more conservative predictions, which improves somewhat the results of small column to effective depth ratios (Figure 8.26c).

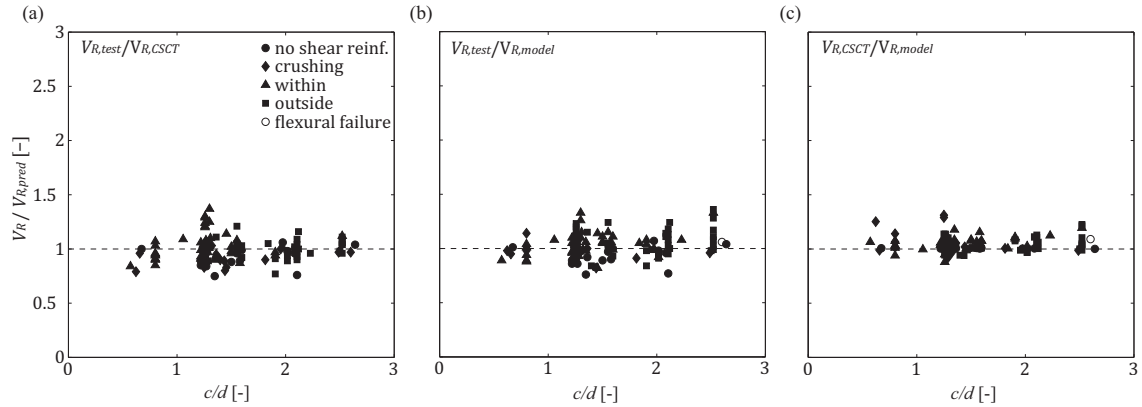


Figure 8.26: Punching strength ratio (a)  $V_{R,test}/V_{R,CSCT}$ , (b)  $V_{R,test}/V_{R,model}$ , and (c)  $V_{R,CSCT}/V_{R,model}$  as a function of the column size to the effective depth ratio

#### 8.4.5. Flexural reinforcement ratio

Figure 8.27 shows the ratio of the experimentally obtained punching strength and the predicted strength as a function of the flexural reinforcement ratio. The flexural reinforcement influences only the calculation of the load-rotation response. Thus, the failure criteria are independent of the flexural reinforcement ratio. This applies for the CSCT as well as for the proposed model. Regarding the comparison to the test results, no tendency with respect to the flexural reinforcement ratio can be noted for the comparison of the results of the proposed model to the test results (Figure 8.27b). Additionally, it can be noted that the proposed model considers the influence of the flexural reinforcement similarly to the CSCT since no tendency can be seen by comparing the results of the two approaches (Figure 8.27c).

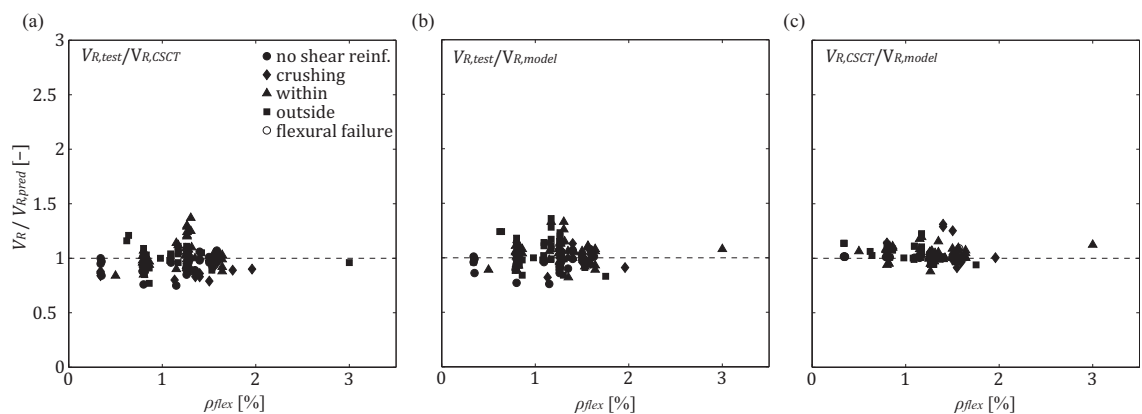


Figure 8.27: Punching strength ratio (a)  $V_{R,test}/V_{R,CSCT}$ , (b)  $V_{R,test}/V_{R,model}$ , and (c)  $V_{R,CSCT}/V_{R,model}$  as a function of the flexural reinforcement ratio

### 8.4.6. Concrete compressive strength

Figure 8.28 shows the ratio of the experimentally obtained punching strength and the predicted strength as a function of the concrete compressive strength. The CSCT and the proposed model consider the concrete strength for the calculation of the flexural strength influencing somewhat the load-rotation response. Regarding the failure criteria, the CSCT relates the punching strength to the square root of the compressive strength for punching of slabs without shear reinforcement, for the concrete contribution for failure within the shear-reinforced area and for the crushing of the concrete strut. The proposed model relates also the punching strength to the square root of the compressive strength for punching of slabs without shear reinforcement, for the concrete contribution for failure within the shear-reinforced area and for the concrete contribution for failure of the concrete strut. However, the proposed model relates the strength of the compression strut directly to the compressive strength. With respect to the comparison with the test results, it can be noted that most tests were performed with normal strength concrete leading to a cloud of points as already observed in the code validation in Chapter 4. Consequently, no clear tendency can be seen for the proposed model or the CSCT. Although from a theoretical point of view, an investigation of higher strength concrete may lead to interesting observations, from a practical point of view, it has to be noted that the general gains by using high-strength concrete for flat slabs are rather limited.

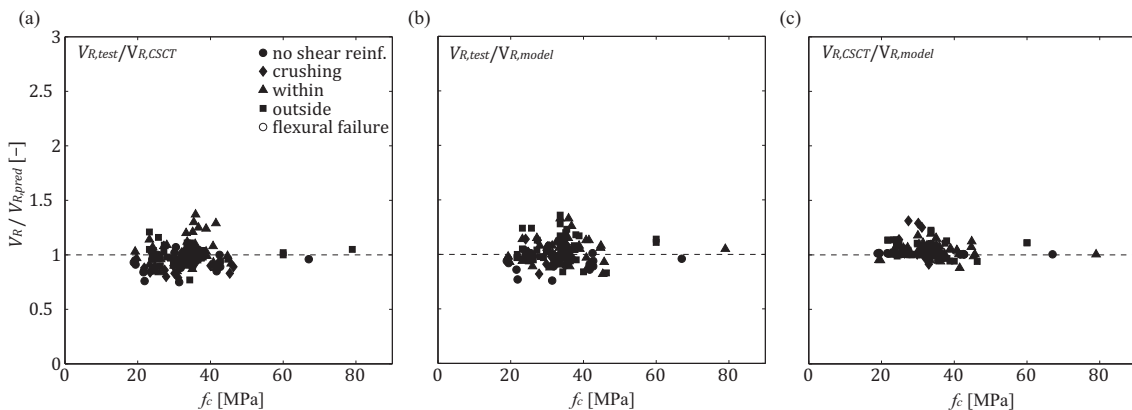


Figure 8.28: Punching strength ratio (a)  $V_{R,test}/V_{R,CSCT}$ , (b)  $V_{R,test}/V_{R,model}$ , and (c)  $V_{R,CSCT}/V_{R,model}$  as a function of the concrete compressive strength

### 8.4.7. Maximum aggregate size

Figure 8.29 shows the ratio of the experimentally obtained punching strength and the predicted strength as a function of the maximum aggregate size. The proposed model considers the aggregate size only in the calculation of the concrete contribution to the punching strength for both failure modes. Thus, the proposed model does not account for the aggregate size for the strength of the compression strut. In contrast, the CSCT considers the aggregate size for all



failure modes. Nevertheless, the proposed model leads to good predictions for all aggregate sizes (Figure 8.29b) and shows similar tendency as the CSCT does (Figure 8.29c).

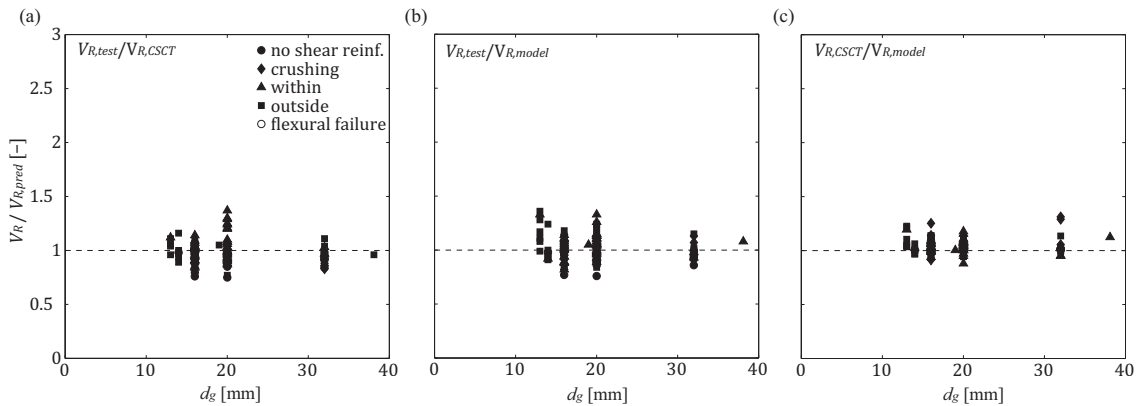


Figure 8.29: Punching strength ratio (a)  $V_{R,test}/V_{R,CSCT}$ , (b)  $V_{R,test}/V_{R,model}$ , and (c)  $V_{R,CSCT}/V_{R,model}$  as a function of the maximum aggregate size

#### 8.4.8. Predicted rotation at failure

Similar to the CSCT and the fib Model Code 2010 (MC 2011), the proposed model defines the punching strength as a function of the rotation of the slab. Therefore, an interesting aspect is the prediction of the rotation at failure. Figure 8.30 shows the ratio of the experimentally obtained punching strength and the predicted strength as a function of the predicted rotation at failure for MC 2010, the CSCT, and the proposed model. Generally, it can be noted that MC 2010 and the CSCT predict smaller rotations at failure than the proposed model does. Since MC 2010 is a code provision and thus lower strength are predicted, the prediction of the rotations are smaller as well, which explains the lower predicted rotations compared to the predictions of the CSCT and the proposed model. However, more important in this case is that MC 2010 does not show any tendency regarding the ratio of the experimentally obtained punching strength and the predicted strength with respect to the predicted rotations.

The CSCT seems to have a tendency of predicting lower ratios of the experimentally obtained punching strength and the predicted strength when larger rotations are predicted. This tendency can be explained by the overestimation of the slab stiffness. For slab specimens for which smaller rotations are predicted, the discrepancies in the load-rotation response are smaller leading to better estimates of the punching strength. Furthermore, it can be seen that this affects mainly the predicted failure mode of crushing of the concrete strut since generally larger rotations are predicted for this failure mode. This observation corresponds with the statistical values presented in Chapter 4 by which it can be seen that for failure due to crushing of the concrete strut the average of the ratios of the experimentally obtained punching strength and the predicted strength is smaller (Average = 0.92) than for failure within and outside the shear-reinforced area (Average = 1.03 and 1.00, respectively).

In contrast, the proposed model shows the opposite tendency. The proposed model predicts larger ratios of the experimentally obtained punching strength and the predicted strength for specimens by which larger rotations are predicted. Additionally, Figure 8.30c shows that for larger predicted rotation, a failure outside the shear-reinforced area is estimated. It can be noted that all the tests with predictions of large rotations ( $\psi > 30\%$ ) had either a ratio of the column size to the effective depth  $c/d > 2.0$  or a flexural reinforcement ratio  $\rho < 0.5\%$  so that the flexural limit is obtained. Consequently, the proposed model may underestimate the flexural strength in the case of failure outside the shear-reinforced area. In addition, it can be noted that due to the prediction of a less stiff response of the slabs, the proposed model generally leads to larger estimates of rotations at failure than the CSCT does.

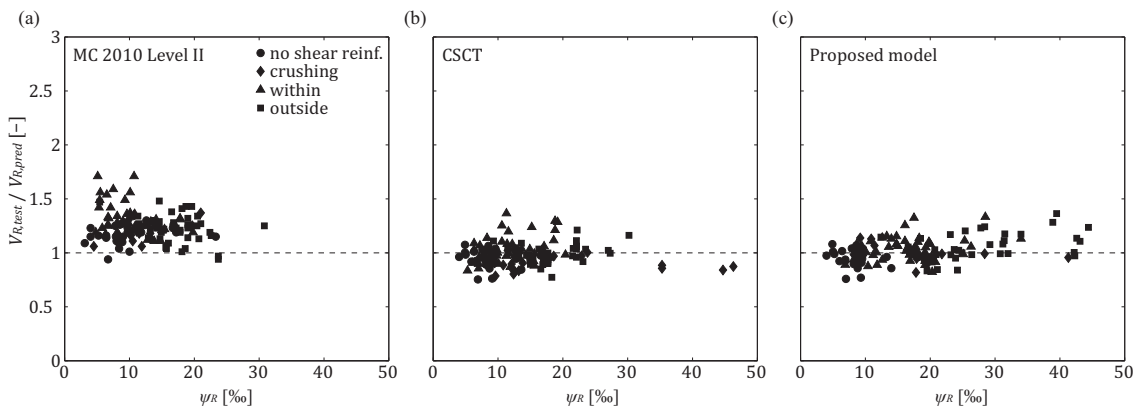


Figure 8.30: Ratio of the experimentally obtained punching strength of tests from literature to the predicted punching strength as a function of the predicted rotation at failure

In addition to the ratio of the experimentally obtained punching strength and the predicted strength, the ratio of the experimentally obtained rotation at failure and the predicted rotation at failure was investigated. However, since the rotation was not measured or published in most experimental tests, only a small selection of tests was considered. In fact, the set of specimens consists of 26 test specimens from the test campaign performed within this research project and from a test campaign performed by Gomes and Regan (Gomes and Regan 1999a).

Figure 8.31 shows the ratio of the experimentally obtained rotation at failure and the predicted rotation at failure as a function of the shear reinforcement ratio for MC 2010, the CSCT, and the proposed model. MC 2010 shows rather scattered results. Additionally, it can be noted that a clear tendency exists with respect to the shear reinforcement ratio. The larger the shear reinforcement ratio is the larger the ratio of the experimentally obtained rotation at failure and the predicted rotation at failure is. Nevertheless, it has to be reminded that MC 2010 is a design provision and thus it is supposed to rather deliver safe estimate for the punching strength than to predict the actual rotation capacity.

Compared to MC 2010, the CSCT shows less scatter and a lower average. However, the same tendency occurs with respect to the shear reinforcement ratio. The larger the shear reinforcement ratio is the larger the ratio of the experimentally obtained rotation at failure and the predicted rotation at failure is. This can be explained by the overestimation of the stiffness as it was already discussed in Chapter 4. This overestimation is more dominant in the case of larger load levels as it is the case for large shear reinforcement ratios. This leads to the tendency that the rotations will be clearly underestimated if large amount of shear reinforcement is present.

In contrast to MC 2010 and the CSCT, the proposed model leads to an average that is close to 1.0 and to a rather small scatter with a coefficient of variation of only 13.9%. Moreover, no tendency occurs with respect to the shear reinforcement ratio. Thus, it can be concluded that the load-rotation response of the slab and the failure criteria are properly addressed.

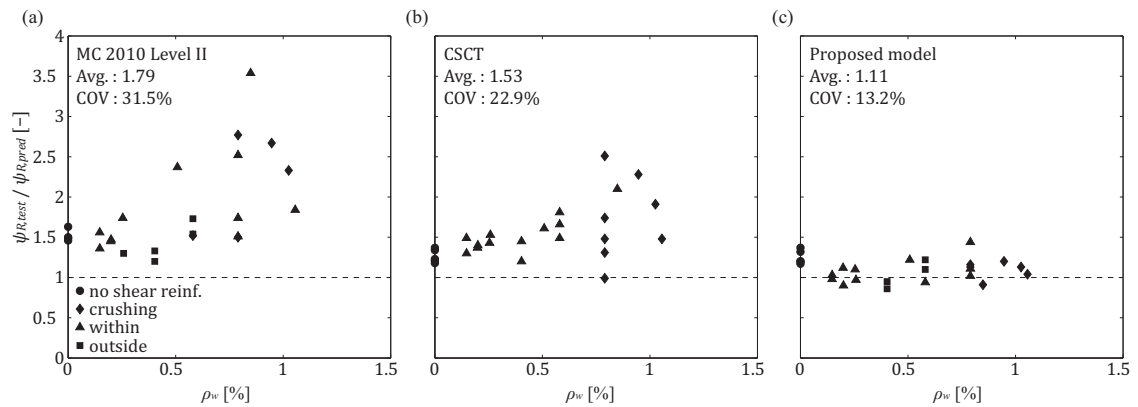


Figure 8.31: Ratio of the measured rotation at failure by tests from literature (Gomes and Regan 1999a) and from within this research project to the predicted rotation at failure as a function of the shear reinforcement ratio



## 9. Conclusions and Future Research

The research presented herein focused on the investigation of punching of flat slabs with large amounts of shear reinforcement. In addition to an experimental and numerical investigation of the test specimens, a principal objective of the research project was the development of an analytical model that enables accurate predictions of the punching strength and the rotation capacity of flat slabs with large amounts of shear reinforcement.

The experimental campaign consisted of sixteen full-scale flat slab specimens. The investigated parameters were the column size, the slab thickness, the amount of shear reinforcement, and the type of the shear reinforcement system. Various continuous measurements such as the slab rotation, the vertical displacement and the strains in the shear reinforcement were taken. Additionally, certain values could be estimated based on measurements such as the shear deformations at the column face and the forces transferred by the shear reinforcement.

With respect to the parameter varied in the experimental campaign, current design codes and the CSCT were validated. Thereby, the predicted punching strength was shown as a function of the experimentally investigated parameters. In addition, results of 132 punching tests from within this research and from literature were used for the validation of the design codes and the CSCT. The predicted punching strength was compared to the experimentally obtained strength. The ratio of the predicted and the experimentally obtained strength was investigated for slabs with and without shear reinforcement and for slabs with different predicted failure modes. This ratio was again shown as a function of several parameters.

The flexural slab responses of the test specimens were numerically modeled to investigate the slab deformations. For this, an approach based on the finite element method was developed by which the moment-curvature relationships were calculated using plane stress fields. The thereby obtained bending and torsional stiffness served as input parameters for a linear-elastic finite element analysis. The results of these calculations were validated with the load-displacement response of pure bending tests and pure torsion tests found in literature. Additionally, the predicted load-rotation curves were compared to load-rotation measurements of punching tests of specimens with and without shear reinforcement.

The flexural finite element approach was combined with an existing in-plane analysis program. This combination enabled the in-depth analysis of the global and local slab behavior. The calculated deformation of the slab was compared to displacement and surface strain measurements. In addition, the force transfer path in the vicinity of the column was analyzed in detail.

Based on the experimental and numerical investigation, an analytical model was developed. For this, a general slab behavior and failure mechanisms with respect to failure within the shear-reinforced area and to failure of the concrete strut close to the column were described. Based on the assumed slab behavior and failure mechanisms, formulations for the prediction of the load-rotation response of the slab and for failure criteria were developed enabling the prediction of the punching strength and the rotation capacity.

The proposed model was analyzed with respect to the parameters investigated in the experimental campaign. Thereby, the predicted punching strength and the predicted rotation at failure were shown as a function of the investigated parameters. Additionally, the proposed model was validated with results of 132 punching tests from within this research and from literature. Furthermore, a direct comparison to the predictions of the CSCT for the same set of tests showed the different performance of the two approaches as a function of several parameters such as the effective depth, the column size, the flexural reinforcement ratio, and the shear reinforcement ratio.

## 9.1. Conclusions

The measurement during the experimental campaign delivered valuable information concerning the behavior of the slab and the performance of the shear reinforcement. The measurements and the observations of the experimental tests lead to the following conclusions:

- Shear reinforcement improves the performance of flat slab-column connections with respect to the punching strength and the deformation capacity. In comparison to slabs without shear reinforcement, the punching strength as well as the rotation capacity increased significantly. The improvement in performance of the slab is influenced by several parameters such as the slab geometry, the amount of shear reinforcement, and the type of the shear reinforcement system.
- The strain measurements on the studs showed that the stresses in the shear reinforcement may be below the yielding strength prior to punching failure. Thus, the shear reinforcement may not be fully activated depending on the slab rotation and the arrangement of the shear reinforcement.
- The strain measurements on the studs indicated additionally that forces are directly transferred from the first and from the second row of studs to the column. However, a certain amount of force is transferred from the second row of studs to the first row of studs. Considering this aspect, it can be noted that the amount of the forces transferred by the shear reinforcement is less than the applied shear force, which confirms that the concrete contributes as well to the punching strength. Moreover, it was shown that the concrete contribution to the punching strength depends on the slab rotation.

- Vertical displacement measurements showed that large shear deformation occur at the column face for specimens with shear reinforcement. Since these shear deformations are much larger than the measured strain in the shear reinforcement, it can be concluded that the shear deformations occur localized at the column face. Thus, the opening of the cracks crossing the shear reinforcement can mainly be attributed to the slab rotation confirming a main hypothesis of the CSCT.

The comparison of codes and the CSCT to tests within this research and to tests found in literature showed generally a good agreement. From this comparison, following conclusions are drawn:

- ACI 318-11 leads generally to conservative results compared to test results within this research and from literature. However, a large scatter of the results is obtained, which may in certain cases lead to unsafe design. While the results for predicted failure within the shear-reinforced area and failure due to crushing of the concrete strut are rather conservative but showing acceptable agreement with the test results, the failure outside the shear-reinforced area lead to conservative and largely scattered results.
- EC2 2004 showed in several cases concerning overestimations of the punching strength when compared to test results within this research and from literature. While the ratios of the predicted to the experimentally obtained punching strength are in an acceptable range for specimens without shear reinforcement, with predicted failure within the shear-reinforced area, and with predicted failure outside the shear-reinforced area, the ratios of specimens with predicted failure due to crushing of the concrete strut show a rather large scatter in combination with a low average. This may potentially lead to unsafe design if crushing of the concrete strut is governing.
- The National German Annex (NAD 2011) improves the drawbacks of EC2 2004 leading to significant improvement of the strength predictions. Especially, for the prediction of failure due to crushing of the concrete strut, the scatter is reduced leading to safe estimates. With respect to failure outside the shear-reinforced area, it has to be noted that the effective depth was reduced leading to more conservative results. This reduction however is not in the code but proposed by Hegger et al. (Hegger et al. 2010). If this reduction is not considered the predicted punching strength will be larger leading to somewhat lower safety levels.
- SIA262 2003 leads generally to rather conservative results compared to test results within this research and from literature. Especially in the case of the prediction of failure within the shear-reinforced area, the punching strength is underestimated. This is due to the fact that SIA262 2003 neglects any concrete contribution to the punching strength. This is however already recognized and will be improved in a future revision

of Swiss code by which the punching shear provisions will be similar to the provisions of MC 2010.

- MC 2010 leads to the best agreement with test results within this research and from literature in comparison to the other investigated codes. Especially, the low scatter of the ratio of the predicted to the experimentally obtained punching strength is notable. Additionally, it can be noted that all failure modes are equally well addressed so that no tendency occurs for a certain failure mode or for a certain parameter.
- The strength predictions of the CSCT, which is the basis of the MC 2010, are generally in a good agreement with the experimentally obtained punching strength for tests within this research and for tests found in literature. However, the comparison of the load-rotation response revealed that the Quadrilinear method used in the combination with the CSCT leads to the prediction of a stiffer response than the experimentally measured one. Consequently, the predictions of the rotation at failure are generally lower than the experimentally measured rotation.

The development of the constitutive model for the nonlinear finite element analysis (NLFEA) enabled the modeling of the moment-curvature relationship of a slab element subjected to bending and torsion. Using the determined moment-curvature response in combination with the finite element method the slab specimens could be analyzed. Thereby, the numerical analysis leads to following conclusions:

- The analysis of a reinforced concrete slab element shows that the state of deformation influences significantly the bending and torsional stiffness of the element. Moreover, the interaction between bending and torsional behavior is pertinent. Thus, the bending stiffness is influenced by the torsional curvature and the torsional stiffness is strongly influenced by the bending curvature.
- The nonlinear finite element approach developed within this research allows the consideration of the interaction of the bending and torsional behavior. The comparison to slab specimen subjected to pure bending and to pure torsion showed good agreement between the predicted and the experimentally obtained load-displacement response. Additionally, the predictions of the load-rotation response of slab specimens without shear reinforcement agreed well with the experimentally obtained load-rotation curve. However, in the case of slabs with shear reinforcement, which allows larger shear forces to develop, the purely flexural analysis did not lead to acceptable results. Generally, the NLFEA led to a prediction of a stiffer response compared to the experimentally measured response. Thus, in regions with large concentrated shear forces, a numerical analysis solely considering the flexural behavior is not sufficient to model the response of the slab accurately.



- The combination of the flexural response and an existing in-plane finite element program improved the modeling of the test specimens with shear reinforcement allowing the prediction of the slab deformations. These predictions were compared to several test measurements such as the rotation, the vertical displacement, and the surface deformation on the top and bottom side of the slab. This comparison showed that the predictions correspond well to the measurements leading to the conclusion that the general response of such a slab specimen can be well captured by the numerical analysis.

The analytical model developed within this research project enables the prediction of the punching strength and rotation capacity. Compared to the CSCT, improvements could be achieved by slight changes in the calculation method of the load-rotation response and in the formulations for the failure criteria.

- The developed model for the load-rotation response considers a global slab part and a local, shear-critical slab part. This separation allows for different calculation approaches for the global part, which is mainly dependent on the flexural slab behavior, and for the shear-critical part that is mainly dependent on the force transfer path in the column vicinity. The importance of the estimated curvature at the intersection plane defining the forces in the shear-critical region. The application of the proposed approach results in excellent agreement with the experimentally obtained load-rotation response.
- The developed failure criterion for failure within the shear-reinforced area, which is based on the mechanical model of the CSCT, shows good agreement with the test results. Moreover, the model allows the applicable consideration of the actual location of the shear reinforcement so that the activation phase of the shear reinforcement can be accurately modeled leading to a good agreement with experimentally obtained results.
- The developed failure criterion for crushing of the concrete strut accounts for several parameters such as the concrete compressive strength, the transverse strain in the compression strut, the anchorage condition of the shear reinforcement, the location of the shear reinforcement, and the amount of compression at the column face. The consideration of these parameters is seen as beneficial enabling a good prediction of the punching strength and the rotation capacity.

## 9.2. Recommendations for future research

The research presented within this thesis focused on the investigation of punching of flat slabs with large amounts of shear reinforcement. Several aspects such as non-symmetric slabs (geometry and/or loading), slabs with inclined shear reinforcement, and prestressed slabs were not considered in this research. Additionally, the failure modes investigated within this thesis were limited to failure within the shear-reinforced area and failure due to crushing of the concrete strut. Thus, other failure modes such as failure outside the shear-reinforced area were not considered. Therefore, research on special slab configurations and on other failure modes is recommended for a further enhancement of the understanding of punching of flat slabs with shear reinforcement and for the validation of the applicability of the herein presented numerical and analytical model.

In addition to the topics that were out of the scope of this thesis, certain aspects were limited to the problematic of this research which could be extended to other problems and certain hypothesis were made with respect to the analytical model that should be further investigated. Generally, the following two recommendations are seen as the most interesting:

- The nonlinear finite element approach presented within this research was developed for the analysis of the load-deformation response of the punching test specimens. However, this approach can be extended to calculations of deformations of more general slabs. For this, the interaction of bending and torsional moments should be further investigated and for more cases experimentally validated. In addition, the implementation should be considered so that the structure can be analyzed within one simple program.
- With respect to failure due to crushing of the concrete strut, the research showed that the consideration of the transverse strains, the spacing of the shear reinforcement, and the anchorage conditions enables a good prediction of the punching strength and the rotation capacity. However, the influence of each parameter is solely based on empirical data. An experimental and numerical analysis of a local model considering the state of deformation is recommended.

## Bibliography

**ACI 318**, *Building Code Requirements for Structural Concrete*, ACI 318-11, American Concrete Institute, ACI Committee 318, 503 pp., Detroit, USA, **2011**.

**Alexander, S. D. B. and Hawkins, N. M.**, *A Design Perspective on Punching Shear*, ACI, SP 232, pp. 97-108, USA, **2005**.

**Alvarez, M., Köppel, S., and Marti, P.**, *Rotation capacity of reinforced concrete slabs*, ACI Structural Journal, Vol. 97, No. 2, pp. 235-242, **2000**.

**Andersson, J. L.**, *Punching of Concrete Slabs with Shear Reinforcement*, Transactions of the Royal Institute of Technology, 56 pp., Stockholm, Sweden, **1963**.

**Andrä, H.-P.**, *Dübelleisten zur Verhinderung des Durchstanzens bei hochbelasteten Flachdecken*, Bautechnik, Nr. 56, H7, pp. 244-247, **1979**.

**Andrä, H.-P., Dilger, W. H., and Ghali, A.**, *Durchstanzbewehrung für Flachdecken*, Beton- und Stahlbetonbau, Vol. 74, No. 5, pp. 129-132, Berlin, Germany, **1979**.

**Andrä, H.-P.**, *Zum Tragverhalten von Flachdecken mit Dübelleisten, Bewehrung in Auflagerbereich*, Beton- und Stahlbetonbau, Nr. 76, pp. H3.53-57, H4.100-104, **1981**.

**Bell, J. C. and Elms, D. G.**, *Non-linear Analysis of Reinforced Concrete Slabs*, Magazine of Concrete Research, Vol. 24, No. 79, pp. 63-70, UK, **1972**.

**Beutel, R.**, *Durchstanzen schubbewehrter Flachdecken im Bereich von Innenstützen*, RWTH, 267 pp., Aachen, Germany, **2003**.

**Birkle, G.**, *Punching of Flat Slabs: The Influence of Slab Thickness and Stud Layout*, Dissertation, University of Calgary, 217 pp., Calgary, Canada, **2004**.

**Birkle, G. and Dilger, W. H.**, *Influence of Slab Thickness on Punching Shear Strength*, ACI Structural Journal, Vol. 105, No. 2, pp. 180-188, **2008**.

**Broms, C. E.**, *Punching of Flat Plates - A Question of Concrete Properties in Biaxial Compression and Size Effect*, ACI Structural Journal, Vol. 87, No 3, pp. 292-304, **1990a**.

**Broms, C. E.**, *Shear Reinforcement for Deflection Ductility of Flat Plates*, ACI Structural Journal, Vol. 87, No. 6, pp. 696-705, **1990b**.

**Broms, C. E.**, *A method to avoid the punching failure mode*, pp. 117-124, Stockholm, Sweden, **2000a**.

**Broms, C. E.**, *Elimination of Flat Plate Punching Failure Mode*, ACI Structural Journal, Vol. 97, No. 1, pp. 94-101, **2000b**.

**Broms, C. E.**, *Concrete flat slabs and footings : Design method for punching and detailing for ductility*, KTH, Civil and Architectural Engineering, 114 pp., Stockholm, Sweden, **2005**.

**Broms, C. E.**, *Ductility reinforcement for flat slabs in seismic areas*, Magazine of Concrete Research, Thomas Telford, Vol. 58, No 4, pp. 243-254, London, England, **2006**.

**Broms, C. E.**, *Ductility of Flat Plates: Comparison of Shear Reinforcement Systems* , ACI Structural Journal, Vol. 104, No.6, pp. 703-711, **2007a**.

**Broms, C. E.**, *Flat Plates in Seismic Areas: Comparison of Shear Reinforcement Systems* , ACI Structural Journal, Vol. 104, No.6, pp. 712-721, **2007b**.

**Carvalho, A. L., Melo, G. S., Gomes, R. B., and Regan, P. E.**, *Punching Shear in Post-Tensioned Flat Slabs with Stud Rail Shear Reinforcement*, ACI Structural Journal, Vol. 108, No. 5, pp. 523-531, Farmington Hills, USA, **2011**.

**Chana, P. S.**, *A prefabricated shear reinforcement system for flat slabs*, Proceedings of the Institution of Civil Engineers: Structures and Buildings, Vol. 99, pp. 345-358, UK, **1993**.

**Chana, P. S. and Desai, S. B.**, *Design of shear reinforcement against punching*, The Structural Engineering, Vol. 70, pp. 159-164, **1992**.

**Condron, T. L.**, *Principles of Design and Results of Tests on Girderless Floor Construction of Reinforced Concrete*, ACI Journal Proceedings, Vol. 9, No. 12, pp. 116-126, USA, **1913**.

**Cook, R. D., Malkus, D. S., Plesha, M. E., and Witt, R. J.**, *Concepts and Application of Finite Element Analysis*, John Wiley and Sons Inc., 4<sup>th</sup> ed., 719 pp., USA, **2002**.

**Dechka, D. C.**, *Response of Shear-Stud-Reinforced Continuous Slab-Column Frames to Seismic Loads*, University of Calgary (Alberta), Departement of Civil Engineering, 471 pp., Calgary, Canada, **2001**.

**Dilger, W. H. and Ghali, A.**, *Shear Reinforcement for Concrete Slabs*, Journal of the Structural Division - ASCE, Vol. 107, pp. 2403-2420, USA, **1981**.

**EC2**, *Eurocode 2 Design of concrete structures, part 1-1 : General rules and rules for buildings*, 241 pp., **2004**.

**EC2 Commentary**, *Commentary Eurocode 2*, European Concrete Platform, 168 pp., Brussels, Belgium, **2008**.

**Eddy, H.T. and Turner, C.A.P.**, *Concrete-Steel Construction* , Heywood Mfg. Co., 438 pp., Minneapolis, USA, **1914**.

**Elgabry, A. and Ghali, A.**, *Design of Stud-Shear Reinforcement for Slabs*, ACI Structural Journal, Vol. 87, No. 3, pp. 351-361, USA, **1990**.

**Fernández Ruiz, M., Muttoni, A., and Kunz, J.**, *Strengthening of flat slabs against punching shear using post-installed shear reinforcement*, ACI Structural Journal, Vol. 107, No. 4, pp. 434-442, USA, **2010**.

**Fernández Ruiz, M. and Muttoni, A.**, *On Development of Suitable Stress Fields for Structural Concrete*, ACI, Structural Journal, Vol. 104, No. 4, pp. 495-502, Farmington Hills, USA, **2007**.

**Fernández Ruiz, M. and Muttoni, A.**, *Applications of the critical shear crack theory to punching of R/C slabs with transverse reinforcement*, ACI Structural Journal, Vol. 106 N° 4, pp. 485-494, USA, **2009**.

**FIB**, *Punching of structural concrete slabs*, fib bulletin 12, 307 pp., Lausanne, Switzerland, **2001**.

**Ghali, A.**, *An Efficient Solution to Punching of Slabs*, Concrete International, pp. 50-54, USA, **1989**.

**Ghali, A. and Hammill, N.**, *Effectiveness of Shear Reinforcement in Slabs*, Concrete International, pp. 60-65, USA, **1992**.

**Gomes, R. B. and Regan, P. E.**, *Punching Resistance of RC Flat Slabs with Shear Reinforcement*, ASCE Journal of Structural Engineering, Vol. 125, No. 6, pp. 684-692, Reston, USA, **1999a**.

**Gomes, R. B. and Regan, P. E.**, *Punching strength of slabs reinforced for shear with offcuts of rolled steel I-section beams*, Magazine of Concrete Research, Vol. 51, No. 2, pp. 121-129, London, UK, **1999b**.

**Guandalini, S.**, *Poinçonnement symétrique des dalles en béton armé*, Thèse de doctorat No. 3380, 289 pp., Lausanne, Switzerland, **2005**.

**Guandalini, S. and Muttoni, A.**, *Essais de poinçonnement symétrique des dalles en béton armé sans armature à l'effort tranchant*, Rapport d'essai, 85 pp., Lausanne, **2004**.

**Guidotti, R., Fernández, Ruiz M., and Muttoni, A.**, *Essais de poinçonnement de dalles en béton vibré et béton autocompactant avec différentes tailles maximales du granulat*, Rapport d'essai, 67 pp., Lausanne, **2009**.

**Guidotti, R.**, *Poinçonnement des planchers-dalles avec colonnes superposées fortement sollicitées*, Thèse EPFL No. 4812, 230 pp., Lausanne, Switzerland, **2010**.

**Hammill, N. and Ghali, A.**, *Punching Shear Resistance of Corner Slab-Column Connections*, ACI Structural Journal, Vol. 91, No. 6, pp. 697-707, Detroit, USA, **1994**.

**Hand, F. R., Pecknold, D. A., and Schnobrich, W. C.**, *Nonlinear Layered Analysis of RC Plates and Shells*, Journal of the Structural Division, Proceedings of the American Society of Civil Engineers, Vol. 99, pp. 1491-1505, USA, **1973**.

- Häusler, F.**, *Zum maximalen Durchstanzwiderstand von Flachdecken mit und ohne Vorspannung*, RWTH, 213 pp., Aachen, Germany, **2009**.
- Hawkins, N. M.**, *Shear Strength of Slabs with Shear Reinforcement*, ACI SP-42-34, Vol. 2, pp. 785-815, Detroit, USA, **1974**.
- Hegger, J., Ricker, M., Ulke, B., and Ziegler, M.**, *Untersuchungen zum Durchstanzverhalten von Stahlbetonfundamenten*, Beton- und Stahlbetonbau, Vol. 101, No 4, pp. 233-243, Germany, **2006**.
- Hegger, J., Häusler, F., and Ricker, M.**, *Zur maximalen Durchstanztragfähigkeit von Flachdecken*, Beton - und Stahlbetonbau, Vol. 102, pp. 770-777, Berlin, Germany, **2007**.
- Hegger, J., Ricker, M., and Sherif, A.**, *Punching Strength of Reinforced Concrete Footings*, ACI Structural Journal, Vol. 106, pp. 706-716, USA, **2009**.
- Hegger, J., Walraven, J. C., and Häusler, F.**, *Zum Durchstanzen von Flachdecken nach Eurocode 2*, Beton - und Stahlbetonbau, Vol. 105, pp. 206-215, Berlin, Germany, **2010**.
- Jofriet, J. C. and McNeice, G. M.**, *Finite Element Analysis of Reinforced Concrete Slabs*, Journal of the Structural Division, Proceedings of the American Society of Civil Engineers, Vol. 97, pp. 785-806, USA, **1971**.
- Kaufmann, W. and Marti, P.**, *Structural concrete: cracked membrane model*, Journal of Structural Engineering, Vol. 124, No. 12, pp. 1467-1475, USA, **1998**.
- Kenel, A. and Marti, P.**, *Faseroptische Dehnungsmessungen an einbetonierten Bewehrungsstäben*, IBK Bericht, 93 pp., Zürich, Switzerland, **2001**.
- Kinnunen, S.**, *Punching of Concrete Slabs with two-way Reinforcement*, Transactions of the Royal Institute of Technology, No. 198, 108 pp., Stockholm, Sweden, **1963**.
- Kinnunen, S. and Nylander, H.**, *Punching of Concrete Slabs Without Shear Reinforcement*, Transactions of the Royal Institute of Technology, No. 158, 112 pp., Stockholm, Sweden, **1960**.
- Kostic, N.**, *Topologie des champs de contraintes pour le dimensionnement des structures en béton armé*, Thèse EPFL, No. 4414, 235 pp., Lausanne, Switzerland, **2009**.
- Kupfer, H. and Gerstle, H.**, *Behavior of Concrete under Biaxial Stresses*, ASCE Journal of Engineering Mechanics, Vol. 99, No. 4, pp. 853-866, USA, **1973**.
- Langohr, P. H., Ghali, A., and Dilger, W. H.**, *Special Shear Reinforcement for Concrete Flat Plates*, ACI Journal, Vol. 73, pp. 141-146, Detroit, USA, **1976**.
- Lips, S., Muttoni, A., and Fernández-Ruiz, M.**, *Durchstanzversuche an Deckenausschnitten mit FIDECA Durchstanzbewehrung*, EPFL-IBéton, 55 pp., Lausanne, Switzerland, **2010**.
- Lips, S., Muttoni, A., and Fernández-Ruiz, M.**, *Durchstanzversuche an Deckenausschnitten mit Durchstanzbewehrung*, EPFL-IBéton, 88 pp., Lausanne, Switzerland, **2012a**.

**Lips, S., Muttoni, A., and Fernández-Ruiz, M.,** *Experimental Investigation on the Punching Strength and the Deformation Capacity of Shear-Reinforced Slabs*, ACI Structural Journal, USA, **2012b**. (Accepted for publication)

**Loov, R. E.,** *Review of A23.3-94 Simplified Method of Shear Design and Comparison with Results using Shear Friction*, Canadian Journal of Civil Engineering, Vol. 25, pp. 437-450, Canada, **1998**.

**Maillart, R.,** *Zur Entwicklung der unterzuglosen Decke in der Schweiz und in Amerika*, Schweizerische Bauzeitung, Vol. 87, No. 21, pp. 263-267, Zürich, Switzerland, **1926**.

**Marti, P., Leesti, P., and Khalifa, W. U.,** *Torsion Tests on Reinforced Concrete Slab Elements*, ASCE Journal of Structural Engineering, Vol. 113, pp. 994-1010, **1987**.

**Marti, P., Alvarez, M., Kaufmann, W., and Sigrist, V.,** *Tension chord model for structural concrete*, Structural Engineering International, Vol. 8, No. 4, pp. 287-298, USA, **1998**.

**MC,** *Model Code 2010 (Final Draft)*, Fédération internationale du béton fib, Lausanne, Switzerland, **2011**.

**Megally, S. H. and Ghali, A.,** *Design Considerations for Slab-Column Connections in Seismic Zones*, ACI Structural Journal, Vol. 91, No. 3, pp. 303-314, Detroit, USA, **1994**.

**Mokhtar, A. S., Ghali, A., and Dilger, W. H.,** *Stud Shear Reinforcement for Flat Concrete Plates*, ACI Journal, No. 82-60, pp. 676-683, Detroit, USA, **1985**.

**Muttoni, A.,** *Punching shear strength of reinforced concrete slabs without transverse reinforcement*, ACI Structural Journal, Vol. 105, No. 4, pp. 440-450, **2008**.

**Muttoni, A., Fernández Ruiz, M., and Kostic, N.,** *Champs de contraintes et méthode des bielles et tirants - Applications dans la conception et le dimensionnement des structures en béton armé*, EPFL - IBETON, 117 pp., Lausanne, Switzerland, **2011**.

**Muttoni, A. and Fernández Ruiz, M.,** *The Critical Shear Crack Theory as a mechanical model for punching shear design and its application to code provisions*, Fédération Internationale du Béton, Bulletin 57, pp. 31-60, Lausanne, Switzerland, **2010**.

**NAD,** *DIN EN 1992-1-1/NA:2011 Nationaler Anhang - Eurocode 2: Bemessung und Konstruktion von Stahlbeton- und Spannbetontragwerken*, 101 pp., Berlin, Germany, **2011**.

**Oliveira, D. R., Melo, G. S., and Regan, P. E.,** *Punching Strengths of Flat Plates with Vertical or Inclined Stirrups*, ACI Structural Journal, Vol. 97, pp. 485-491, USA, **2000**.

**Polak, M. A.,** *Nonlinear Analysis of Reinforced Concrete Shells*, University of Toronto, 195 pp., Toronto, Canada, **1992**.

**Polak, M. A. and Vecchio, F. J.,** *NonLinear Analysis of Reinforced-Concrete Shells*, ASCE Journal of Structural Engineering, Vol. 119, No. 12, pp. 3439-3462, **1993**.

- Regan, P. E.**, *Punching Shear in Prestressed Concrete Slab Bridges*, Engineering Structures Research group, Polytechnic of Central London, 230 pp., London, UK, **1983**.
- Regan, P. E.**, *Shear Combs, Reinforcement against Punching*, The Structural Engineering, Vol. 63B, No. 4, pp. 76-84, **1985**.
- Regan, P. E.**, *Symmetric Punching of Reinforced Concrete Slabs*, Magazine of Concrete Research, Vol. 38, pp. 115-128, England, **1986**.
- Regan, P. E. and Samadian, F.**, *Shear Reinforcement against punching in reinforced concrete flat slabs*, The Structural Engineer, pp. 24-31, London, England, **2001**.
- Seible, F., Ghali, A., and Dilger, W. H.**, *Preassembled shear reinforcing units for flat plates*, ACI Journal, Proceedings 77, No. 1, pp. 28-35, **1980**.
- Shehata, I. A. E. M.**, *Theory of punching in RC slabs*, Ph.D Thesis, Polytechnic of Central London, UK, **1985**.
- Shehata, I. A. E. M.**, *Rational Method for Designing RC Slabs to Resist Punching*, Journal of Structural Engineering, Vol. 116, No. 7, pp. 2055-2060, USA, **1990**.
- Shehata, I. A. E. M and Regan, P. E.**, *Punching in R.C. Slabs*, Journal of Structural Engineering, Vol. 115, No. 7, pp. 1726-1740, USA, **1989**.
- SIA 262**, *SIA 262 - Construction en béton*, Société Suisse des Ingénieurs et des Architectes, 94 p., Zürich, Switzerland, **2003**.
- Siburg, C. and Hegger, J.**, *Punching of flat slabs - comparison of models*, fib Symposium Prague 2011, pp. 151-154, Prague, Czech Republic, **2011**.
- Sigrist, V.**, *Zum Verformungsvermögen von Stahlbetonträgern*, Dissertation, 160 pp., Zürich, Switzerland, **1995**.
- Smulski, E.**, *A Test of the S-M-I System of Flat-Slab Construction*, ACI Journal Proceedings, Vol. 14, No. 6, pp. 206-232, USA, **1918**.
- Talbot, A. N. and Gonnerman, H. F.**, *Test of a Flat Slab Floor of the Western Newspaper Union Building*, University of Illinois Bulletin, Vol. XV, No. 38, 62 pp., USA, **1918**.
- Tassinari, L.**, *Poinçonnement symétrique des dalles en béton armé avec armature de poinçonnement*, Thèse EPFL No. 5030, 197 pp., Lausanne, Switzerland, **2011**.
- Taylor, F. W. and Thompson, S. E.**, *A treatise on Concrete Plain and Reinforced*, John Wiley and Sons Inc., 3<sup>rd</sup> ed., 885 pp., New York, USA, **1916**.
- Thorenfeldt, E., Tomaszewics, A., and Jensen, J. J.**, *Mechanical properties of high-strength concrete and application in design*, Proceeding on Utilisation of High Strength Concrete, Stavanger, Norway, **1987**.



**Tozser, O.**, *Shear Analysis Using Shear Friction - Size Effect and Prestressing*, University of Calgary (Alberta), Departement of Civil Engineering, 194 pp., Calgary, Canada, **1998**.

**Trautwein, L. M., Bittencourt, T. N., Gomes, R. B., and Bella, J. C. D.**, *Punching Strength of Flat Slabs with Unbraced Shear Reinforcement*, ACI Structural Journal, Vol. 108, pp. 197-205, USA, **2011**.

**Van der Voet, A. F., Dilger, W. H., and Ghali, A.**, *Concrete Flat Plates with Well-Anchored Shear Reinforcement Elements*, Canadian Journal of Civil Engineering, Vol. 9, No. 1, pp. 107-114, Canada, **1982**.

**Vaz Rodrigues, R.**, *Shear Strength of Reinforced Concrete Bridge Deck Slabs*, Thèse EPFL No. 3739, 289 pp., Lausanne, Switzerland, **2007**.

**Vecchio, F. J.**, *Nonlinear Finite Element Analysis of Reinforced Concrete Membranes*, ACI Structural Journal, Vol. 86-S4, pp. 26-35, USA, **1989**.

**Vecchio, F. J. and Collins, M. P.**, *The modified compression-field theory for reinforced concrete elements subjected to shear*, ACI Journal, Vol. 83, pp. 219-231, USA, **1986**.

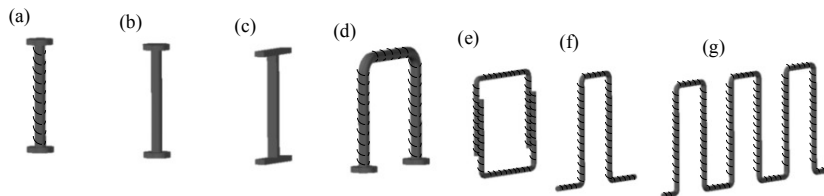
**Vollum, R. L., Abdel-Fattah, T., Eder, M., and Elghazouli, A.Y.**, *Design of ACI-type punching shear reinforcement to Eurocode 2*, Magazine of Concrete Research, Vol. 62, No. 01, pp. 3-16, London, UK, **2010**.



# Appendix A Test Database

## Parameters

$l$	[mm]	Slab dimensions and shape where $l$ correspond to the side length of a square slab (sq) or to the diameter of a circular or octagonal slab (ci)
$h$	[mm]	Thickness of the slab
$d$	[mm]	Effective depth of the slab (distance from extreme compression fiber to the centroid of the longitudinal tensile reinforcement)
$c$	[mm]	Column size and shape where $c$ correspond to the side length of a square column (sq) or to the diameter of a circular column (ci)
$\rho_L$	[%]	Average flexural reinforcement ratio
$\rho_w$	[%]	Shear reinforcement ratio calculated according to Appendix C
$f_c$	[MPa]	Mean cylindrical concrete compressive strength (Conversion factors $f_c=0.83f_{c,cube150mm}$ ; $f_c=0.79f_{c,cube100mm}$ )
$d_g$	[mm]	Maximum diameter of the aggregate
$f_y$	[MPa]	Mean yielding strength of the flexural reinforcement steel
$f_{yw}$	[MPa]	Mean yielding strength of the shear reinforcement steel
system		Shear reinforcement system: (MC: $k_{sys}$ ; CSCT: $\lambda$ ; mod: $k_2$ )
		(a) corrugated double headed shear studs (2.8; 3.0; 0.75)
		(b) smooth double headed shear studs (2.8; 3.0; 0.75)
		(c) steel offcuts (2.8; 3.0; 0.75)
		(d) headed stirrups (2.8; 3.0; 0.75)
		(e) stirrups with lap at the vertical branch (2.4; 2.5; 0.50)
		(f) stirrups or shear links (2.4; 2.5; 0.50)
		(g) continuous stirrups or cages of shear links (2.4; 2.5; 0.50)



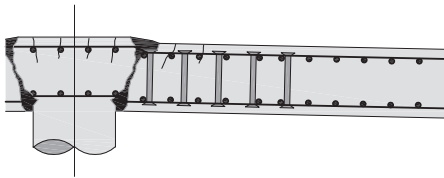
$V_{test}/V_{pred}$  [-] Ratio of the experimentally obtained punching strength to the predicted punching strength where following definitions are used:

ACI: Calculated according to ACI 318-11 (ACI 318 2011)  
 EC: Calculated according to Eurocode 2 2004 (EC2 2004)  
 NAD: Calculated according to German National Annex (NAD 2011)  
 (Values in parenthesis: Changes if factor 1.9 is used instead of 1.4 for double headed studs)  
 SIA: Calculated according to Swisscode 262 2003 (SIA 262 2003)  
 MC: Calculated according to Modelcode 2010 (MC 2011)  
 CSCT: Calculated according to the Critical Shear Crack Theory (Muttoni 2008, Fernández-Ruiz and Muttoni 2008)  
 mod: Calculated according to the proposed model

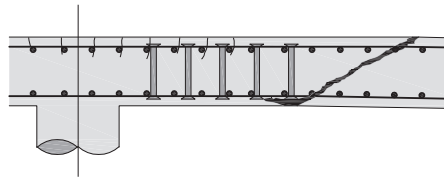
and the predicted failure mode where following definitions are used:

- p: punching without shear reinforcement
- c: crushing of the concrete strut
- w: failure within the shear-reinforced area
- o: failure outside the shear-reinforced area
- f: flexural failure

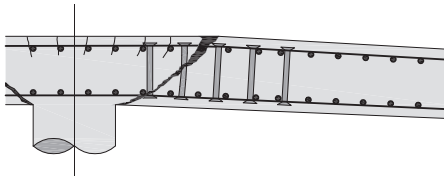
c: crushing of concrete strut



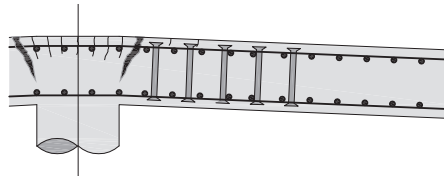
o: failure outside shear-reinforced area



w: failure within shear-reinforced area



f: flexural failure



**Andersson, J. L.**, *Punching of Concrete Slabs with Shear Reinforcement*, Transactions of the Royal Institute of Technology, Stockholm, Sweden, **1963**.

	$l$ [mm]	$h$ [mm]	$d_m$ [mm]	$c$ [mm]		$\rho_L$ [%]	$\rho_w$ [%]	$f_c$ [MPa]	$d_g$ [mm]	$f_y$ [MPa]	$f_{yw}$ [MPa]	system	
A-S2-82	1840	(ci)	150	120	300	(ci)	1.08	0.58	28.1	32	442	294	g
A-S2-83	1840	(ci)	150	119	300	(ci)	1.09	0.58	24.3	32	442	294	g

	$V_{R,test}$ [kN]	$V_{R,test}/V_{R,ACI}$ (2011)		$V_{R,test}/V_{R,EC}$ (2004)		$V_{R,test}/V_{R,NAD}$ (2011)		$V_{R,test}/V_{R,SIA}$ (2003)		$V_{R,test}/V_{R,MC}$ (2010)		$V_{R,test}/V_{R,CSCCT}$		$V_{R,test}/V_{R,mod}$	
A-S2-82	459	1.64	o	1.23	o	1.39	o	1.34	w	1.22	o	0.98	o	0.98	o
A-S2-83	459	1.78	o	1.30	o	1.47	o	1.42	w	1.29	o	1.04	o	1.02	o

**Beutel, R. and Hegger, J.,** *The effect of anchorage on the effectiveness of the shear reinforcement in the punching zone*, Cement and Concrete Composites, 11 pp., **2002**.

**Beutel, R.,** *Durchstanzen schubbewehrter Flachdecken im Bereich von Innenstützen*, RWTH, 267 pp., Aachen, Germany, **2003**.

	$l$ [mm]		$h$ [mm]	$d_m$ [mm]	$c$ [mm]		$\rho_L$ [%]	$\rho_w$ [%]	$f_c$ [MPa]	$d_g$ [mm]	$f_y$ [MPa]	$f_{yw}$ [MPa]	system
Z1	2980	(sq)	285	250	200	(ci)	0.80	0.65	24.8	16	889	580	a
Z2	2980	(sq)	285	250	200	(ci)	0.80	0.65	26.3	16	889	580	a
Z3	2980	(sq)	285	250	200	(ci)	0.80	0.70	24.1	16	889	580	a
Z4	2980	(sq)	285	250	200	(ci)	0.80	0.75	31.5	16	889	580	a
Z5	2980	(sq)	285	250	264	(ci)	1.25	0.80	28.0	16	562	540	a
Z6	2980	(sq)	285	250	200	(ci)	1.25	0.91	37.3	16	562	540	a
V1	2750	(ci)	290	250	200	(ci)	0.80	0.57	30.8	16	917	544	a
V2	2750	(ci)	290	250	200	(ci)	0.80	0.54	36.2	16	917	544	a
V3	2980	(sq)	285	250	200	(ci)	0.80	0.57	23.2	16	901	544	a
V4	2980	(sq)	383	350	200	(ci)	0.50	0.44	26.0	16	917	544	a
P1	2820	(ci)	230	190	400	(sq)	0.80	-	21.9	16	572	-	-
P1-I	2820	(ci)	230	190	400	(sq)	0.80	0.33	27.3	16	572	570	e
P1-II	2820	(ci)	230	190	400	(sq)	0.80	0.33	26.2	16	572	570	f
P2-I	2820	(ci)	230	190	400	(sq)	0.80	0.60	37.9	16	549	592	e
P2-II	2750	(ci)	230	190	400	(sq)	0.81	0.50	29.8	16	549	592	f
P2-III	2750	(ci)	230	190	400	(sq)	0.81	0.64	37.5	16	549	592	f
P3-I	2750	(ci)	270	220	320	(sq)	1.15	0.33	23.2	16	557	597	e
P4-III	2750	(ci)	267	222	320	(sq)	1.13	0.53	27.8	16	557	597	f
P5-I	2750	(ci)	270	220	320	(sq)	1.35	0.55	45.3	16	557	596	e
P6-I	2750	(ci)	273	223	320	(sq)	1.75	0.93	46.3	16	532	563	e
P7-I	2750	(ci)	275	229	320	(sq)	1.30	0.79	40.0	16	557	596	e

	$V_{R,test}$ [kN]	$V_{R,test}$ $/V_{R,ACI}$ (2011)		$V_{R,test}$ $/V_{R,EC}$ (2004)		$V_{R,test}/V_{R,NAD}$ (2011)		$V_{R,test}$ $/V_{R,SI}$ (2003)		$V_{R,test}$ $/V_{R,MC}$ (2010)		$V_{R,test}$ $/V_{R,CSCCT}$		$V_{R,test}$ $/V_{R,mod}$	
Z1	1323	1.13	c	1.26	c	1.28 (0.94)	c	1.13	c	1.25	w	0.90	w	1.02	c
Z2	1442	1.19	c	1.30	c	1.36 (1.00)	c	1.20	c	1.33	w	0.96	w	0.98	c
Z3	1616	1.40	c	1.57	c	1.57 (1.16)	c	1.39	c	1.54	w	1.07	w	1.14	c
Z4	1646	1.24	c	1.27	c	1.47 (1.10)	c (o)	1.29	c	1.42	w	0.94	w	1.01	w
Z5	2024	1.42	c	1.31	c	1.40 (1.03)	c	1.35	c	1.56	w	1.09	w	1.08	w
Z6	1954	1.36	c	1.31	c	1.42 (1.04)	c	1.28	c	1.49	w	1.03	w	1.04	w
V1	1250	0.96	c	0.98	c	1.12 (0.83)	c	1.14	w	1.17	w	0.85	w	0.88	w
V2	1424	1.00	c	0.98	c	1.21 (0.89)	c	1.38	w	1.26	w	0.95	w	0.89	w
V3	1182	1.04	c	1.19	c	1.17 (0.86)	c	1.08	w	1.23	w	0.91	w	0.94	w
V4	1680	0.98	o	1.09	c	1.18 (1.12)	c	1.15	w	1.19	w	0.84	w	0.89	w
P1	615	0.88	p	0.87	p	0.87	p	0.97	p	1.01	p	0.76	p	0.77	p
P1-I	1187	1.52	o	1.32	o	1.56	o	1.50	w	1.48	o	1.09	o	1.13	o
P1-II	1091	1.43	o	1.24	o	1.45	o	1.37	w	1.19	o	0.90	o	0.95	o
P2-I	1362	1.28	o	0.97	f	1.15	o	1.27	c	1.34	o	1.04	o	1.18	o
P2-II	1109	1.36	o	1.01	o	1.17	o	1.11	o	1.23	o	0.93	o	1.03	o
P2-III	1276	1.29	o	0.97	o	1.12	o	1.19	c	1.25	o	0.97	o	1.08	o
P3-I	1624	1.42	c	1.12	w	1.24	c	1.90	w	1.59	w	1.14	w	1.14	w
P4-III	1522	1.20	c	0.82	o	1.09	c	1.12	c	1.06	c	0.80	c	0.82	c
P5-I	1936	1.21	c	0.89	w	1.12	c	1.36	w	1.21	w	0.83	c	0.82	w
P6-I	2349	1.43	c	0.92	o	1.21	c	1.23	c	1.16	c	0.89	c	0.83	o
P7-I	2117	1.33	c	0.94	o	1.22	c	1.25	c	1.18	c	0.90	c	0.84	o

**Birkle, G.,** *Punching of Flat Slabs: The Influence of Slab Thickness and Stud Layout,* Dissertation, University of Calgary, 217 pp., Calgary, Canada, **2004.**

	$l$ [mm]		$h$ [mm]	$d_m$ [mm]	$c$ [mm]		$\rho_L$ [%]	$\rho_w$ [%]	$f_c$ [MPa]	$d_g$ [mm]	$f_y$ [MPa]	$f_{yw}$ [MPa]	system
S1	2300	(ci)	160	124	250	(sq)	1.53	-	36.2	14	488	-	-
S2	2300	(ci)	160	124	250	(sq)	1.53	0.45	29.0	14	488	393	b
S3	2300	(ci)	160	124	250	(sq)	1.53	0.45	31.6	14	488	393	b
S4	2300	(ci)	160	124	250	(sq)	1.53	0.68	38.0	14	488	465	b
S5	2300	(ci)	160	124	250	(sq)	1.53	0.68	36.3	14	488	465	b
S6	2300	(ci)	160	124	250	(sq)	1.53	0.68	33.4	14	488	465	b
S7	3260	(ci)	230	190	300	(sq)	1.35	-	35.0	20	531	-	-
S8	3260	(ci)	230	190	300	(sq)	1.35	0.32	35.0	20	531	460	b
S9	3260	(ci)	230	190	300	(sq)	1.35	0.21	35.2	20	531	460	b
S10	4000	(ci)	300	260	350	(sq)	1.15	-	31.4	20	524	-	-
S11	4000	(ci)	300	260	350	(sq)	1.15	0.35	30.0	20	524	409	b
S12	4000	(ci)	300	260	350	(sq)	1.15	0.23	33.5	20	524	409	b

	$V_{R,test}$ [kN]	$V_{R,test}/V_{R,ACI}$ (2011)		$V_{R,test}/V_{R,EC}$ (2004)		$V_{R,test}/V_{R,NAD}$ (2011)		$V_{R,test}/V_{R,SIA}$ (2003)		$V_{R,test}/V_{R,MC}$ (2010)		$V_{R,test}/V_{R,CSCCT}$		$V_{R,test}/V_{R,mod}$	
S1	483	1.30	p	1.11	p	1.11	p	1.20	p	1.23	p	0.98	p	0.98	p
S2	574	1.27	o	1.19	o	1.42	o	1.54	w	1.22	o	0.97	o	0.97	o
S3	572	1.18	o	1.12	o	1.37	o	1.49	w	1.13	o	0.89	o	0.92	w
S4	634	1.66	o	1.21	o	1.43	o	1.32	o	1.23	o	0.98	o	0.95	o
S5	624	1.21	o	1.21	o	1.43	o	1.31	o	1.23	o	0.98	o	0.94	o
S6	615	1.20	o	1.22	o	1.45	o	1.41	o	1.19	o	0.94	o	0.91	o
S7	825	1.12	p	0.93	p	0.93	p	1.07	p	1.11	p	0.89	p	0.90	p
S8	1050	1.21	o	0.97	o	1.13	o	1.36	w	1.22	w	0.87	w	1.00	w
S9	1091	1.20	w	1.05	w	1.17	o	1.41	w	1.27	w	1.00	w	1.06	w
S10	1046	0.88	p	0.77	p	0.77	p	0.90	p	0.94	p	0.75	p	0.76	p
S11	1620	1.22	o	0.98	o	1.09	o	1.42	w	1.28	w	0.90	w	1.06	w
S12	1520	1.00	w	0.88	o	0.99	o	1.28	w	1.16	w	0.90	w	0.98	w

**Chana, P. S. and Desai, S. B.**, *Design of shear reinforcement against punching*, The Structural Engineering, Vol. 70, pp. 159-164, **1992**.

**Chana, P. S.**, *A prefabricated shear reinforcement system for flat slabs*, Proceedings of the Institution of Civil Engineers: Structures and Buildings, Vol. 99, pp. 345-358, **1993**.

	$l$ [mm]		$h$ [mm]	$d_m$ [mm]	$c$ [mm]		$\rho_L$ [%]	$\rho_w$ [%]	$f_c$ [MPa]	$d_g$ [mm]	$f_y$ [MPa]	$f_{yw}$ [MPa]	system
S1	3000	(sq)	240	200	300	(sq)	0.79	-	31.8	20	500 <sup>1)</sup>	-	-
S2	3000	(sq)	240	200	300	(sq)	0.79	0.13	35.1	20	500 <sup>1)</sup>	520	f
S3	3000	(sq)	240	200	300	(sq)	0.79	0.13	32.5	20	500 <sup>1)</sup>	520	f
S4	3000	(sq)	240	200	300	(sq)	0.79	0.26	35.9	20	500 <sup>1)</sup>	520	f
S5	3000	(sq)	250	210	400	(sq)	0.86	0.16	30.3	20	500 <sup>1)</sup>	520	f
S6	3000	(sq)	250	210	400	(sq)	0.86	0.26	34.3	20	500 <sup>1)</sup>	520	f
S7	3000	(sq)	250	210	400	(sq)	0.86	0.26	31.9	20	500 <sup>1)</sup>	520	f
S8	3000	(sq)	250	210	400	(sq)	0.86	0.10	31.4	20	500 <sup>1)</sup>	520	f
S1	3000	(sq)	228	188	300	(sq)	0.83	-	34.0	20	500 <sup>1)</sup>	-	-
S2	3000	(sq)	228	188	300	(sq)	0.83	0.50	32.5	20	500 <sup>1)</sup>	520	g
S3	3000	(sq)	228	188	300	(sq)	0.83	0.50	34.8	20	500 <sup>1)</sup>	520	g
S4	3000	(sq)	228	188	300	(sq)	0.83	0.50	33.6	20	500 <sup>1)</sup>	520	f

<sup>1)</sup> The steel for flexural reinforcement was not tested. Values were estimated based on the indicated steel quality.

	$V_{R,test}$ [kN]	$V_{R,test}/V_{R,ACI}$ (2011)		$V_{R,test}/V_{R,EC}$ (2004)		$V_{R,test}/V_{R,NAD}$ (2011)		$V_{R,test}/V_{R,SLA}$ (2003)		$V_{R,test}/V_{R,MC}$ (2010)		$V_{R,test}/V_{R,C SCT}$		$V_{R,test}/V_{R,mod}$	
S1	805	1.07	p	1.03	p	1.03	p	1.14	p	1.19	p	0.88	p	0.89	p
S2	1094	1.28	w	1.07	w	1.07	w	1.51	w	1.24	w	0.96	w	1.05	w
S3	1139	1.36	w	1.13	w	1.13	w	1.61	w	1.31	w	1.02	w	1.11	w
S4	1302	1.30	o	0.94	o	1.14	c	1.78	w	1.19	w	0.98	w	1.06	w
S5	1382	1.37	o	1.02	w	1.08	o	1.59	w	1.22	w	0.94	w	1.04	w
S6	1283	1.20	o	0.85	o	0.97	o	1.37	w	1.01	o	0.77	o	0.84	o
S7	1492	1.44	o	1.01	o	1.15	o	1.17	c	1.20	o	0.91	o	0.98	o
S8	1324	1.38	w	1.17	w	1.17	w	1.51	w	1.29	w	0.97	w	1.08	w
S1	851	1.19	p	1.16	p	1.16	p	1.28	p	1.34	p	0.99	p	1.00	p
S2	981	1.41	o	1.07	o	1.30	o	1.12	w	1.21	o	0.92	o	0.93	o
S3	1286	1.40	o	1.01	o	1.24	c	1.47	w	1.27	o	1.03	o	1.11	w
S4	1135	1.26	o	0.90	o	1.11	c	1.30	w	1.13	o	0.92	o	0.99	w



**Elstner, R. C. and Hognestad, E.,** *Shearing Strength of Reinforced Concrete Slabs*, ACI Materials Journal, Vol. 53-2, pp. 29-58, **1956**.

	$l$ [mm]	$h$ [mm]	$d_m$ [mm]	$c$ [mm]	$\rho_L$ [%]	$\rho_w$ [%]	$f_c$ [MPa]	$d_g$ [mm]	$f_y$ [MPa]	$f_{yw}$ [MPa]	system
B12	1828 (sq)	152.4	114	254 (sq)	3.00	0.73	44.8	38.1	331.6	323	g

	$V_{R,test}$ [kN]	$V_{R,test}/V_{R,ACI}$ (2011)	$V_{R,test}/V_{R,EC}$ (2004)	$V_{R,test}/V_{R,NAD}$ (2011)	$V_{R,test}/V_{R,SLA}$ (2003)	$V_{R,test}/V_{R,MC}$ (2010)	$V_{R,test}/V_{R,CSCT}$	$V_{R,test}/V_{R,mod}$
B12	787	2.10 o	1.22 o	1.56 o	1.64 w	1.14 o	0.96 o	1.08 w

**Etter, S., Heinzmann, D., Jäger, T., and Marti, P.,** *Versuche zum Durchstanzverhalten von Stahlbetonplatten*, 64 pp., Zurich, Switzerland, **2009**.

	$l$ [mm]	$h$ [mm]	$d_m$ [mm]	$c$ [mm]	$\rho_L$ [%]	$\rho_w$ [%]	$f_c$ [MPa]	$d_g$ [mm]	$f_y$ [MPa]	$f_{yw}$ [MPa]	system
SP1	4100 (sq)	350	294	400 (ci)	1.26	-	35.5	32	601	529	-
SP2	4100 (sq)	350	294	400 (ci)	1.26	0.79	34.5	32	601	529	a
SP3	4100 (sq)	350	294	400 (ci)	1.26	0.79	33.4	32	601	529	a

	$V_{R,test}$ [kN]	$V_{R,test}/V_{R,ACI}$ (2011)	$V_{R,test}/V_{R,EC}$ (2004)	$V_{R,test}/V_{R,NAD}$ (2011)	$V_{R,test}/V_{R,SLA}$ (2003)	$V_{R,test}/V_{R,MC}$ (2010)	$V_{R,test}/V_{R,CSCT}$	$V_{R,test}/V_{R,mod}$
SP1	1710	1.34 p	1.01 p	1.01 p	1.08 p	1.15 p	0.92 p	0.92 p
SP2	3080	2.37 o	1.63 o	1.83 o	1.30 c	1.47 o	1.11 o	1.15 o
SP3	3350	1.36 c	1.04 c	1.44 (1.06) c	1.43 c	1.29 c	0.95 c	1.00 c

**Fernández-Ruiz, M., Muttoni, A., and Kunz, J.,** *Strengthening of flat slabs against punching shear using post-installed shear reinforcement*, ACI Structural Journal, Vol. 107, pp. 434-442, **2007**.

	$l$ [mm]	$h$ [mm]	$d_m$ [mm]	$c$ [mm]	$\rho_L$ [%]	$\rho_w$ [%]	$f_c$ [MPa]	$d_g$ [mm]	$f_y$ [MPa]	$f_{yw}$ [MPa]	system
PV1	3000 (sq)	250	210	260 (sq)	1.50	-	34.0	16	709	-	-

	$V_{R,test}$ [kN]	$V_{R,test}/V_{R,ACI}$ (2011)	$V_{R,test}/V_{R,EC}$ (2004)	$V_{R,test}/V_{R,NAD}$ (2011)	$V_{R,test}/V_{R,SLA}$ (2003)	$V_{R,test}/V_{R,MC}$ (2010)	$V_{R,test}/V_{R,CSCT}$	$V_{R,test}/V_{R,mod}$
PV1	974	1.27 p	0.96 p	0.96 p	1.12 p	1.16 p	1.01 p	1.02 p

**Gomes, R. B. and Regan, P. E.,** *Punching Resistance of RC Flat Slabs with Shear Reinforcement*, ASCE Journal of Structural Engineering, Vol. 125, Issue 6, pp. 684-692, 1999.

	$l$ [mm]	$h$ [mm]	$d_m$ [mm]	$c$ [mm]	$\rho_L$ [%]	$\rho_w$ [%]	$f_c$ [MPa]	$d_g$ [mm]	$f_y$ [MPa]	$f_{yw}$ [MPa]	system
S1	3000 (sq)	200	159	200 (sq)	1.26	-	41.7	20	680	-	-
S1A	3000 (sq)	200	159	200 (sq)	1.26	-	42.7	20	680	-	-
S2	3000 (sq)	200	153	200 (sq)	1.31	0.15	35.8	20	680	430	c
S3	3000 (sq)	200	158	200 (sq)	1.27	0.20	40.7	20	670	430	c
S4	3000 (sq)	200	159	200 (sq)	1.26	0.26	33.3	20	670	430	c
S5	3000 (sq)	200	159	200 (sq)	1.26	0.40	36.0	20	670	430	c
S6	3000 (sq)	200	159	200 (sq)	1.26	0.40	38.8	20	670	430	c
S7	3000 (sq)	200	159	200 (sq)	1.26	0.58	35.1	20	670	430	c
S8	3000 (sq)	200	159	200 (sq)	1.26	0.58	35.4	20	670	430	c
S9	3000 (sq)	200	159	200 (sq)	1.26	0.58	41.5	20	670	430	c
S10	3000 (sq)	200	154	200 (sq)	1.31	0.15	36.7	20	670	430	c
S11	3000 (sq)	200	154	200 (sq)	1.31	0.20	35.9	20	670	430	c

	$V_{R,test}$ [kN]	$V_{R,test}/V_{R,ACI}$ (2011)	$V_{R,test}/V_{R,EC}$ (2004)	$V_{R,test}/V_{R,NAD}$ (2011)	$V_{R,test}/V_{R,SLA}$ (2003)	$V_{R,test}/V_{R,MC}$ (2010)	$V_{R,test}/V_{R,C SCT}$	$V_{R,test}/V_{R,mod}$
S1	560	1.14 p	0.93 p	0.93 p	1.07 p	1.10 p	0.91 p	0.91 p
S1A	587	1.18 p	0.97 p	0.97 p	1.11 p	1.15 p	0.94 p	0.94 p
S2	693	1.61 o	1.25 w	1.28 o	1.47 w	1.37 w	1.10 w	1.15 w
S3	773	1.61 o	1.19 w	1.31 o	1.51 w	1.36 w	1.08 w	1.13 w
S4	853	1.94 o	1.26 o	1.45 o	1.77 w	1.30 o	1.20 w	1.14 w
S5	853	1.75 o	1.22 o	1.41 o	1.72 w	1.22 o	1.03 w	1.03 o
S6	1040	1.55 o	1.23 o	1.41 o	2.04 w	1.38 o	1.24 w	1.17 o
S7	1120	1.99 o	1.37 o	1.56 o	2.17 w	1.41 o	1.21 w	1.20 o
S8	1200	1.87 o	1.46 o	1.67 o	2.33 w	1.43 o	1.30 w	1.23 o
S9	1227	1.28 o	1.08 o	1.46 c	2.35 w	1.37 c	1.29 w	1.13 w
S10	800	1.49 w	1.27 w	1.27 w	1.67 w	1.56 w	1.25 w	1.26 w
S11	907	1.66 o	1.29 w	1.33 o	1.91 w	1.71 w	1.37 w	1.33 w

**Hegger, J., Häusler, F., and Ricker, M.,** *Zur maximalen Durchstanstragfähigkeit von Flachdecken*, Beton - und Stahlbetonbau, Vol. 102, pp. 770-777, **2007**.

	$l$ [mm]	$h$ [mm]	$d_m$ [mm]	$c$ [mm]		$\rho_L$ [%]	$\rho_w$ [%]	$f_c$ [MPa]	$d_g$ [mm]	$f_y$ [MPa]	$f_{yw}$ [MPa]	system
EM1	2800 (sq)	200	160	290	(sq)	1.96	1.21	29.8	16	558	584	f

	$V_{R,test}$ [kN]	$V_{R,test}/V_{R,ACI}$ (2011)	$V_{R,test}/V_{R,EC}$ (2004)	$V_{R,test}/V_{R,NAD}$ (2011)	$V_{R,test}/V_{R,SIA}$ (2003)	$V_{R,test}/V_{R,MC}$ (2010)	$V_{R,test}/V_{R,CSCCT}$	$V_{R,test}/V_{R,mod}$							
EM1	1213	1.54	c	0.83	c	1.27	c	1.26	c	1.18	c	0.90	c	0.91	c

**Ladner, M.,** *Untersuchungsbericht Durchstanversuche an Flachdeckenausschnitten*, 38 pp., Luzern, **1998**.

	$l$ [mm]	$h$ [mm]	$d_m$ [mm]	$c$ [mm]		$\rho_L$ [%]	$\rho_w$ [%]	$f_c$ [MPa]	$d_g$ [mm]	$f_y$ [MPa]	$f_{yw}$ [MPa]	system
V1	3300 (ci)	280	240	300	(ci)	1.40	-	25.4	32	510	-	-
V2	3300 (ci)	280	240	300	(ci)	1.40	0.79	30.1	32	510	646	g
V4	3300 (ci)	280	240	300	(ci)	1.40	0.79	27.4	32	510	646	g

	$V_{R,test}$ [kN]	$V_{R,test}/V_{R,ACI}$ (2011)	$V_{R,test}/V_{R,EC}$ (2004)	$V_{R,test}/V_{R,NAD}$ (2011)	$V_{R,test}/V_{R,SIA}$ (2003)	$V_{R,test}/V_{R,MC}$ (2010)	$V_{R,test}/V_{R,CSCCT}$	$V_{R,test}/V_{R,mod}$							
V1	1095	1.60	p	1.02	p	1.03	p	1.12	p	1.19	p	0.98	p	0.99	p
V2	1784	1.60	c	0.99	c	1.13	c	1.10	c	1.06	c	0.83	c	1.07	c
V4	1799	1.69	c	1.09	c	1.17	c	1.15	c	1.11	c	0.86	c	1.13	c

**Lips, S., Muttoni, A., and Fernández-Ruiz, M.,** *Durchstanzversuche an Deckenausschnitten mit FIDECA Durchstanzbewehrung*, EPFL-IBéton, 55 pp., Lausanne, Switzerland, **2010**.

**Lips, S., Muttoni, A., and Fernández-Ruiz, M.,** *Durchstanzversuche an Deckenausschnitten mit Durchstanzbewehrung*, EPFL-IBéton, 88 pp., Lausanne, Switzerland, **2012**.

**Lips, S., Muttoni, A., and Fernández-Ruiz, M.,** *Experimental Investigation on the Punching Strength and the Deformation Capacity of Shear-Reinforced Slabs*, ACI Structural Journal, **2012**.

	$l$ [mm]	$h$ [mm]	$d_m$ [mm]	$c$ [mm]	$\rho_L$ [%]	$\rho_w$ [%]	$f_c$ [MPa]	$d_g$ [mm]	$f_y$ [MPa]	$f_{yw}$ [MPa]	system		
PL1	3000	(sq)	250	193	130	(sq)	1.63	-	42.5	16	583	-	-
PL3	3000	(sq)	250	197	520	(sq)	1.59	-	36.5	16	583	-	-
PL4	3000	(sq)	320	267	340	(sq)	1.58	-	30.5	16	562	-	-
PL5	3000	(sq)	400	353	440	(sq)	1.50	-	31.9	16	580	-	-
PL6	3000	(sq)	250	198	130	(sq)	1.59	1.06	36.6	16	583	519	a
PL7	3000	(sq)	250	197	260	(sq)	1.59	1.03	35.8	16	583	519	a
PL8	3000	(sq)	250	200	520	(sq)	1.57	0.97	36.0	16	583	519	a
PL9	3000	(sq)	320	266	340	(sq)	1.59	0.95	32.1	16	562	516	a
PL10	3000	(sq)	400	343	440	(sq)	1.55	0.85	33.0	16	580	563	a
PL11	3000	(sq)	250	201	260	(sq)	1.56	0.25	34.2	16	554	592	a
PL12	3000	(sq)	250	201	260	(sq)	1.56	0.51	34.6	16	554	592	a
PF1	3000	(sq)	250	209	130	(sq)	1.50	0.79	31.1	16	583	536	g
PF2	3000	(sq)	250	208	260	(sq)	1.51	0.79	30.4	16	583	536	g
PF3	3000	(sq)	250	209	520	(sq)	1.50	0.79	37.1	16	583	536	g
PF4	3000	(sq)	320	274	340	(sq)	1.54	0.79	32.5	16	562	550	g
PF5	3000	(sq)	400	354	440	(sq)	1.50	0.79	33.4	16	580	550	g

	$V_{R,test}$ [kN]	$V_{R,test}/V_{R,ACI}$ (2011)	$V_{R,test}/V_{R,EC}$ (2004)	$V_{R,test}/V_{R,NAD}$ (2011)	$V_{R,test}/V_{R,SIA}$ (2003)	$V_{R,test}/V_{R,MC}$ (2010)	$V_{R,test}/V_{R,CSCCT}$	$V_{R,test}/V_{R,mod}$							
PL1	1135	1.37	p	0.86	p	0.99	p	1.12	p	1.15	p	1.00	p	1.01	p
PL3	1324	1.16	p	1.06	p	1.06	p	1.22	p	1.27	p	1.04	p	1.04	p
PL4	1625	1.36	p	1.06	p	1.06	p	1.19	p	1.23	p	1.07	p	1.08	p
PL5	2491	1.18	p	0.99	p	0.99	p	1.05	p	1.09	p	0.96	p	0.98	p
PL6	1363	1.30	c	1.41	c	1.36 (1.00)	c	1.38	c	1.19	w	0.96	c	0.95	c
PL7	1773	1.23	c	0.94	c	1.32 (0.97)	c	1.47	c	1.27	c	1.03	c	0.99	c
PL8	2256	0.98	c	0.87	f	1.27 (0.94)	c	1.41	c	1.24	c	0.97	c	1.06	f
PL9	3132	1.29	c	1.03	c	1.44 (1.06)	c	1.50	c	1.30	c	1.02	c	0.99	c
PL10	5193	1.26	c	1.00	c	1.51 (1.11)	c	1.49	c	1.71	w	1.04	w	0.95	c
PL11	1176	1.11	w	1.03	w	1.03	w	1.46	w	1.32	w	1.01	w	1.11	w
PL12	1633	1.12	c	1.05	w	1.20 (1.05)	c (w)	1.75	w	1.49	w	1.03	w	1.10	w
PF1	1043	1.32	c	1.17	c	1.04	c	1.03	c	1.16	w	0.79	c	0.98	c
PF2	1567	1.46	c	0.90	c	1.15	c	1.28	c	1.20	c	0.96	c	1.02	w
PF3	2242	1.21	c	0.82	f	1.20	c	1.32	c	1.25	c	0.97	c	0.96	c
PF4	2667	1.39	c	0.84	c	1.18	c	1.22	c	1.19	w	0.91	c	0.94	w
PF5	4717	1.45	c	0.87	c	1.32	c	1.29	c	1.42	w	0.98	c	1.06	w

**Marti, P., Pralong, J., and Thürlimann, B.,** *Schubversuche an Stahlbeton-Platten*, Institut für Baustatik und Konstruktion, Nr. 7305-2, 123 pp., Zürich, 1977.

	$l$ [mm]	$h$ [mm]	$d_m$ [mm]	$c$ [mm]	$\rho_L$ [%]	$\rho_w$ [%]	$f_c$ [MPa]	$d_g$ [mm]	$f_y$ [MPa]	$f_{yw}$ [MPa]	system
P2	2750 (ci)	180	152	300 (ci)	1.40	0.00	34.3	16	596		-
P3	2750 (ci)	180	152	300 (ci)	1.40	0.35	33.5	16	596	563	f <sup>1)</sup>

<sup>1)</sup> special shear reinforcement system

	$V_{R,test}$ [kN]	$V_{R,test}/V_{R,ACI}$ (2011)	$V_{R,test}/V_{R,EC}$ (2004)	$V_{R,test}/V_{R,NAD}$ (2011)	$V_{R,test}/V_{R,SIA}$ (2003)	$V_{R,test}/V_{R,MC}$ (2010)	$V_{R,test}/V_{R,CSCT}$	$V_{R,test}/V_{R,mod}$							
P2	628	1.49	p	1.11	p	1.11	p	1.26	p	1.30	p	1.06	p	1.07	p
P3	824	1.32	c	1.03	w	1.05	c	1.66	w	1.34	w	1.01	w	1.00	w

**Marzouk, H. and Jiang, D.,** *Experimental Investigation on Shear Enhancement Types for High-Strength Concrete Plates*, ACI Structural Journal, Vol. 94, pp. 49-58, 1997.

	$l$ [mm]	$h$ [mm]	$d_m$ [mm]	$c$ [mm]	$\rho_L$ [%]	$\rho_w$ [%]	$f_c$ [MPa]	$d_g$ [mm]	$f_y$ [MPa]	$f_{yw}$ [MPa]	system
HS17	1950 (sq)	150	120	250 (sq)	1.09	-	67.0	20	490	-	-
HS22	1950 (sq)	150	120	250 (sq)	1.09	1.47	60.0	20	490	400	a
HS23	1950 (sq)	150	120	250 (sq)	1.09	1.47	60.0	20	490	400	a

	$V_{R,test}$ [kN]	$V_{R,test}/V_{R,ACI}$ (2011)	$V_{R,test}/V_{R,EC}$ (2004)	$V_{R,test}/V_{R,NAD}$ (2011)	$V_{R,test}/V_{R,SIA}$ (2003)	$V_{R,test}/V_{R,MC}$ (2010)	$V_{R,test}/V_{R,CSCT}$	$V_{R,test}/V_{R,mod}$							
HS17	511	1.05	p	1.13	p	1.13	p	1.16	p	1.19	p	0.96	p	0.96	p
HS22	605	1.32	o	1.17	o	1.38	o	1.15	o	1.19	o	1.02	o	1.14	o
HS23	590	1.21	o	1.13	o	1.35	o	1.12	o	1.16	o	1.00	o	1.11	o

**Mueller, F. X., Muttoni, A., and Thürlimann, B.,** *Durchstanzversuche an Flachdecken mit Aussparungen*, IBK - Bericht (ETHZ), Institut für Baustatik und Konstruktion der ETH Zürich, Birkhäuser Verlag, 7305-5, 118 pp., Zürich, 1984.

	$l$ [mm]	$h$ [mm]	$d_m$ [mm]	$c$ [mm]	$\rho_L$ [%]	$\rho_w$ [%]	$f_c$ [MPa]	$d_g$ [mm]	$f_y$ [MPa]	$f_{yw}$ [MPa]	system
P22	2824 (ci)	185	153.5	300 (ci)	1.31	0.89	32.9	16	575	565	d

	$V_{R,test}$ [kN]	$V_{R,test}/V_{R,ACI}$ (2011)	$V_{R,test}/V_{R,EC}$ (2004)	$V_{R,test}/V_{R,NAD}$ (2011)	$V_{R,test}/V_{R,SIA}$ (2003)	$V_{R,test}/V_{R,MC}$ (2010)	$V_{R,test}/V_{R,CSCT}$	$V_{R,test}/V_{R,mod}$							
P22	1044	1.33	o	0.86	f	1.34	c	1.43	c	1.25	c	1.00	c	0.99	o

**Regan, P. E. and Samadian, F.,** *Shear Reinforcement against punching in reinforced concrete flat slabs*, The Structural Engineer, pp. 24-31, **2001**.

	$l$ [mm]	$h$ [mm]	$d_m$ [mm]	$c$ [mm]	$\rho_L$ [%]	$\rho_w$ [%]	$f_c$ [MPa]	$d_g$ [mm]	$f_y$ [MPa]	$f_{yw}$ [MPa]	system
1	3000 (sq)	200	164	200 (sq)	1.26	-	41.7	20	670	-	-
1A	3000 (sq)	200	164	200 (sq)	1.26	-	42.7	20	670	-	-
R1	3000 (sq)	200	164	200 (sq)	1.26	0.57	35.2	20	670	442	a
R2	3000 (sq)	200	164	200 (sq)	1.26	0.49	39.0	20	670	442	a
R3	3000 (sq)	200	164	200 (sq)	1.26	0.49	34.7	20	670	442	a
R4	3000 (sq)	200	164	200 (sq)	1.26	0.57	40.8	20	670	442	a
A1	3000 (sq)	200	160	200 (sq)	1.64	0.40	38.8	20	670	519	a
A2	3000 (sq)	200	160	200 (sq)	1.64	0.34	44.7	20	670	519	a
S1	3000 (sq)	200	160	200 (sq)	1.64	0.40	41.3	20	540	635	f
S2	3000 (sq)	200	160	200 (sq)	1.64	0.70	45.7	20	540	350	f

	$V_{R,test}$ [kN]	$V_{R,test}/V_{R,ACI}$ (2011)	$V_{R,test}/V_{R,EC}$ (2004)	$V_{R,test}/V_{R,NAD}$ (2011)	$V_{R,test}/V_{R,SLA}$ (2003)	$V_{R,test}/V_{R,MC}$ (2010)	$V_{R,test}/V_{R,CSCCT}$	$V_{R,test}/V_{R,mod}$
1	560	1.09 p	0.88 p	0.88 p	1.01 p	1.04 p	0.85 p	0.86 p
1A	587	1.13 p	0.92 p	0.92 p	1.05 p	1.09 p	0.89 p	0.89 p
R1	1050	1.56 o	1.20 o	1.44 o	1.92 w	1.21 o	1.06 w	1.10 w
R2	950	1.42 o	1.05 o	1.26 o	1.76 w	1.21 w	0.99 w	1.05 w
R3	850	1.35 o	0.98 o	1.17 o	1.64 w	1.11 w	0.91 w	0.96 w
R4	950	1.31 o	1.04 o	1.24 o	1.73 w	1.04 o	0.93 w	0.97 w
A1	1000	1.45 o	1.07 o	1.28 o	1.78 w	1.05 o	1.03 w	1.08 w
A2	950	1.37 o	1.02 w	1.16 o	1.61 w	1.25 w	0.99 w	1.06 w
S1	900	1.35 o	0.99 w	0.99 w	1.59 w	1.12 w	0.88 w	0.89 w
S2	950	1.35 o	0.80 o	0.99 c	1.62 w	1.11 w	0.92 w	0.93 w

**Rizk, E., Marzouk, H., and Hussein, A.,** *Punching Shear of Thick Plates with and without Shear Reinforcement*, ACI Structural Journal, Vol. 108, No. 5, pp. 581-591, **2011**.

	$l$ [mm]	$h$ [mm]	$d_m$ [mm]	$c$ [mm]	$\rho_L$ [%]	$\rho_w$ [%]	$f_c$ [MPa]	$d_g$ [mm]	$f_y$ [MPa]	$f_{yw}$ [MPa]	system
HSS2	2650 (sq)	300	217.5	400 (sq)	1.42	0.41	79.0	19	460	400	c

	$V_{R,test}$ [kN]	$V_{R,test}/V_{R,ACI}$ (2011)	$V_{R,test}/V_{R,EC}$ (2004)	$V_{R,test}/V_{R,NAD}$ (2011)	$V_{R,test}/V_{R,SLA}$ (2003)	$V_{R,test}/V_{R,MC}$ (2010)	$V_{R,test}/V_{R,CSCCT}$	$V_{R,test}/V_{R,mod}$
HSS2	2172	1.22 o	1.09 o	1.36 o	1.53 w	1.34 o	1.05 o	1.05 w

**Seible, F., Ghali, A., and Dilger, W. H.,** *Preassembled shear reinforcing units for flat plates,* ACI Journal, Proceedings 77, No. 1, pp. 28-35, **1980.**

	$l$ [mm]	$h$ [mm]	$d_m$ [mm]	$c$ [mm]	$\rho_L$ [%]	$\rho_w$ [%]	$f_c$ [MPa]	$d_g$ [mm]	$f_y$ [MPa]	$f_{yw}$ [MPa]	system		
SC7	1800	(sq)	150	121	305	(sq)	1.17	0.38	33.6	13	450	350	c
SC8	1800	(sq)	150	121	305	(sq)	1.17	0.42	33.6	13	450	490	g
SC9	1800	(sq)	150	121	305	(sq)	1.17	0.28	33.6	13	450	490	g
SC10	1800	(sq)	150	121	305	(sq)	1.17	0.31	33.6	13	450	490	g
SC11	1800	(sq)	150	121	305	(sq)	1.17	0.15	33.6	13	450	500	b
SC12	1800	(sq)	150	121	305	(sq)	1.17	0.33	33.6	13	450	500	b
SC13	1800	(sq)	150	121	305	(sq)	1.17	0.73	33.6	13	450	500	b

	$V_{R,test}$ [kN]	$V_{R,test}/V_{R,ACI}$ (2011)	$V_{R,test}/V_{R,EC}$ (2004)	$V_{R,test}/V_{R,NAD}$ (2011)	$V_{R,test}/V_{R,SIA}$ (2003)	$V_{R,test}/V_{R,MC}$ (2010)	$V_{R,test}/V_{R,CSCT}$	$V_{R,test}/V_{R,mod}$							
SC7	623	1.56	o	1.10	o	1.37	o	1.69	w	1.32	o	1.11	o	1.36	o
SC8	592	1.49	o	1.04	o	1.30	o	1.48	w	1.26	o	1.06	o	1.28	o
SC9	594	1.49	o	1.05	o	1.30	o	1.61	w	1.26	o	1.06	o	1.17	o
SC10	537	1.35	o	0.95	o	1.18	o	1.45	w	1.14	o	0.96	o	0.99	o
SC11	596	1.50	o	1.34	w	1.34	w	1.61	w	1.32	w	1.12	w	1.33	w
SC12	595	1.49	o	1.05	o	1.30	o	1.61	w	1.31	w	1.06	o	1.11	o
SC13	580	1.46	o	1.02	o	1.27	o	1.12	o	1.23	o	1.04	o	1.08	o

**Stein, T., Ghali, A., and Dilger, W. H.,** *Distinction between Punching and Flexural Failure Modes of Flat Plates,* ACI Structural Journal, Vol. 104, pp. 357-365, **2007.**

	$l$ [mm]	$h$ [mm]	$d_m$ [mm]	$c$ [mm]	$\rho_L$ [%]	$\rho_w$ [%]	$f_c$ [MPa]	$d_g$ [mm]	$f_y$ [MPa]	$f_{yw}$ [MPa]	system		
V2	1900	(sq)	150	118	250	(sq)	0.98	0.62	26.2	14	438	457	a
V3	1900	(sq)	150	118	250	(sq)	0.62	0.62	25.7	14	438	457	a

	$V_{R,test}$ [kN]	$V_{R,test}/V_{R,ACI}$ (2011)	$V_{R,test}/V_{R,EC}$ (2004)	$V_{R,test}/V_{R,NAD}$ (2011)	$V_{R,test}/V_{R,SIA}$ (2003)	$V_{R,test}/V_{R,MC}$ (2010)	$V_{R,test}/V_{R,CSCT}$	$V_{R,test}/V_{R,mod}$							
V2	438	1.39	o	1.18	o	1.41	o	1.19	o	1.25	o	1.00	o	1.00	o
V3	365	1.17	o	1.16	o	1.38	o	1.22	o	1.28	o	1.16	o	1.24	o

**Tolf, P.**, *Influence of the slab thickness on the strength of concrete slabs at punching. Tests with circular slabs. (In Swedish: Plattjocklekens inverkan på betongplattors hållfasthet vid genomstansning. Försök med cirkulära plattor.)*, Royal Institute of Technology, Dep. of Structural Mechanics and Engineering, Bulletin 146, 64 pp., **1988**.

	$l$ [mm]		$h$ [mm]	$d_m$ [mm]	$c$ [mm]		$\rho_L$ [%]	$\rho_w$ [%]	$f_c$ [MPa]	$d_g$ [mm]	$f_y$ [MPa]	$f_{yw}$ [MPa]	system
S1.1	1270	(ci)	120	100	125	(ci)	0.80	-	30.1	16	706	-	-
S1.2	1270	(ci)	120	99	125	(ci)	0.81	-	23.8	16	701	-	-
S1.3	1270	(ci)	120	98	125	(ci)	0.35	-	26.0	16	720	-	-
S1.4	1270	(ci)	120	99	125	(ci)	0.34	-	25.5	16	712	-	-
S1.1s	1270	(ci)	120	97	125	(ci)	0.82	0.55	24.1	16	706	610	f
S1.2s	1270	(ci)	120	99	125	(ci)	0.81	0.54	24.8	16	711	630	f
S1.3s	1270	(ci)	120	100	125	(ci)	0.34	0.54	23.4	16	709	620	f
S1.4s	1270	(ci)	120	99	125	(ci)	0.34	0.54	24.0	16	710	620	f
S2.1	2540	(ci)	240	200	250	(ci)	0.80	-	19.4	32	657	-	-
S2.2	2540	(ci)	240	199	250	(ci)	0.80	-	18.9	32	670	-	-
S2.3	2540	(ci)	240	200	250	(ci)	0.34	-	19.3	32	668	-	-
S2.4	2540	(ci)	240	197	250	(ci)	0.35	-	21.6	32	664	-	-
S2.1s	2540	(ci)	240	195	250	(ci)	0.82	0.27	19.3	32	669	700	f
S2.2s	2540	(ci)	240	195	250	(ci)	0.82	0.27	19.7	32	673	640	f
S2.3s	2540	(ci)	240	198	250	(ci)	0.34	0.27	21.8	32	671	670	f
S2.4s	2540	(ci)	240	198	250	(ci)	0.34	0.27	21.7	32	669	670	f

	$V_{R,test}$ [kN]	$V_{R,test}/V_{R,ACI}$ (2011)		$V_{R,test}/V_{R,EC}$ (2004)		$V_{R,test}/V_{R,NAD}$ (2011)		$V_{R,test}/V_{R,SIA}$ (2003)		$V_{R,test}/V_{R,MC}$ (2010)		$V_{R,test}/V_{R,CSCCT}$	$V_{R,test}/V_{R,mod}$		
S1.1	216	1.67	p	1.26	p	1.27	p	1.22	p	1.26	p	1.02	p	1.03	p
S1.2	194	1.71	p	1.24	p	1.24	p	1.22	p	1.25	p	1.03	p	1.04	p
S1.3	145	1.24	p	1.21	p	1.21	p	1.19	p	1.23	p	0.97	p	0.99	p
S1.4	148	1.26	p	1.23	p	1.24	p	1.21	p	1.26	p	1.00	p	1.01	p
S1.1s	261	2.27	o	1.34	o	1.34	o	1.16	w	1.09	o	0.89	o	0.98	o
S1.2s	259	2.16	o	1.29	o	1.29	o	1.09	w	1.04	o	0.85	o	0.94	o
S1.3s	144	1.22	o	0.96	o	0.97	o	0.84	f	0.84	f	0.84	c	0.96	o
S1.4s	147	1.25	o	0.99	o	0.99	o	0.87	f	0.87	f	0.87	c	0.99	o
S2.1	603	1.45	p	1.02	p	1.03	p	1.08	p	1.14	p	0.91	p	0.92	p
S2.2	600	1.48	p	1.03	p	1.04	p	1.09	p	1.16	p	0.93	p	0.94	p
S2.3	489	1.18	p	1.10	p	1.11	p	1.17	p	1.26	p	0.95	p	0.96	p
S2.4	444	1.04	p	0.98	p	0.98	p	1.04	p	1.13	p	0.84	p	0.86	p
S2.1s	894	2.15	o	1.23	o	1.23	o	1.66	w	1.36	w	1.03	w	0.98	w
S2.2s	851	2.03	o	1.16	o	1.16	o	1.56	w	1.28	w	0.97	w	0.93	w
S2.3s	562	1.25	o	0.97	o	0.98	o	1.11	w	0.97	o	0.88	c	1.00	o
S2.4s	542	1.21	o	0.94	o	0.94	o	1.07	w	0.94	o	0.86	c	0.97	o



**Vollum, R. L., Abdel-Fattah, T., Eder, M., and Elghazouli, A.Y. , *Design of ACI-type punching shear reinforcement to Eurocode 2*, Magazine of Concrete Research, 62-01, pp. 3-16, 2010.**

	$l$ [mm]	$h$ [mm]	$d_m$ [mm]	$c$ [mm]	$\rho_L$ [%]	$\rho_w$ [%]	$f_c$ [MPa]	$d_g$ [mm]	$f_y$ [MPa]	$f_{yw}$ [MPa]	system
S1	3000 (sq)	220	174	270 (sq)	1.28	-	24.0	20	567	-	-
S2	3000 (sq)	220	174	270 (sq)	1.28	0.29	24.0	20	567	560	f
S3	3000 (sq)	220	174	270 (sq)	1.28	0.29	27.2	20	567	560	f
S4	3000 (sq)	220	174	270 (sq)	1.28	0.18	27.2	20	567	485	f
S5	3000 (sq)	220	174	270 (sq)	1.28	0.37	23.2	20	567	485	f
S6	3000 (sq)	220	174	270 (sq)	0.64	0.37	23.2	20	567	485	f

	$V_{R,test}$ [kN]	$V_{R,test}/V_{R,ACI}$ (2011)	$V_{R,test}/V_{R,EC}$ (2004)	$V_{R,test}/V_{R,NAD}$ (2011)	$V_{R,test}/V_{R,SIA}$ (2003)	$V_{R,test}/V_{R,MC}$ (2010)	$V_{R,test}/V_{R,CSCCT}$	$V_{R,test}/V_{R,mod}$
S1	614	1.22 p	0.96 p	0.96 p	1.11 p	1.15 p	0.96 p	0.97 p
S2	843	1.11 c	1.18 o	1.32 o	1.52 w	1.22 o	1.00 o	1.01 o
S3	903	1.33 o	1.22 o	1.35 o	1.56 w	1.25 o	1.03 o	1.04 o
S4	906	1.33 w	1.22 o	1.36 o	1.56 w	1.35 w	1.08 w	1.15 w
S5	872	1.17 c	1.24 o	1.38 o	1.59 w	1.27 o	1.05 o	1.05 o
S6	740	1.09 f	1.32 o	1.47 o	1.47 w	1.43 o	1.21 o	1.24 o



## Appendix B Example PL7

Given slab parameters

$h =$	250 mm	$\rho =$	1.59%	$f_c =$	35.8 MPa
$d =$	197 mm	$d_w =$	14 mm	$E_c =$	33000 MPa
$l =$	3000 mm	$A_{sw1} =$	2463 mm <sup>2</sup>	$f_{ct} =$	3.26 MPa
$c =$	260 mm	$s_0 =$	80 mm	$d_g =$	16 mm
$r_q =$	1505 mm	$s_1 =$	160 mm	$f_y =$	583 MPa
$b =$	1200 mm	$l_{ai} =$	104 mm	$E_s =$	200000 MPa
$b_1 =$	120 mm	$l_{as} =$	106 mm	$f_{yw} =$	519 MPa
		$n_{cut} =$	1	$E_{sw} =$	200000 MPa

Constant parameters

$$r_c = \frac{2}{\pi} \cdot c = 165.5 \text{ mm} \quad \text{Eq. 8.4}$$

$$r_s = \frac{8}{l - c} \cdot \frac{\left(l^2 - l \cdot c - \frac{c^2}{4}\right) \cdot (r_q - r_c)}{2\pi \cdot [l + b - 2 \cdot (c + b_1)]} = 1484 \text{ mm} \quad \text{Eq. 8.7}$$

$$r_1 = r_c + s_0 + \frac{s_1}{2} \cdot (n_{cut} - 1) = 245.5 \text{ mm}$$

$$r_2 = r_c + s_0 + s_1 \cdot n_{cut} = 405.5 \text{ mm}$$

$$r_0 = \max(r_c + 1.5d; r_2 + 0.5d) = 504 \text{ mm} \quad \text{Eq. 7.69}$$

$$\beta = 0.75$$

$$b_0 = (2r_c + d)\pi = 1659 \text{ mm}$$

$$\lambda_s = \frac{s_0 + \frac{s_1}{2}}{d} = 0.81 \quad \text{Eq. 7.75}$$

$$\tan(\alpha_b) = 0.5$$

$$s_c = s_0 = 80 \text{ mm}$$

$$w_{lim,1} = \frac{4 \cdot \tau_b}{E_s \cdot d_w} \cdot l_{ai}^2 = 0.10 \text{ mm} \quad \text{Eq. 7.51}$$

$$w_{lim,2} = \frac{2 \cdot \tau_b}{E_s \cdot d_w} \cdot [(l_{as} + l_{ai})^2 - 2 \cdot l_{ai}^2] = 0.10 \text{ mm} \quad \text{Eq. 7.55}$$

$$k_2 = 0.75$$

$$\kappa = 0.35$$

Moment-curvature relationship

$$EI_0 = \frac{E_c \cdot h^3}{12} = 4.29 \cdot 10^{10} \text{ Nmm}^2 \quad \text{Eq. 7.7}$$

$$x_{el} = \rho \cdot \beta \cdot \frac{E_s}{E_c} \cdot d \cdot \left( \sqrt{1 + \frac{2 \cdot E_c}{\rho \cdot \beta \cdot E_s}} - 1 \right) = 62.1 \text{ mm} \quad \text{Eq. 7.10}$$

$$EI_1 = \rho \cdot \beta \cdot E_s \cdot d^3 \cdot \left( 1 - \frac{x_{el}}{d} \right) \cdot \left( 1 - \frac{x_{el}}{3d} \right) = 1.12 \cdot 10^{10} \text{ Nmm}^2 \quad \text{Eq. 7.9}$$

$$m_{cr} = \frac{f_{ct} \cdot h^2}{6} = 33.9 \text{ kNm/m} \quad \text{Eq. 7.6}$$

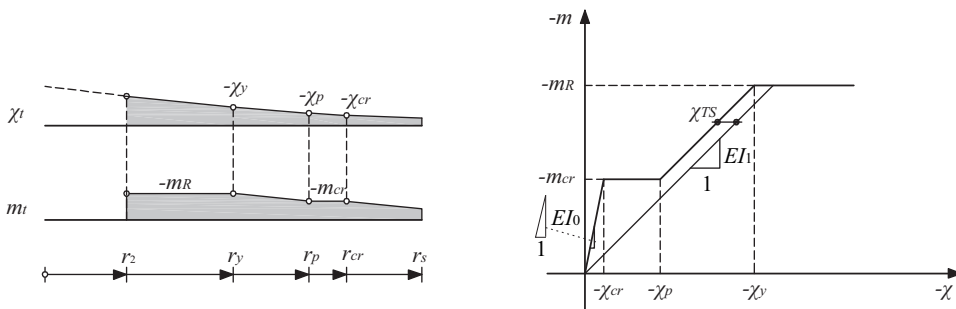
$$m_R = \rho \cdot f_y \cdot d^2 \cdot \left( 1 - \frac{\rho \cdot f_y}{2 \cdot f_c} \right) = 314 \text{ kNm/m} \quad \text{Eq. 7.11}$$

$$\chi_{cr} = \frac{m_{cr}}{EI_0} = \frac{2 \cdot f_{ct}}{h \cdot E_c} = 7.91 \cdot 10^{-7} \text{ mm}^{-1} \quad \text{Eq. 7.8}$$

$$\chi_{TS} = \frac{f_{ct}}{\rho \cdot \beta \cdot E_s} \cdot \frac{1}{6 \cdot h} = 9.08 \cdot 10^{-7} \text{ mm}^{-1} \quad \text{Eq. 7.12}$$

$$\chi_p = \frac{m_{cr}}{EI_1} - \chi_{TS} = 2.12 \cdot 10^{-6} \text{ mm}^{-1} \quad \text{Eq. 7.13}$$

$$\chi_y = \frac{m_R}{EI_1} - \chi_{TS} = 2.71 \cdot 10^{-5} \text{ mm}^{-1} \quad \text{Eq. 7.14}$$

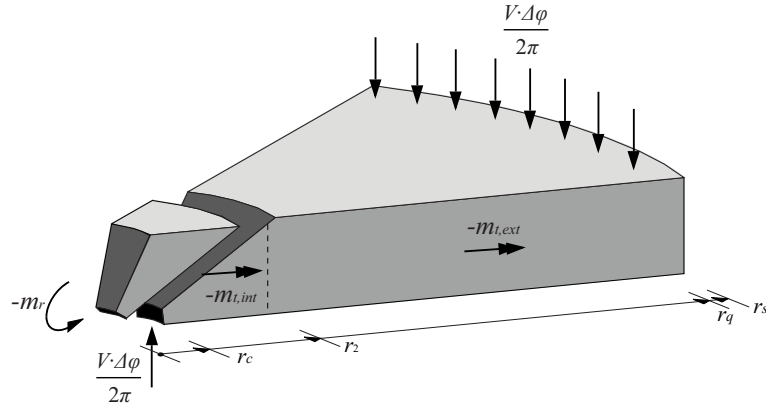


Parameters for quadratic rotation function

$$a = \frac{2}{r_c + r_0} = 2.99 \cdot 10^{-3} \text{ mm}^{-1} \quad \text{Eq. 7.3}$$

$$c = -\frac{a}{2(r_0 - r_c)} = -4.41 \cdot 10^{-6} \text{ mm}^{-2} \quad \text{Eq. 7.4}$$

This example shows the calculation for a rotation of  $\psi_0=25\%$ . In order to obtain the punching strength, the rotation needs to be adjusted until the shear force of the calculated load-rotation response  $V$  corresponds to the punching strength  $V_R$ .



In a first step the tangential moments at the outer perimeter can be calculated:

$$\chi_t @ r_0 = \frac{\psi_0}{r_0} = 4.96 \cdot 10^{-5} \text{ mm}^{-1} \quad \text{Eq. 7.5}$$

$$\chi_t @ r_0 > \chi_y \rightarrow r_y = \frac{\psi_0}{\chi_y} = 922 \text{ mm} \quad \text{Eq. 7.30}$$

$$\chi_t @ r_0 > \chi_p \rightarrow r_p = \frac{\psi_0}{\chi_p} \leq r_s \rightarrow r_p = 1484 \text{ mm} \quad \text{Eq. 7.31}$$

$$\chi_t @ r_0 > \chi_{cr} \rightarrow r_{cr} = \frac{\psi_0}{\chi_{cr}} \leq r_s \rightarrow r_{cr} = 1484 \text{ mm} \quad \text{Eq. 7.32}$$

$$\Delta\varphi \int_{r_2}^{r_s} m_{t,ext} \cdot dr = \Delta\varphi \int_{r_0}^{r_s} m_t \cdot dr + \Delta\varphi \int_{r_2}^{r_0} m_t \cdot dr \quad \text{Eq. 7.27}$$

As the tangential moment within the area between  $r_2$  and  $r_0$  is equal to the flexural strength, the integration of the tangential moment becomes:

$$\int_{r_2}^{r_0} m_t \cdot dr = m_R \cdot (r_0 - r_2) = 30.9 \text{ kNm} \quad \text{Eq. 7.33}$$

Since  $r_p$  and  $r_{cr}$  is equal to  $r_s$ , the general equation

$$\int_{r_0}^{r_s} m_t \cdot dr = \left[ \begin{array}{l} m_R(r_y - r_0) + EI_1\psi_0 \ln\left(\frac{r_p}{r_y}\right) \\ + EI_1\chi_{TS}(r_p - r_y) + m_{cr}(r_{cr} - r_p) + EI_0\psi_0 \ln\left(\frac{r_s}{r_{cr}}\right) \end{array} \right] \quad \text{Eq. 7.28}$$

can be simplified to

$$\int_{r_0}^{r_s} m_t \cdot dr = \left[ m_R(r_y - r_0) + EI_1 \psi_0 \ln\left(\frac{r_s}{r_y}\right) + EI_1 \chi_{TS}(r_s - r_y) \right] = 270 \text{ kNm}$$

Thus, the integral of the tangential moment at the outer slab segment becomes

$$\Delta\varphi \int_{r_2}^{r_s} m_{t,ext} \cdot dr = 301 \text{ kNm} \cdot \Delta\varphi$$

Inner slab element

$$\chi_{r,lim} = \frac{\chi_y}{[2 \cdot c \cdot (r_1 - r_c) + a]} \cdot [2 \cdot c \cdot (r_2 - r_c) + a] = 1.03 \cdot 10^{-5} \text{ mm}^{-1} \quad \text{Eq. 7.68}$$

$$\chi_r @ r_2 = -[2 \cdot c \cdot (r_2 - r_c) + a] \cdot \psi_0 \leq \chi_{r,lim} \rightarrow \chi_r @ r_2 = 1.03 \cdot 10^{-5} \text{ mm}^{-1} \quad \text{Eq. 7.15}$$

$$\chi_p < \chi_r \rightarrow \sigma_s = (\chi_p + \chi_{TS}) \cdot (d - x_{el}) \cdot E_s \cdot \beta = 227 \text{ MPa} \leq f_y \quad \text{Eq. 7.16}$$

$$C_{r_2} = \rho \cdot d \cdot \sigma_s \cdot 2\pi r_2 = 1820 \text{ kN} \quad \text{Eq. 7.17}$$

Since the radial and the tangential moment need to be found by iteration, a start value of them need to be chosen. However, for the first step, it is easier to estimate the height of the compression zone. Thus, the assumption of

$$x_1 = x_{el} = 62.1 \text{ mm}$$

and

$$x_c = \frac{x_1}{3} = 20.7 \text{ mm}$$

leads to the moment

$$m_r = x_1 \cdot f_c \cdot \left(d - \frac{x_1}{2}\right) = 369 \text{ kNm/m} \quad \text{Eq. 7.22}$$

and

$$m_{t,int} = x_c \cdot f_c \cdot \left(d - \frac{x_c}{2}\right) = 138 \text{ kNm/m} \quad \text{Eq. 7.23}$$

With this, a first approximation of the shear force is obtained.

$$V \cdot \frac{\Delta\varphi}{2\pi} \cdot (r_q - r_c) = -\Delta\varphi \cdot m_r \cdot r_c - \Delta\varphi \cdot m_{t,int}(r_2 - r_c) - \Delta\varphi \int_{r_2}^{r_s} m_{t,ext} \cdot dr \quad \text{Eq. 7.26}$$

$$V = \frac{2\pi}{(r_q - r_c)} \cdot \left[ m_r \cdot r_c + m_{t,int}(r_2 - r_c) + \int_{r_2}^{r_s} m_{t,ext} \cdot dr \right] = 1855 \text{ kN}$$

Failure criterion: failure within shear reinforced area

$$V_{Rc} = \frac{\frac{3}{4} \cdot b_0 \cdot d \cdot \sqrt{f_c}}{1 + \frac{15 \cdot \psi_0 \cdot d}{d_{g,0} + d_g}} = 443 \text{ kN} \quad \text{Eq. 7.42}$$

$$w_1 = \kappa \cdot \psi \cdot s_0 = 0.70 \text{ mm} \quad \text{Eq. 7.46}$$

$$\sigma_{w1} = \frac{E_s \cdot w_i}{l_{as} + l_{ai}} + \frac{2 \cdot \tau_b}{d_w} \cdot \frac{l_{as}^2 + l_{ai}^2}{l_{as} + l_{ai}} \leq f_{yw} \rightarrow \sigma_{w1} = 519 \text{ MPa} \quad \text{Eq. 7.56}$$

$$V_{Rs,I} = A_{sw} \cdot \sigma_w(\psi) = 1278 \text{ kN} \quad \text{Eq. 7.45}$$

$$V_{R,I} = \frac{V_{Rs,1}}{\lambda_s} + V_{Rc} = 2017 \text{ kN} \quad \text{Eq. 7.44}$$

Failure criterion: crushing of the concrete strut

$$x_2 = \frac{2}{3} \cdot x_{el} = 41.4 \text{ mm}$$

$$k_1 = \frac{1}{1.0 + 135 \cdot \frac{\psi_0 \cdot (d - x_2)}{r_2}} = 0.436 \quad \text{Eq. 7.61}$$

$$V_{Rs,II} = k_1 \cdot k_2 \cdot f_c \cdot \left(r_c + \frac{s_c}{2}\right) \cdot 2\pi \cdot s_c = 1209 \text{ kN} \quad \text{Eq. 7.63}$$

$$V_{R,II} = \frac{V_{Rs,1}}{\lambda_s} + V_{Rc} = 1931 \text{ kN} \quad \text{Eq. 7.44}$$

From the previously calculated values, one can determine a new set of parameters:

$$\lambda = \frac{V_R - V_{Rc}}{V_R} \cdot \lambda_s = 0.626 \quad \text{Eq. 7.71}$$

$$C_a = \lambda \cdot V \cdot \frac{r_1 - r_c}{d - \frac{x_1}{2}} = 560 \text{ kN} \quad \text{Eq. 7.21}$$

$$C_b = (1 - \lambda) \cdot V \cdot \cot \alpha_b = 1389 \text{ kN} \quad \text{Eq. 7.18}$$

$$C_c = C_{r2} - C_b = 431 \text{ kN} \quad \text{Eq. 7.19}$$

$$x_c = \frac{C_c}{f_c \cdot 2\pi r_2} = 4.7 \text{ mm} \quad \text{Eq. 7.25}$$

$$x_1 = \frac{C_b + C_a}{f_c \cdot 2\pi r_c} + x_c = 57.1 \text{ mm} \quad \text{Eq. 7.24}$$

$$m_r = x_1 \cdot f_c \cdot \left(d - \frac{x_1}{2}\right) = 344 \text{ kNm/m} \quad \text{Eq. 7.22}$$

$$m_{t,int} = x_c \cdot f_c \cdot \left(d - \frac{x_c}{2}\right) = 33.0 \text{ kNm/m} \quad \text{Eq. 7.23}$$

$$V = \frac{2\pi}{(r_q - r_c)} \cdot \left[ m_r \cdot r_c + m_{t,int}(r_2 - r_c) + \int_{r_2}^{r_s} m_{t,ext} \cdot dr \right] = 1718 \text{ kN}$$

$$x_2 = \frac{C_b}{f_c \cdot 2\pi r_c} + x_c = 42.0 \text{ mm}$$

$$k_1 = \frac{1}{1.0 + 135 \cdot \frac{\psi_0 \cdot (d - x_2)}{r_2}} = 0.437 \quad \text{Eq. 7.61}$$

$$V_{RS1} = k_1 \cdot k_2 \cdot f_c \cdot \left(r_c + \frac{s_c}{2}\right) \cdot 2\pi \cdot s_c = 1211 \text{ kN} \quad \text{Eq. 7.63}$$

$$V_{R,II} = \frac{V_{RS,1}}{\lambda_s} + V_{Rc} = 1935 \text{ kN} \quad \text{Eq. 7.44}$$



Calculation of new set of parameters

$$\lambda = \frac{V_R - V_{RC}}{V_R} \cdot \lambda_s = 0.626 \quad \text{Eq. 7.71}$$

$$C_a = \lambda \cdot V \cdot \frac{r_1 - r_c}{d - \frac{x_1}{2}} = 511 \text{ kN} \quad \text{Eq. 7.21}$$

$$C_b = (1 - \lambda) \cdot V \cdot \cot \alpha_b = 1284 \text{ kN} \quad \text{Eq. 7.18}$$

$$C_c = C_{r2} - C_b = 536 \text{ kN} \quad \text{Eq. 7.19}$$

$$x_c = \frac{C_c}{f_c \cdot 2\pi r_2} = 5.87 \text{ mm} \quad \text{Eq. 7.25}$$

$$x_1 = \frac{C_a + C_b}{f_c \cdot 2\pi r_c} + x_c = 54.1 \text{ mm} \quad \text{Eq. 7.24}$$

$$m_r = x_1 \cdot f_c \cdot \left(d - \frac{x_1}{2}\right) = 329 \text{ kNm/m} \quad \text{Eq. 7.22}$$

$$m_{t_{int}} = x_c \cdot f_c \cdot \left(d - \frac{x_c}{2}\right) = 40.8 \text{ kNm/m} \quad \text{Eq. 7.23}$$

$$V = \frac{2\pi}{(r_q - r_c)} \cdot \left[ m_r \cdot r_c + m_{t_{int}}(r_2 - r_c) + \int_{r_2}^{r_s} m_{t_{ext}} \cdot dr \right] = 1715 \text{ kN}$$

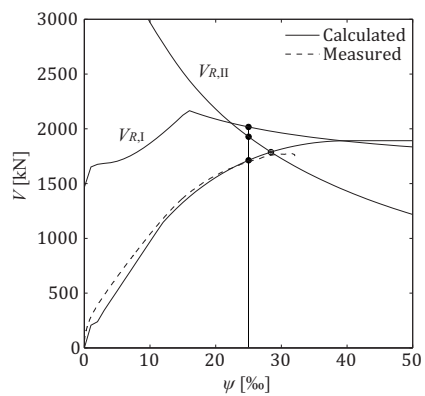
$$x_2 = \frac{C_b}{f_c \cdot 2\pi r_c} + x_c = 40.4 \text{ mm}$$

$$k_1 = \frac{1}{1.0 + 135 \cdot \frac{\psi_0 \cdot (d - x_2)}{r_2}} = 0.434 \quad \text{Eq. 7.61}$$

$$V_{RS1} = k_1 \cdot k_2 \cdot f_c \cdot \left(r_c + \frac{s_c}{2}\right) \cdot 2\pi \cdot s_c = 1204 \text{ kN} \quad \text{Eq. 7.63}$$

$$V_{R,II} = \frac{V_{RS1}}{\lambda_s} + V_{RC} = 1926 \text{ kN} \quad \text{Eq. 7.44}$$

Already after two iterations, the difference in results between the iteration steps is small. Thus, the rotation can be changed to calculate the next points of the load-rotation curve and the failure criterion curves.



## Appendix C Shear Reinforcement Ratio

Within this thesis the shear reinforcement ratio is for regularly distributed shear reinforcement defined by the cross sectional area of shear reinforcement within a unit area or for radially or orthogonally arranged shear reinforcement calculated at a control perimeter set at  $d/2$  of the border of the support region where  $d$  is the effective depth. In the latter case, the shear reinforcement is given by:

$$\rho_w = \frac{A_{sw,i} \cdot n_r}{b_0 \cdot s} \quad (\text{C.1})$$

where  $b_0$  is the control perimeter set at  $d/2$  of the border of the support region,  $A_{sw,i}$  is the cross sectional area of one vertical branch of the shear reinforcement,  $n_r$  is the number of vertical branches of shear reinforcement in the first perimeter and  $s$  is defined by:

$$s = s_0 + \frac{s_1}{2} > s_1 \quad (\text{C.2})$$

Where  $s_0$  is the distance between the border of the support region and the first perimeter of shear reinforcement and  $s_1$  is the distance between the first and the second perimeter of shear reinforcement.

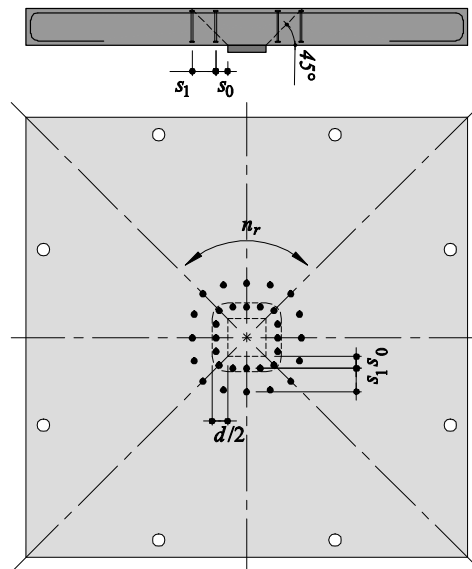


Figure C.1: Definitions of parameters used for the calculation of the shear reinforcement ratio



# ***Curriculum Vitae***

## ***Personal***

Name	Lips
First name	Stefan
Date of birth	December 4, 1980
Birthplace	Zurich, Switzerland
Nationality	Swiss
E-Mail	stlips@bluewin.ch

## ***Education***

MS in Civil Engineering, Georgia Institute of Technology, Atlanta GA, USA, 2007  
BS in Civil Engineering, University of Applied Sciences Rapperswil, Switzerland, 2004  
Vocational Degree as a Structural Drafter, Zurich, Switzerland, 2000

## ***Work Experience***

Research Assistant, Ecole Polytechnique Fédérale de Lausanne, Switzerland, 2008-2012  
Project Engineer, University of Applied Sciences Rapperswil, Switzerland, 2004-2006  
Structural Drafter Apprentice, WEWO AG Zurich, Switzerland, 1996-2000

## ***Languages***

German, native language  
English, fluent  
French, intermediate

## ***Professional Affiliations***

Swiss Engineering, STV  
American Concrete Institute, ACI  
Fédération internationale du béton *fib*  
Gesellschaft für Ingenieurbaukunst

## ***Selected Publications***

**Lips, S., Muttoni, A., and Fernández-Ruiz, M.,** *Experimental Investigation on the Punching Strength and the Deformation Capacity of Shear-Reinforced Slabs*, ACI Structural Journal, USA, (Accepted for publication)

**Tassinari L., Lips S., Muttoni A., Fernández Ruiz M.,** *Applications of bent-up bars as shear and integrity reinforcement in R/C slabs*, Proceedings of the fib Symposium Prague 2011, pp. 631-634, Prague, Czech Republic, 2011.

**Lips S., Muttoni A., Fernández Ruiz M.,** *NMC2010 - Punching shear of flat slabs: Design example*, Ecole Polytechnique Fédérale de Lausanne, 13 pp., Lausanne, Switzerland, 2010.

**Lips S., Muttoni A.,** *Experimental investigation of reinforced concrete slabs with punching shear reinforcement*, Proceedings of the 8th fib-PhD Symposium, pp. 105-110, Copenhagen, Denmark, 2010.